Spring 2018

Fine Structure in the Ionosphere

Bruce Fritz
University of New Hampshire, Durham

Fine Structure in the Ionosphere

BY

Bruce Fritz

B.S. in Physics, United States Air Force Academy, 2008

DISSERTATION

Submitted to the University of New Hampshire
in partial fulfillment of
the requirements for the degree of

Doctor of Philosophy

in

Physics

May, 2018

This dissertation has been examined and approved in partial fulfillment of the requirements for the degree of Doctor of Philosophy in Physics by:

Dissertation Director, Marc Lessard
Assistant Professor of Physics, University of New Hampshire

Roy Torbert
Professor of Physics

Lynn Kistler
Professor of Physics

Kristina Lynch
Professor of Physics and Astronomy, Dartmouth College

Jiadong Zang
Professor of Physics

On April 20, 2018

Original approval signatures are on file with the University of New Hampshire Graduate School.

Acknowledgments

First and foremost, I would like to thank my advisor, Marc, for the incredible opportunities he gave me as a graduate student. My experiences over the past five years have been absolutely amazing, unlike anything I could have ever imagined. From field work at the South Pole to the rocket launch in Norway, I couldn't have asked for a more memorable time as a student. The faith he showed in my ability to function independently has given me the confidence to succeed on my own, and I will be forever grateful.

My work at UNH would not have been possible without the help of many, many people. Mark Widholm and Paul Riley were both critical in the success of my instrumentation work. I am grateful to Phil Demaine and Aaron Bolton for helping me troubleshoot mechanical designs, and especially for accomodating my panic-stricken, last-minute changes leading up to RENU 2 integration. I am also grateful for Stan Ellis and Todd Jones who always had time to discuss ideas and had the patience to teach me how to solder like a professional.

I want to thank everyone that helped make RENU 2 a success. Kristina Lynch, Jim Clemmons, Jim Hecht and Steve Powell were all critical to the success of the mission. Dave Collins and Meghan Harrington from Dartmouth were extremely helpful throughout integration and the launch campaign. Meghan's comic relief during the launch window was even appreciated during some of the super early mornings at the observatory. Fellow MIRL graduate students Ian Cohen and Kristoff Paulsen were a huge part of preparing the RENU 2 instruments and David Kenward has been crucial helping in the post-launch analysis. Several MIRL undergraduate students were also critical to mission success, including Chrystal Moser, Meghan Fischer, Tyler Chapman, and Anthony Velte. Finally, the NASA Wallops

team was incredible in their support of the RENU 2 mission and none of this would have been possible without their tireless support.

Outside of the primary mission, I want to thank Supriya Chakrabarti, Tim Cook, and several of their students at UMass Lowell for helping with UV PMT calibration. I also would like to thank Ken Dymond at NRL for joining the analysis effort on RENU 2 so late in the game. The SSULI analysis was the key to pull the rocket work together for this dissertation and I don't know where I'd be without it. I hope all future collaborators are as easy to work with as those I've met at UML and NRL.

My trip to the South Pole would not have been possible without the financial support of Bob Clauer at Virginia Tech. I also want to thank Zhonghua Xu and Peter Marquis for keeping me alive and sane down on the ice. The logistical and science support at both McMurdo and South Pole Stations were top notch and made for a very smooth and enjoyable experience in an otherwise extreme environment.

For magnetometer work aside from the field work in Antarctica I'd like to thank Hyomin Kim for his help with troubleshooting the ELF system, he has always been willing to go above and beyond where anyone could expect and I am very grateful for all of his help over the years. Former MIRL undergraduate students John Heavisides and Matt Blandin have also been a huge help along the way, helping me sift through the piles of data.

Last, but certainly not least, I'd like to thank my friends, Nicki, Bill, and Eric for their support over the years. Even in the bleakest of times, I always looked forward to Tuesday nights together, they were the highlight of many weeks.

Table of Contents

List of Tables

List of Figures

ABSTRACT

Fine Structure in the Ionosphere

by

Bruce Fritz

University of New Hampshire, May, 2018

Fine-scale structure plays an important role in the ionosphere and can be used to learn new information about a whole host of phenomena. This dissertation presents three separate studies of fine-scale ionospheric phenomena. First, morphological behavior of black aurora with pulsating aurora provides new information on how pulsating aurora interacts with the ionosphere. Black curls in conjunction with pulsating aurora indicate diverging electric fields in and above the ionosphere, which is visual evidence that black aurora is part of an ionospheric feedback mechanism. Next, a year of magnetometer observations in the extremely-low frequency (ELF) range placed new physical constraints on the conditions necessary for detecting narrow bandwidth, whistler-like spectral features. Solar zenith angle at the time of detection illustrated the dependence of ELF whistlers on a sunlit ionosphere. Sources of free energy in the ionosphere like solar photoionization may generate instabilities in the ionosphere that produce the fine-scale spectral features. Finally, results from the RENU 2 sounding rocket are analyzed to investigate fine-scale, anomalous density structures in the high latitude ionosphere. Observations from an ultraviolet detector indicate significant levels of small scale structuring. Supporting observations from orbital spacecraft supplement the study with a new technique for two-dimensional tomographic reconstructions of photon emission in the region. Analysis of multiple measurements in the thermosphere provides an unprecedented view of fine structure at high latitudes.

Chapter 1

Introduction

Mankind has watched the skies overhead throughout its existence. The stars at night have been used for navigation, and they were considered so important that certain groups were named in honor of gods. Rain and snow have always been monitored for their impact on day-to-day life and long-term survival, but despite the rituals the weather is impossible to predict. Reports of aurora even date back to ancient history, in some cases as far back as Biblical times [Silverman, 2006]. Ancient sightings were often described in almost mythical language.

What was once thought to be the work of vengeful gods, however, we now understand is due to extremely complex physical processes in Earth's atmosphere. Heat from the sun, wind patterns, and ocean currents are some of the countless factors driving dynamic behavior in the atmosphere. Centuries of scientific research have helped to understand the physics of these processes, but not just so that local weather forecasters might tell us if it will rain or snow tomorrow.

As is often the case, scientific research has led to nearly as many questions as it has provided answers. For example, a summer day that is 100° F at sea level will feel much cooler at higher elevation, like on top of a mountain. Why does your skin feel cold, but alpine skiers can still get a sunburn, even at sub-zero temperatures? Thinner air at higher altitudes carries less heat and provides less protection from harmful ultraviolet (UV) radia-

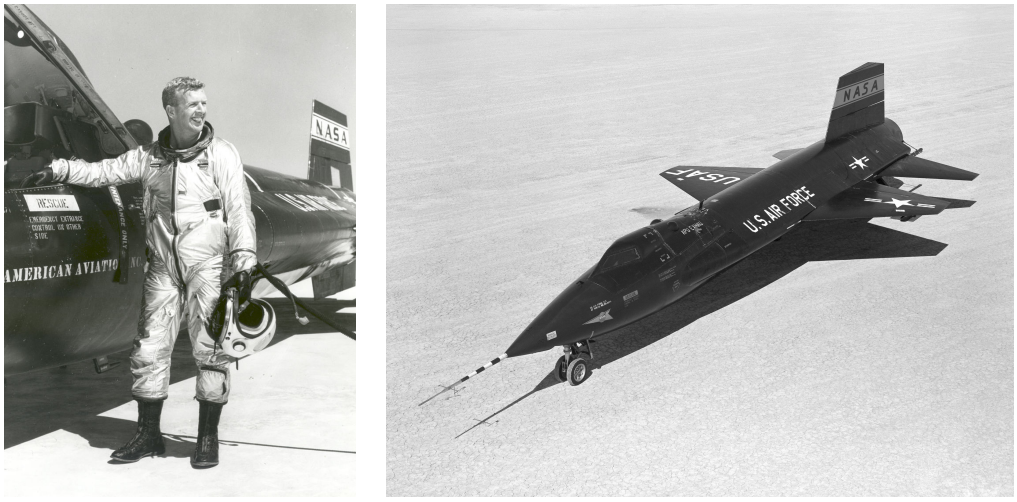

Figure 1-1: NASA and the U.S. Air Force used the X-plane series of experimental aircraft to push the limits of sub-orbital flight. In 1962, NASA test pilot Joe Walker (left) was the first American civilian to successfully breach the edge of space. He flew the X-15 (right), a hypersonic rocket-powered aircraft, reaching a record altitude of 67 miles. These photographs are publicly available through NASA Commons at https://www.flickr.com/photos/nasacommons

tion produced by the sun. Exactly how thin will the air get? How low does the temperature drop? How high do you have to go before the atmosphere ends and outer space begins?

The atmosphere that people know first-hand extends from sea level to less than 10 miles above the Earth's surface in a layer we call the troposphere. The bravest (or craziest, depending on your definition) mountain climbers have never escaped the troposphere. Even passenger jet airliners cruising high above the clouds are still well within this lowest layer.

The atmosphere continues far above the troposphere, however, through several different layers as the air pressure and density continue to drop. At just over 60 miles ($\approx$ 100 km) above the surface of the Earth, the air is too thin for an airplane wing to generate enough lift for flight without going into orbit. NASA and the U.S. Air Force broke that altitude barrier with a series of experimental aircraft (see Figure 1), but rockets are the preferred method of propulsion above 60 miles. NASA eventually adopted this altitude as its official definition for space, awarding astronaut wings to any person who crosses the boundary.

Aside from those fortunate few who have slipped the surly bonds of Earth,[1] humans spend their entire lives within the troposphere where the environment is moderately stable and safe. Beyond the edge of space, however, the sun has a dramatic impact on the sparse layer of atmosphere that persists for hundreds of miles above Earth. UV radiation, similar to the kind that causes a sunburn, is so energetic at higher altitudes that it rips atoms and molecules apart. The remaining fragments, ions and electrons, make up a plasma in a layer of atmosphere called *the ionosphere*.

Radio operators were the first to demonstrate the existence of the ionosphere at the turn of the 20th century. Guglielmo Marconi[2] (see Figure 1-2) demonstrated that he could transmit wireless radio signals over great distances, well beyond the line of sight between transmitter and receiver. In 1901, Marconi successfully received a radio message sent from a transmitter in Cornwall to the receiver in St. John's, Newfoundland, across the entire Atlantic ocean [Marconi, 2002]. The radio signals could only travel thousands of miles around the curvature of the Earth by bouncing off some conductive surface in the atmosphere (i.e. the ionosphere).

After Marconi, the effects of the ionosphere were repeatedly demonstrated by amateur radio operators and scientists alike (e.g. Appleton and Barnett [1925] and Booker and Wells [1938]), but for decades a direct measurement remained out of reach. Weather balloons could graze the top of the troposphere, which was much higher than any airplane could reach at the time, but that was still many miles away from the edge of space. A surplus of rockets left behind after the conclusion of World War 2, however, presented an opportunity. By 1946, a team of rocket scientists at White Sands Missile Range in New Mexico launched the first of many V2 rockets up over 100 km, over 5 times higher than any previous scientific

[1] Reference to the poem *High Flight* by John Gillespie Magee Jr.

[2] Fun fact: G. Marconi is the son of Italian aristocrat Giuseppe Marconi and his Irish wife, Annie Jameson, granddaughter of John Jameson, founder of Irish whiskey distiller Jameson & Sons.

(a) Guglielmo Marconi (1874 - 1937), Nobel Laureate (Photo on file with Library of Congress, ID cph.3a40043)

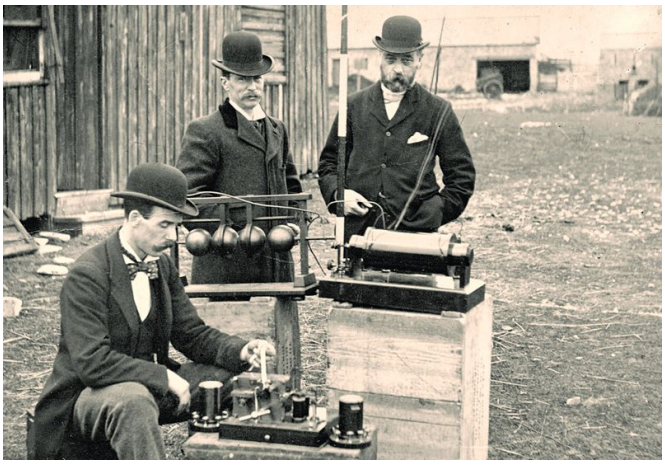

(b) British Post Office engineers inspect Guglielmo Marconi's wireless telegraphy (radio) equipment, during a demonstration on Flat Holm island, 13 May 1897 (Photo provided by Cardiff Council Flat Holm Project)

Figure 1-2: G. Marconi's first demonstration of a radio transmission over open sea occurred between Lavernock Point and Flat Holm Island, a distance of 3 miles. By 1899 he had sent transmissions across the English Channel, and eventually the Atlantic Ocean.

measurements [Golian et al., 1946].

Some of the first rocket experiments measured cosmic rays, solar radiation spectra, and plasma density in the ionosphere [Seddon et al., 1954]. As rocket technology progressed and people continued launching objects (and eventually people) into space, characterization of the ionosphere became an important objective for space research. The first American orbital spacecraft, Explorer 1 (see Figure 1-3), which launched a few months after the Soviet Sputnik 1, housed an instrument to detect highly energetic protons and electrons, the first measurement of the Earth's radiation belts [Van Allen et al., 1958]. Suborbital rockets continued to play an important role as well, particularly in the fields of auroral and ionospheric research (e.g. McIlwain [1960]).

Despite its remote location, the ionosphere has an impact on the human race and modern society. Apart from the NASA Apollo missions to the moon, any human that has been to space operated within the ionosphere (including those currently on the International Space

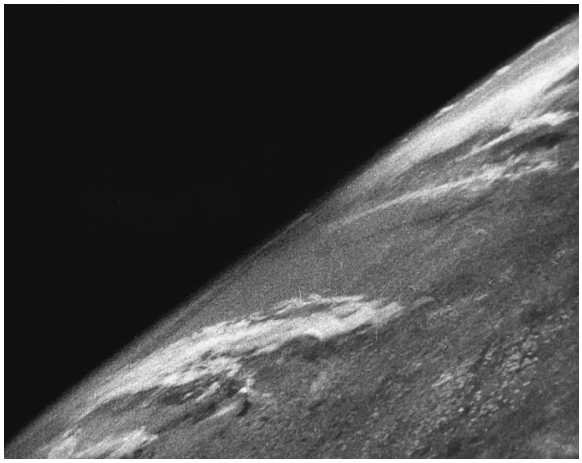

Figure 1-3: Left: The first photos taken from space on October 24, 1946 on a V-2 rocket (flight #13), launched from White Sands, NM. (Photograph from White Sands Missile Range / Applied Physics Laboratory) Right: Dr. William H. Pickering, Dr. James A. Van Allen and Dr. Wernher von Braun at a press conference hold a model of Explorer 1, which launched into orbit on January 31, 1958. (Photograph available on NASA Commons at https://www.flickr.com/photos/nasacommons

Station). A large number of satellites operate exclusively within the ionosphere as well. Millions of users rely on communication, navigation, and weather forecasting capabilities that are provided by spacecraft that spend years orbiting Earth in this region. Space weather, or variability within the ionosphere, can disrupt or degrade satellite signals meant to reach the ground. Moderate changes in the ionosphere can also have unexpected consequences on orbital decay, reducing the lifespan of a spacecraft.

The sun is responsible for a large majority of variability in the ionosphere. Radiation from the sun ionizes the atmosphere to form the ionosphere, and the solar wind contains particles that impart large amounts of energy on Earth. The Earth's magnetic field protects it from most adverse effects of the solar wind, allowing only relatively small amounts of particles to make their way into the atmosphere. The solar wind that manages to reach the ionosphere causes the Northern Lights, or the aurora. In extreme cases, explosions of particles and radiation from massive solar flares or coronal mass ejections can have significantly adverse effects on Earth. Geomagnetic storms that result from the extreme

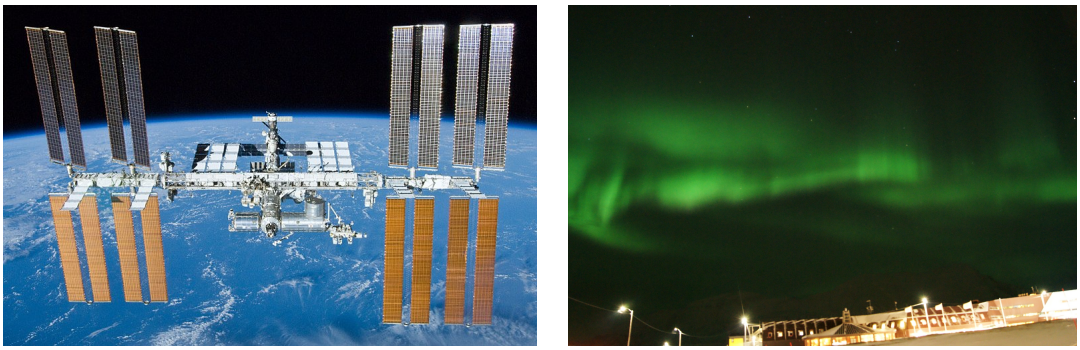

Figure 1-4: Left: The International Space Station photographed by an STS-132 crew member on board the Space Shuttle Atlantis, May 23, 2010. Right: Aurora Borealis photographed over the University Center in Svalbard. ISS image catalogued by Johnson Space Center (NASA) under Photo ID: S132-E-012208

solar activity generate large electrical currents in the ionosphere.

Large electrical currents in the ionosphere will induce electrical currents on the Earth's surface, and have a major impact on modern society. On 1 Sepember 1859, Richard Christopher Carrington[3] and Richard Hodgson each independently observed a massive white light solar flare, and the effects on Earth were global in scale [Green et al., 2006]. A ship located as far south as 11° latitude (e.g. Nicaragua) reported the appearance of aurora [Green and Boardsen, 2006].

Impacts on the ground at the time were most obvious in the telegraph system. For example, "The French telegraph communications at Paris were greatly affected, and on interrupting the circuit of the conducting wire strong sparks were observed. The same thing occurred at the same time at all the telegraphic stations in France" (*The Illustrated London News, September 24, 1859*) [Green et al., 2006]. Many telegraph operators also reported using only the ground induced current to power their systems. *The Daily Chronicle and Sentinel, Augusta, Georgia, Thursday AM, September 8, 1859* recounts a conversation between one telegraph operator in Boston, MA and another in Portland, ME.

[3]Fun fact: Richard Christopher Carrington was the second son of Richard Carrington, the proprietor of a large brewery in Brentford. [Cliver, 2006]

- Boston operator (to Portland operator) - "Please cut off your battery entirely from the line for fifteen minutes."
- Portland operator - "Will do so. It is now disconnected."
- Boston - "Mine is disconnected, and we are working with the auroral current. How do you receive my writing?"
- Portland - "Better than with our batteries on. Current comes and goes gradually."
- Boston - "My current is very strong at times, and we can work better without the batteries, as the Aurora seems to neutralize and augment our batteries alternately, making currents too strong at times for our relay magnets. Suppose we work without batteries while we are affected by this trouble."
- Portland - "Very well. Shall I go ahead with business?"
- Boston - "Yes. Go ahead."

The 1 September 1859 flare was certainly large, but its effects were maximized due to its location close to the sun center and the occurrence near an equinox, when the Earth is most susceptible to solar effects [Cliver, 2006]. More recently, a large solar flare in 1989 caused a widespread power outage in Québec, Canada. Power transformers were damaged or destroyed due to induced ground currents, and more than six million people lost power for nine hours. After a Carrington-level storm nearly missed Earth in 2012, estimates of the modern economic impact of such an event total in the trillions of dollars.

Comprehensive understanding of a complex system like the ionosphere requires learning about it on a variety of scales, both large and small. *Fine-scale structure* is defined in many ways, depending upon the context. For example, a particle physicist might call something

on the order of 10^{-15} meters fine-scale structure[4] if compared to the radius of a hydrogen atom ($a_0 = 5.29 \times 10^{-11}$ m). A cosmologist, on the other hand, might consider something on the order of 10^{+15} meters fine scale structure when the size of galaxies are measured in light years (1 ly $= 9.46 \times 10^{15}$ m).

Large, global-scale ionospheric behavior changes daily, annually or even on decade-long timescales, much like weather or climate in the troposphere. Variation in atmospheric pressure over hundreds of miles in the span of a few hours might be considered fine-scale structure relative to global scales. Close to the surface, fine-scale structures can mean anything from the extreme, like a lightning bolt in a thunderstorm, to the mundane, like a wave pattern in the clouds. In the ionosphere, that might mean a 1 mile thick layer embedded in aurora that spans 100s of miles across the sky.

Fine-scale structure in this dissertation will be defined relative to the context in which it's studied. Different chapters will focus on structures that are fine-scale in either time/frequency space or in spatial structure. First, Chapter 2 will cover some basic physics behind the concepts discussed in the introduction, including an in-depth description of the atmosphere and ionosphere. Basic plasma physics principles will be introduced and used to discuss the behavior of particles and waves in a plasma. Applied physics and chemistry topics will be introduced briefly for necessary background to understand later chapters.

Chapter 3 will discuss two types of scientific instrumentation that have been developed by the Magnetosphere-Ionosphere Research Laboratory (MIRL) at the University of New Hampshire to study ionospheric structure. The first is a white light imager designed to operate on a spinning sounding rocket payload. The second is a UV photometer, a very simple instrument capable of providing remote diagnostics of the ionosphere from a space-based platform. Both instruments flew on the Rocket Experiment for Neutral Upwelling

[4]Note: $10^{-15} = 0.000000000000001$

Figure 1-5: Left: The RENU 2 sounding rocket launch on 13 December 2015 from Andøya Space Station, Andenes, Norway (Photo credit: T. Zaperach, NASA Wallops) Right: The Amundsen-Scott South Pole Station which houses the ELF magnetometer system.

(RENU) 2 mission on 13 December, 2015. Design principles and lessons learned from each instrument will be discussed.

Chapter 4 presents the results of a scientific study on the interaction between two specific types of aurora called black aurora and pulsating aurora. The fine-scale interaction between these two specific types of aurora had never been documented before and is evidence of an electrical current structure in the ionosphere.

Chapter 5 is a year-long statistical study about narrow-band frequency signatures in the extremely low frequency (ELF) range called ELF whistlers. These fine-scale structures in frequency space have been observed for several decades but still lack an explanation for what generates them. Observations and analysis from an ELF magnetometer located at the geographic South Pole provide new physical constraints that may be used to determine their origin.

Finally, Chapter 6 discusses results from the RENU 2 sounding rocket mission. Small-scale perturbations in the ionosphere and thermosphere have been observed for years in a specific high-latitude region known as the cusp, but current physics models still struggle to explain what exactly causes them. The RENU 2 mission was designed to fly through the cusp and measure the density perturbation in far greater detail than ever before. Results

from the experiment are presented from conditions prior to launch to supporting observations after the mission, with particular emphasis on results from the RENU 2 UV PMT. Supporting measurements from orbital spacecraft provide additional information about structure in the ionosphere using new tomographic reconstruction techniques.

All three scientific studies presented in this dissertation are unique perspectives on ionospheric processes and behavior. The unifying theme is the importance that fine-scale structure plays within each. Ionospheric physics is a multi-scale discipline, and fine-scale structure plays an important role in understanding the overall dynamics of the system.

Chapter 2

Physics of the Ionosphere

The ionosphere is a highly dynamic and complex upper layer of the Earth's atmosphere. A partially ionized plasma embedded in the background neutral gas results in physical behavior not observed anywhere else in the atmosphere. The geospace environment is dramatically affected by the electromagnetic, fluid and plasma dynamics in the ionosphere. Changes are driven by energetic inputs ranging from solar radiation above to gravity waves below.

This chapter will provide a description of the ionosphere and a selection of important physical processes that govern its behavior. The first three sections provide a description of the Earth's thermosphere-ionosphere-magnetosphere system to illustrate the role of the ionosphere within the geospace environment. Next, basic plasma physics principles are covered, as they drive behavior that distinguishes the ionosphere from the other neutral layers of the atmosphere. Chemical kinetic processes are introduced, as they are critical to understanding ionospheric behavior. Several special topics are discussed as well, including instabilities in the ionosphere and the outflow of heavy ions into the magnetosphere. Finally, a brief introduction to aurora will describe the basic physics and general details of several specific types of aurora.

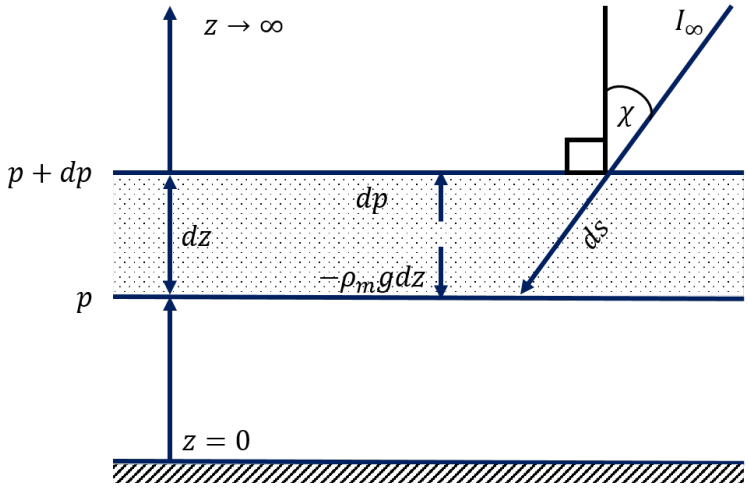

Figure 2-1: Slab diagram illustrates a section of atmosphere with thickness dz under the influence of gravity, g. In hydrostatic equilibrium, the thermal pressure, dp, of the slab pushes up and the weight of the slab, $\rho_m g dz$ pushes down. Solar intensity, I_∞ is indicated in relation to solar zenith angle, χ. For simplicity, temperature is assumed constant. Figure adapted from Parks [2004].

2.1 The Neutral Atmosphere

The Earth is enveloped by an atmosphere, a gravitationally-bound blanket of neutral gas that may be described in terms of its fluid characteristics. The fluid equation of motion (Eq. 2.1) describes how mass density, ρ_m, and pressure, p, balance with the gravitational potential, Ψ, in the atmosphere.[1]

$$\rho_m \frac{dU}{dt} = -(\nabla p + \rho_m \nabla \Psi) \tag{2.1}$$

In a hydrostatic atmosphere, the fluid remains stationary ($dU/dt \to 0$). As a result, the two remaining forces must balance: $\nabla p = -\rho_m \nabla \Psi$. Figure 2-1 illustrates how thermal gas pressure and the gravitational force balance in order to maintain equilibrium on a layer of fluid of height, dz.

Assuming a single-fluid atmosphere, mass density is the simple product of number den-

[1]The derivation in the following section follows the method of Parks [2004].

sity, n, and molecular mass, m. Thermal pressure below the slab balances the weight of the gas layer, $\rho_m g = nmg$, and downward gravitational pressure, $-dp$, balances the upward thermal pressure within the layer.

$$dp = -nmg\ dz \tag{2.2}$$

Gravitational effects are consistent and predictable, but thermal pressure depends on the gas temperature. The Ideal Gas Law relates gas pressure (p) and number density (n) to the kinetic gas temperature (T) and Boltzmann's constant, $k_B = 1.38066 \times 10^{-23}\ J/K$.

$$p = nk_BT \tag{2.3}$$

The Ideal Gas Law holds for a gas in thermodynamic equilibrium, which means that the particle velocities may be described by a Maxwell-Boltzmann distribution ($\propto\ v^2\ e^{-v^2/\alpha^2}$, α = const.). Dividing the pressure balance by the Ideal Gas Law results in a first-order differential equation.

$$\frac{dp}{p} = -\frac{mg}{k_BT}dz \tag{2.4}$$

Scale height, $H = k_BT/mg$, is used as a constant in atmospheric models, and is a valid assumption so long as a thin, slowly-varying, layer is considered. Consolidation of constants simplifies the solution to the differential equation.

$$p(z) = p_0 e^{-\int_{z_0}^{z} dz/H} = p_0 e^{-(z-z_0)/H} \tag{2.5}$$

Atmospheric pressure decreases exponentially as a function of altitude, $p(z)$, relative to the pressure, p_0, at some reference height, z_0. The derivative of the Ideal Gas Law can

be used to show the same exponential dependence for number density, assuming that the atmosphere is isothermal ($dT/T \to 0$).

$$n(z) = n_0 e^{-(z-z_0)/H} \tag{2.6}$$

Plots of density and pressure in Figure 2-2 show the exponential decay with altitude (data is from the 1962 U.S. Standard Atmosphere). The temperature profile is much more complicated, however, due to multiple competing factors. The temperature drops along with the density and pressure up to $\approx$ 10 km in altitude, through the region called the **troposphere**.

Above the tropopause, the upper boundary of the troposphere, gas density and pressure continue to decrease, but the temperature begins to *increase*. In this layer, the **stratosphere** ($\sim 10 - 50$ km in altitude), ultraviolet (UV) radiation from the sun is strongly absorbed by molecules like ozone, producing the inverted temperature profile. Figure 2-3 is a spectrum of solar radiation intensity as a function of wavelength, which illustrates the UV-absorbing effect of ozone. Solar UV radiation levels at Earth (yellow) are very low relative to the visible and infrared regions, but the amount of UV radiation that reaches the surface (red) is almost zero due to atmospheric absorption. At the top of the stratosphere (i.e. the stratopause) the density of UV-absorbing molecules drops off enough that they are no longer able to heat the gas.

The **mesosphere** is the layer above the stratopause, and once again the temperature drops off with the decreasing gas density. This layer is the coldest region of the atmosphere, and is also one of the most difficult to study. It is far too high in altitude for typical airplanes or even high-altitude weather balloons, but yet too low for orbital spacecraft to reach. The mesopause, the upper boundary of the mesosphere (alt. $\approx$ 85 km), is typically the coldest place on Earth.

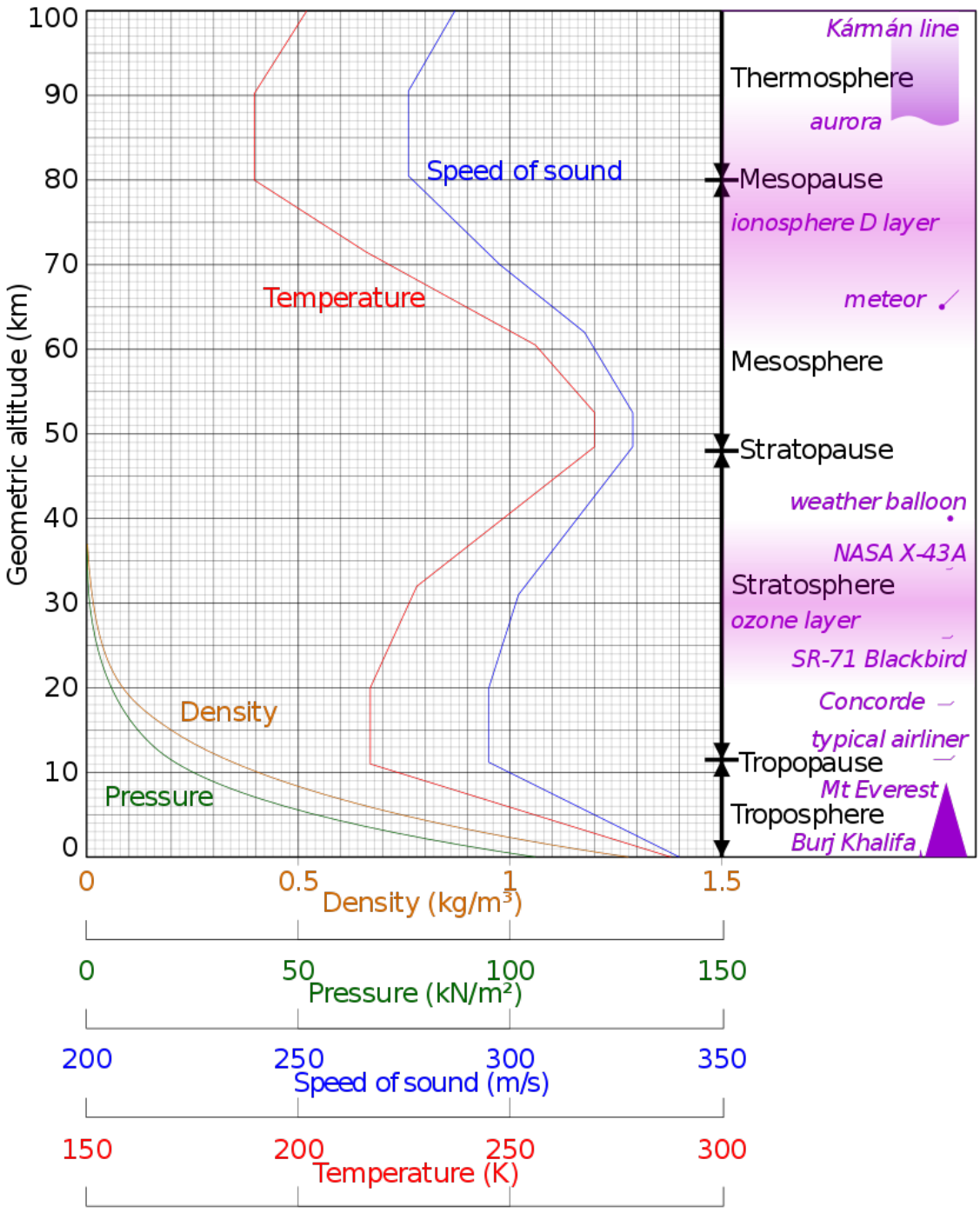

Figure 2-2: Comparison of atmospheric density, pressure, the speed of sound and temperature as a function of geometric altitude, compared to approximate altitudes of various objects. Profiles represent idealized, mid-latitude, year-round mean conditions for moderate solar activity. Figure by CMGlee, based on the *U.S. Standard Atmosphere, 1962* (https://ntrs.nasa.gov/archive/nasa/ casi.ntrs.nasa.gov/19630003300.pdf). The *U.S. Standard Atmosphere, 1962* is an idealized, mid-latitude ($\approx 45°$) year-round mean over the range of solar activity between sunspot minimum and maximum. Local time is not specified.

The mesopause happens to roughly coincide with the turbopause, where gas density becomes too low for turbulent mixing to occur and particle species begin to stratify by mass density. At this point, the density of each particle species must be treated as independent functions of altitude.

$$\rho_m(z) = \sum_i n_i(z) m_i \tag{2.7}$$

The turbopause coincides with the Kármán line, the altitude at which aerodynamic lift becomes insufficient to keep an aircraft in flight without reaching orbital speeds. This boundary is how the U.S. Air Force and NASA adopted 100 km as their official definition for the boundary of space.

Above the mesopause, solar heating begins to dominate and temperatures again increases with altitude in a region called the thermosphere. The thermosphere is the region above 100 km characterized by exponentially *increasing* temperature in the neutral gas population.

Near UV (λ_{NUV} = 300-400 nm), middle UV (λ_{MUV} = 200-300 nm) and far UV (λ_{FUV} = 100-200 nm) radiation heats the thermosphere at relatively low energy. NUV and MUV are partially absorbed by the atmosphere but a small fraction reaches the surface of Earth. FUV begins the vacuum UV (λ_{VUV} = 10-200 nm) range, which implies that the radiation will only propagate through a vacuum. At λ = 102.8 nm, radiation in the extreme UV range (λ_{EUV}) becomes energetic enough to ionize atomic oxygen, which is sometimes used as the delimiter between FUV and EUV radiation [Huffman, 1992]. The region of weakly ionized plasma generated by EUV radiation within the thermosphere is called the ionosphere.

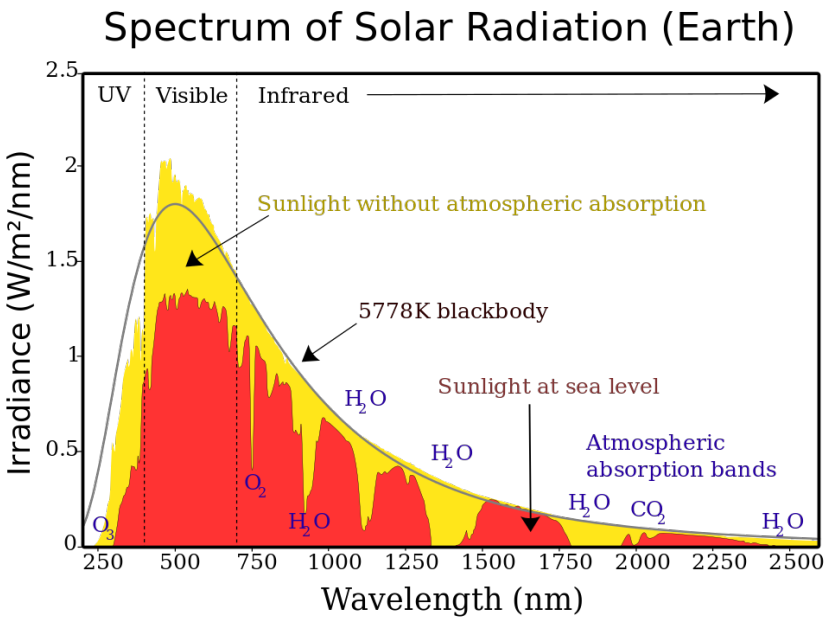

Figure 2-3: Solar irradiance of the sun (yellow) based on the 2000 ASTM Standard Extraterrestrial Spectrum Reference E-490-00 [Wu et al., 2011]. Atmospheric effects alter the blackbody shape of the spectrum at sea level (red), due primarily to absorption by O_2, O_3, H_2O and CO_2.

2.2 The Ionosphere

Ionization caused by solar EUV radiation creates the ionosphere and determines its general structure. Figure 2-1 showed a diagram of an atmospheric slab of thickness dz. Ionization in the slab may be determined from the effects incoming radiation, I_∞, on the background gas population. Some amount of radiation as a function of wavelength, $dI(\lambda, z)$, is attenuated over the path length, $ds = \sec\chi dz$, before it reaches the bottom of the slab.[2]

$$dI(\lambda, z) = -I(\lambda, z)n_i(z)\sigma_i(\lambda)\sec\chi dz \tag{2.8}$$

The ionization rate in the slab due to the differential solar intensity, dI, depends on the angle, χ, between the sun-Earth vector and the local Earth radial vector, also known

[2]The derivation in the following section follows the method of Parks [2004].

as the solar zenith angle. Attenuation of the solar intensity also depends on the density of the i^{th} absorbing species, $n_i(z)$, and the interaction cross-section of the species, $\sigma_i(\lambda)$. This relation is simplified by assuming a single species atmosphere ($n_i(z) \rightarrow n(z)$, $\sigma_i(\lambda) \rightarrow \sigma(\lambda)$), and monochromatic solar flux ($I(\lambda, z) \rightarrow I(z)$, $\sigma(\lambda) \rightarrow \sigma$). The background neutral thermosphere is treated as a fluid governed by the continuity equation.

$$\frac{\partial n}{\partial t} = q - L - \nabla \cdot (n\vec{v}) \tag{2.9}$$

In a steady state atmosphere, $\partial n/\partial t = \nabla \cdot (n\vec{v}) = 0$, leaving the source term, q, and the loss term, L, in equilibrium: $q = L$. The source of ionized particles, $q(z)$, is a function of the density, $n(z)$, the cross section, σ, and the intensity of radiation, $I(z)$. The ionization rate assumes that each photon produces one ion/electron pair.

$$q(z) = n(z)\sigma I(z) \tag{2.10}$$

Radiation intensity, $I(z)$, is determined by integrating Equation 2.8 in its simplified, monochromatic form, with I_∞ the unattenuated solar flux level.

$$I(z) = I_\infty e^{-\int_\infty^z n(z)\sigma \sec\chi dz} \tag{2.11}$$

The background gas density, $n(z)$, was defined in Equation 2.6, with $z_0 = 0$ for simplicity. The ionization rate, $q(z)$, can then be expressed as a function of several constants and the altitude (z).

$$q(z) = n_0 e^{-z/H}\sigma I_\infty \exp[-n_0 H\sigma \sec\chi e^{-z/H}] \tag{2.12}$$

The altitude of maximum ionization is determined by setting the derivative of Equa-

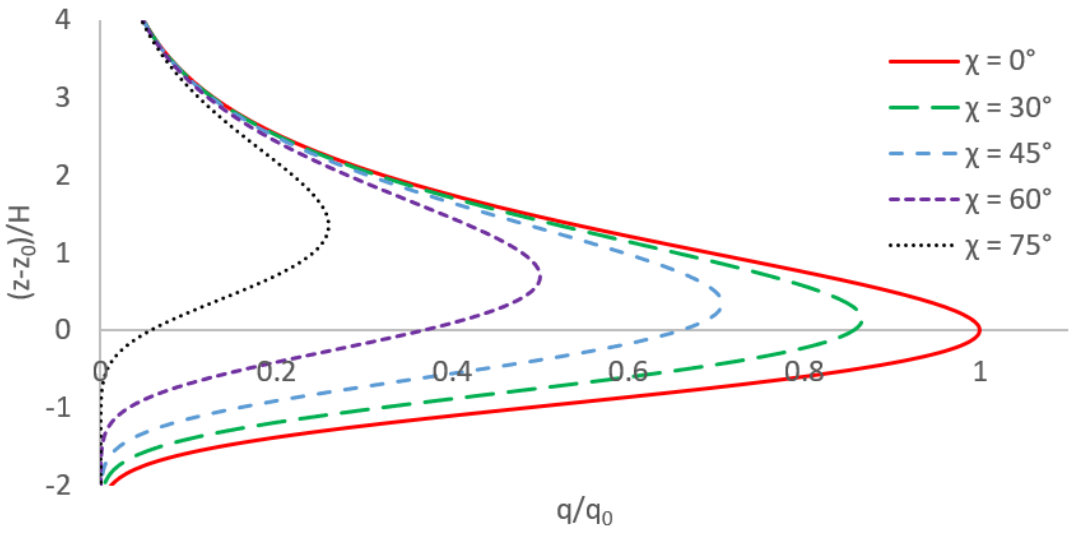

Figure 2-4: The Chapman Production Function, q, plotted against normalized height, is shown for various values of χ.

tion 2.12, $dq(z)/dz = 0$, and solving for z_m.

$$z_m = H \ln(n_0 \sigma H \sec \chi) \tag{2.13}$$

This height is used to determine the rate of maximum production, $q(z_m)$.

$$q(z_m) = \frac{I_\infty}{eH \sec \chi} \tag{2.14}$$

When the sun is directly overhead ($\chi = 0$), $z_m = z_0 = H \ln(n_0 \sigma H)$ and $q_m = q_0 = I_\infty / He$. Insertion of z_0 and q_0 into Equation 2.12 results in a simple model for the ionosphere referred to as the Chapman Function, after Sydney Chapman who first derived it.

$$q = q_0 \exp[1 + \frac{z_0 - z}{H} - \sec \chi \; e^{(z_0 - z)/H)}] \tag{2.15}$$

The Chapman Function, shown in Figue 2-4, is a simple but realistic model for the region of highest ionization in the ionosphere, the F-region. In reality, many competing fac-

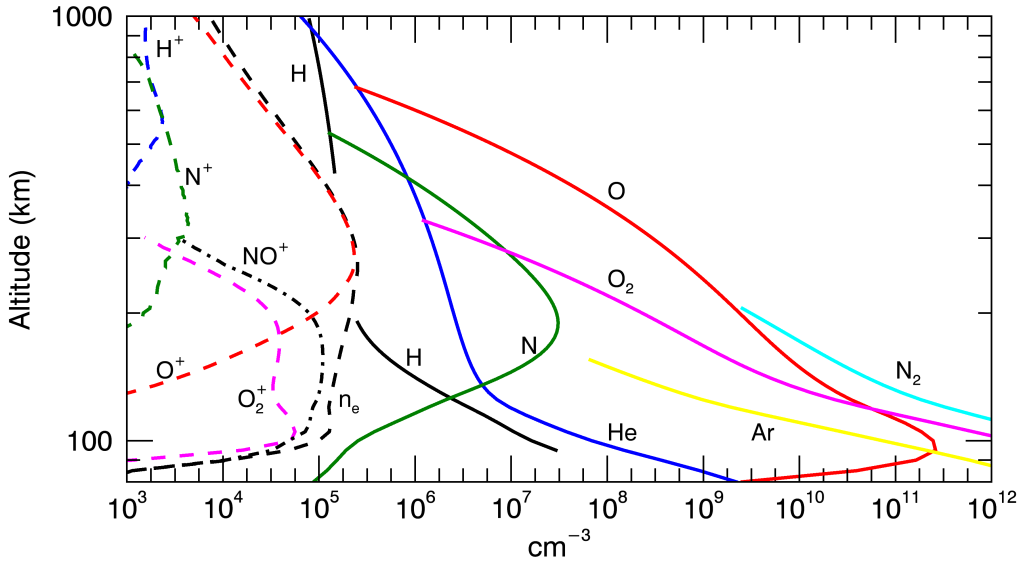

Figure 2-5: Number density of primary species in the ionosphere-thermosphere for local noon above New Hampshire (43° N, 71° W) on 28 May, 2008. Thermosphere densities are generated by NRLMSISE-00 [Picone et al., 2002] and ionosphere densities by IRI-2016 [Bilitza et al., 2017].

tors determine the overall structure of the ionosphere. Multiple particle species, each with their own ionization rates, create several layers within the ionosphere. Figure 2-5 shows the composition of several particle species in the ionosphere and thermosphere as a function of altitude. Neutral densities are determined from the empirical Naval Research Laboratory Mass Spectrometer and Incoherent Scatter radar Exosphere (NRLMSISE-00) model [Picone et al., 2002]. Plasma densities are determined from the empirical International Reference Ionosphere (IRI-2016) model. Both models are available through the NASA GSFC Community Coordinated Modeling Center (CCMC).

The values in Figure 2-5 were calculated for 1200 LT on 28 May, 2008 over New Hampshire (43° N, 71° W geographic). Stable neutral species in the thermosphere decay exponentially as expected. The overall density of the plasma is approximated by the electron density, n_e The first takeaway is the relative abundance of plasma density relative to the neutral thermospheric population. At its peak the ionosphere is 4 to 5 orders of magnitude

less dense than the thermosphere.

The peak in electron density around 100 km was the first feature discovered in the ionosphere by early radio experiments [Appleton and Barnett, 1925]. The peak was named the E-layer for its electrically conductive properties. The large peak closer to 250 km was discovered shortly thereafter and was named F-layer in alphabetic order. Likewise a D-region was found below the E-region, although not obvious in Figure 2-5. The ionospheric structure varies by latitude and local time of day. Different energy sources at different latitudes produce different rates of ionization. At night the source of ionizing EUV radiation is removed and the densities slowly drop as ion species chemically recombine with electrons.

The ionosphere continues up to roughly 1000 km above the surface of the Earth. Beyond 1000 km is the exosphere, a region where collisional processes are no longer a significant factor in the behavior of particles that are still gravitationally bound to Earth. The transition to the exosphere coincides with the lower boundary of the magnetosphere.

2.3 The Magnetosphere

The Sun is the largest source of free energy in the solar system. Electromagnetic radiation from the sun drives a multitude of physical processes on Earth, including formation of the ionosphere. The sun also radiates charged particles, a continuous outward flow of plasma accelerated out of the corona and into the planetary medium. The outflow of plasma is called the **solar wind**, and is tied to the interplanetary magnetic field (IMF) generated by the sun. The rotation of the sun causes the IMF to spiral through the solar system as it is carried by the radial outward flow of plasma.

The solar wind is primarily composed of protons ($\sim 96\%$) and helium ions ($\sim 4\%$), with trace amounts of heavier ions ($< 1\%$ C, N, O, etc) [Robbins et al., 1970]. When measured near Earth ($\approx$ 150 km from the sun), the solar wind is typically traveling at supersonic

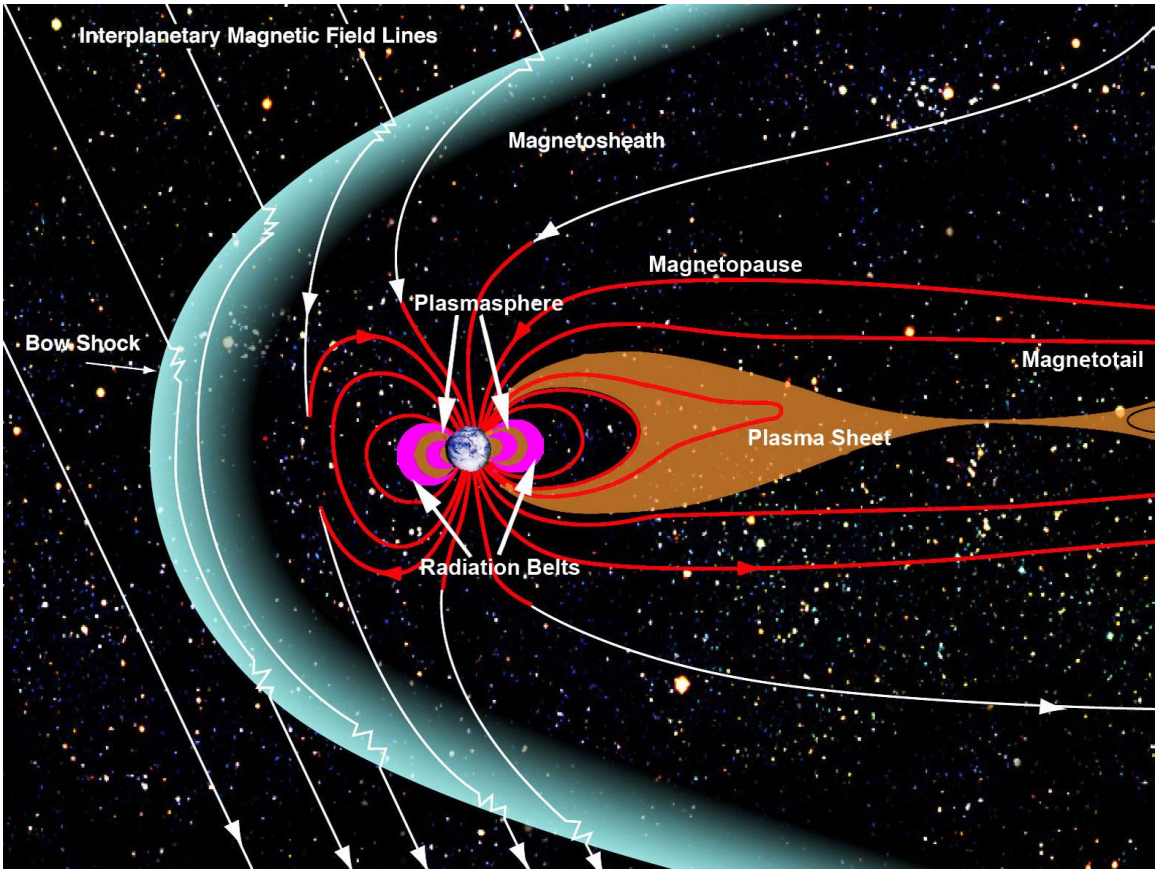

Figure 2-6: Diagram of the Earth's magnetosphere from NASA website (www.nasa.gov/mission_pages/sunearth/science/magnetosphere2.html)

speeds that range between $300 - 800$ km/s on average. The solar wind is collisionless, with typical densities, $n \approx 1 - 20$ cm^{-3}. The collisionless solar wind plasma remains "frozen in" with the IMF, trapped by the Lorentz force, until it collides with an obstacle.

The **magnetosphere** is the region surrounding Earth dominated by the geomagnetic field that protects it from the solar wind. The same Lorentz force that keeps a collisionless plasma "frozen in" with the IMF also prevents it from easily crossing an external magnetic boundary. When the supersonic solar wind encounters the geomagnetic field it forms a **bow shock**, or a free-standing shock wave, on average located $\sim$ 12 Earth radii (R_E) upwind from Earth. The location of the bow shock relative to Earth and the IMF is indicated in Figure 2-6.

Plasma is decelerated, heated, and deflected around Earth as it slowly works its way through the shock boundary in a region called the **magnetosheath**. The "shocked" solar wind dynamic pressure eventually reaches equilibrium with the magnetic pressure of the compressed geomagnetic field, a point called the **magnetopause**. Along the Sun-Earth line the magnetopause is $\sim 9\ R_E$ from Earth. Within the magnetopause is the magnetosphere, where the geomagnetic field dominates the plasma behavior.

Most of the solar wind plasma that piles up in the magnetosheath is deflected around Earth. A strong current flows within the region, establishing an electric potential across either side of the magnetosphere. Some solar wind plasma makes its way into the magnetosphere, either by diffusion across the magnetosheath or by direct entry. The IMF reconnects with the geomagnetic field on the sunward side of Earth, establishing a path for particles to reach the atmosphere called the **cusp**.

The solar wind carries the IMF, now connected to the geomagnetic field, over the polar caps toward the night side of Earth. The field lines stretch out into the **magnetotail**, which reaches beyond the orbit of the moon. Light ions in the polar cap with thermal energies greater than the gravitational force stream out from the ionosphere along the open magnetic field lines in a **polar wind**. Solar wind particles make their way into the magnetotail and join the ionospheric plasma that has escaped the Earth's atmosphere, forming a region of high energy plasma called the **plasma sheet**. The energetic plasma sheet particles stream along geomagnetic field lines (i.e. field-aligned currents) at all longitudes to establish the **auroral oval** in the ionosphere.

Closer to Earth within the magnetopause is the **plasmasphere**, a donut-shaped region of cold, dense plasma that extends out to $\sim 4\ R_E$ and corotates with Earth. Most of the plasma in this region is ionospheric in origin and is trapped on dipole geomagnetic field lines. The Van Allen **radiation belts**, home to large populations of high energy particles, are

also tied to dipole geomagnetic field lines. Some of the trapped particles drift azimuthally around Earth and create the **ring current**.

The magnetosphere is inextricably tied to the ionosphere and thermosphere, forming an overall Ionosphere-Thermosphere-Magnetosphere (ITM) system. The magnetosphere acts as a filter for the constant stream of solar wind and is a source of energetic particles that impact the ionosphere via the cusp and field-aligned currents. The ionosphere provides a feedback mechanism via the polar wind and ion outflow. The plasma within the ITM system is all governed, at least in part, by plasma physics, discussed in the next section.

2.4 Space Plasmas

Plasma, sometimes called the 4th state of matter in addition to solids, liquids, and neutral gases, is the most prevalent state of matter in the known universe. A substantial fraction of visible matter in space exists in some sort of charged, plasma state, and has a unique set of physical properties. Plasmas are **quasi-neutral**, which means that individual components of a plasma have an electrical charge, but on a macro-scale a plasma does not maintain a net charge. Quasi-neutrality holds for length scales beyond the Debye length, λ_D, the distance at which charged particles will rearrange themselves to shield a stray electric potential.

$$\lambda_{Ds} = \sqrt{\frac{\varepsilon_0 k_B T_s}{n_{0s} e^2}} \tag{2.16}$$

The Debye shielding length varies, depending on the temperature, T_s, and density, n_{0s}, of each particular species, the elementary charge, $e = 1.602 \times 10^{-19}$ C and the permittivity of free space, $\varepsilon_0 = 8.85 \times 10^{-12}$ F/m. At any length scale, however, charged particles in a plasma respond to electromagnetic forces. The **Lorentz Force** describes how a particle with charge, q, reacts to electric fields, $\mathbf{E}$, and magnetic fields, $\mathbf{B}$. Many basic properties of

a plasma are derived by examining the behavior of the Lorentz equation of motion.

$$\mathbf{F} = q(\mathbf{E} + \mathbf{v} \times \mathbf{B}) \tag{2.17}$$

The simplest case sets $\mathbf{B}_0 = 0$, where the subscript 0 indicates a background field. If $\mathbf{E}_0 \neq 0$ particles will accelerate in response to the field, but non-zero bulk electric fields typically do not last long because plasmas will rearrange to cancel out the field. Even when both $\mathbf{B}_0 = \mathbf{E}_0 = 0$, a small perturbation, δx, that separates two charged particles will create a small perturbation electric field E_1 between them.[3]

$$m_e \frac{\mathrm{d}^2 \delta x}{\mathrm{dt}^2} = -eE_1$$

The mass of an electron is $m_e = 9.11 \times 10^{-31}$ kg $= 5.49 \times 10^{-4}$ u, where u is the atomic mass unit, u $\approx m_p = 1.673 \times 10^{-27}$ kg. Ions in the plasma are assumed to remain stationary while the electrons move about because of the large difference in inertia. **Gauss's Law** is used to determine the magnitude of the perturbed electric field, E_1.

$$\nabla \cdot \mathbf{E} = \frac{\rho_c}{\varepsilon_0} \tag{2.18}$$

The perturbed field strength is $E_1 = en_e\delta x/\varepsilon_0$, where the charge density is $\rho_c = en_e$. Using this value for E_1, the simplified form of the Lorentz force equation becomes that of a harmonic oscillator.

$$m_e \frac{\mathrm{d}^2 \delta x}{\mathrm{dt}^2} + \frac{e^2 n_e \delta x}{\varepsilon_0} = 0$$

The constant in the solution is the oscillation frequency of electrons in a plasma, ω_{pe},

[3]Derivation method from Gurnett and Bhattacharjee [2005]

which can be be determined in terms of constants and plasma properties.

$$\omega_{pe}^2 = \frac{n_e e^2}{m_e \varepsilon_0} \tag{2.19}$$

The **plasma frequency**, ω_p, is a fundamental property of particles in a plasma defined by physical characteristics like number density, n, and particle mass, m. Quasi-neutrality dictates that ion density and electron density are equal, $n \approx n_e \approx n_i$. The mass difference between electrons and ions means that, $\omega_{pe} \gg \omega_{pi}$, and the electron plasma frequency is typically the characteristic frequency of a plasma. Several other important properties of plasmas become apparent by looking at the motion of a single charged particle.

2.4.1 Single particle motion

Another simple case using the Lorentz force is $\mathbf{E}_0 = 0$ and $\mathbf{B}_0 \neq 0$. A charged particle moving with velocity, $\mathbf{v}$, is accelerated by the magnetic field, $\mathbf{F} = q\mathbf{v} \times \mathbf{B}_0$. Assuming $\mathbf{B}_0 = \mathrm{B}_0\hat{z}$, evaluation of the Lorentz equation in component terms (e.g. $dv_x/dt = qB_0v_y/m$) shows that only the $\mathbf{v} \perp \mathbf{B}_0$ terms are non-zero. Simple substitution results in a set of second order differential equations with sinusoidal solutions.

$$v_x = v_\perp \cos \Omega_c t \qquad \text{and} \qquad v_y = v_\perp \sin \Omega_c t$$

The rate at which the particle gyrates in a magnetic field, Ω_c, is called the **cyclotron frequency**, and depends on the charge of the particle, q, the strength of the field, B_0, and the mass of the particle, m.

$$\Omega_c = \frac{qB_0}{m} \tag{2.20}$$

The charge of the particle, q, determines the direction of rotation, which means that

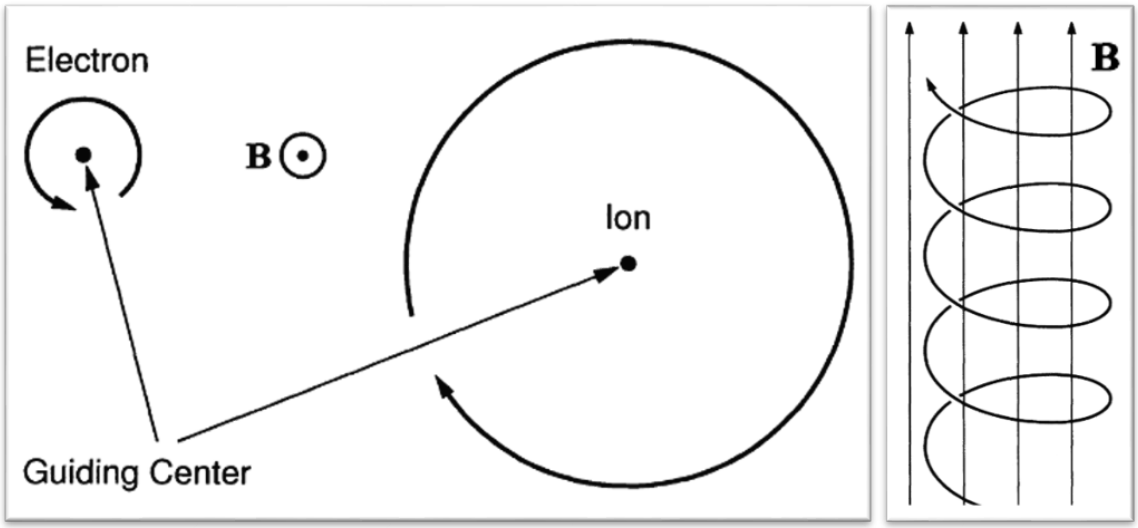

Figure 2-7: Left: Motion of positively and negatively charged particles gyrating around a uniform magnetic field, pointed out of the page. Right: Helical motion of a positively charged particle moving along a field line. Figures from Baumjohann and Treumann [2012]

electrons and ions rotate in opposite directions. Figure 2-7 (left) demonstrates the motion of particles in a uniform magnetic field directed out of the page. The magnetic field exerts no force on a particle along the direction of the field. Particles are allowed to move freely along the field lines as they gyrate, producing a helical motion, illustrated by Figure 2-7 (right). The **pitch angle**, α, of a particle that gyrates relative to the background field, $\mathbf{B}_0$, is a ratio of the particle velocity components, $\alpha = \tan^{-1} v_\perp / v_\parallel$. Particles gyrate around the magnetic field line at the **cyclotron radius**, r_c, determined by the velocity component of the particle, $v_\perp$, perpendicular to $\mathbf{B}$.

$$r_c = \frac{v_\perp}{\Omega_c} = \frac{m v_\perp}{qB} \tag{2.21}$$

The center of the gyro-motion is called the guiding center. Figure 2-7 (left) illustrates how a less massive particle like an electron will gyrate with a smaller r_c relative to a more massive particle, like a proton. The motion of a particle in a magnetic field is tied directly to its energy (via $v_\perp$) and its charge. Absent any external forces, charged particles will

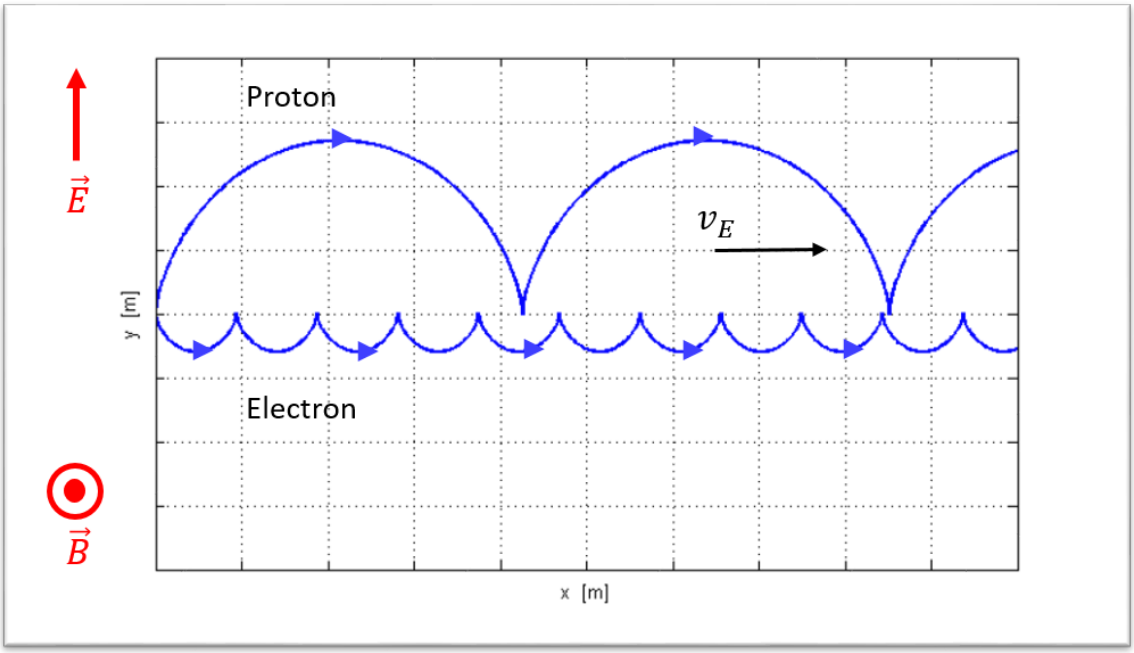

Figure 2-8: Sample motion for positive and negative particles in the presence of an electric field ($\mathbf{E} = E\hat{y}$) and magnetic field ($\mathbf{B} = B\hat{z}$). Relative size of electron cyclotron motion exaggerated for illustrative purposes.

remain tied to a magnetic field line.

Drift motion

Solutions to the Lorentz equation with both $\mathbf{E}_0 \neq 0$ *and* $\mathbf{B}_0 \neq 0$ reveal the first of several drift motions for charged particles in electromagnetic fields. Plasmas with $\mathbf{E}_0 \parallel \mathbf{B}_0$ will quickly rearrange to neutralize the field, which makes $\mathbf{E}_\parallel$ difficult to sustain for long periods of time. If $\mathbf{E}_0 \perp \mathbf{B}_0$, however, a velocity increase due to $\mathbf{E}_0$ will also increase the $q\mathbf{v}_\perp \times \mathbf{B}_0$ force. The balance between $q\mathbf{E}_0$ and $q\mathbf{v}_\perp \times \mathbf{B}_0$ oscillates in response to the magnitude and direction of $\mathbf{v}$. The net result is a drift of the particle guiding center at a drift velocity, $\mathbf{v}_E$.

$$\mathbf{v}_E = \frac{\mathbf{E} \times \mathbf{B}}{B^2} \tag{2.22}$$

Figure 2-8 illustrates the drift behavior for both positive and negative species in the

presence of electric and magnetic fields. The net particle motion, named the **E × B drift**, is orthogonal to the plane that contains both $\mathbf{E}_0$ and $\mathbf{B}_0$ and independent of charge. Positive and negative species drift in the same direction despite the opposite direction of cyclotron rotation.

The addition of any linear force, $\mathbf{F}$, to the Lorentz $\mathbf{v} \times \mathbf{B}$ force will generate a drift motion relative to the background magnetic field.

$$\mathbf{v}_D = \frac{1}{q}\frac{\mathbf{F} \times \mathbf{B}}{B^2}$$

Gravity is one example of a constant external force, but drifting due to gravity in the geospace environment is typically negligible. The most relevant forces instead result from non-uniform magnetic fields. A *gradient* in the magnetic field, ∇B, produces a non-uniform Lorentz force as a particle gyrates around the field (i.e. a particle feels different field strengths on opposite sides of its orbit due to the field gradient). The net effect is a drift perpendicular to both the magnetic field and the gradient directions, called the **Gradient-B** drift, $\mathbf{v}_G$.

$$\mathbf{v}_G = \left(\frac{mv_\perp^2}{2qB^4}\right)\ \mathbf{B} \times \frac{\nabla B^2}{2}$$

The Gradient-B drift depends on the perpendicular motion of a particle, $v_\perp$. A particle that moves parallel to a curved magnetic field ($v_\parallel$) also feels a centrifugal force, $\mathbf{F}_c = mv_\parallel^2 \mathbf{R}_c / R_c^2$. The strength of the force depends on the local radius of curvature R_c, so the resulting drift motion is called the **Curvature-B** drift, $\mathbf{v}_C$. The drift motion is perpendicular to both the direction of the centrifugal force and the background field, but R_c has been re-written in terms of $\mathbf{B}$ to show $\mathbf{v}_C$ in a familiar form.

$$\mathbf{v}_C = \left(\frac{mv_\parallel^2}{qB^4}\right)\ \mathbf{B} \times \frac{\nabla B^2}{2}$$

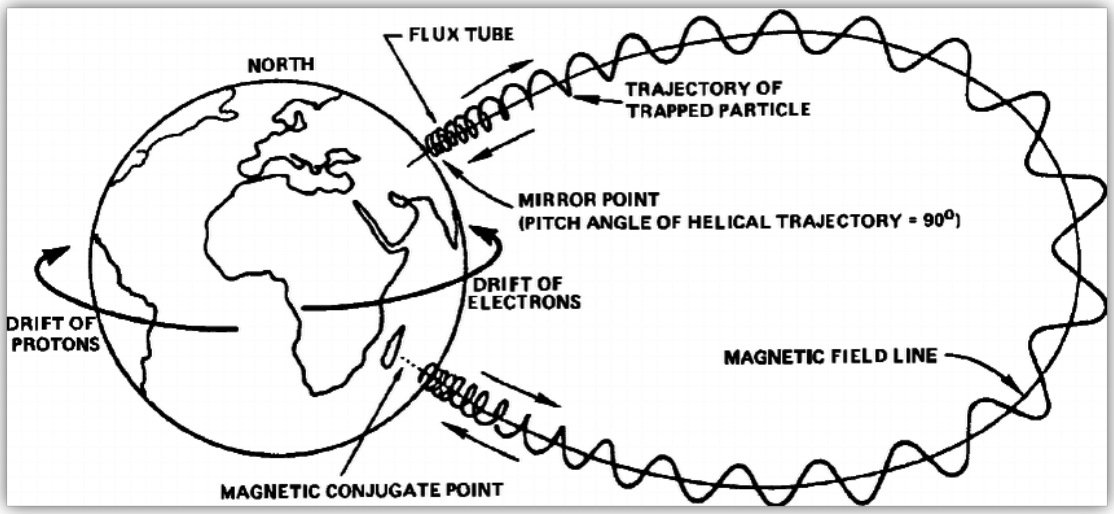

Figure 2-9: Diagram of charged particle motion in the Earth's dipole magnetic field. Directions for $\mathbf{v}_{GC}$ are indicated for protons and electrons. Figure from Gruntman [1997], adapted from *Handbook of Geophysics and the Space Environment* (Air Force Geophysics Laboratory)

A dipole magnetic field like Earth's will naturally result in both $\mathbf{v}_G$ and $\mathbf{v}_C$ drifts. The drifts can written as one net drift motion that describes the combined effect, called the **Gradient-curvature drift**, $\mathbf{v}_{GC}$.

$$\mathbf{v}_{GC} = \frac{m}{qB^4}\left(v_{\parallel}^2 + \frac{1}{2}v_{\perp}^2\right)\ \mathbf{B} \times \frac{\nabla B^2}{2} \tag{2.23}$$

The strength of the gradient-curvature drift in a given field depends on the total energy of the particle, the gradient drift on perpendicular kinetic energy and the curvature drift on parallel kinetic energy. Both drifts depend on the charge of the particle, whch means species with opposite charges will drift in opposite directions and generate a net electrical current. In the magnetosphere the differential drift generates the ring current. Directions of relative particle drift motion are indicated in Figure 2-9.

Another non-uniform magnetic field occurs in regions of converging/diverging $\mathbf{B}$, for example where lines converge near the pole of a dipole field. The field will generate a force

opposite the direction of convergence, pushing a particle away.

$$\mathbf{F}_{\parallel} = -\frac{mv_{\perp}^2}{2B}\nabla_{\parallel}B \tag{2.24}$$

The force, $\mathbf{F}_{\parallel}$ will eventually overcome the parallel energy of a particle moving toward converging field lines, reversing the direction of the particle's motion. The change in particle direction is called the **magnetic mirror** force, and is also depicted in Figure 2-9. The mirror force is directly related to the first of three conserved plasma quantities.

Conserved quantities

Three adiabatic invariant quantities are useful for describing behavior in a space plasma, and are important descriptors of particle motion in the magnetosphere. They remain constant so long as temporal changes to the system are made on slower time scales than the relevant periodic motion. The **magnetic moment**, μ_m, of a charged particle is the first conserved quantity in a plasma. Charged particles in cyclotron orbit create a tiny electrical current, and as a result generate a small magnetic field with a magnetic moment, $\mu_m = I\pi r_c^2 = mv_{\perp}^2/2B$. Equation 2.24 then may be written $\mathbf{F}_{\parallel} = -\mu_m \nabla_{\parallel} B$.

A particle that moves into a converging magnetic field will try to maintain constant magnetic flux, per **Gauss's Law** for magnetism, $\nabla \cdot \mathbf{B} = 0$, by increasing $v_{\perp}$. The perpendicular velocity can be written in terms of pitch angle, $v_{\perp} = v \sin\alpha$.

$$\mu_m = \frac{mv^2}{2}\frac{\sin^2\alpha}{B} \tag{2.25}$$

The total kinetic energy of the particle, $mv^2/2$, will be conserved along with μ_m, so $\sin^2\alpha/B$ must be conserved as well. As B increases in the converging field, α increases to compensate. Eventually all kinetic energy is directed into $v_{\perp}$ and $v_{\parallel} \to 0$. As B increases

further, $\mathbf{F}_{\|}$ forces the particle back out along the field line. Particles will "bounce" between mirror points in a closed system.

Particles that penetrate too deep into the atmosphere before reaching their "mirror point" will collide with a particle, often generating an auroral emission. The "loss cone" is the range of pitch angles that are too small for a given particle to mirror back before being lost to atmospheric scatter (i.e. α too close to 0 will be lost). The bounce motion is associated with the **longitudinal invariant**, the second conserved quantity, J.

$$J = \oint m v_{\|} \mathrm{ds}$$

The velocity along the field line is $v_{\|}$ and ds is an element of the guiding center path. Over a full oscillation between mirror points, the invariant is conserved as long as changes to the system occur on timescales slower than the bounce period. Particles trapped in the bounce motion will drift in longitude due to the gradient-curvature drift, $\mathbf{v}_{GC}$. This invariant implies that particles will preserve the total length of the particle trajectory. The third conserved quantity is a **drift invariant**, and is tied to conservation of magnetic flux, Φ, similar to the first invariant.

$$\Phi = \oint v_d r \, d\psi$$

Particles that drift azimuthally, ψ, with drift velocity, v_d, must maintain a constant flux. The ring current will adjust itself to maintain this invariant as long as any perturbation to the system occurs on a timescale longer than the drift time of the particles.

2.4.2 Plasma conductivity

The ionosphere is a partially ionized, *collisional* plasma, which means collisions between plasma particles and neutral particles must be considered. The **neutral collision frequency**, ν_n, is the number of collisions per second between a charged particle and a population of neutral particles with density, n_n.

$$\nu_n = n_n \sigma_n \langle v \rangle \tag{2.26}$$

The collision cross section of neutral particles is $\sigma_n \approx 10^{-19}$ m^2 and $\langle v \rangle$ is the average velocity of a charged particle. The **mean free path**, λ_n, is the average distance a charged particle will travel before colliding with a neutral particle.

$$\lambda_n = \frac{\langle v \rangle}{\nu_n} \tag{2.27}$$

Coulomb collisions are also important in a fully ionized plasma, but for a partially ionized, ionospheric plasma, Coulomb effects relative to neutral effects are small enough to ignore. A collisional term, $\mathbf{F} = -m\nu_n(\mathbf{v} - \mathbf{u})$, is added to the Lorentz Force equation of motion to capture the momentum lost due to collsions. In a steady state plasma, an electron moves with velocity $\mathbf{v}_e$ relative to a stationary background of ions and neutrals ($\mathbf{u} = 0$). In an unmagnetized plasma ($\mathbf{B}_0 = 0$), the net current generated by the electron motion, $\mathbf{j} = -en_e\mathbf{v}_e$, results in a simple Ohm's Law relation.

$$\mathbf{E} = \frac{m_e \nu_n}{n_e e^2}\,\mathbf{j} \tag{2.28}$$

The coefficient is the plasma resistivity, $\eta = m_e\nu_n/n_e e^2$. The inverse of resistivity is the plasma conductivity, σ_0.

$$\sigma_0 = \frac{n_e e^2}{m_e \nu_n} \tag{2.29}$$

In a fully ionized, collisionless plasma, the conductivity is near infinite. In that case, a magnetized plasma may be described by a **generalized Ohm's Law**.

$$\mathbf{j} = \sigma(\mathbf{E} + \mathbf{v} \times \mathbf{B}) \tag{2.30}$$

In the ionosphere, however, collisions play a more meaningful role. The generalized Ohm's Law for a magnetized plasma imparts collisional effects on both terms.

$$\mathbf{j} = \sigma_0 \mathbf{E} - \frac{\sigma_0}{n_e e} \mathbf{j} \times \mathbf{B} \tag{2.31}$$

The magnetic field may be defined as $\mathbf{B} = \mathrm{B}\hat{z}$, and the coefficients re-written in terms of the electron cyclotron frequency, $\Omega_{ce} = qB/m_e$.

$$j_x = \sigma_0 E_x + \frac{\Omega_{ce}}{\nu_c} j_y \qquad j_y = \sigma_0 E_y - \frac{\Omega_{ce}}{\nu_c} j_x \qquad j_z = \sigma_0 E_z$$

After substitution of j_x and j_y, the equations are cast in matrix form, $\mathbf{j} = \sigma \cdot \mathbf{E}$. The conductivity becomes a tensor with three primary components.

$$\sigma = \begin{bmatrix} \sigma_P & -\sigma_H & 0 \\ \sigma_H & \sigma_P & 0 \\ 0 & 0 & \sigma_\parallel \end{bmatrix}$$

$$\sigma_P = \frac{\nu_n^2}{\nu_n^2 + \Omega_{ce}^2} \sigma_0 \qquad \sigma_H = -\frac{\Omega_{ce} \nu_n}{\nu_n^2 + \Omega_{ce}^2} \sigma_0 \qquad \sigma_\parallel = \sigma_0 = \frac{n_e e^2}{m_e \nu_c} \tag{2.32}$$

The Pedersen conductivity, σ_P, allows the **Pedersen current** to flow parallel to $\mathbf{E}_\perp$,

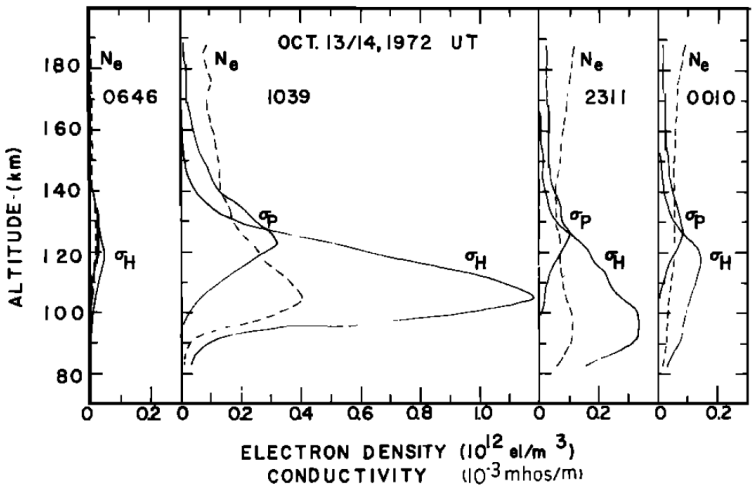

Figure 2-10: Altitude profiles for electron density measured by incoherent scatter radar in Chatanika, AK, and the derived Pedersen and Hall conductivity for various times of day. Figure from Brekke et al. [1974].

the electric field perpendicular to **B**. The Hall conductivity, σ_H, allows the **Hall current** to flow in the $-\mathbf{E}\times\mathbf{B}$ direction. The parallel conductivity $\sigma_\parallel$ enables field aligned currents driven by $E_\parallel$. The generalized Ohm's law is easily re-written in terms of the conductivity terms.

$$\mathbf{j} = \sigma_\parallel \mathbf{E}_\parallel + \sigma_P \mathbf{E}_\perp - \sigma_H (\mathbf{E}\times\mathbf{B})/B \tag{2.33}$$

In a highly collisional, weakly magnetized plasma, collisions dominate ($\Omega_{ce} \ll \nu_c$), and the conductivity tensor reduces to a scalar ($\sigma_H \to 0$, $\sigma_P \approx \sigma_0$). In a collisionless space plasma ($\Omega_{ce} \gg \nu_c$), current mostly flows along the field line ($\sigma_P \approx \sigma_H \approx 0$). These conductivities are most relevant in a regime where $|\Omega_{ce}| \approx \nu_c$ (e.g. the ionosphere).

When $|\Omega_{ce}| > \nu_c$, electrons are able to $\mathbf{E}\times\mathbf{B}$ drift as they experience enough gyrations prior to being scattered, which means σ_H dominates. For $|\Omega_{ce}| < \nu_c$, scattering drives electrons in the direction of $E_\perp$ before they are allowed to drift, and therefore σ_P dominates. At $|\Omega_{ce}| \approx \nu_c$, the conductivities mostly balance and electrons move at roughly 45° to the

two currents. An example of conductivity as a function of altitude in the auroral ionosphere is shown in Figure 2-10.

At high latitudes, convecting flux tubes are highly conductive and magnetospheric potentials map down into the ionosphere. Convection patterns in the polar cap ionosphere result in equipotential contours that generate electric fields. High-latitude magnetic fields are nearly vertical and the conductivity along the field lines becomes nearly height-independent, which means the conductivity can be height integrated.

$$\Sigma_P = \int \sigma_P \, dz \qquad \Sigma_H = \int \sigma_H \, dz \qquad \mathbf{J}_\perp = \int \mathbf{j}_\perp \, dz \tag{2.34}$$

At auroral latitudes, the parallel electric field is often much smaller than the perpendicular field and is ignored. In that case, Ohm's law (Equation 2.33) only deals with the perpendicular fields in the height-integrated sense.

$$\mathbf{J}_\perp = \Sigma_P \mathbf{E}_\perp - \Sigma_H (\mathbf{E}_\perp \times \mathbf{B})/B \tag{2.35}$$

The perpendicular current, $\mathbf{J}_\perp$, is driven only by the perpendicular field, $\mathbf{E}_\perp$, but field-aligned currents, $\mathbf{J}_\parallel$, still flow parallel to the magnetic field. Assuming that the current is divergenceless, then $\nabla \cdot \mathbf{J} = 0$. The total current, $\mathbf{J} = \mathbf{J}_\perp + \mathbf{J}_\parallel$, can then be related to current continuity. [Parks, 2004]

$$\nabla \cdot \left(\mathbf{J}_\perp + \mathbf{J}_\parallel \right) = 0 \tag{2.36}$$

Ionospheric convection currents can therefore close currents that flow in from the magnetosphere, but they are also responsible for heating the atmosphere by Ohmic dissipation, or **Joule heating**. The rate of Joule heating Q_J, is proportional to the current flowing parallel to the electric field. [Baumjohann and Treumann, 2012]

$$Q_J = \mathbf{J}_\perp \cdot \mathbf{E}_\perp \tag{2.37}$$

Only Pedersen currents flow parallel to the electric field, so they are the only contribution to the height-integrated heating rate ($Q_J = \Sigma_P E_\perp^2$). The Joule heating relation depends more on the level of convection than on the number of precipitating particles.

2.4.3 Plasma waves

Electromagnetic waves propagate differently through a plasma than they do in a vacuum. Maxwell's equations, including Gauss' Law (Equation 2.18) and Gauss' Law for magnetism ($\nabla \cdot \mathbf{B} = 0$), are used to describe the propagation of light.[4]

$$\nabla \times \mathbf{E} = -\frac{\partial \mathbf{B}}{\partial t} \tag{2.38}$$

$$\nabla \times \mathbf{B} = \mu_0 \mathbf{J} + \mu_0 \epsilon_0 \frac{\partial \mathbf{E}}{\partial t} \tag{2.39}$$

Electromagnetic waves may be expressed in Fourier representation, with wave vector $\mathbf{k}$ and angular frequency ω.

$$\mathbf{E} = \mathbf{E}_0 e^{i(\mathbf{r}\cdot\mathbf{k} - \omega t)} \qquad \mathbf{B} = \mathbf{B}_0 e^{i(\mathbf{r}\cdot\mathbf{k} - \omega t)} \tag{2.40}$$

Equations 2.38 and 2.39 may be re-written with the plane wave forms of $\mathbf{E}$ and $\mathbf{B}$ and reduced to equations in terms of the wave vector, wave frequency, and the background fields $\mathbf{E}_0$ and $\mathbf{B}_0$. For simplicity, no currents are assumed present ($\mathbf{J} = 0$).

[4]Plasma wave derivations in the method of Gurnett and Bhattacharjee [2005]

$$\mathbf{k} \cdot \mathbf{B}_0 = 0$$

$$\mathbf{k} \cdot \mathbf{E} = \rho_c / \varepsilon_0$$

$$\mathbf{k} \times \mathbf{E}_0 = \omega \mathbf{B}_0$$

$$\mathbf{k} \times \mathbf{B}_0 = \mu_0 \epsilon_0 \omega \mathbf{E}_0$$

Fourier representation of Maxwell's equations can be used to solve for the dispersion relation of light in a vacuum, with roots $\omega = \pm ck$.

$$D(\mathbf{k}, \omega) = -k^2 + \frac{\omega^2}{c^2} = 0 \tag{2.41}$$

The phase velocity of the wave, $\mathbf{v}_p = (\omega/k)\hat{\mathbf{k}}$, in this case is simply $v_p = \pm c$. In this simple case, the group velocity, $\mathbf{v}_g = \nabla_{\mathbf{k}} \omega$, is the same as the phase velocity, $v_p = v_g = c$. Charged particles in a plasma interact with electromagnetic radiation in additional ways that must be taken into consideration, however. To determine a dispersion relation, a linear set of equations is used to examine the response of a plasma to small perturbations. For example, the plasma density may be re-written in terms of a background, uniform density and small perturbation, $n_s = n_{s0} + n_{s1}$. The rest of the relevant parameters in the plasma are treated in the same manner.

$$\mathbf{v}_s = \mathbf{v}_{s0} + \mathbf{v}_{s1} \qquad \mathbf{E} = \mathbf{E}_0 + \mathbf{E}_1 \qquad \mathbf{B} = \mathbf{B}_0 + \mathbf{B}_1$$

In a cold, stationary, unmagnetized plasma, ($\mathbf{v}_{s0} = \mathbf{E}_0 = \mathbf{B}_0 = 0$), only the first order, perturbation terms remain. The Lorentz equation of motion and current density are both solved in a linear fashion (i.e. second order terms, $\mathbf{v}_{s1} \times \mathbf{B}_1 \to 0$) using the Fourier

representation for each.

$$m_s(-i\omega)\mathbf{v}_{s1} = e_s\mathbf{E}_1$$

$$\mathbf{J}_1 = \sum_s n_{s0}e_s\mathbf{v}_{s1}$$

The current is related to the electric field through Ohm's Law, $\mathbf{J} = \sigma \cdot \mathbf{E}$, in which σ is the conductivity tensor.

$$\sigma = \sum_s \frac{n_{s0}e_s^2}{(-i\omega)m_s} \tag{2.42}$$

The conductivity tensor is similar to the ionospheric conductivity derived due to convection, however this form has a frequency dependence and is purely imaginary. The charged components of a plasma act as a dielectric medium, and the conductivity is used to determine the dielectric tensor, $\mathbf{K}$.

$$\mathbf{K} = \mathbf{1} - \frac{1}{i\omega\epsilon_0}\sigma = 1 - \frac{\omega_p^2}{\omega^2} \tag{2.43}$$

The dielectric tensor relates the microscopic behavior of electromagnetic interactions to the macroscopic behavior of waves propagating through a plasma. The plasma frequency, ω_p, is important for determining the dielectric properties of the plasma, which in most cases is set by the electron plasma frequency, ω_{pe}. The dielectric tensor is then combined with Maxwell's equations to determine a dispersion relation in an unmagnetized plasma.

$$D(k,\omega) = (-c^2k^2 + \omega^2 - \omega_p^2)^2(\omega^2 - \omega_p^2) = 0$$

The dispersion relation has two roots. One root is the longitudinal mode, in which the propagation is parallel to perturbations in the field.

$$\omega^2 = \omega_p^2 \tag{2.44}$$

The second root describes the transverse mode in which perturbations to the field, $\mathbf{E}_1$, are perpendicular to the the wave vector, k.

$$\omega^2 = \omega_p^2 + c^2 k^2 \tag{2.45}$$

The wave vector, $k = \pm(\omega^2 - \omega_p^2)^{1/2}/c$, describes the propagation of the wave through a plasma. For $\omega < \omega_p$, k becomes imaginary (i.e. damping) and the wave will not propagate through the plasma. For $\omega \gg \omega_p$, the relation simplifies to the vacuum dispersion relation, Equation 2.41. These relations hold for an unmagnetized plasma, but the addition of a background magnetic field, $\mathbf{B}_0$, changes the behavior.

In a cold, *magnetized* plasma ($\mathbf{B}_0 \neq 0$), the plasma is once again assumed stationary ($\mathbf{v}_0 = 0$), which also means the background electric field must be zero ($\mathbf{E}_0 = 0$). In the linear treatment, the equation of motion now retains the term associated with the magnetic field.

$$m_s \frac{\partial \mathbf{v}_{s1}}{\partial t} = e_s[\mathbf{E}_1 + \mathbf{v}_{s1} \times \mathbf{B}_0]$$

Assuming the background magnetic field is in the $\hat{z}$ direction, $\mathbf{B}_0 = (0, 0, B_0)$, the equation of motion can be reduced into vector components, using Fourier notation and the cyclotron frequency, $\Omega_{cs} = e_s B_0/m_s$.

$$\begin{bmatrix} -i\omega & -\Omega_{cs} & 0 \\ \Omega_{cs} & -i\omega & 0 \\ 0 & 0 & -i\omega \end{bmatrix} \begin{bmatrix} v_{sx1} \\ v_{sy1} \\ v_{sz1} \end{bmatrix} = \frac{e_s}{m_s} \begin{bmatrix} E_{x1} \\ E_{y1} \\ E_{z1} \end{bmatrix}$$

Inversion of the left side of the matrix re-solves the system in terms of velocity, which can be used to determine the current density, $\mathbf{J}_1 = \sum_s n_{s0} e_s \mathbf{v}_1$. The current density then relates to the electric field through Ohm's Law, $\mathbf{J} = \sigma \cdot \mathbf{E}$. As in the unmagnetized case, σ is the conductivity tensor, which now contains extra terms due to the effects of $\mathbf{B}_0$.

$$\sigma = \sum_s \frac{n_{s0} e_s^2}{m_s} \begin{bmatrix} \frac{-i\omega}{\Omega_{cs}^2 - \omega^2} & \frac{\Omega_{cs}}{\Omega_{cs}^2 - \omega^2} & 0 \\ \frac{-\Omega_{cs}}{\Omega_{cs}^2 - \omega^2} & \frac{-i\omega}{\Omega_{cs}^2 - \omega^2} & 0 \\ 0 & 0 & \frac{i}{\omega} \end{bmatrix} \tag{2.46}$$

From the conductivity tensor, the dielectric tensor may be expressed in the shorthand form of Stix [1962].

$$\mathbf{K} = \begin{bmatrix} S & -iD & 0 \\ iD & S & 0 \\ 0 & 0 & P \end{bmatrix} \tag{2.47}$$

The dielectric tensor $\mathbf{K}$ is the basic form for a cold plasma, which is valid at wavelengths much larger than the gyroradius of the particles and for high phase velocities much larger than the thermal velocity of the electrons. Three primary components describe the dielectric properties in a plasma.

$$P = 1 - \frac{\omega_{pe}^2}{\omega^2} - \sum_i \frac{\omega_{pi}^2}{\omega^2} \tag{2.48}$$

$$S = 1 - \sum_s \frac{\omega_{ps}^2}{\omega^2 - \Omega_{cs}^2} \tag{2.49}$$

$$D = \sum_s \frac{\Omega_{cs} \omega_{ps}^2}{\omega(\omega^2 - \Omega_{cs}^2)} \tag{2.50}$$

The P component along the field line is the same as for the unmagnetized case, separated out into electron and ion components. To understand electron behavior in the plasma, ions are slow enough to be considered stationary and the ion terms in the dielectric tensor, $\mathbf{K}$, may be dropped ($\omega_{pi}, \Omega_{ci} \to 0$). In that case, P reduces to the electron plasma frequency, $\omega = \omega_{pe}$. The remaining coefficients, S and D, are the transverse components of the oscillations and may be re-written in a more suggestive form.

$$S = 1/2(R + L) \qquad \text{and} \qquad D = 1/2(R - L) \tag{2.51}$$

For full clarity, the ion terms (ω_i, Ω_i) are temporarily retained.

$$R = 1 - \frac{\omega_{pe}^2}{\omega(\omega - \Omega_e)} - \sum_i \frac{\omega_{pi}^2}{\omega(\omega + \Omega_i)} \tag{2.52}$$

$$L = 1 - \frac{\omega_{pe}^2}{\omega(\omega + \Omega_e)} - \sum_i \frac{\omega_{pi}^2}{\omega(\omega - \Omega_i)} \tag{2.53}$$

Once again the dielectric tensor is used along with Maxwell's equations to determine the dispersion relation. The wave vector, $\mathbf{k}$ is replaced by the index of refraction, $\mathbf{n} = c\mathbf{k}/\omega$ to simplify notation and defined to exist in only the x-z plane, $\mathbf{n} = (n\sin\theta, 0, n\cos\theta)$. The result is a set of equations in terms of the dielectric tensor components and n^2.

$$\begin{bmatrix} S - n^2\cos^2\theta & -iD & n^2\sin\theta\cos\theta \\ iD & S - n^2 & 0 \\ n^2\sin\theta\cos\theta & 0 & P - n^2\sin^2\theta \end{bmatrix} \begin{bmatrix} E_{x1} \\ E_{y1} \\ E_{z1} \end{bmatrix} = 0 \tag{2.54}$$

Solving for the determinant of this equation results in a dispersion relation.

$$D(\mathbf{n}, \omega) = An^4 - Bn^2 + PLR = 0 \tag{2.55}$$

The two coeffecients are $A = S\sin^2\theta + P\cos^2\theta$ and $B = RL\sin^2\theta + PS(1+\cos^2\theta)$. The dispersion relation is quadratic in terms of n^2 and can be solved.

$$n^2 = \frac{B \pm \sqrt{(RL-PS)^2\sin^4\theta + 4P^2D^2\cos^2\theta}}{2A}$$

Since A and B are real, the index of refraction must be either purely real ($n^2 > 0$, i.e. propagating), or imaginary ($n^2 < 0$, non-propagating). A complex index of refraction, with non-zero real and imaginary parts, cannot occur because such an index of refraction would imply absorption of wave energy by the plasma. In the absence of collisions, energy absorption cannot occur in a cold plasma because there is no mechanism for converting the ordered motions associated with the wave into random thermal motions.

One specific case is for propagation parallel to the magnetic field ($\theta = 0$). In this case, the dielectric tensor is simplified further.

$$\begin{bmatrix} S-n^2 & -iD & 0 \\ iD & S-n^2 & 0 \\ 0 & 0 & P \end{bmatrix} \begin{bmatrix} E_{x1} \\ E_{y1} \\ E_{z1} \end{bmatrix} = 0 \tag{2.56}$$

Three solutions to this tensor are $P = 0$, $n^2 = L$, and $n^2 = R$, where R and L were defined above. The relations for R and L are high frequency, transverse, electromagnetic waves that propagate along the magnetic field with a circular polarization in either the right-hand (R) or left-hand (L) direction. Keeping only the electron terms, the R mode dispersion relation has a divergence at the electron cyclotron frequency, $\omega = \Omega_{ce}$.

$$\omega^2 = k^2c^2 + \frac{\omega_{pe}^2}{1-\Omega_{ce}/\omega} \tag{2.57}$$

The R mode is also known as the whistler mode, and an example power spectrum is

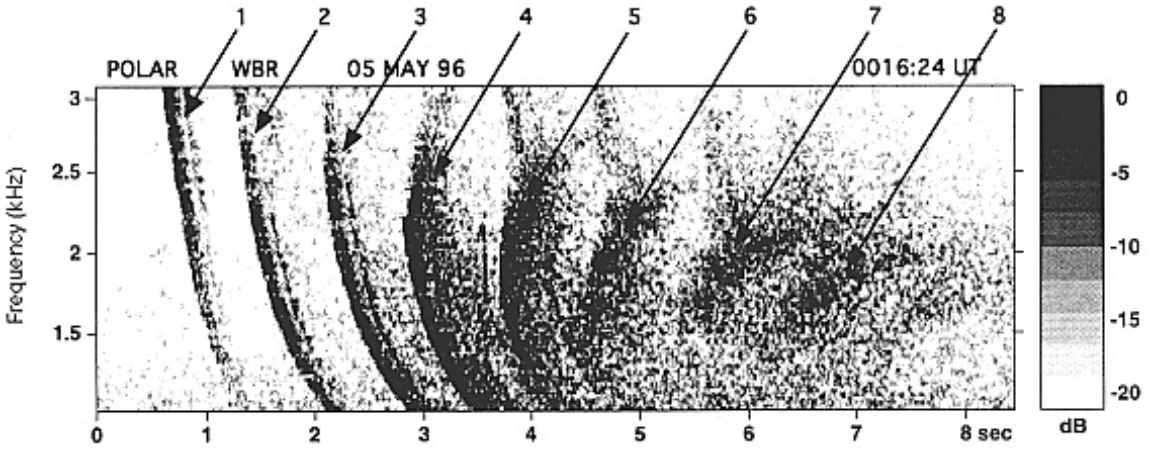

Figure 2-11: Very Low Frequency (VLF) spectrogram showing an example of an electromagnetic whistler wave [Bortnik et al., 2002], observed on the Polar spacecraft. Numbers indicate number of "hops" from a whistler originating from a single lightning discharge.

shown in Figure 2-11. The L mode has a similar dispersion relation to the R mode, but the resonance is now at the ion cyclotron frequency, $\omega = \Omega_{ci}$.

$$\omega^2 = k^2c^2 + \sum_s \frac{\omega_{pi}^2}{1 - \Omega_{ci}/\omega} \tag{2.58}$$

The resonance changes due to the charge dependence of Ω_c. Both R and L modes resonate with tranverse waves because the eigenvectors of the field perturbation rotate around the wave vector, k, in the same sense as the charged particles rotate around the magnetic field.

2.5 Chemical kinetics

Ionospheric dynamics are highly dependent upon chemical processes in addition to plasma physics. Chemical kinetics describes how chemical reactions physically occur, including rates and methods of reaction. Photochemical reactions (i.e. photoionization) create the majority of plasma within the ionosphere. Chemical recombination of ions and electrons in

the absence of EUV light is responsible for the decay of the ionosphere on the nightside.

$$O^+ + e^- \rightarrow O + h\nu \tag{2.59}$$

Particle collisions are another important path for energy exchange. Precipitating particles at high latitudes, for example, can dissociate molecules and produce ions or excited neutrals. This section will introduce basic principles of photochemistry, which describes how particles absorb and emit light. A brief discussion on spectroscopy will describe how emissions by ionospheric species may be used as a diagnostic tool to learn about the physics and chemistry occurring there.

2.5.1 Photochemistry

The study of interactions between light and matter, or photochemistry, has relevant applications across all disciplines within chemistry. Photochemical processes are often used as a macroscopic indicator or diagnostic tool of microscopic physical processes. The same is true in the ionosphere, where remote diagnostics are often a useful way, and sometimes the only way, to monitor physical phenomena. Solar photons, $h\nu$, at EUV and higher energies ionize particles like oxygen in the neutral thermosphere to generate the ionosphere.

$$O + h\nu \rightarrow O^+ + e^- \tag{2.60}$$

Lower frequency light (i.e. lower energy), like FUV radiation, may instead excite the particles into higher energy states.

$$O + h\nu \rightarrow O^* \tag{2.61}$$

The observed intensity of light, I, is attenuated from an initial intensity, I_0, by a mul-

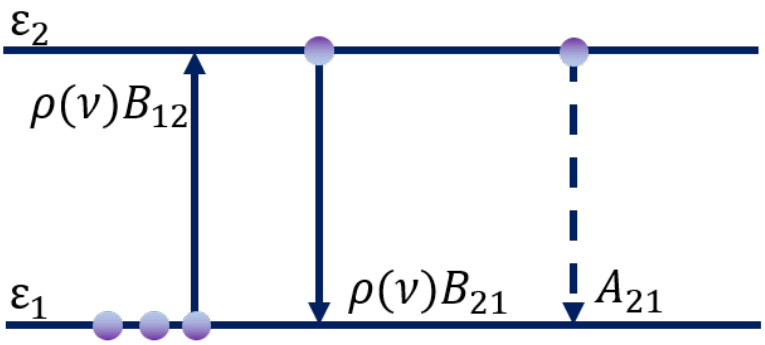

Figure 2-12: Illustration of a simple energy level diagram

titude of photochemical processes after traveling some path length, l, through a medium. The attenuation is described by the Beer-Lambert law.

$$I = I_0\, e^{-\sigma(\nu) l n} \tag{2.62}$$

The attenuated signal is a function of the density of interacting species, n, and the cross section for those species, $\sigma(\nu)$, as a function of frequency. The Beer-Lambert law is one way to describe the **optical depth** of a specific emission in the atmosphere. Photons passing through the medium will interact with particles at a rate proportional to $\sigma(\nu)$ and excite electrons within the particles from a ground state, ε_1, to a higher energy excited state, ε_2. A simple diagram in Figure 2-12 shows particles in both states.

Particles are excited to the higher energy at a rate proportional to some excitation coeffecient, B_{12}, and the energy density of the light, $\rho(\nu)$. The radiation energy density, $\rho(\nu)$, is a function of frequency, ν, and is assumed to be a blackbody spectrum.

$$\rho(\nu) = \frac{8\pi h\nu^3/c^3}{e^{h\nu/k_B T} - 1} \tag{2.63}$$

Photons can also interact with particles in an excited state and de-excite the electron at a rate proportional to B_{21}. Excited electrons may also spontaneously transition back to

a lower energy state at a rate A_{21}. The number of particles in the lower energy state, N_1, will change based on the rates of excitation and the energy density of light.

$$\frac{dN_1}{dt} = -N_1 B_{12}\rho(\nu) + N_2 \left[B_{21}\rho(\nu) + A_{21}\right] \tag{2.64}$$

If the system is in equilibrium, $dN_1/dt = 0$, the two populations may be expressed as a ratio.

$$\frac{N_2}{N_1} = \frac{B_{12}\rho(\nu)}{B_{21}\rho(\nu) + A_{21}}$$

Each population, N_i, is assumed to be a Boltzmann distribution.

$$\frac{N_2}{N_1} = \left(\frac{g_2}{g_1}\right) e^{-h\nu/k_B T} \tag{2.65}$$

The g_i terms represent the degeneracy in each energy level, ε_i. Combined with Equation 2.63, two relations between the excitation rates may be determined.

$$B_{12} = B_{21}\left(\frac{g_2}{g_1}\right) \qquad\qquad A_{21} = \frac{8\pi h\nu^3}{c^3} B_{21} \tag{2.66}$$

The factors A_{21}, B_{21}, and B_{12} are known as the Einstein coefficients. Using Equation 2.62, the excitation, or absorption, probability can be expressed in terms of the particle cross-section.

$$B_{12} = \frac{c\sigma(\nu)d\nu}{h\nu} \tag{2.67}$$

This relation can be integrated over some band of frequencies to find B_{12} or for just a specific frequency, ν. The spontaneous emission coefficient can be written in terms of physical constants as well.

$$A_{21} = \frac{64\pi^2\nu^3}{3hc^3}|\mu_{21}|^2 = \frac{\omega_0^3|\mathfrak{p}|^2}{3\pi\varepsilon_0\hbar c^3} \tag{2.68}$$

The spontaneous emission coefficient, A_{21}, is related to the dipole moment, μ_{21}, which is related to electric and magnetic dipole transitions. The electric dipole moment is typically dominated by the electric dipole transition, $\mathfrak{p}$, but in certain cases symmetry will force $\mathfrak{p} \to 0$. The electric dipole component ($\mathfrak{p}$) is $\sim 10^5$ larger than the magnetic dipole component, and $\sim 10^8$ times larger than the electric quadrupole component [Schunk and Nagy, 2009]. For the $\mathfrak{p} = 0$ case, the transition probability becomes very unlikely and is considered a "forbidden" transition. Due to the magnetic dipole and electric quadrupole moments, however, even "forbidden" transitions (e.g. OI 1356 Å), have a non-zero transition probability.

The relative magnitude of the Einstein coefficients (A_{21}, B_{12}, B_{21}) depends on many environmental factors in addition to the dipole moment terms. In the absence of external forces ($B_{21} = 0$) or alternative decay channels (e.g. molecular vibration), the fluorescence lifetime of an excited state is determined by the spontaneous emission coefficient, A_{21}.

$$\tau = \frac{1}{A_{21}} \tag{2.69}$$

At high enough altitudes in the ionosphere, collisions become infrequent enough that $B_{21} \ll A_{21}$ and Equation 2.69 applies. For example, the long-lived auroral red line transition at O I 6300 Å ($\tau_r \approx 110$ s) is the dominant emission at 250 km. At lower altitudes (e.g. 110 km) collisions become important enough that $B_{21} > A_{21}$ and the red line often becomes *quenched* before it can emit a photon. In this case, the dominant emission becomes the green line transition, O I 5577 Å. The lifetime of this transition ($\tau_g \approx 0.7$ s) is short enough to emit a photon before collisional processes quench the excited state atom.

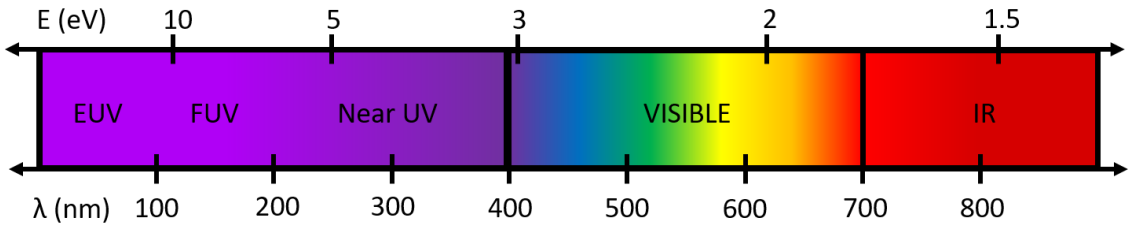

Figure 2-13: Electromagnetic spectrum and associated energies

2.5.2 Spectroscopy

The electromagnetic spectrum is used to determine a wide variety of information. Atoms and molecules absorb or emit radiation at discrete intervals that depend on the spacing between electronic states. Chemical composition of a remote source may be determined by matching the spectral lines in a spectrum to the known transitions of the particles. Most atmospheric species emit strongly at wavelengths in the ultraviolet, visible, and infrared wavelengths.

The 100 - 200 nm wavelength range (see Figure 2-13), or the Far Ultraviolet (FUV), contains strong spectral signatures for many atmospheric species in the thermosphere (e.g. H, N, O, N_2, O_2). As an example, Figure 2-14 shows a partial energy level diagram for electronic transitions in atomic oxygen [Schulman et al., 1985]. The energy of FUV photons ($\approx$ 10 eV) is near the transition energy for the lowest optically allowed transition, $^3S \rightarrow {}^3P$.

The two lowest energy transitions are the "forbidden" red (6300 Å) and green (5577 Å) lines often associated with the aurora, because an external energy source like precipitating particles is required to excite the oxygen atom to the state. The green line transition ($^1S \rightarrow {}^1D$) has a lifetime of $\sim$ 0.7 s, but the red line transition ($^1D \rightarrow {}^3P$) takes $\sim$ 110 seconds to decay back to the ground state.

Spectroscopic measurements are used to determine densities in the atmosphere given certain assumptions about the source population. Steady state emission sources are often

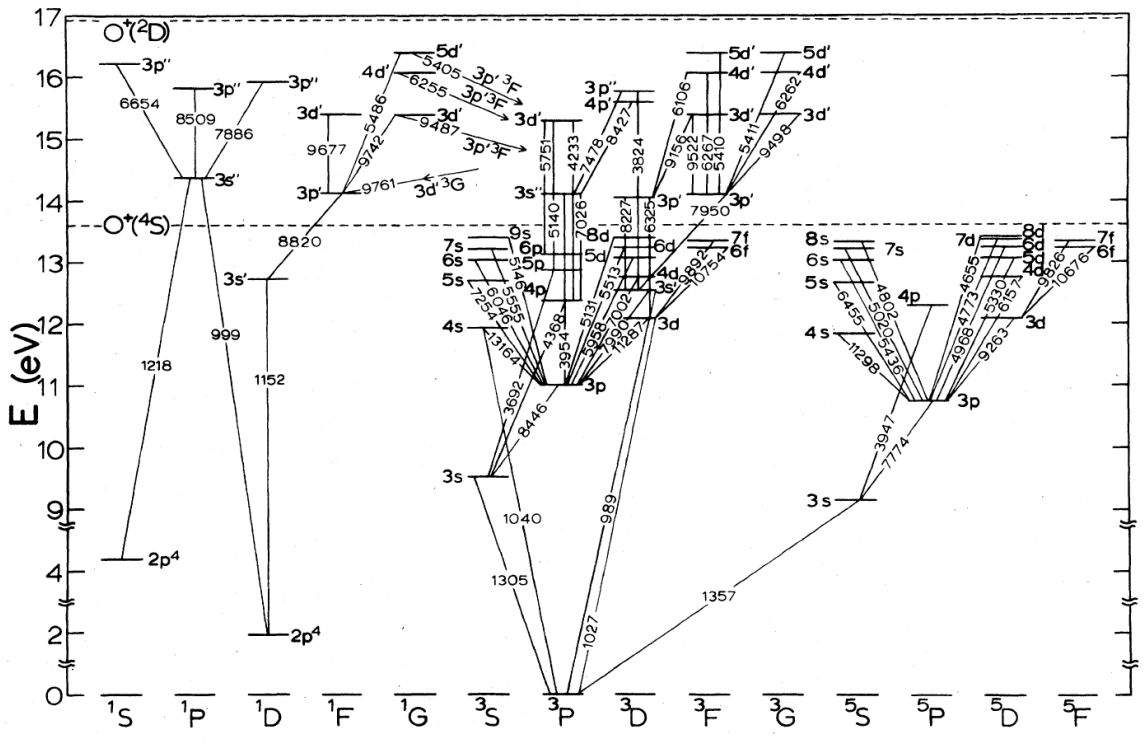

Figure 2-14: Partial energy-level diagram for atomic oxygen (OI), with wavelengths of transitions given in Å [Schulman et al., 1985]

the easiest to determine absolute densities. More often the ratio of particle populations (e.g. $[N_2]/[O]$) is easier to determine based on relative emission profiles. UV spectroscopy is a common method used by spacecraft missions for remote diagnostics of the ionosphere and thermosphere.

2.6 Atmospheric Processes

Many atmospheric mechanisms involve multiple physical processes acting together to produce one combined effect. Two important atmospheric processes important in ionospheric dynamics are presented in this section. First, instabilities occur throughout the atmosphere, including both fluid instabilities due to kinetic effects and plasma instabilities (in the ionosphere), driven largely by Coulomb interactions. Second, ion outflow is a critical component of magnetosphere-ionosphere coupling that supplies heavy ions from the iono-

sphere to the magnetosphere. The outflow process is driven by a combination of kinetic and electromagnetic effects.

2.6.1 Instabilities

Large-scale, or macro-instabilities occur as a result of fluid behavior in a plasma. Perturbation in a hydrodynamic system are often approximated by evaluating a plane wave solution, $e^{i(\mathbf{k}\cdot\mathbf{r}-\omega_R t)}e^{\omega_I t}$, where ω_R and ω_I represent the real and imaginary components of the wave frequency. The imaginary component describes whether the wave will grow ($\omega_I > 0$) or decay ($\omega_I < 0$).[5]

The **Rayleigh-Taylor Instability** occurs at the interface between two fluids of different density (see Figure 2-15 for illustration). When one fluid with density ρ_t is suspended on top of another fluid with density ρ_b, a small perturbation at the interface (red line) can grow unstable depending on the relative densities of the fluids. Assuming the two fluids are inviscid and incompressible, the growth rate, ω_{RT}, of an instability may be determined by linearized treatment of the momentum equation, continuity equation, and equation of motion. Gravity, g, acts in the direction normal to the stable interface between the fluids.

$$\omega_{RT}^2 = -gk\,\frac{\rho_t - \rho_b}{\rho_t + \rho_b} \tag{2.70}$$

A top layer less dense than the bottom layer ($\rho_t < \rho_b$) has a positive growth rate and the system is stable. A top layer with a higher density ($\rho_t > \rho_b$) has a negative growth rate and the instability will grow. This effect is akin to a layer of water suspended above a less dense layer of oil. Even a slight perturbation will cause the disturbed interface to grow unstable as the water displaces the oil.

If the two fluids are layers of plasma in the presence of a magnetic field, things become

[5]Instability criteria from Parks [2004]

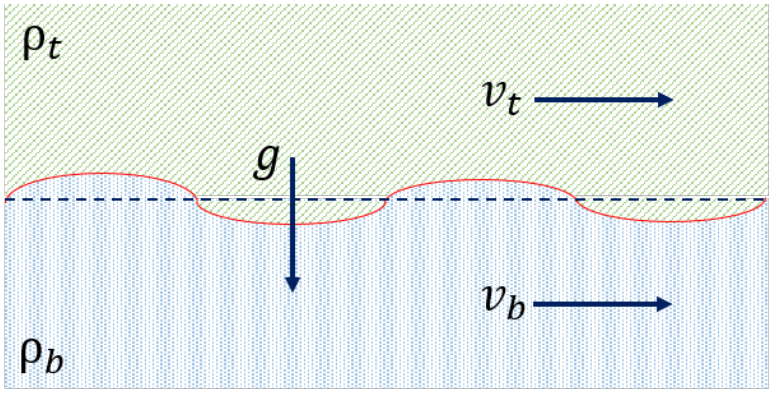

Figure 2-15: Illustration of a perturbation to the interface in simple two fluid system with gravity acting in the downward direction. The top (bottom) layer has a mass density, ρ_t (ρ_b), and moves with velocity, v_t (v_b).

more complex. A magnetic field parallel to the gravitational field ($B \parallel g$) will have no effect on the stability. A magnetic field orthogonal to the gravitational field ($B \perp g$) will, however, provide a restoring force for potential instabilities in a plasma which adds a second term to the growth rate.

$$\omega_{RT}^2 = -gk\,\frac{\rho_t - \rho_b}{\rho_t + \rho_b} + \frac{2B^2k_\perp^2}{\mu(\rho_t + \rho_b)} \tag{2.71}$$

When the two fluids in Figure 2-15 are stable in terms relative density ($\rho_t \leq \rho_b$), the next effect to consider is the relative velocity between the fluids. The top and bottom layers in Figure 2-15 flow with a velocity, v_t and v_b respectively [Parks, 2004]. The **Kelvin-Helmholtz Instability** arises in the presence of a flow shear ($v_t \neq v_b$). A magnetic field perpendicular to the flow shear ($B \perp k$) has no effect on the solution. For a magnetic field oriented in the same plane as the flow ($\mathbf{B} \cdot \mathbf{v} \neq 0$), the wave growth rate (ω_{KH}) is derived similar to the Rayleigh-Taylor Instability.

$$\omega_{KH} = \frac{\rho_t \mathbf{v_t} \cdot \mathbf{k} + \rho_b \mathbf{v_b} \cdot \mathbf{k}}{\rho_t + \rho_b} \pm \frac{\sqrt{(\rho_t + \rho_b)[\rho_t (\mathbf{V}_{At} \cdot \mathbf{k})^2 + \rho_b (\mathbf{V}_{Ab} \cdot \mathbf{k})^2] - \rho_t \rho_b (\Delta \mathbf{v} \cdot \mathbf{k})^2}}{\rho_t + \rho_b} \tag{2.72}$$

The flow shear is $\Delta \mathbf{v} = \mathbf{v}_t - \mathbf{v}_b$ and $\mathbf{V}_{Ai} = \mathbf{B}_i \cdot \mathbf{k}/\sqrt{\mu_0 \rho_i}$ is the Alfvén velocity along $\mathbf{B}_0$. The instability will grow if the quadratic contains a negative frequency component.

$$\rho_t \rho_b (\Delta \mathbf{v} \cdot \mathbf{k})^2 > \frac{\rho_t + \rho_b}{\mu_0} [(\mathbf{B}_t \cdot \mathbf{k})^2 + (\mathbf{B}_b \cdot \mathbf{k})^2]$$

In the absence of any magnetic fields, the instability criteria is simplified to the fluid terms, the classical analog to wind creating ripples on the surface of a body of water.

$$k > \frac{g(\rho_b^2 - \rho_t^2)}{\rho_b \rho_t (v_b - v_t)^2} \tag{2.73}$$

In a plamsa, instabilities also arise in more subtle ways due to Coulomb interactions between the charged particles. Plasma instabilities are important because they are capable of transferring free energy from non-equilibrium structures to fluctuations that grow in time. Instability criteria are determined by solving for the dispersion relation in a plasma and examining the real and imaginary components. Plasma instabilities are sometimes described as a micro-instabilities, with perhaps the simplest example being beams of cold flowing plasma. The dispersion relation is determined from a kinetic treatment of the plasma.

$$k^2 = \sum_j \frac{\omega_{pj}^2}{(v_j - \omega/k)^2} \tag{2.74}$$

The dispersion relation contains terms for the velocity, v_j, and plasma frequency, ω_{pj} of the j^{th} beam. When examined by component, $\omega = \omega_r \pm i\gamma$, where ω_r is the real component

of the frequency, a positive growth rate, $\gamma > 0$, means that an instablity will arise. This is sometimes referred to as the two-stream instability because it requires two populations of streaming particles.

Other plasma instabilities arise from anisotropies within a plasma population. Temperature anisotropies ($T_\perp > T_\parallel$) are capable of driving wave-generating instabilities such as the mirror and ion cyclotron anisotropy instabilities [Gary, 1992]. This anisotropy-driven instability is a common source of electromagnetic ion cyclotron (EMIC) waves in the magnetosphere.

2.6.2 Ion outflow

The ionosphere is the source for most of the heavy ions (e.g. O^+) in the magnetosphere. **Ion outflow** is a two step process through which ions are able to escape the gravitational well of Earth. The first stage of ion outflow requires the deposition of energy at ionospheric heights, usually in the F region. Ions upflow hundreds of km higher than their equilibrium state. The second step of ion outflow requires a second source of energy to give the ions the final kick out of the ionosphere before the atmosphere relaxes and the heavy ion species fall back down to an equilibrium height. The diagram in Figure 2-16 illustrates the pathways in which energy flows throughout the ion outflow process.

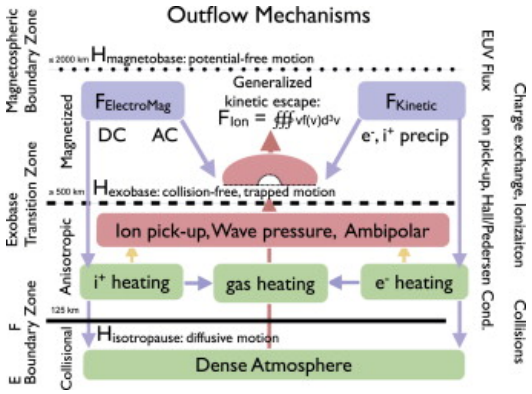

Figure 2-16: Flow diagram from Moore et al. [2014] (derived from figure in Strangeway et al. [2005]), shows the multiple pathways of energy exhange in the ionosphere that contribute to ion outflow

Ion outflow is divided into two broad categories that are defined by the mechanism responsible for the upflow process [Wahlund et al., 1992]. **Type 1 upflow** is the result of electromagnetic energy, or Poynting flux, flowing into the ionosphere. Enhanced electric fields increase the convection currents in the auroral region, seen in incoherent scatter radar signature as enhanced ion temperatures. The increased Joule heating rate, Q_J heats the background neutral gas, which then expands as a result.

Type 2 upflow is the result of kinetic energy flowing into the ionosphere, most often in the form of precipitating electrons. Radar measurements show this upflow by enhanced electron temperature and ambipolar electric field in the ionosphere. Electrons are heated directly by precipitating particles and adiabatically expand, establishing a vertical, ambipolar field. The heavier ions accelerate upward in response to the ambipolar electric field.

The second step of the ion outflow process occurs at higher altitudes. Transverse ion acceleration due to broadband ELF waves (BBELF) resonantly excites the ions to provide the additional kick of energy needed to escape Earth's gravity (e.g. see Kintner et al. [1996]). As shown in Figure 2-16, the ion outflow process is influenced by a wide range of energetic sources, and many of them are discussed in further detail by Strangeway et al. [2005] and Moore et al. [2014].

2.7 Aurora

Aurora is an optical phenomenon that occurs when energetic particles, most often in the form of precipitating ions and electrons, collide with other particles in the ionosphere-thermosphere (I-T). Atmospheric particles excited by the collisions emit light when they relax to a lower energy state (see Section 2.5.1). Spectral methods have shown many discrete emission lines within the aurora, but the most dominant emissions are from the neutral atomic oxygen emission spectrum (OI). The two lowest energy emission lines in

aurora are the red (O I 6300 Å) and green (O I 5577 Å) lines, which often makes them the brightest visible emissions seen from the Earth's surface.

Most auroral forms are grouped into a few general categories. This dissertation is focused on auroral types that are observed within the auroral zone, typically between $60° - 75°$ magnetic latitude on the nightside and $70° - 80°$ on the dayside [Hardy et al., 1985]. Auroral research is still a very active field where new discoveries have been made as recently as last year. The modern proliferation of scientific observatories as well as the leveraging of citizen science led to the categorization of Strong Thermal Emission Velocity Enhancement (STEVE) [MacDonald et al., 2018] in the subauroral zone.

Discrete aurora is the well-known display that appears in the auroral zone, typically as bright, colorful bands that stretch across the sky. **Alfvénic aurora** is similar in structure to discrete aurora, but is different in terms of emission intensity and generation mechanism. **Diffuse aurora** appears as a dim, hazy form in the night sky, barely detectable by the naked eye. **Pulsating aurora** is often lumped under a larger umbrella with diffuse aurora, but is in fact a separate form due form of aurora to its unique characteristics relative to diffuse aurora. Finally, **black aurora** is perhaps one of the most unique auroral types and is best described as the peculiar lack of emission in a well-defined region.

2.7.1 Discrete Aurora

Discrete aurora is a well-defined region of auroral emission that is generated by intense bursts of energy into the IT system. Features often take the form of banded or arc structures along a common magnetic latitude. Precipitating particles that cause discrete aurora are accelerated by quasi-static electric fields that produce monoenergetic peaks in the electron distribution.

Many of the first observations of precipitating particles in aurora were of the monoener-

getic type [McIlwain, 1960; Evans, 1968]. Precipitating electrons accelerated by quasi-static electric fields are often characterized as "inverted v" due to the distinctive spatial distribution of energy [Frank and Ackerson, 1971]. Theories to explain the "inverted v" signature include electric potential structures above the auroral forms to locally accelerate precipitating particles to the observed energy. Figure 2-17 shows a cartoon diagram of one type of potential structure that causes discrete aurora. Discrete aurora caused by monoenergetic precipitation tends to occur on the nightside and is often associated with substorms, which release massive bursts of energy into the atmosphere. The physics of substorms are not fully resolved, but the energy release is associated with reconnection in the magnetotail.

2.7.2 Alfvénic Aurora

Broadband electron precipitation accelerated by dispersive Alfvén waves causes several types of discrete-looking aurora seen on the dayside [Chaston et al., 2003], including poleward moving auroral forms (PMAFs) in the cusp region. The thin, arc structure associated with PMAFs [Fasel, 1995] look spatially similar to discrete aurora on the nightside, although the emission intensities are *much* lower and the acceleration mechanism is much different. As Chapter 6 will demonstrate, PMAFs are much more finely structured than the bright substorm arcs, forming wispy patterns that are not

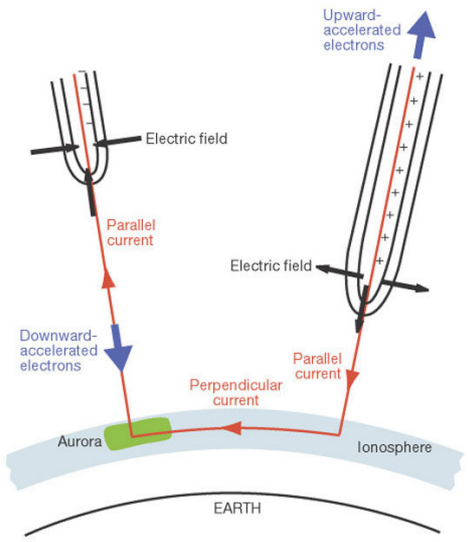

Figure 2-17: Cartoon from Marklund et al. [2001] showing the potential structures associated with current closure in discrete aurora

well captured by long-exposure images.

2.7.3 Diffuse Aurora

Diffuse aurora, as the name implies, is a dim, hazy glow in the night sky visible from the surface, defined broadly as auroral precipitation without a localized acceleration mechanism, like those that produce monoenergetic peaks in discrete aurora. Newell et al. [2009] showed through the use of an empirical model that diffuse aurora is the dominant supply of energy flux into the ionosphere. Diffuse aurora is responsible for 84% of the energy flux during conditions of low solar wind driving (63% electrons, 21% ions) and 71% of the flux during high solar wind-driving conditions (57% electrons, 14% ions).

Diffuse precipitation is triggered by pitch angle scattering of energetic plasma sheet particles into the loss cone [Kletzing et al., 2003]. Newell et al. [2009] argued that broad-band electrostatic waves are mostly responsible for the pitch angle scattering of diffuse precipitation. Thorne et al. [2010], on the other hand, argued that scattering by chorus waves is the dominant cause of diffuse auroral precipitation, much more so than electron cyclotron harmonic (ECH) waves. Khazanov et al. [2017] (and other recent works by the same author) examined the mechanisms responsible for diffuse aurora and found that the dynamics of particle precipitation in diffuse aurora is far more complicated than the initial wave-particle interactions that scatter plasma sheet electrons into the loss cone. Figure 2-18 shows the multiple pathways for particles within the magnetosphere as they relate to diffuse precipitation.

Energetic electrons initially scattered by whistler-mode and ECH waves in the plasma sheet create a secondary electron population in their collisonal cascade to lower altitudes in the ionosphere. Some of the lower energy electrons are created above the mirror point and accelerated out of the ionosphere back into the magnetosphere, where they are either

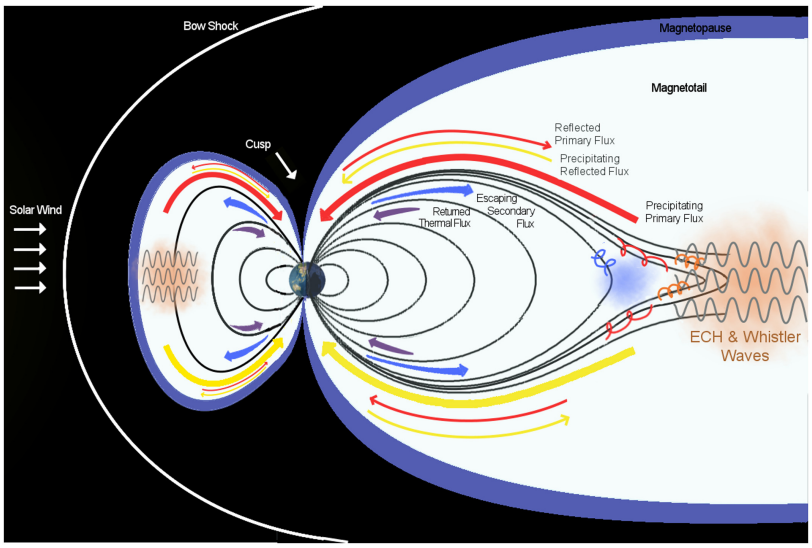

Figure 2-18: Cartoon from Khazanov et al. [2017] showing the pathways of diffuse auroral particles

trapped in the plasma sheet or scattered in the conjugate ionosphere. This implies a much stronger level of MI coupling than previously understood regarding diffuse aurora, where the ionosphere would otherwise just represent a passive display for magnetospheric inputs of energy. The ionospheric supplement to the simplistic model of diffuse auroral precipitation has been observed by rocket measurements of diffuse aurora [Rees et al., 1969] and ground-based optical measurements of pulsating aurora at conjugate locations [Samara et al., 2017].

2.7.4 Pulsating Aurora

Pulsating aurora is another optically dim form of aurora, often lumped together with diffuse aurora because of similarities in luminosity and generation mechanisms, but pulsating aurora is unique in spatial, temporal, and energetic characteristics. Often, observers note pulsating aurora during the recovery phase of a substorm [Lessard, 2013] as it transitions to from bright curtains to dim, diffuse patches (hence the term "breakup") that eventually begin to pulsate (e.g. Akasofu [1968]).

Luminosities of pulsating auroral patches are often faint, even sub-visual. Patches typ-

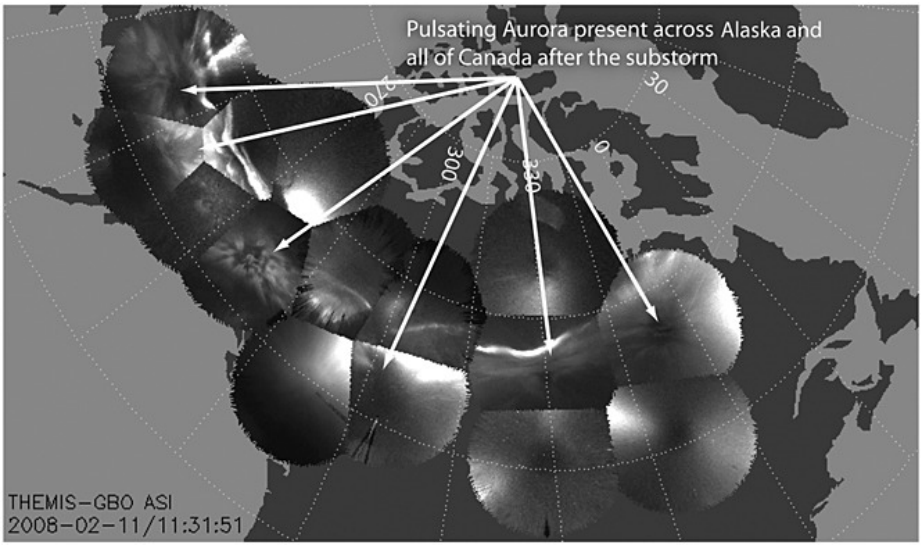

Figure 2-19: THEMIS all-sky imager data from Jones et al. [2013] that shows pulsating aurora spread across 10+ hours in local time

ically span tens to hundreds of kilometers in horizontal extent, often maintaining spatial shapes for several minutes despite the on-off modulation in brightness [Johnstone, 1978]. Pulsation periods range anywhere from 2 to 20 seconds, with an average of 8 seconds [Royrvik and Davis, 1977].

Pulsating aurora most often occurs in the post-midnight sector, and the most probable duration of an individual event is approximately 1.5 hours [Jones et al., 2011]. Extreme cases can last as long as 15 hours and extend across 9 hours in magnetic local time (MLT) [Jones et al., 2013]. Figure 2-19 shows pulsating aurora across the entire North American continent. Jones et al. [2013] showed pulsating aurora may occur independently of substorms but is enhanced locally by the presence of substorm activity.

Coordinated measurements by ground-based ASI and space-based assets from the Time History of Events and Macroscale Interactions during Substorms (THEMIS) mission showed a strong correlation between magnetospheric measurements of lower-band chorus waves and fluctuations in ionospheric optical emission intensity (i.e. pulsating aurora) [Nishimura et al., 2010]. Likewise, particle flux measurements by GOES 13 at geostationary orbit

correlated extremely well with modulation of pulsating aurora intensity measurements by THEMIS ASIs on the ground [Jaynes et al., 2013].

The Exploration of energization and Radiation in Geospace (ERG) spacecraft recently measured a strong correlation between bursts of lower-band chorus waves near the equatorial magnetosphere and particle flux modulations of high-energy electrons ($10 - 30$ keV) within the loss cone [Kasahara et al., 2018]. Coincident measurements by the THEMIS all-sky camera array at the ionospheric footprint of ERG show that pulsating aurora occurred concurrently with the modulation of particle flux. This tied together Nishimura et al. [2010] and [Jaynes et al., 2013] in one comprehensive measurement.

2.7.5 Black Aurora

Black aurora was first described as a lack of emission in well-defined regions [Davis, 1978], often in diffuse aurora or in the transition region between diffuse and discrete aurora (see Figure 2-20). It is often viewed as fine structure embedded within larger auroral forms, but there are two competing ideas about what causes black aurora. The first idea is that black aurora is nothing more than an absence of aurora, a simple explanation that assumes a dropout in precipitation due to structuring in the source region. Peticolas et al. [2002] suggests that black aurora occur in regions where ECH or upper-band chorus waves are locally suppressed in the plasma sheet. Sakaguchi et al. [2011] suggests that black auroral forms may be associated with the passage of a dipolarization front during a substorm.

The first idea about black aurora is driven by processes in the magnetosphere, and the resulting black aurora is an ionospheric indicator of remote magnetospheric processes. The second idea for black aurora is as an indicator of feedback systems within the ionosphere. The Freja satellite measured intense (1-2 V/m), small-scale (1 km) divergent electric fields that were associated with black auroral curls Marklund et al. [1997]. The divergent fields

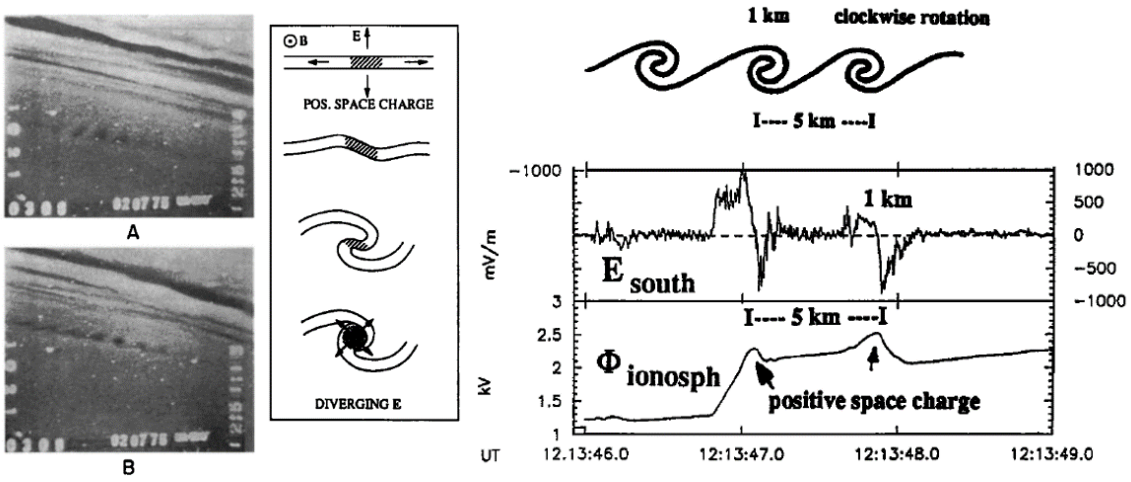

Figure 2-20: TV images taken 7 seconds apart of black aurora show black vortex streets [Davis, 1978]. Schematics of the vortex street and curl development are shown in the middle and top right. Freja measurements of the positive space charge associated with black aurora are shown in the bottom right. Figure from Marklund et al. [1997]

and the resulting curl structure are indicative of a return current region, which implies black aurora is a visual indicator of current closure in the ionosphere.

The most likely explanation for black aurora is a combination of both ideas. Fritz et al. [2015] (Chapter 4) presents a recent study about newly observed interaction between black aurora and pulsating aurora that supports the active feedback theory. The study points out, however, that the pulsating-black aurora interaction does nothing to argue against the validity of magnetospheric source mechanisms in addition to the active ionospheric feedback structure.

Chapter 3

Instrumentation

The Magnetosphere-Ionosphere Research Laboratory (MIRL) at the University of New Hampshire has a long history of developing space-flight instrumentation. This chapter discusses two instruments I was involved with developing at MIRL for sub-orbital, sounding rocket payloads. The first was a de-spun, white light ***imager*** *designed for stable, low-light imaging of the aurora. I implemented a thermal management system based on designs from the first RENU mission. I designed the de-spun platform based on parts available at UNH and that generated a proper spin rate. I designed the baffle based on available literature for light-suppressing systems and generated drawings for production. Finally, I assembled and tested the imager prior to integration, and then re-focused and calibrated the imager between integration and the launch window.*

The second instrument I worked on was an ***ultraviolet photomultiplier tube*** *(UV PMT) for remote measurement of thermospheric emissions of atomic oxygen. I was not involved with construction of the RENU 2 flight instrument. After the launch I built a spare instrument for post-flight calibration because the flight instrument was flown uncalibrated. I collaborated with Dr. Supriya Chakrabarti and Dr. Tim Cook at UMass Lowell to calibrate the spare UV PMT as a method of approximating the flight results.*

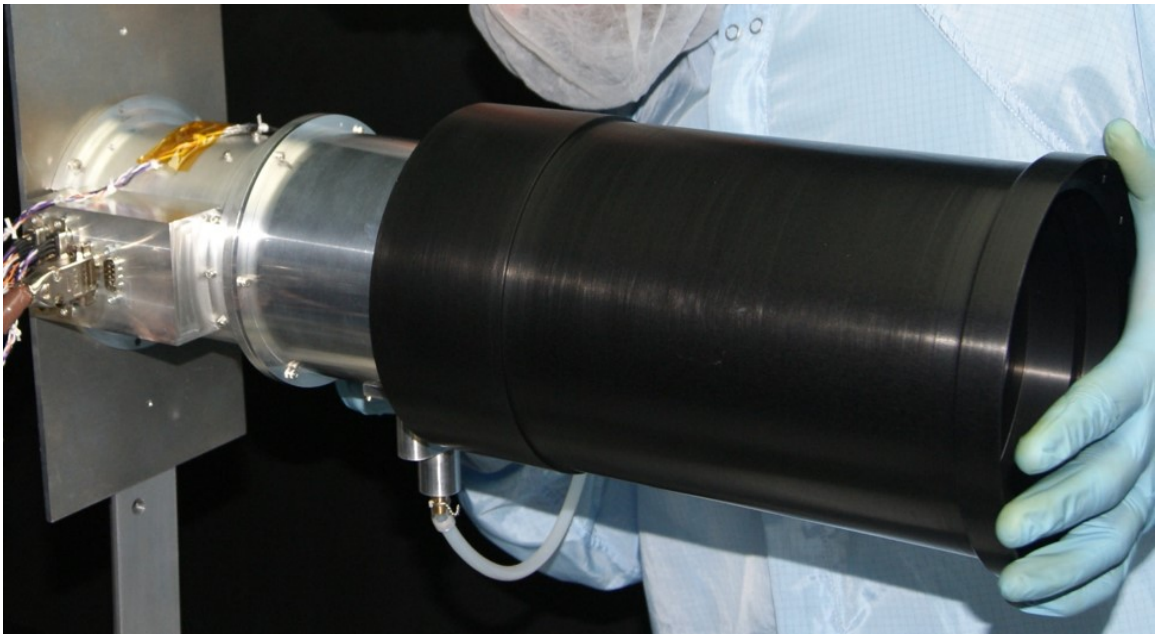

Figure 3-1: RENU 2 de-spun imager in the UNH MIRL optical calibration facility

3.1 De-spun Imager

A low-light imager was developed for spin-stabilized, sub-orbital sounding rocket payloads. The most recent version of the design flew on the Rocket Experiment for Neutral Upwelling (RENU) 2 sounding rocket (NASA Mission 52.002). The RENU 2 design was based heavily upon the De-spun Rocket Borne Imager 2 (DERBI 2) described in detail by Ellis et al. [2006] and Jones et al. [2008].

Figure 3-1 shows a full view of the RENU 2 imager in the MIRL optical calibration facility. The base aluminum section of the instrument on the left of the image houses the power conversion boards and rotating mechanism. The center aluminum section contains the sensor and associated electronics. A nitrogen purge line can be seen protruding from the bottom of this section. The right half of the image shows the black anodized, light-suppressing baffle, with the technician hand for scale-size reference.

Three primary design aspects of the RENU 2 imager are described in this section:

1. Thermal management: cooling the EMCCD on a spinning platform without a thermal path to the payload structure required a heat sink

2. Stray light attenuation: a light-suppressing baffle enabled sunlit operation

3. De-spun platform: low-light imaging requires long integration times ($\sim$ 1 s); producing a stable image required counteracting the spinning payload

In addition to the design challenges, a summary at the end of this section will address lessons learned from the RENU 2 mission that may be applied to future missions.

3.1.1 Thermal management

The RENU 2 imager sensor was a CCD97-00 Back Illuminated 2-Phase IMO Series Electron Multiplying CCD (EMCCD; from E2V Technologies). The EMCCD was chosen to image low light levels at a high cadence and with a large dynamic range. The active sensor area contained 512 x 512 pixels (8.192 mm x 8.192 mm). The imager used a 25 mm F/0.95 CCTV lens (Universe Kogaku, Inc., P/N EL1025B). A standard 25 mm CCTV lens produces a 9.6 mm x 12.8 mm (16.0 mm diag.) image at the focal plane, large enough to cover the active pixels on the EMCCD. The field of view focused at infinity is $21.7^\circ \times 28.7^\circ$ (35.2° diag.).

The lens and EMCCD locations are noted in the cutaway diagram of Figure 3-2. The EMCCD operating temperature was -120° C to $+75^\circ$ C, but the quantum efficiency (QE) of the instrument peaked in visible wavelengths at T = -20° C. Dark signal in the sensor scales logarithmically with temperature, so maximizing signal-to-noise ratio for the EMCCD required keeping the sensor temperature below 0° C. The image processing section was kept under nitrogen purge to eliminate moisture on the sensor.

A 3.0 A Peltier Module thermoelectric cooling (TEC) device (CUI Inc. Model #CP30338) was used to cool the sensor. The hot side of the the TEC was mounted directly to an aluminum heat sink. The EMCCD board was mounted to the heat sink above the TEC so the

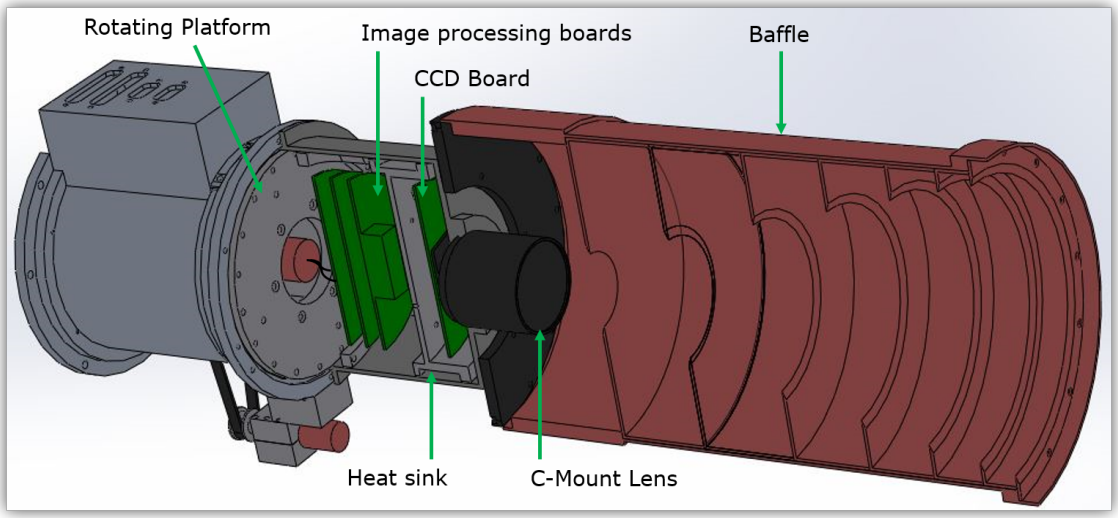

Figure 3-2: Partial cutaway view of the RENU 2 de-spun imager: visible are the interior of the rotating, image-processing section and the light-suppressing baffle.

cold side of the TEC made thermal contact with the back side of the sensor via an aluminum "nub." Thermal grease maximized thermal contact between the TEC and "nub," and a thermal gap filler pad (P/N TGF600M) did the same between the "nub" and the sensor. The temperature was monitored by a Series B57703 Thermistor affixed to the aluminum nub.

The heat sink was fit around the image processing electronic boards and mounted directly to the rotating platform. The rotating mechanism prevented a direct thermal path to the rest of the payload, but the heat sink provided an effective solution. The TEC was activated shortly after launch and quickly cooled the sensor to optimal temperatures prior to the science portion of the flight. The heat sink provided an adequate heat reservoir for the relatively short duration of the sounding rocket flight. Housekeeping thermistor data from the first RENU flight (not shown) confirmed that a similar system cooled the CCD rapidly in flight and maintained sub-zero temperatures for the duration of the mission.

3.1.2 RENU 2 baffle design

The RENU 2 mission flew into the cusp, located on the dayside of Earth, which meant the payload was sunlit for the majority of its flight. A light suppressing baffle was designed to prevent sunlight from striking the lens surface. Experiments have shown that a two-stage baffle with blackened knife edge blades is far superior to a single stage system [Heinisch and Jolliffe, 1971; Leinert and Klüppelberg, 1974], attenuating signals by as much as a factor of 10^{-11} [Marette and Gérard, 1976]. With that in mind, a two stage baffle was designed according to four guiding principles [Heinisch and Jolliffe, 1971]:

1. No optical elements (i.e. the lens) are allowed to view any sunlit wall or baffle edge. At least two reflections from blackened surfaces are required between any stray light source and the lens.

2. Light from within the baffles is required to experience a maximum number of surface reflections from blackened surfaces before entering the sensor.

3. A minimum number of edges exposed to the sun are to be used.

4. Surfaces that are not optical components in the field of view are blackened.

The baffle design followed an iterative process [Bucsela, 1994; Lee et al., 2000]. Three initial parameters were used to determine the total baffle size, all defined with respect to the center axis of the instrument. The lens diameter (D_L = 1.037 in) defined the first parameter, a, the innermost baffle aperture, $a = D_L/2 = 0.518$ in. The second parameter, α, was the minimum angle that prevented the lens from viewing the Earth's limb. For RENU 2, this restriction fell well within the CCTV lens field of view (FOV = 26°). With a small margin included, $\alpha = FOV/2 = 14°$, set the geometry of the inner, first stage. The third initial parameter is β, the solar aspect angle, which prevents direct solar illumination

on the inner first stage, and drove the geometry of the outer second stage. For the nominal RENU 2 trajectory plus two sigma margin of error, $\beta = 31.5°$. The length (l_1) and outer aperture size (D_1) of the first stage were calculated using a, α, and β.

$$\begin{aligned} l_1 &= \frac{D_L}{\tan\beta - \tan\alpha} \\ D_1 &= \frac{\tan\beta + \tan\alpha}{\tan\beta - \tan\alpha} D_L \end{aligned} \tag{3.1}$$

For the RENU 2 imager baffle, $l_1 = 2.83$ in and $D_1 = 2.5$ in. The dimensions of the second, outer stage were calculated similarly.

$$\begin{aligned} l_2 &= \frac{\tan\beta + \tan\alpha}{(\tan\beta - \tan\alpha)^2} D_L \\ D_2 &= \frac{(\tan\beta + \tan\alpha)^2}{(\tan\beta - \tan\alpha)^2} D_L \end{aligned} \tag{3.2}$$

For the RENU 2 imager, $l_2 = 6.75$ in and $D_2 = 5.85$ in, which meant the total baffle length was $L = l_1 + l_2 = 9.64$ in. The size of the outermost, second stage, D_2, drove the mechanical width of the system, with margin for mechanical strength.

The size and spacing of the additional vanes within the baffle was determined by an iterative process, calculated separately for both stages. The process started with the outermost vane ($x_0 = 0$ and radial size $y_0 = D_2/2$) and worked inward toward the lens. The radial size of the next vane, y_{i+1}, was calculated by the geometry of the initial parameters, α and β.

$$y_{i+1} = r - \frac{r + a}{1 + q_i} \tag{3.3}$$

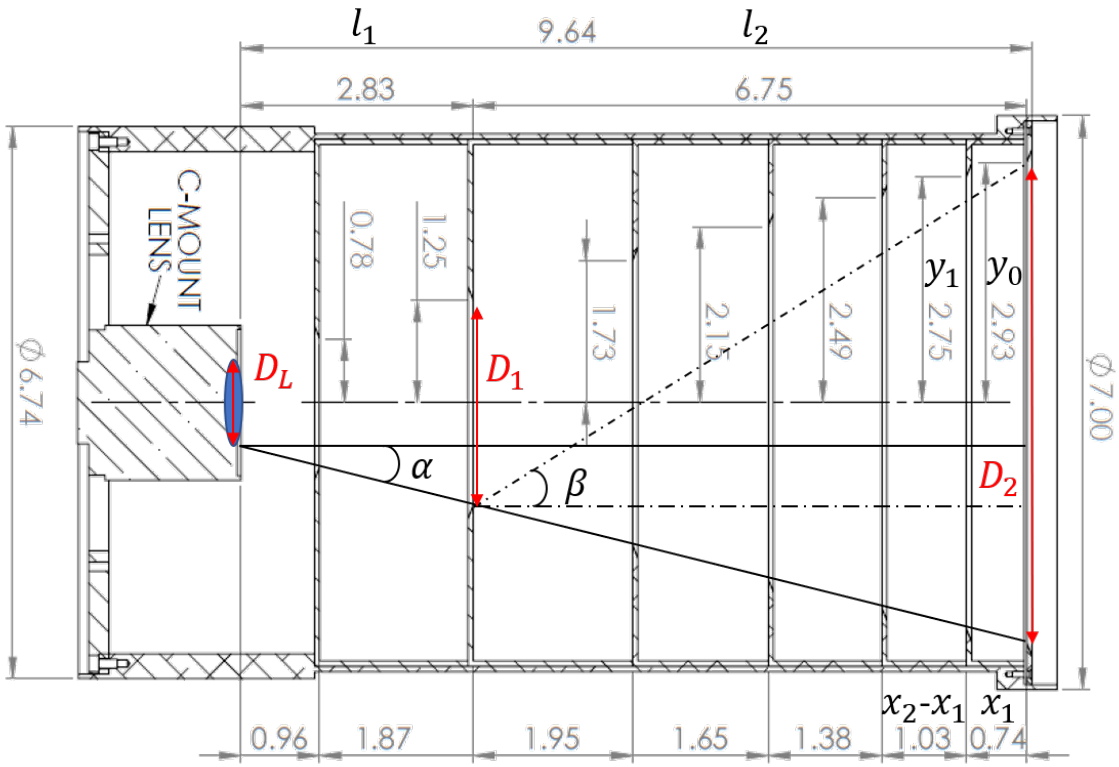

Figure 3-3: Drawing of the RENU 2 imager baffle with calculated dimensions (in inches)

$$q_i = 2a\left[r - y_0 + x_i\left(\frac{y_0 - a}{s}\right)\left(\frac{y_0 + r}{y_0 + y_i}\right)\right]^{-1} \tag{3.4}$$

In Equation 3.3, a is the inner aperture of the stage, which for the second stage $a = D_1/2$, and r is the radius of the baffle housing. The value of q_i is determined by Equation 3.4, where the overall length of the stage, $s = l_2$. The spacing of the next vane, x_{i+1}, is calculated as well.

$$x_{i+1} = (y_0 - y_{i+1})\frac{s}{y_0 - a} \tag{3.5}$$

The calculations were iterated until $x_n > x$. The process was then repeated for the inner baffle stage, with $a = D_L/2$, $s = l_1$, and $y_0 = D_1/2$.

Vane edges within the baffle were sharpened with an asymmetric bevel and were oriented to minimize the effects of scattered light in the system [Breault, 1977]. In the outer, second stage, where the vane edges can potentially see an off-axis source of radiation, the bevel was oriented away from the lens. In the inner, first baffle stage, the bevel faced the lens to reduce the chances for reflected light to reach the lens.

3.1.3 De-spun platform

The RENU 2 payload was spin-stabilized at ~ 0.5 Hz for the science portion of the flight. The MIRL imager was located on the aft end of the payload to capture aurora along the spin axis at the payload footpoint. Long integration time (~ 1 sec) was desired for imaging low light-levels. Producing a stable image required rotating the EMCCD counter to the payload spin at exactly the same rate.

The RENU 2 EMCCD board, heat sink, and image processing electronic assembly were mounted on the rotating platform indicated in Figure 3-4. A commercial camera (Watec Inc. WAT-910HX) is included in the diagram to illustrate the independence of the de-spun assembly from the imaging assembly and its potential applicability to future missions. A slip ring inside an aluminum housing is mounted to the base of the rotating platform. The RENU 2 imager required a slip ring with 24 electrical connections (P/N Moog SRA-73587) to provide communication between the rotating imager assembly and the payload.

Silverthin Bearings (P/N SA025BR3K) were slip-fit around the top of the slip ring housing to minimize the torque required to rotate the platform. The rotating platform and slip ring housing were belt-driven by an electric motor (Maxon Motor Assembly No. 508486). The RENU 2 motor assembly was comprised of an encoder (P/N 110778), a DC brushless motor (P/N 118701), and a gearbox (P/N 110322), which reduced the motor spin rate (ω) and increased the output torque (τ), both proportional to its gear ratio, $g_r = 19$.

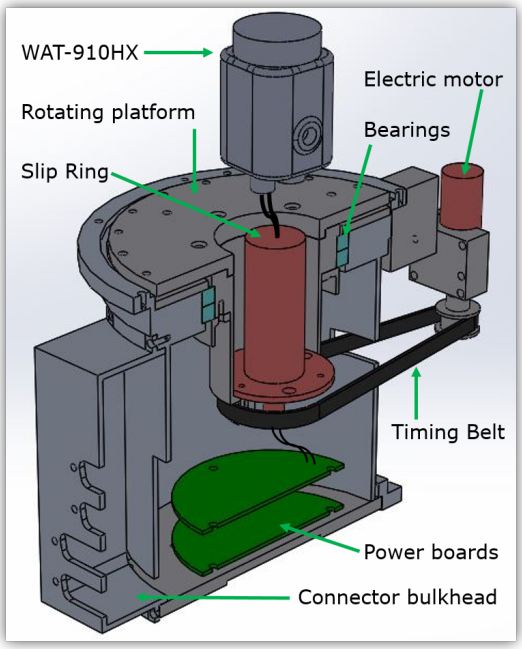

Figure 3-4: Cutaway view of de-spun imager platform, with a commercial camera (Watec Inc. WAT-910HX) above the platform

$$\frac{\omega_{in}}{g_r} = \omega_{out} \qquad \tau_{in} g_r = \tau_{out}$$

A timing pulley attached to the shaft of the electric motor (Sterling Instrument P/N A 6A16-012DF2504) drove the timing belt (S.I. P/N SDP A 6Z16 123 025/060) attached to another timing pulley press-fit onto the bottom of the slip-ring housing (S.I. P/N A 6A16-060NF2508). The RENU 2 combination of timing pulleys had a gear reduction, $g_r = 5$, which is a simple ratio between the gear sizes.

$$g_r = \frac{\#\text{ driven gear teeth}}{\#\text{ driving gear teeth}} \tag{3.6}$$

The gearbox ($g_r = 19$) and timing pulley system ($g_r = 5$) reduced the nominal motor speed of 5030 rpm to $\sim$ 52 rpm and increased the torque from 5.48 mNm to $\sim$ 0.52 Nm, which was adequate to rotate the RENU 2 EMCCD assembly.

The payload rate of rotation was determined by a deck-mounted QRS11 single-axis analog gyroscope. The rotation rate was fed to the motor encoder via the imager control electronics. The spin rate of the rotating stage was monitored by a slot-type photomicrosensor (Omron Model EE-SX672A), which acted as an active feedback system to the motor control circuit. The input voltage to the motor varied based on the rate sensor feedback in

order to match the sensor rotation rate to the payload roll rate received from the QRS11 sensor.

3.1.4 Imager summary

The RENU 2 de-spun imager was deemed a mechanical success. Housekeeping data in the rocket telemetry indicated that the instrument powered on and rotated at the appropriate rate. Unfortunately, the data has been deemed unusable, with the most likely cause being glint from the sunlit, aluminum sub-payload directly below the main payload within the imager FOV. Two primary lessons were learned from the loss of data on the RENU 2 flight.

- The baffle design should be thoroughly tested in addition to the imager itself prior to flight. Due to time constraints prior to integration, angular calibration tests were not performed to verify the level of light suppression with the baffle. Complete baffle testing would provide additional confidence that the loss of data was not due to glint from the sub-payload and not due to a design flaw.

- There should be a simple method for verifying focus and functionality of the imager during payload integration. A "baffle cap" with a small back-lit image would provide a focus check capability between integration tests. Once the imager left UNH, there was no way to verify instrument focus on the payload prior to launch. Verification of instrument focus and functionality on the payload would have provided further certainty that the poor data quality is due to external contamination.

In addition to the lessons provided by the loss of mission results, the design, assembly, test, and integration of the imager provided several engineering considerations that future designs should consider for improvement.

- The imager housing was cylindrical with a removeable bottom plate. A rectangular

instrument base with removeable side panels would provide easier access to internal components for assembly of the instrument. Flat housing surfaces also simplifies mounting components, such as the electric motor, and would preclude the need for an elaborate connector mount.

- The motor and timing belt are currently mounted to the exterior of the instrument housing, a possible point for critical failure during operation. Adequate space to mount the motor and belt system interior to the instrument base would reduce the risk for failure.

- The TEC required a large DC power supply in a separate housing, which complicated the total system design and increased the instrument footprint on the payload deck. Future designs that require a TEC should include the power system within the instrument base.

The RENU 2 telemetry provided adequate verification of several subsystems within the imager, including the thermal management and the de-spun mechanism, both of which could be considered for use on future sounding rocket payloads. The de-spun platform in particular is a useful assembly for any future spin-stabilized, space-based payload.

3.2 Ultraviolet Photomultiplier Tube

An ultraviolet photomultiplier tube (UV PMT) on RENU 2 measured spectral emissions of atomic oxygen (OI) above the payload. Space-based UV sensors are commonly found on spacecraft because the atmosphere is opaque to the Far UV (FUV) spectrum, preventing ground observations. The opacity presents its own unique set of advantages, however, including measurements free from contamination due to ground sources.

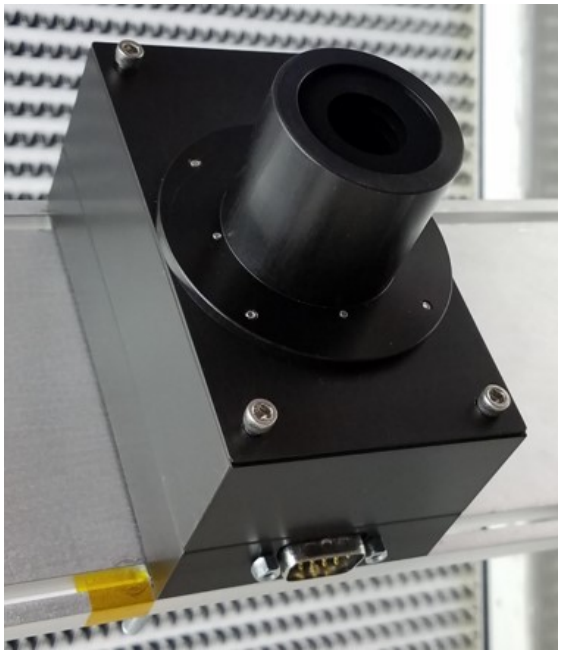

Figure 3-5: RENU 2 UV PMT flight spare

The RENU 2 UV PMT was a simple instrument with low resource requirements. Figure 3-5 shows the complete instrument mounted on a test bracket. This section will cover some basic information about the PMT instrument, as well as basic mechanical and electrical design information to illustrate its simplicity. Calibration procedures carried out in collaboration with the University of Massachusetts, Lowell are described and how they provided an estimate for the light levels measured on RENU 2.

3.2.1 PMT information

PMTs are commonly used for remote sensing at low light levels, down to photon-counting levels, and have been in use for over 80 years [Bay, 1938]. The RENU 2 instrument was built around a Hamamatsu R10825 Photomultiplier Tube (PMT). This PMT is highly sensitive in the wavelength range $1150 - 1950$ Å, with a maximum response at 1300 Å. The peak quantum effiiency is approximately 26.0%

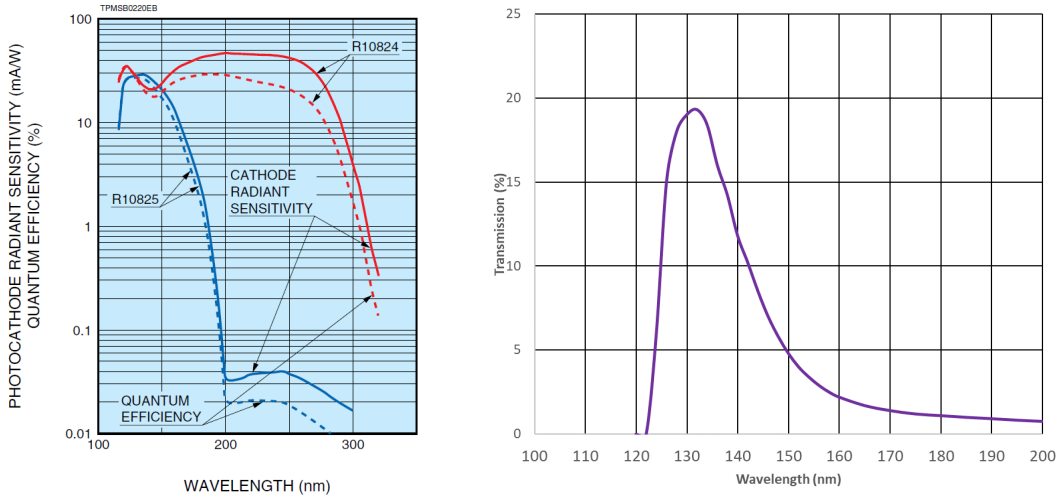

Figure 3-6: Left: Typical spectral response for Hamamatsu FUV PMT; the solid blue curve represents the sensor used on RENU 2 (R10825). Right: Spectral transmission curve for RENU 2 UV PMT filter.

with an anode sensitivity of $1.0 \times 10^5 A/W$ at 121.6 nm (see Fig 3-6, left). The photocathode is cesium iodide ($Cs - I$) and the detector window is magnesium flouride (MgF_2).

FUV emissions are not visible from the ground due to the absorption optical depth of molecules in the atmosphere like O and O_2. Two common FUV emissions of neutral atomic oxygen (O I) in the thermosphere are O I 1304 Å and O I 1356 Å. The triplet at 1304 Å is the lowest-energy, optically-allowed transition to the ground state of oxygen (^{3}P), which means at even modest densities the optical depth makes it a very challenging spectral feature to interpret. The spin-forbidden doublet at 1356 Å, however, is optically thin enough to be useful for general characterization of the lower ionosphere, including the F-peak region.

The RENU 2 instrument was filtered to look at both O I 1304 Å and O I 1356 Å using a randomly polarized, CaF_2 quartz interference filter (Pelham Research Optical, LLC P/N 135-NB-.5DC). The filter provided a peak transmission of 18.0% at 1304 Å with a FWHM of 195 Å (see Fig 3-6, right). The out of band rejection is a minimum of 10^{-4} in order to suppress Lyman α hydrogen emissions.

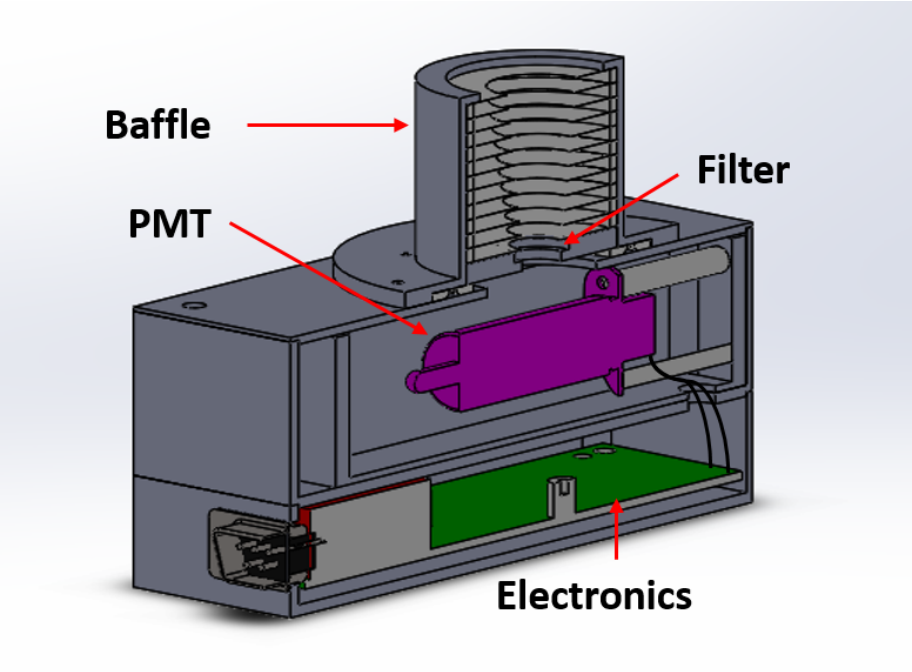

Figure 3-7: Cutaway diagram of the RENU 2 UV PMT

3.2.2 PMT instrument design

The PMT sensor was mounted inside a small enclosure just larger than the detector itself. Standoffs provided clearance between the bottom of the instrument and the side wall of the enclosure. The space around the PMT was filled with an optically-clear, silicone rubber sealant (RTV-615), which provided mechanical stability and helped prevent high-voltage discharge between the exposed electrodes. Figure 3-7 shows the layout of the instrument interior, including the placement of the PMT within the enclosure.

A black-anodized, knife-edge baffle was located directly above the PMT sensor window to help collimate the incoming signal and reduce glare from unwanted sources. The baffle FOV was approximately 12.5°. Brass baffle blades are separated by simple VITON gaskets, and the baffle assembly was pinched in place by the bottom blade. This assembly also included the UV filter, located at the bottom aperture, closest to the PMT window. The baffle blades were blacked and the rest of the aluminum instrument body was black anodized

to reduce reflectivity.

Photons enter the PMT through the baffle FOV and filter, where they strike the surface of the photocathode and eject a photoelectron, which then cascades through a series of electrodes (dynodes) before reaching the anode. The quantum efficiency, highlighted above, signifies the probability of photoelectron emission when a single photon strikes the photocathode. The current out of the anode, used to determine photon flux, passed through the bottom of the PMT enclosure and down to the electronics board below.

The lower half of the case housed the electronics board, which supplied high voltage to the PMT dynode chain. The same board also converted the output anode current to a voltage (0-5 V) and then amplified the analog output voltage. For RENU 2 the analog output was digitized at 1 kHz by the payload telemetry system with 12 bit resolution.

3.2.3 Calibration

The RENU 2 UV PMT was not calibrated prior to launch, which is a limitation of the flight measurement. An identical spare instrument was built and calibrated to provide a rough estimate of photon flux in the RENU 2 data. The instrument was calibrated at the Lowell Center for Space, Science & Technology at UMass-Lowell through a collaboration with Dr. Supriya Chakrabarti and Dr. Tim Cook.

A continuous gaseous discharge source [Paresce et al., 1971] was used to generate an OI spectrum (see Figure 3-8, left). A hollow, water-cooled cathode tube was filled with industrial-grade oxygen, where high voltage between the cathode and anode created a plasma discharge that dissociated the O_2 molecules. The resulting excited atomic oxygen (O^*) atoms emit photons when relaxing to the ground state.

$$O^* \rightarrow O + h\nu \text{ (1304 Å)}$$

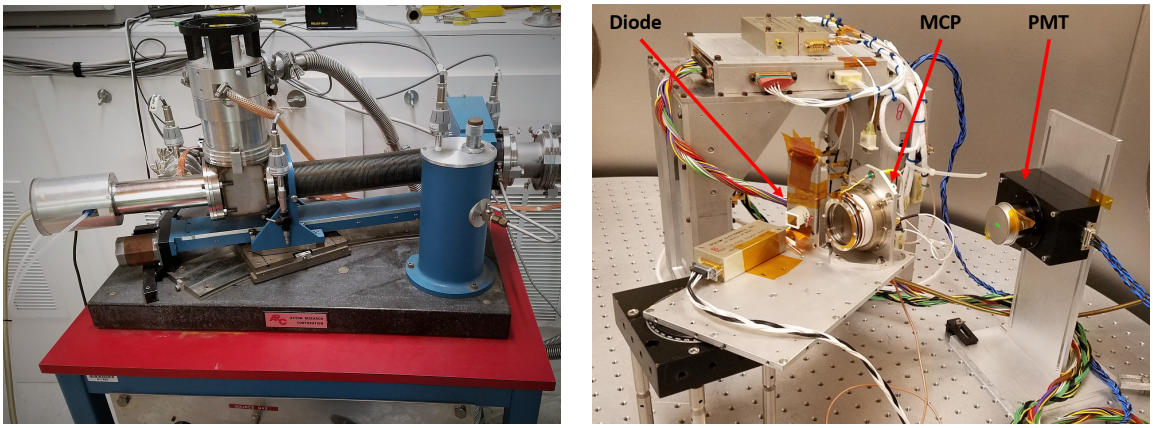

Figure 3-8: UMass Lowell facility used for UV calibration. Left: Paresce continuous gas discharge source. Right: Detectors mounted within the vacuum system for calibration.

The output radiation passed through a monochromator to isolate the desired wavelength (λ = 1304 Å), through an interlock system, and into the detector chamber. The process required use of the UV PMT, a microchannel plate (MCP) detector and a NIST-calibrated photo-diode for cross-calibration. First, the PMT and MCP detector were used to determine a linear relationship between a count rate in the known, MCP detector and the unknown PMT response.

The experiment setup is shown in Figure 3-8 (right). The green dot on the front of the PMT aperture (covered by a metal cap) is from the laser alignment with the monochromator grating. The photo-diode and MCP detector were mounted to a rotating stage, which allowed them to rotate into the light path when necessary, and out of the light path to provide an unobstructed view for the PMT.

The results of PMT-MCP comparison are shown in Figure 3-9. PMT voltage measured on an oscilloscope was compared to an MCP measurement of the same signal up to the maximum output of the source. 5 V on the PMT represents zero signal and 0 V is the saturation point. Data points represent the mean voltage recorded by the oscilloscope and the error bars represent the maximum and minimum values recorded. The dashed black line represents the PMT baseline voltage of $\sim$ 3.8 V, which is a combination of dark current

noise and built-in offset to avoid saturation on the low end.

A linear fit to the data (red dash-dot line) shows very good linear response between the PMT and the MCP. The solid red line, howeve, is a linear fit to the data with the intercept set to 5 V. The dynamic range of the PMT circuit is 0-5 V, and forcing the trend to fit this range provided an equation to convert voltage output from the PMT to cts/sec

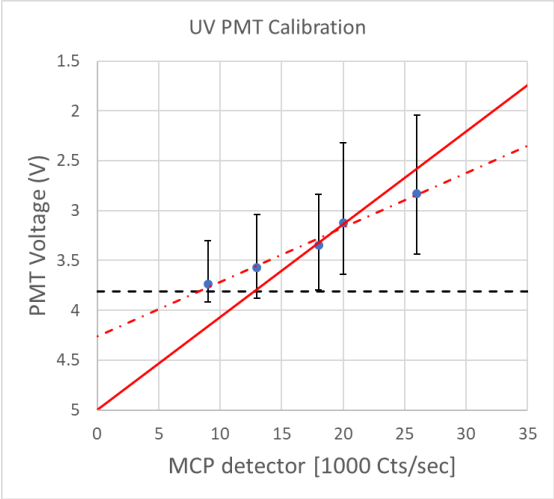

Figure 3-9: Relationship between the UNH UV PMT voltage output and the UML MCP cts/sec measurement. Linear fits to the data in red represent the unconstrained (dash-dot) and constrained fit (solid) at 5 V.

$$\left(\frac{\text{cts}}{\text{sec}}\right)_{MCP} = \frac{5 - V_{\text{PMT}}}{9.31 \times 10^{-5}}$$

Data points near the baseline do not fit the constrained trend, because the minima are truncated near the baseline. The truncated measurements affect the mean voltage measured by the oscilloscope, but the linear fit aligns more closely with the higher values where the PMT signal is not truncated. With the MCP fit, the PMT voltage can be converted to cts/sec, which was used to determine the radiance, B, based on the physical characteristics of the instrument [Huffman, 1992].

$$\left(\frac{\text{cts}}{\text{sec}}\right) = B\ A\ \Omega\ E\ K \tag{3.7}$$

A is the effective area of the collecting aperture. The photocathode of the Hamamatsu R10825 PMT is 0.95 cm $\times$ 0.4 cm, so $A = 0.38$ cm^2. The instrument field of view is Ω (steradians), and is assumed well defined for the sensor with good rejection out of view.

$$\Omega = \int_0^{2\pi} \int_0^{\theta} \sin\theta' \mathrm{d}\theta' \mathrm{d}\phi$$

The UV PMT FOV was $\theta = 12.5°$, so $\Omega = 2\pi(1 - \cos\theta)|_0^{12.5°/2} = 0.0373$ sr. The sensor efficiency (E) includes both the PMT efficiency as well as the filter transmission. According to Hamamatsu, the R10825 PMT has a quantum efficiency of 26.0% at T = $25°C$ (at $\lambda = 121.6$ nm). The peak transmission for the filter is 18.0% at 134.0 nm. Taken together, the maximum efficiency for the instrument is $E = 0.26 \times 0.18 = 0.0468$.

Radiance (B) is the radiation emitted in a given wavelength interval ($\Delta\lambda$) from an extended source (i.e. not a point source) per unit area and unit solid angle. Units can be either W/cm^{2}sr ($\Delta\lambda$) or, more conveniently, Rayleigh/$\Delta\lambda$. The Rayleigh (R) unit of measurement was originally defined for the purposes of quantifying airglow and aurora [Hunten et al., 1956].

$$1 \text{ R} = \frac{10^6 \text{ photons}}{\text{sec cm}^2 \ (4\pi \text{ sr})(\Delta\lambda)}$$

For single wavelength emission, $\Delta\lambda$ is typically implied rather than stated explicitly. K is a radiometric constant for converting to Rayleigh, $K = 10^6/4\pi$. The calculated values for the instrument are often combined and reported as a sensor efficiency: $(\text{cts/sec})(1/B) = (0.38 \text{ cm}^2)(0.0373 \text{ sr})(0.0468)(10^6/4\pi)$.

$$\left(\frac{\text{cts}}{\text{sec}}\right)\left(\frac{1}{B}\right) = 53 \text{ cts/s/R}$$

Next, the NIST-calibrated diode provided a cross-calibration for the MCP count rates and the associated PMT measurement. The first step compared the "off" measurement of the photo-diode (i.e. gate valve closed) to the "on" measurement , a difference of $\sim$ 1.8 $\pm$ 0.2 pA on an electrometer (1.1×10^7 electrons/sec). The NIST calibration

report (dated 9/14/1995) states the diode produces 1.16 electrons/photon at 1304 Å, which makes the photon flux from the differential photo-diode test $\approx 9.5 \times 10^6$ photons/sec. This photon flux corresponds to a radiance $B = 121\ R$.

The PMT measured 3.24 V on the oscilloscope for the same differential on/off test used with the photo-diode. In the MCP-PMT linear fit equation, this measured voltage corresponds to a count rate (cts/sec) $\approx 18,700$. Equation 3.7 can now be used to determine a radiance from the count rate, $B = 353$ R. Due to all the sources of error in the experiment and instrumentation, it is reasonable to assume that a measurement of 3.26 V by the PMT corresponds to a few hundred R.

Results from the RENU 2 sounding rocket mission are presented in Section 6.3. Data from the flight UV PMT are presented there along with data from a variety of other mission measurements, which provide several calibrated measurements for comparison to the estimates provided by the post-flight calibration.

Chapter 4

Structure of black aurora associated with pulsating aurora

The following chapter is adapted from:

> Fritz, B. A., M. R. Lessard, M. J. Blandin, and P. A. Fernandes (2015), Structure of black aurora associated with pulsating aurora, *J. Geophys. Res. Space Physics*, 120, 1009610106, doi:10.1002/2015JA021397.

This work was a collaborative effort. I performed the analysis focused on the relationship between black aurora and pulsating aurora, connected the black curl structure to an ionospheric feedback mechanism via enhanced ionospheric conductivity and produced the conclusions and text below. Co-author Philip Fernandes conducted a preliminary analysis of basic statistics of the observations (e.g. Figure 4-4). Co-author Matthew Blandin digitized the images from tape and expanded the basic data statistics.

The intent of this study was to illustrate newly observed behavior in the ionosphere related to pulsating aurora. Black aurora curls are evidence of a return current structure, which implies the existence of an ionospheric feedback mechanism in response to pulsating aurora. A return current in the ionosphere would also contribute to overall current closure in the coupled ionosphere-magnetosphere system.

4.1 Introduction

Early definitions describe black aurora as a lack of emission in well-defined regions [Davis, 1978], often in diffuse aurora or in the transition region between diffuse and discrete aurora. This description is sufficient for most observed events but it neglects the presence of black aurora with pulsating aurora. One of the earliest reported observations of black aurora in connection with pulsating aurora by Royrvik and Davis [1977] describes narrow regions of little or no emission in the presence of pulsating aurora. Others have reported seeing black aurora with pulsating aurora since then [Trondsen and Cogger, 1997; Kimball and Hallinan, 1998a; Blixt et al., 2005; Archer et al., 2011; Sakanoi et al., 2013] but no significant relation has been demonstrated between the two.

Several different explanations for the generation of black aurora have been offered. Marklund et al. [1994] use electric field measurements from the Freja satellite to show downward field-aligned currents in conjunction with black aurora. An intense, divergent electric field structure forms and the resulting positive space charge accelerates cold electrons upward creating a void of emission, but this explanation is primarily applicable to black aurora observed in conjunction with discrete aurora. Peticolas et al. [2002] use data from the FAST satellite to explain black aurora in a diffuse background as localized suppression of pitch angle scattering at the plasma sheet source. Sakaguchi et al. [2011] assert that periodic black patches that appear in the post-midnight sector on the equatorward boundary of diffuse aurora during a substorm may occur as a result of relaxation of enhanced plasma pressure near the inner boundary of the plasma sheet. The theories of Peticolas et al. [2002] and Sakaguchi et al. [2011] explain the presence of black aurora in diffuse aurora but do not rule out a connection between pulsating aurora and black aurora.

Black aurora has been described as separate from pulsating aurora in the sense that the pulsating patches move independently of black aurora embedded in diffuse aurora. Black

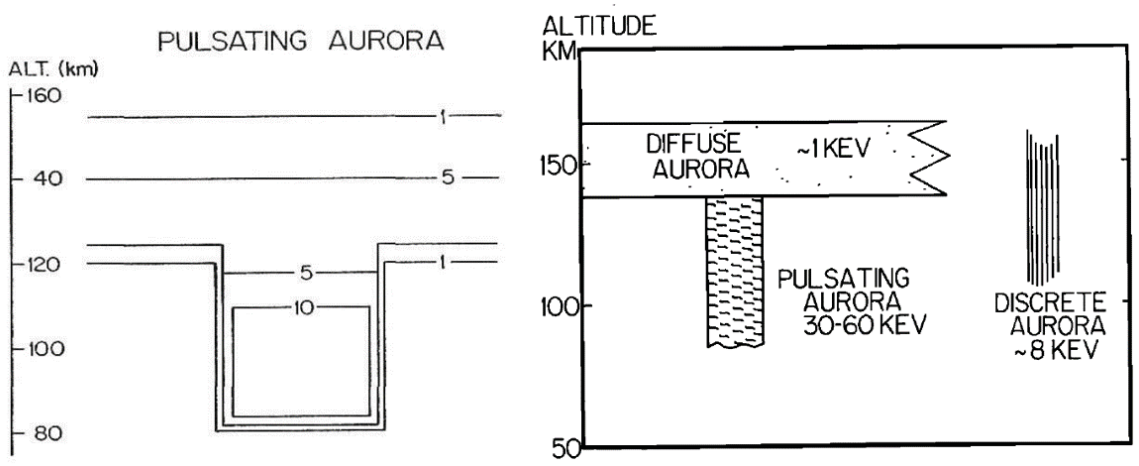

Figure 4-1: Cartoons that represent the difference in altitude for diffuse and pulsating aurora are taken from Davis [1978] (left) and Brown et al. [1976] (right). The plot on the left shows contours of relative luminosity representing the diffuse background at $\sim$ 140 km and the pulsating aurora below. The cartoon on the right shows a more general representation of the populations along with discrete aurora for reference.

aurora in a diffuse background is in fact not completely black but rather is only a localized reduction in emission intensity that falls below the detection threshold of the human eye Gustavsson et al. [2008]; Obuchi et al. [2011]. Patches of pulsating aurora have been shown to either add to the luminosity of the black aurora additively along with the surrounding diffuse aurora or by saturating the black region in the veiling fashion described by Kimball and Hallinan [1998a]. This behavior is consistent with the description of black aurora as a feature in a diffuse background with pulsating aurora merely a coincident event.

It is important to note the distinct difference between diffuse and pulsating aurora due to the significant energy difference between the precipitating particle populations that cause diffuse ($\sim$ 1 keV) and pulsating aurora (typically $\geq$ 10 keV). The cartoons in Figure 4-1 illustrate the difference in altitude for diffuse and pulsating aurora as a result of the differeng energies in precipitating particle populations. Davis [1978] (left) suggests a structure associated with pulsating aurora relative to diffuse aurora. Triangulations by Brown et al. [1976] (right) support the idea that higher energy precipitating particles result in a lower altitude for pulsating aurora than for diffuse aurora. The difference between diffuse and

pulsating aurora supports the notion that black aurora could be found embedded in diffuse aurora while pulsating aurora would appear as a separate event in the same region.

Observations presented in this paper provide evidence that black aurora may be connected to pulsating aurora in ways that have not been reported before. The morphology of black aurora in conjunction with pulsating aurora shown here indicates the ionosphere could play a role in how black aurora is generated and/or evolves.

4.2 Observations

This study is based on optical data recorded over a total of 6 nights between 10 January 2007 and 12 February 2007. Seven total hours of pulsating aurora observations were recorded at Poker Flat Research Range (PFRR), Alaska in support of the ROPA rocket campaign. 13.5 minutes of the data contained black aurora and the average length of these events was 31 seconds. This study focuses on events recorded on 18 and 19 January, 2007.

4.2.1 Supporting Data

Solar wind parameters from the ACE SWEPAM instrument are shown in Panel 1 of Figure 4-2 for the period 16-22 January 2007. Proton speeds (solid red line) are elevated on 18 and 19 January but the proton density (black dashed line) remains at a normal level. The Disturbance Storm Index, D_{st}, shown in Panel 2 (black dashed line) never drops below -50 nT throughout this period which indicates little to no geomagnetic storm activity. Also shown in Panel 2 is the IMF B_z (solid red line) measured by the ACE MAG instrument. The field repeatedly turns southward during this time period. Variations in the field strength are relatively small but the activity correlates well with the AU and AL Auroral Electrojet Indices shown in Panel 3. The indices indicate an abundance of substorm activity in the auroral zone, particularly leading up to and during 18 and 19 January.

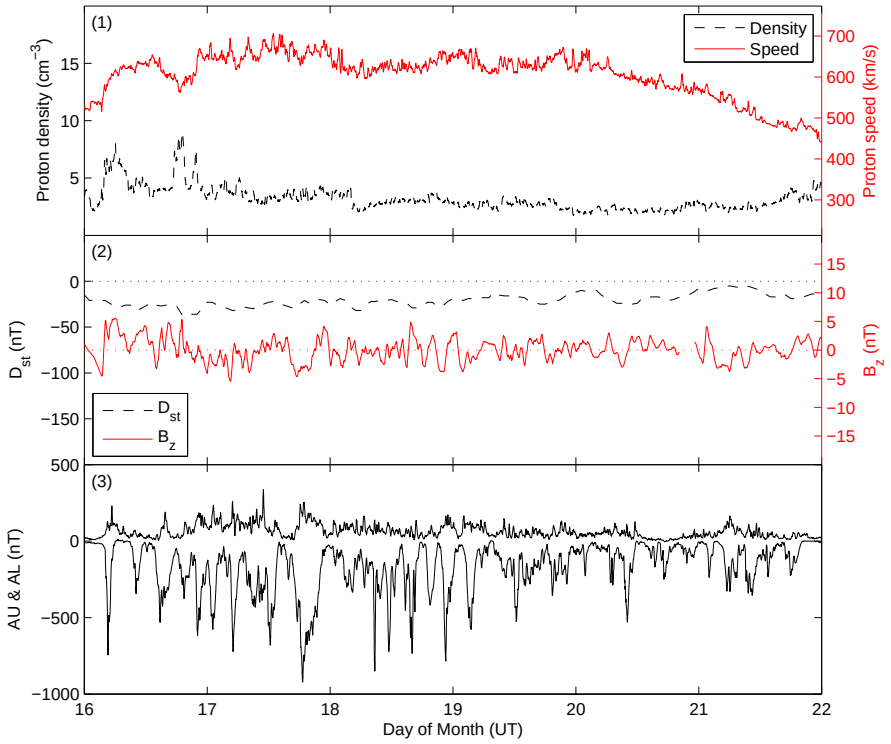

Figure 4-2: All data shown here is for the time period 16-22 January 2007. Panel (1) shows particle data from the ACE SWEPAM instrument including proton density (black dashed line) and proton speed (solid red line). Panel (2) shows the D_{st} index (black dashed line) with a zero nT reference line and the IMF B_z (solid red line) from the ACE MAG instrument, also with a zero nT reference line. Panel (3) shows the Geomagnetic Auroral Electrojet indices AU and AL.

The Poker Flat Incoherent Scatter Radar (PFISR) facility opened in 2007 and was operated in support of the ROPA rocket launch. Jones et al. [2009] present radar measurements from the launch campaign as part of a study on pulsating aurora. The radar measurements had a time resolution ($\sim$ 5 s) too low to resolve the fine-scale structures of pulsating aurora that are the focus of this paper but the altitude and energy profiles support the typical assumptions made with pulsating aurora. The density profiles show enhanced density from $\sim$ 90 km to $\sim$ 125 km and the peak density varied from event to event, likely depending on the peak energy of the precipitating population.

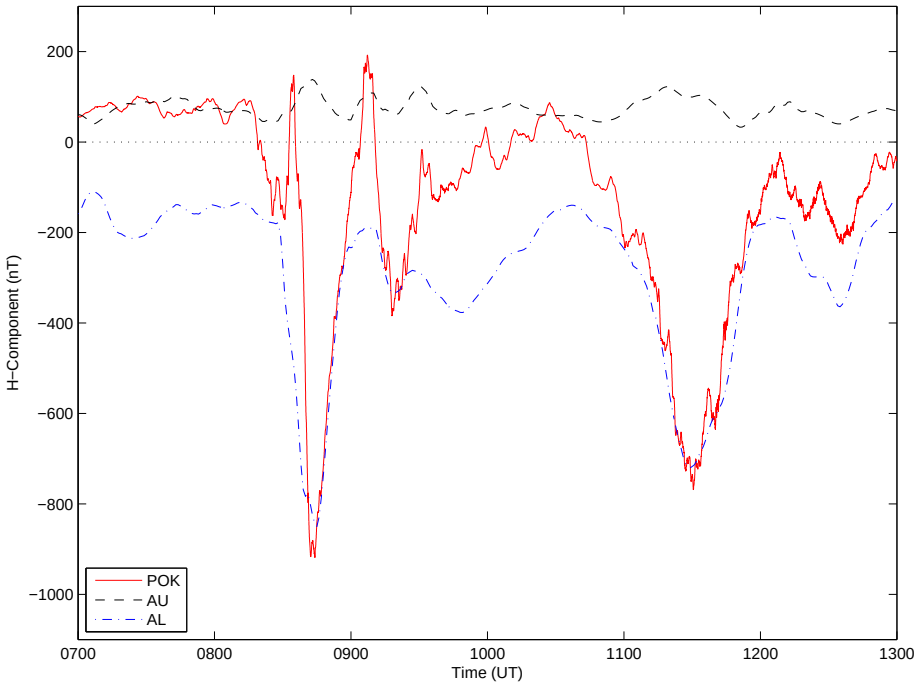

Figure 4-3: H-component of the Poker Flat Research Range fluxgate magnetometer (solid red line) compared to the Geomagnetic Auroral Electrojet indices AU (black dash line) and AL (blue dot-dash line) for the period 0700 - 1300 UT, 18 January 2007.

A fluxgate magnetometer was also operated at PFRR (65.1 degree, 212.5 degree geographic) during the ROPA campaign. Figure 4-3 compares the H-Component (i.e. the component horizontal to the earth's surface) of the Poker Flat magnetometer data (solid red line) to the AU and AL indices (black dash line and blue dot-dash lines respectively) on 18 January 2007. Despite being only 34 km from the nearest station in the AE index network at College, AK (64.9 degree, 212.1 degree geographic), the difference between the two signals is clear. The AL index matches the most substantial minima in the Poker Flat measurement very closely (e.g. the minima at $\sim$ 0838 UT and $\sim$ 1131 UT). The AL index fails to track some of the more moderate, localized substorm activity, however, such as the minimum at 0922 UT.

4.2.2 Instrumentation

Optical measurements were recorded at 30 fps on Hi8 MP 120 particle tape using a Xybion Electronic Systems Corporation ISS-750-R3 intensified CCD video camera with a f/1.4, 25 mm lens. The camera recorded images with an automatic iris and manual intensifier gain control that allowed for detection sensitivities as low as 100 R. The combination of instrument sensitivity and high-pass filter created a band pass of approximately 150 nm between 700 and 850 nm. Assuming the observed features were located at an altitude of 100 km the $45.0^\circ \times 33.6^\circ$ lens FOV produces an image size of approximately 83×60 km.

Intensity of diffuse and pulsating patches varied substantially but due to the variable gain of the system no values of absolute intensity could be measured. Relative intensities of the pulsating aurora ranged from below the threshold of the camera sensitivity to several tens of kR (for comparison the human eye is sensitive to luminosities down to approximately one kR at 557.7 nm). The Geophysical Institute at the University of Alaska-Fairbanks provided a meridian scanning photometer (MSP) at PFRR in support of rocket campaigns. The MSP was sensitive down to a few Rayleighs and provided a background-subtracted measurement every 16 seconds of up to four emission lines (557.7 nm, 630.0 nm, 486.1 nm, 427.8 nm) [D. Hampton, personal communication, September 28, 2015]. Measurements with the MSP indicated that the diffuse and pulsating auroral intensities were typically 1 - 2 kR.

4.2.3 Optical Measurements

A total of 26 distinct black aurora events were observed and 18 of the events contained pulsating aurora. Black aurora observations ranged from the pre-midnight sector to the late post-midnight sector. All optical data presented in this study will be reported in UT to correspond with supporting measurements. Midnight MLT at PFRR is $\sim$ 1100 UT.

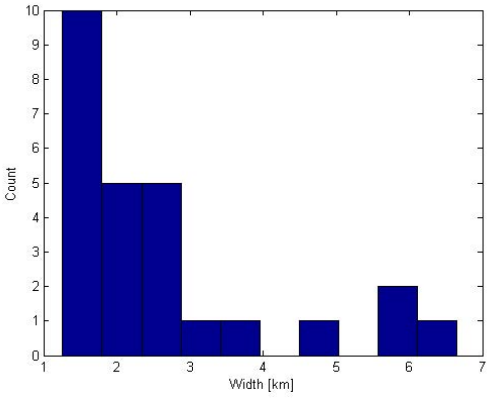

Figure 4-4: Observed horizontal width of black aurora arcs. Average width $\sim$ 2.6 km.

Only 6 of the observed black aurora forms fit entirely within the frame of the image so no clear trend in terms of length was determined. The average observed horizontal width of the black aurora was measured for all events and is $\sim$ 2.6 km with a median value of $\sim$ 1.9 km. Figure 4-4 shows a histogram of the observed measurements to give a sense of the spread of measurements. Trondsen and Cogger [1997] reported an average horizontal width in the 0.5-1.5 km range. The measurements here are slightly higher, possibly owing to a lower resolution in the present measurements.

The most commonly observed black aurora shapes were black arcs elongated in the east-west direction that typically spanned the entire frame (black patches did appear but less frequently). Figure 4-5 is an example of black aurora observed in diffuse aurora that matches well with previous observations such as those by Trondsen and Cogger [1997]. The black aurora appeared on 18 January 2007 at 1103 UT and lasted for 34 seconds. The event begins with one long black arc running east to west across the entire width of the frame that breaks up into smaller black arcs and patches.

Black aurora appeared with pulsating aurora in a variety of ways, most of which appeared during the recovery phase of a substorm. For some events pulsating patches were few in number and barely discernable with the camera, even below the detection threshold of the human eye. Some observations have black aurora completely contained in a diffuse background with pulsating aurora elsewhere in the frame that appears unrelated. Other times black aurora is completely contained within a pulsating patch and the relative inten-

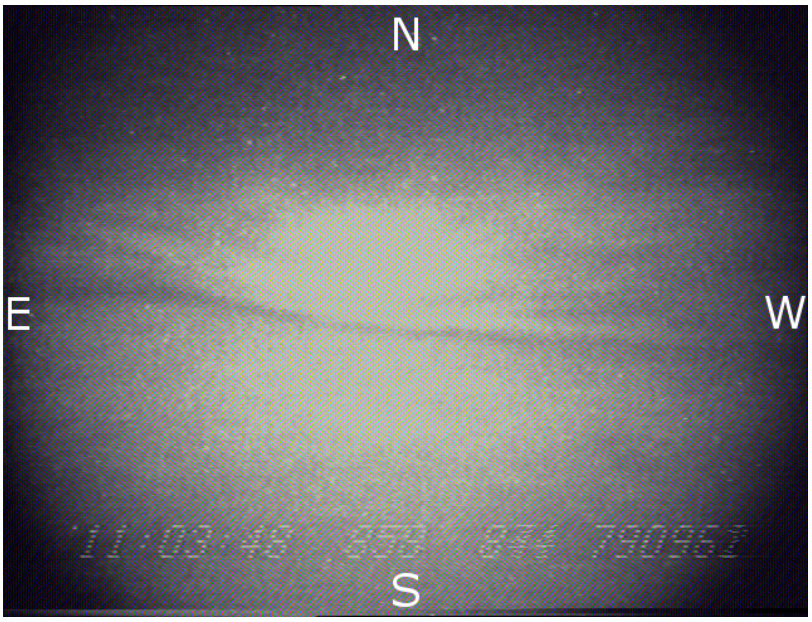

Figure 4-5: Observation from 1103 UT, 18 January 2007 of black aurora in a diffuse background. The event lasted 34 seconds. Letters in the figure indicate geographic orientation of the image. Scale size of all images is 83 × 60 km.

sity of the black aurora varies with the intensity of the pulsating aurora. The pulsating aurora interacts with the black aurora in the "veiling" fashion as described by Kimball and Hallinan [1998a].

Figure 4-6 shows an observation from 19 January 2007 at 1406 UT to illustrate an example of veiling. This fits well with the behavior of dual-layer pulsation, first described in Royrvik [1976]. The term dual-layer pulsation describes the presence of structure in a diffuse background that disappears when the pulsating patch "turns on" and then reappears when the patch "turns off." The implication is that the diffuse aurora and pulsating aurora occur as separate processes, as the pulsating aurora appears to have no impact on the structure of the diffuse aurora [Trondsen and Cogger, 1997]. The pulsating patch in Figure 4-6 begins to pulsate during the substorm recovery phase and lasts for over four minutes. The black arcs maintain their structure even after several pulsations on and off, all similar to the two cycles shown in Figure 4-6.

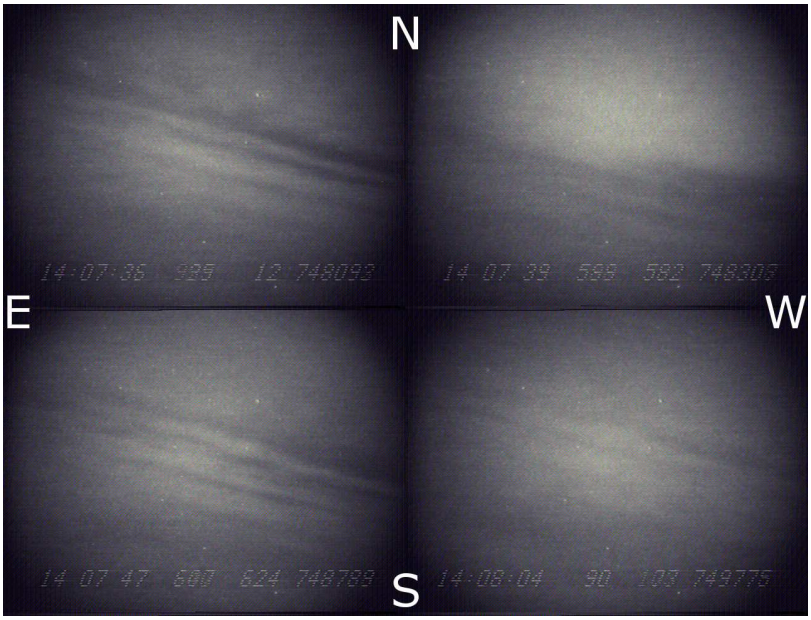

Figure 4-6: Observations of an event that started at 1406 UT, 19 January 2007 and lasted for ~ 4 min. The event shows black aurora in a diffuse background saturated by pulsating patches to demonstrate "veiling" as described by Kimball and Hallinan [1998a]. The black aurora remains stationary throughout the event. The pulsating aurora shows no clear trend in motion, often saturating the entire image frame.

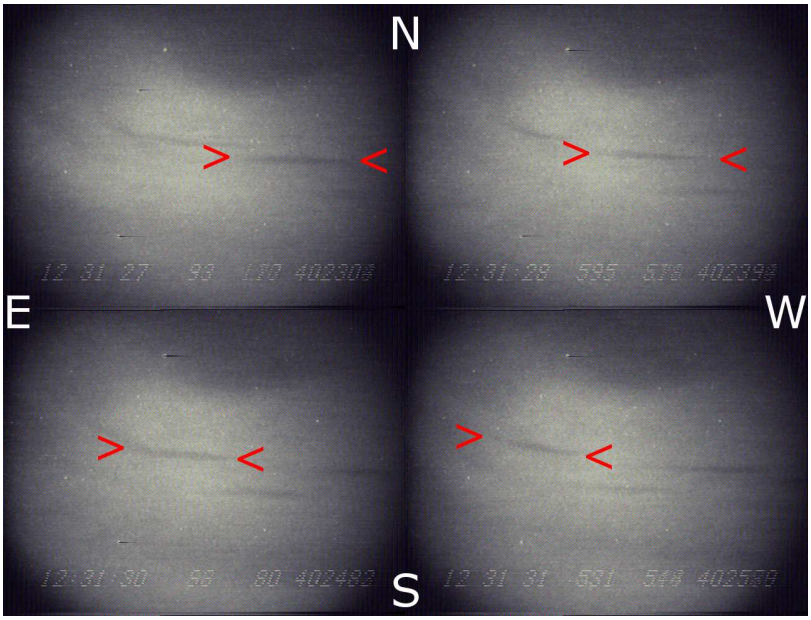

Figure 4-7: Observations of an event that started at 1230 UT, 19 January 2007 and lasted for ~ 2 min. Black arc segments drift eastward across a diffuse background. One black arc segment has been marked in each frame by red arrows to highlight the drift motion.

Two black aurora events, one of which is shown in Figure 4-7, showed black arc segments or patches drifting eastward with a noticeable velocity, which matches previous studies [Trondsen and Cogger, 1997; Peticolas et al., 2002; Blixt et al., 2005]. The drift speeds measured are on the order of 15 km/s, much higher than previous reports like Blixt et al. [2005] who reported a maximum drift of 4 km/s.

Figure 4-7 shows images from one of the two drift examples that was observed on 19 January 2007 at 1230 UT. Red arrows in the images mark the ends of one black patch to illustrate the movement of the patch. A short video is available in the online supporting material to further illustrate this event[1]

Studies have shown the drift motion of black patches to correlate with either the gradient-B curvature drift [Blixt et al., 2005; Gustavsson et al., 2008] or the $E \times B$ drift [Obuchi et al., 2011; Sakanoi et al., 2013]. At Poker Flat, Alaska on 19 January 2007 the IGRF model predicts $B_z = 53\ \mu T$ at 100 km. For this magnetic field strength to produce $E \times B$ drift speeds near 15 km/s would require a divergent electric field of ~ 0.8 V/m, which is consistent with Marklund et al. [1994]. Unfortunately PFISR was not operating at the time of observation to measure the plasma drift speed, so there is no way to determine the relative drift speed of the black arc segments and verify the calculation.

The most interesting features in the ROPA campaign observations show black aurora that appear to define the boundaries of pulsating aurora between either pulsating and diffuse aurora or between separate pulsating patches. This is new behavior that has not been discussed in the literature. The first example shown in Figure 4-8 occurred on 18 January 2007 starting at 1144 UT. The images in the figure show diffuse aurora separated from a pulsating patch by a black arc. The majority of the frame is filled by diffuse aurora that persists throughout 150 seconds of observation while the pulsating patch in the northwest

[1]https://agupubs.onlinelibrary.wiley.com/action/downloadSupplement?doi=10.1002%2F2015JA021397&attachmentId=189249913

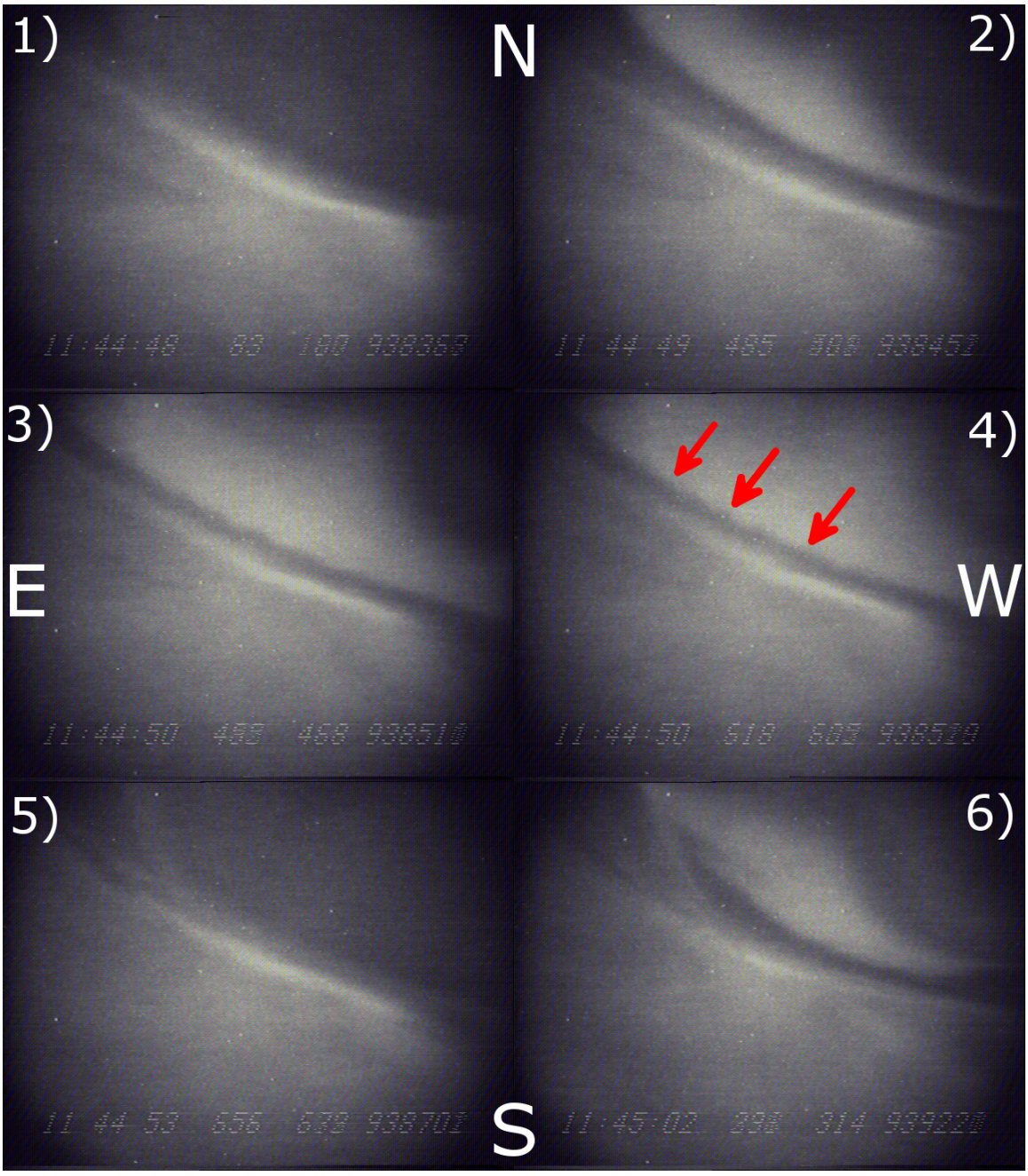

Figure 4-8: Observations from an event that began at 1144 UT, 18 January 2007 and pulsated for 140 sec. Photos are labeled 1) to 6) in chronological order with a GPS time stamp along the bottom of each image. A pulsating patch in the northwest corner is separated from the diffuse aurora by a black arc and pulsates with a period on the order of a few seconds. Red arrows indicate three of the crests of the curl structure. Curl structure is much more apparent in video format, see text for link to supporting video.

corner turns on and off with an average period on the order of a few seconds.

The top two images in Figure 4-8 show the pulsating patch "turn on" in the upper right corner. The middle two images show a point when the pulsating patch reaches a maximum in intensity. The region illuminated by the pulsating patch expands and approaches the diffuse aurora, shrinking the black arc width but not eliminating it, until the pulsating patch recedes again. At the point of maximum intensity, the black aurora begins to show a curl structure that seems to be a trigger for a decrease in brightness. Red arrows in the figure mark several crests in the curl structure and a short video is available in the online supporting material to illustrate the curl effect more clearly.[2] The fifth and sixth images at the bottom of Figure 4-8 then show another pulsation after curls disappear.

The second interesting example occurred at 0921 UT on 18 January 2007 and shows two separate, slowly drifting pulsating patches spatially defined by black aurora. Figure 4-9 shows a sequence of images with one pulsating patch in the top row of images that turns off and back on again. The middle row of images shows the corner patch "turn on," and the strip in the middle subsequently "turn off." The two regions of pulsating aurora clearly pulsate at a different period. The periods of pulsation are irregular but are on the order of a few seconds. As the two patches turn on and off they brighten and expand but never cross the boundary established by the black aurora between them. The bottom row of images shows the corner patch move slowly down in a southwesterly direction and a new patch appears in the corner behind, once again apparently separated by a black arc.

The orientation of the black aurora in relation to the pulsating aurora appears to have no preferential location. In other words, some pulsating patches are seen equatorward of the black aurora while other pulsating patches appear poleward of the black aurora. Obuchi et al. [2011] and Sakanoi et al. [2013] report that on a larger latitudinal scale, pulsating

[2]https://agupubs.onlinelibrary.wiley.com/action/downloadSupplement?doi=10.1002%2F2015JA021397&attachmentId=189249914

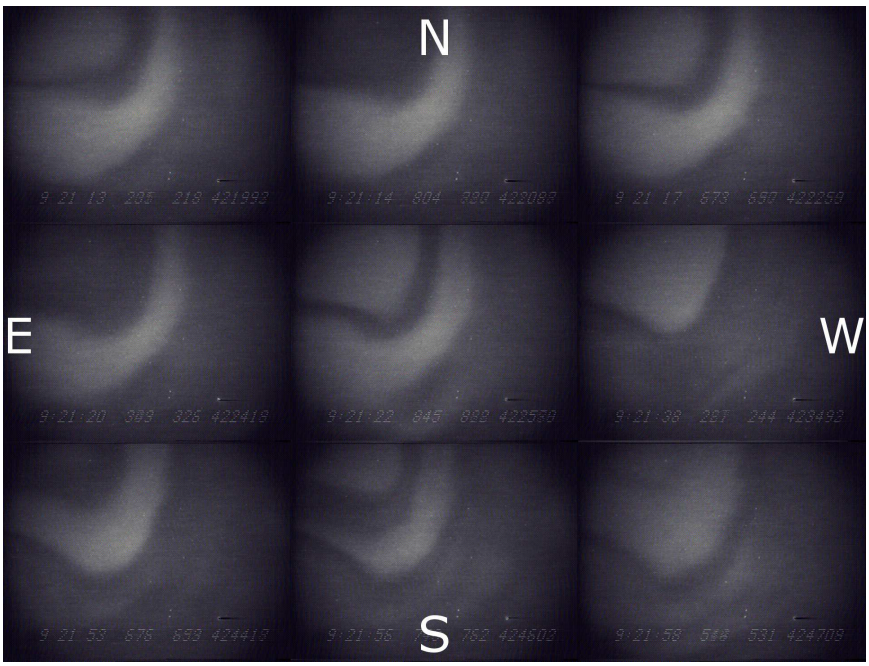

Figure 4-9: Observations from an event that began at 0921 UT, 18 January 2007 and persisted for 65 sec. Pulsating patches are separated by black arcs and pulsate at irregular, asynchronous periods.

patches tend to form equatorward of black aurora. That trend does not, however, appear to translate to the smaller scales presented in these observations.

4.3 Analysis and discussion of black aurora with pulsating aurora

Schoute-Vanneck et al. [1990] describe black aurora as a feature that separates diffuse and discrete aurora or pulsating and discrete aurora. However, no mention is made of a boundary between diffuse and pulsating aurora or between two different patches of pulsating aurora. The boundary is clearly defined and maintained throughout the observations shown in Figures 4-8 and 4-9, between pulsating/diffuse aurora and patches pulsating at different frequencies, respectively.

The behavior shown in Figure 4-8 is evidence of an ionospheric component to the mor-

phology of pulsating aurora and/or black aurora. The curls seen in the middle row of images have a periodic, sinusoidal pattern with a crest separation on the order of ~ 5 km, which agrees very well with the description by Davis [1978] as well as the measurements by Marklund et al. [1997]. The curl structure forms and dissipates in ~ 2 sec, which is consistent with observations of curl structures in the ionosphere including curls in either visible aurora [Hallinan and Davis, 1970] or black aurora [Kimball and Hallinan, 1998b].

Archer et al. [2011] reported observations of black curls in a diffuse background, but as Peticolas et al. [2002] states, black curls have never been observed in conjunction with pulsating aurora. Black vortex streets that resemble the behavior in Figure 4-8 are associated with regions of positive space charge and a diverging electric field [Marklund et al., 1994]. The divergent electric field structure accelerates cold electrons to establish a downward field-aligned current system in the ionosphere. In a fully formed curl structure, or vortex, the black curls should rotate in a clockwise sense when viewed from the ground in the northern hemisphere [Kimball and Hallinan, 1998b]. Fully formed black curls are rare, however, and ripples (a precursor to fully formed curls) like those in Figure 4-8 are much more common [Trondsen and Cogger, 1997]. If the curls, or ripples, seen here are an indication of a return current, then pulsating aurora may be tied to an ionospheric feedback mechanism that defines the shape of pulsating patches. It is worth noting, however, that the vortical orientation of these particular ripples is an open question that cannot be resolved with the current observations.

The ionosphere has long been considered in varying degrees as an active participant in the process of pulsating aurora [Stenbaek-Nielsen, 1980] and not just a passive display for processes occurring in the equatorial magnetosphere. Energetic electrons that cause pulsating aurora have been shown to flow along Region 2 field-aligned current lines in a pair of current sheets [Fujii et al., 1985], indicating a return current in the ionosphere. If

pulsating aurora deposits enough energy in the lower ionosphere, the electric field within the patch will be modified, [Hosokawa et al., 2008] and Pedersen currents will flow in the D-region as a result of the enhanced conductivity [Hosokawa et al., 2010].

An important example of an ionospheric feedback mechanism that can generate fine-scale structure is the Ionospheric Feedback Instability (IFI) [Atkinson, 1970] that describes active feedback of the ionosphere in response to magnetospheric flow. Streltsov and Lotko [2004] used a reduced version of a time-evolving, nonlinear, two-fluid MHD model to describe multiscale electrodynamics of magnetosphere-ionosphere coupled systems based on the IFI. They show that small-scale intense electric fields and currents resulting from ionospheric feedback may be found in density-depleted ionospheric regions accompanying downward field-aligned currents. Results based on this model have shown the ability to reproduce fine-scale field structures measured by Cluster [Streltsov and Marklund, 2006] as well as sounding rocket measurements [Cohen et al., 2013]. Although the Streltsov and Lotko [2004] model describes auroral arcs, Figure 4-8 would be the first known observation of a curl structure in conjunction with pulsating aurora that could serve as an indicator of a similar feedback mechanism.

Magnetospheric processes have also been shown to produce fine-scale structure in the ionosphere, therefore it must be considered that magnetospheric processes could drive black aurora. "Smokelike" fine-scale aurora observed by the Reimei satellite are most likely attributed to scattering processes of hot electrons and possibly a visual manifestation of cold plasma structured by the interchange instability [Ebihara et al., 2010]. Shiokawa et al. [2010] use a high-resolution CCD camera to show fine-scale structures in the ionosphere that may be driven by a Rayleigh-Taylor type instability at the magnetospheric equatorial plane.

Fine scale structures driven by magnetospheric processes develop and/or persist on

longer timescales than the example shown in Figure 4-8. Structures driven by the Rayleigh-Taylor instability in particular typically have a north-south orientation and exhibit no evidence of shear (i.e. sharp velocity gradient). Figure 4-8, however, shows black aurora in an east-west orientation with shear behavior indicated by the black curls. Shear behavior is better correlated with instability morphology similar to the Kelvin-Helmholtz instability. The divergent electric field structure associated with black aurora [Marklund et al., 1997; Kimball and Hallinan, 1998b], in addition to the associated current structures, suggests that the tearing mode is the more likely candidate for generating the black curl structure [Seyler, 1990; Chaston and Seki, 2010].

The clearly defined boundary contrasts the independent behavior of black aurora and pulsating aurora implied by veiling [Kimball and Hallinan, 1998a]. This new behavior should not contradict the many previous observations of veiling, including Figure 4-6, but rather adds a new subset of behavior for black aurora in terms of its relation to pulsating aurora. A possible explanation for the new subset of behavior may be that a certain energy flux or number flux of precipitating particles in a pulsating patch is required to initiate the formation of return currents strong enough to appear as black aurora. It is also possible that conditions for such a feedback mechanism may only exist when a density cavity exists in the ionosphere [Streltsov and Lotko, 2004].

The second example of black aurora with pulsating aurora shows two patches that are pulsating with different periods of pulsation and, as the event goes on, the patches evolve in shape but the black aurora maintains the border between patches. Rather than one pulsating patch moving and either saturating the black aurora or joining with the other pulsating patch, the two patches remain separate. This example demonstrates behavior that contradicts both the veiling behavior and the flow patterns described by Kimball and Hallinan [1998a]. The examples in Figure 4-8 and 4-9 support the notion of a new subset of

black aurora that may act as a barrier, similar to the forbidden regions described by Parsons and Thomas [1973], Schoute-Vanneck et al. [1990], and Kimball and Hallinan [1998b].

Aurora at different altitudes like diffuse and pulsating aurora [Brown et al., 1976] are caused by different energies of precipitating particles, meaning they may or may not be part of the same coherent generation process. PFISR measurements from the time of observation [Jones et al., 2009] show that the height profile of the pulsating aurora is observed at expected altitudes which correlates with the typical energy population of particles that cause pulsating aurora (see Lessard [2013] and sources therein). The PFISR measurements are unable to reveal anything about the structures within the source population, however.

Veiling shows one subset of black aurora in which pulsating aurora is capable of drifting across and covering black aurora patches in a diffuse background. In other words, separate structures from the source region may overlap one another at the ionospheric level. The observations presented here represent a new, different subset of black aurora in which pulsating aurora appears unable to cross the barrier either between pulsating aurora and diffuse aurora or between different patches of pulsating aurora.

Black aurora that separates pulsating patches with different periods of pulsation would comprise part of the new subset of black aurora described above. Nishiyama et al. [2012] identify pulsating patches with different periods of pulsation that are separated by narrow black boundaries. The term "black aurora" is not used to describe the structure but the characteristics of their observations are similar to the description of black aurora discussed here. Nishiyama et al. [2012] discuss fine structure in the ionosphere as a possible result of coherent structure in the equatorial magnetosphere.

The ability for pulsating patches to veil other structures in the ionosphere implies that separate, coherent source populations in the magnetosphere do not always translate to ionospheric altitudes with the same level of structure. Kimball and Hallinan [1998a] report

that pulsating patches were not observed veiling black curls but did veil black patches that exhibited no evidence of shear. The lack of evidence for pulsating patches veiling black curls and the similarity between the behavior shown in Figures 4-8 and 4-9 further support the notion of an active ionospheric component to the presence of black aurora, particularly in the form of black curls.

The feedback mechanisms discussed in this paper could not be verified due to a lack of proper supporting measurements. This study also makes no claim as to the effect an ionospheric feedback mechanism would have on the magnetospheric source region or generating mechanism. The premise of black aurora in conjunction with pulsating aurora that represents an ionospheric feedback system is supported in principle by the various processes discussed [Atkinson, 1970; Stenbaek-Nielsen, 1980; Streltsov and Lotko, 2004; Hosokawa et al., 2010] and is worthy of further study.

4.4 Summary

A collection of observations has been presented that supports the widely held notion that black aurora are commonly seen in the midnight sector late recovery phase. The noteworthy observations from the ROPA rocket campaign are those of black aurora that form the boundary of pulsating aurora. This comes in the form of boundaries between patches of pulsating aurora that pulsate with different periods or between diffuse and pulsating aurora.

Discussions about the generating mechanism of black aurora, particularly those that focus on black aurora in diffuse or pulsating aurora, focus on effects that occur at the plasma sheet source of energetic precipitating particles. Those explanations relegate the ionosphere to a passive role. The observations shown here suggest that the ionosphere may instead have more of an active role in defining the behavior of black aurora in conjunction with pulsating aurora. While this study is unable to eliminate the possibility of magnetospheric

drivers for the fine structure in the ionosphere (such as those listed above), the orientation and morphology of these observations seem to fit the possibility of an ionospheric feedback system.

The first reported observation of a black curl structure in conjunction with pulsating aurora supports the notion of a return current structure in the ionosphere. Black aurora separating diffuse aurora and pulsating aurora shows that black aurora can separate two events occurring at different altitudes. Veiling (i.e. dual-layer pulsation) shows that pulsating aurora and diffuse aurora do not inherently interact with one another. The black curls, however, show a new subset of black aurora in which pulsating patches are unable to cross into a region of black aurora into diffuse aurora or even other pulsating patches, a direct contrast to veiling.

The observations here do not preclude the possibility of any previously proposed generating mechanisms for black aurora, including both ionospheric and magnetospheric. This study reports new behavior that expands the possible ways in which black aurora may occur. Ionospheric feedback may drive black aurora and other fine structure in the ionosphere but this would likely be in addition to magnetospheric mechanisms, not in place of them. Additional quantitative observations are required to fully understand this newly reported behavior. Morphology of black aurora dictated by the influence of pulsating aurora on the ionosphere is an issue that may also be addressed via a simulation of pulsating aurora during substorm recovery phase conditions.

Acknowledgements: The authors thank the ACE SWEPAM instrument team, the MAG instrument team and the ACE Science Center for providing the ACE data. We also thank the AE and D_{st} data suppliers as well as the WDC for Geomagnetism, Kyoto for providing geomagnetic index data. Finally, we'd like to thank the UAF Alaska Satellite Facility for provision of the Poker Flat magnetometer data. This work was supported by NSF PLR 1341677 and NASA Award NNX13AJ94G.

Chapter 5

ELF Whistler Dependence on a Sunlit Ionosphere

The following chapter is adapted from:

> Fritz B.A., J. Heavisides, M.A. Young, H. Kim, and M.R Lessard (2018), ELF Whistler Dependence on a Sunlit Ionosphere, *J. Geophys. Res. Space Physics*, 123, doi:10.1029/2017JA024912.

I was primarily responsible for the analysis presented below. Co-author Matt Young compiled a preliminary database of ELF whistler events and co-author John Heavisides calculated initial solar elevation angles for events in the preliminary database. I expanded the database of events to full coverage of 2004, made the connection to the changes in ionospheric composition, analyzed the IRI and $F_{10.7}$ data, and proposed the instability discussed in the conclusions and text. Co-author Matt Young also provided key suggestions for the instability discussion.

The goal of this research project was to report year-long statistics on ELF whistler occurrence at the South Pole Station, with emphasis on the "blackout" during Antarctic winter months. The correlation between a sunlit ionosphere led to the IRI and $F_{10.7}$ investigations. The ultimate goal is to determine a generating mechanism for ELF whistlers, and the physical constraints provided by this study will help in that determination.

5.1 Introduction

Whistler-like features in the lower end of the Extremely Low Frequency (ELF) range (3 Hz - 3 kHz) have been reported several times [Sentman and Ehring, 1994; Wang et al., 2005; Kim et al., 2006] since they were first observed [Heacock, 1974]. ELF whistlers have a narrow-band spectral signature that typically falls monotonically in frequency as a function of time. The features were originally called whistler-like because their spectral signature is very similar in appearance to whistlers in the Very Low Frequency (VLF) range. ELF whistlers differ, however, in that they typically last on the order of a minute and span less than 100 Hz in frequency. Wang et al. [2011] concluded that the most likely wave mode for the ELF whistlers is right-hand polarized ion cyclotron waves.

ELF whistlers were first observed at Poker Flat, AK (64.9° N) in the auroral zone [Heacock, 1974]. Approximately 8 months of observations revealed many defining features, including a broad, daytime diurnal maximum and a seasonal minimum in the winter. Subsequent observations of ELF whistlers have been reported at mid-latitudes (34.4° N) [Sentman and Ehring, 1994] and low latitudes (23.47° N) [Wang et al., 2005]. Both studies at sub-auroral latitudes also note the diurnal pattern in occurrence, but neither discuss the seasonal pattern. For Sentman and Ehring [1994] this is due to the small sample size, but even with nearly a full year of observations the pattern is not mentioned by Wang et al. [2005]. An additional observation of similar ELF structures at low latitude [Singh et al., 2011] sees ELF whistlers at a higher frequency range ($f > 200$ Hz) with a noontime peak as well as an additional peak closer to midnight, but the different length and frequency range calls into question the similarity of the mechanism.

Finally, Kim et al. [2006] presents the first 70 days of observations from a detector at the geographic South Pole. Once again a clear diurnal pattern is noted in the observations, but the pre-midnight magnetic local time (MLT) distribution contrasts the daytime MLT

prevalence noted previously. The study presented in this paper expands the South Pole observations to include the first full year of operations in 2004. Analysis of a full year of data reaffirms the diurnal pattern noted by Kim et al. [2006] but, more importantly, shows a more extreme example of the seasonal dependence noted by Heacock [1974]. ELF whistlers at the South Pole disappear entirely during polar winter as the sun sets and then reappear once the sun rises again. This observation implies that the daytime maximum is strongly influenced by the effect of solar radiation, not just by the MLT of the observing location.

In this study, a brief description of the instrumentation is followed by a description of the observations, from both the South Pole and Lulin Observatory, Taiwan. Next, analysis of the ELF whistler detection times reveals new connections to physical parameters that were not previously considered, including solar zenith angle, ionospheric composition and solar flux levels. Finally, the context of the new analysis is discussed in terms of past observations of ELF whistlers and how these new results may influence the determination of a generation mechanism.

5.2 Instrumentation and Data Collection

Induction coil magnetometers located at Amundsen-Scott South Pole Station (74.1° S, 18.8° E geomagnetic) were used to detect the ELF whistlers. The sensors were both oriented perpendicular to the local magnetic field, one aligned along magnetic north-south and the other along east-west. EMI BF-4 Magnetic Field Induction Sensors were used and they have a frequency sensitivity of 0.3 V/nT over the range 1-250 Hz.

The instrument receiver uses a 250 Hz anti-aliasing (low-pass) filter to enable sampling up to 500 Hz and an embedded automatic gain control (AGC) circuit that provides a dynamic range of 80 dB. Analog signals from the receiver are digitized and recorded by a Symmetric Research PAR4CH data acquisition system (DAS) at 500 Hz. The DAS utilizes

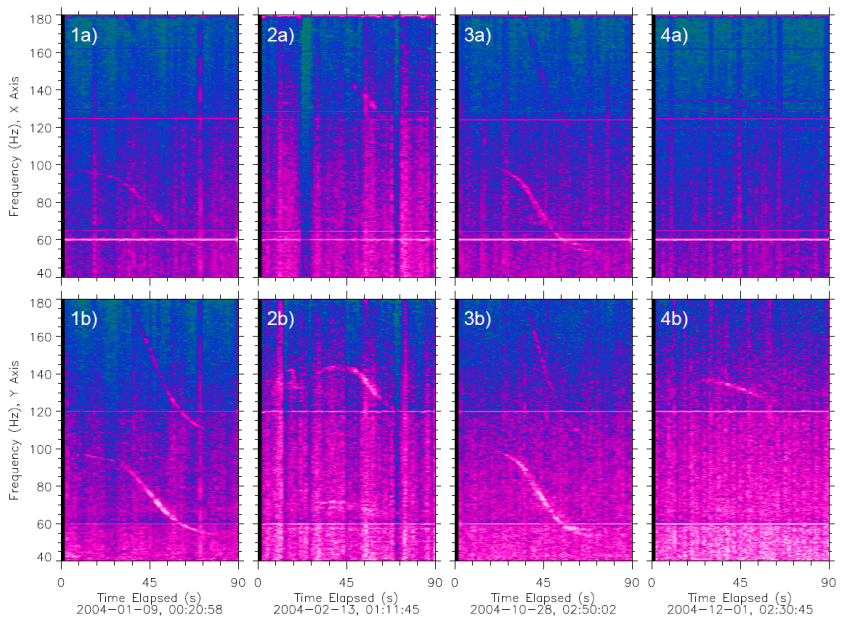

Figure 5-1: Example power spectra of four ELF whistlers detected at the South Pole Station, including two before the polar winter (1 & 2) and two after (3 & 4). The top row (a) is data from the X axis of the system N-S aligned) and the bottom row is from the Y axis (E-W aligned). Color scale in each plot is relative to the event as a result of AGC.

a GPS receiver to provide precise timing for the data. For a more thorough description of the system, see Kim [2004].

5.3 Observations

Observations over the first full year of operation by the South Pole ELF magnetometer system, from 1 January 2004 to 31 December 2004, include the 70 days of observations presented by Kim et al. [2006]. Dynamic power spectra were produced using a 1024-point (0.5 Hz/bin) fast-Fourier transform (FFT), and were visually inspected for evidence of ELF whistlers. Data were available for approximately 94% of the year. Visual inspection revealed a total of 338 ELF whistlers that were individually analyzed to determine their frequency range and event duration.

An average of 3 ELF whistlers per day appear throughout the first 53 days of 2004, with

as many as 11 in a single day. The whistlers suddenly then stop appearing after 22 February and are not seen again until 21 October, 2004. During the last 70 days of 2004 an average of over 2 ELF whistlers per day are observed. The Antarctic winter blackout is not due to any known defect in instrumentation or data acquisition. Rather, the gap appears to be a geophysical phenomenon. Distribution of ELF whistler occurrence in MLT throughout the entirety of 2004 maintains a similar distribution to that shown in Kim et al. [2006], with no notable differences, including peaks around 0300 and 1900 MLT.

When they do appear, ELF whistlers last between 5 and 75 seconds with an average duration of 31 seconds and median duration of 50 seconds. The highest frequency observed in the power spectra was 220 Hz and the lowest was 32 Hz. Events 1 and 3 in Figure 5-1 show typical ELF whistler signatures, one before the winter blackout and one after. Both have a strong signal between 50 and 100 Hz and last on the order of a minute. Nearly 70% of ELF whistlers appear as a multi-trace event, or with a harmonic. This is a much higher occurrence rate than previous studies (no higher than 23%), but is likely the result of a wider frequency response of the instrument. Events 2 and 4 in Figure 5-1 show some events that have a higher primary frequency range than has been reported in the past. Event two still occurs similarly as compared to events 1 and 3, but event 4 has a much flatter frequency variation without any evidence of a lower harmonic.

A limited polarization in the E-W direction was observed in most cases, which is apparent in Figure 5-1. Statistics of the polarization are not presented numerically due to limitations with the data set. Only 50% of ELF whistlers in 2004 had data available in both sensors. The acquisition system channel for the N-S sensor would periodically malfunction, causing a dropout in signal for that channel.

For comparison, the low latitude data set from Wang et al. [2011] is also analyzed, which has an average cutoff frequency range of 62-95 Hz. The upper average cutoff frequency is

lower than observed at the South Pole, though it was acknowledged that a lower system sensitivity above 100 Hz may have resulted in missed signals. The duration ranges from 40 seconds to 5 minutes, averaging 124 seconds. No echoes were observed but 66/296 observations saw multiple traces. Time of observation ranges between 0500-2100 LT, with a peak time of 0900-1000, with additional, smaller, peaks near 1500 and 1900. This shows the same daytime occurrence peak as Heacock [1974] and Sentman and Ehring [1994], but the observations show no obvious seasonal dependence.

5.4 Analysis

The most striking feature of the South Pole data is the blackout during the Antarctic winter season while the sun is near or below the horizon. Kim et al. [2006] analyzed only the first two months of data from the South Pole Station, which was not enough observe the winter blackout. The noontime occurrence maximum noted in prior, low-latitude ELF whistler studies led to a focus on the MLT distribution of the events. Attempts were made to connect ELF whistlers to other dayside physical processes observed in the lower ELF frequency regime, but the pre-midnight MLT distribution noted by Kim et al. [2006] contradicts the notion of a dayside connection.

At extremely high latitudes like the South Pole, the daily rotation of Earth is no longer connected to a diurnal change in solar illumination. The Sun remains above or below the horizon for months at a time, which means that sunlit conditions are no longer tied explicitly to the dayside or nightside. This analysis focuses on the effect of solar illumination of the atmosphere during ELF whistlers by first calculating the solar zenith angle at the time of each ELF whistler detection. Additionally, photoionization plays a clear role in determining ionospheric properties and dynamics on daily and seasonal timescales [Cohen et al., 2015], although other dynamic processes are important as well [Moen et al., 2008],

especially at high latitudes. Ion composition dynamics are illustrated by temporal changes in the International Reference Ionosphere, and source levels of solar flux are shown by the $F_{10.7}$ index.

5.4.1 Solar Zenith Angle of ELF Whistlers

The intensity of solar radiation at a specific point in the ionosphere varies as a function of the solar zenith angle (χ), the angle between the Earth-Sun vector and the Earth's radial vector [Chapman, 1931]. χ may be computed for a specific time and location using Equation 5.1, in which Φ_{LAT} is the local geographic latitude, Ψ_{DEC} is the solar declination, and Λ_{GHA} is the Greenwich Hour Angle, the angle between the Greenwich Meridian and the meridian of the Sun.

$$\cos\chi = \sin\Phi_{LAT}\sin\Psi_{DEC} - \cos\Phi_{LAT}\cos\Psi_{DEC}\cos\Lambda_{GHA} \tag{5.1}$$

With $\Phi_{LAT} = -90°$ and $\Lambda_{GHA} = 0$ (arbitrary at the pole), Equation 5.1 simplifies to $\cos\chi = -\sin\Psi_{DEC}$. At the pole, therefore, χ only varies as a function of the solar declination, a function of both the geographic location and the position of Earth's rotational axis relative to the sun. With geographic position fixed, only Earth's orbital location drives variation in Ψ_{DEC}, and as a consequence, χ. The solid blue line in Figure 5-2 (left) represents the solar zenith angle calculated at the South Pole (χ_{sp}) for the entire year in 2004, which illustrates both the year-long variation in solar position as well as the lack of diurnal variation.

On 1 January, just after winter solstice when solar zenith angle is at a minimum, χ gradually increases each day with no diurnal variability. The + markers along the solid blue curve in Figure 5-2 indicate days of the year when ELF whistlers were detected. On 22 February, χ for the last ELF whistler before the winter blackout is recorded at $\chi = 79.6°$.

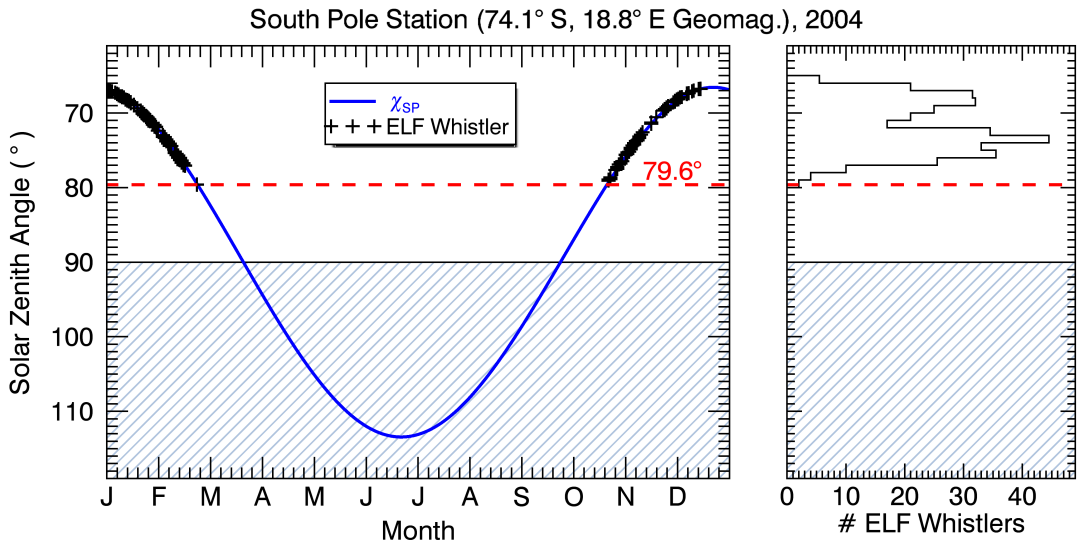

Figure 5-2: Left: The solid blue line is the solar zenith angle at the South Pole in 2004 (χ_{sp}). The shaded region highlights the Antarctic winter when the sun remains below the horizon, and the red dashed line represents the highest value of χ for any ELF whistler detected. Detection times for ELF whistlers are indicated by +. Right: A histogram of all ELF whistlers detected at the South Pole Station in 2004 binned as a function of χ, with a bin size of 1°.

A maximum in χ is reached at summer solstice during the Antarctic winter, highlighted by the hatched region for values of $\chi > 90°$. ELF whistlers then begin to appear again after χ decreases below 80°. The Figure 5-2 histogram shows the distribution of all ELF whistlers detected in 2004 as a function of χ. The bimodal distribution is not considered statistically significant. The plot and histogram both illustrate a lack of detected whistlers for the $80° < \chi < 90°$ range, when the sun is still just above the local horizon.

Solar zenith angle at lower latitudes ($\Phi_{LAT} \neq \pm 90°$) varies much more widely and on a daily basis. The full form of Equation 5.1 is used to calculate χ for each ELF whistler detected at Lulin Station, Taiwan ($\Phi_{LAT} = 23.47°$). The length of day at lower latitudes changes throughout the year, which means that solar position at a given time is not fixed. Figure 5-3 illustrates this variation with plots of solar zenith angle at winter solstice (χ_{min}) and summer solstice (χ_{max}). Comparison of detection times relative to solar posi-

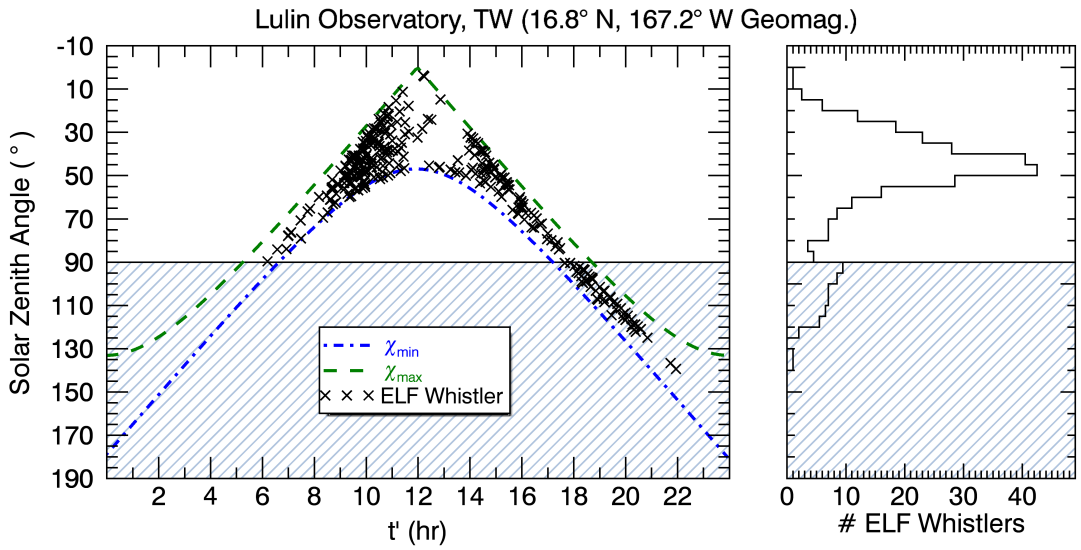

Figure 5-3: Left: Solar zenith angle calculated for winter solstice (χ_{min}) and summer solstice (χ_{max}) are plotted as bounds of χ as a function of day throughout a year at $\Phi_{LAT} = 23.47°$. The solar zenith angle (χ) at the time of each ELF whistler detected at Lulin Observatory is marked by $\times$ as a function of normalized time of day, t' (see text for details of calculation). Right: A histogram of all ELF whistlers detected at Lulin Observatory in the 2003-2004 data set binned as a function of χ, with a bin size of 5°

tion throughout the year is simplified by normalizing the local solar time, t, for each ELF whistler to t', such that the time of observation relative to sunrise (t_r) and sunset (t_s) is consistent.

$$t' = 12\frac{t - t_r}{t_s - t_r} + 6 \tag{5.2}$$

Sunrise and sunset in Equation 5.2 are defined when $\chi = 90°$. For intuitive convenience the normalized times, t', are scaled to a 12 hour period and offset such that the peak of daylight still corresponds to 1200. χ is calculated as a function of t' for each ELF whistler detected between 26 August 2003 and 12 July 2004 in Taiwan and marked by $\times$ in Figure 5-3.

Over nearly a full year of observation at low latitudes, ELF whistlers are not detected until $t' \geq 6$, when $\chi \leq 90°$. After $t' = 6$, the events increase in occurrence rate until

$t' = 12$, where the occurrence rate temporarily drops off. Occurrence rate increases again from $t' = 14$ until after $t' = 20$, well after local sunset. The spread in χ values at any particular value of t' is the result of the variation in Ψ_{DEC} throughout the year. The data show no preferential behavior for any particular season at low latitudes.

The diurnal occurrence pattern of ELF whistlers at Lulin Station is very similar to the annual pattern at the South Pole, but there are some notable differences. One difference is that observations of ELF whistlers at the South Pole have a cutoff at $\chi \approx 80°$, regardless of whether χ is increasing or decreasing. Events at low latitudes, on the other hand, start occurring as soon as the atmosphere is sunlit ($\chi \geq 90°$). ELF whistlers detected at Lulin Station also sometimes persisted after the sun had set below the horizon ($t' > 18$) for up to several hours.

Another primary difference between observations at high and low latitudes is the MLT distribution of the detections, which was shown in Kim et al. [2006]. The MLT distribution of ELF whistlers detected at the South Pole has two clear peaks, one around 1900 MLT and the other around 0300 MLT. The MLT distribution detected at Lulin Observatory has three peaks, at local times of approximately 1000, 1500, and 1900. When binned by χ, however, the histogram in Figure 5-3 shows a very clear peak in the distribution centered around $\chi \approx 45°$, which combines the local time occurrence peaks from both 1000 and 1500. The χ distribution illustrates a common characteristic for two of the peaks in MLT distribution at low latitudes. Other discrepancies in MLT relative to the "broad, daytime maximum" noted in prior studies are the post-sunset peak at low latitudes, and the near-midnight peaks in occurrence distribution at polar latitudes.

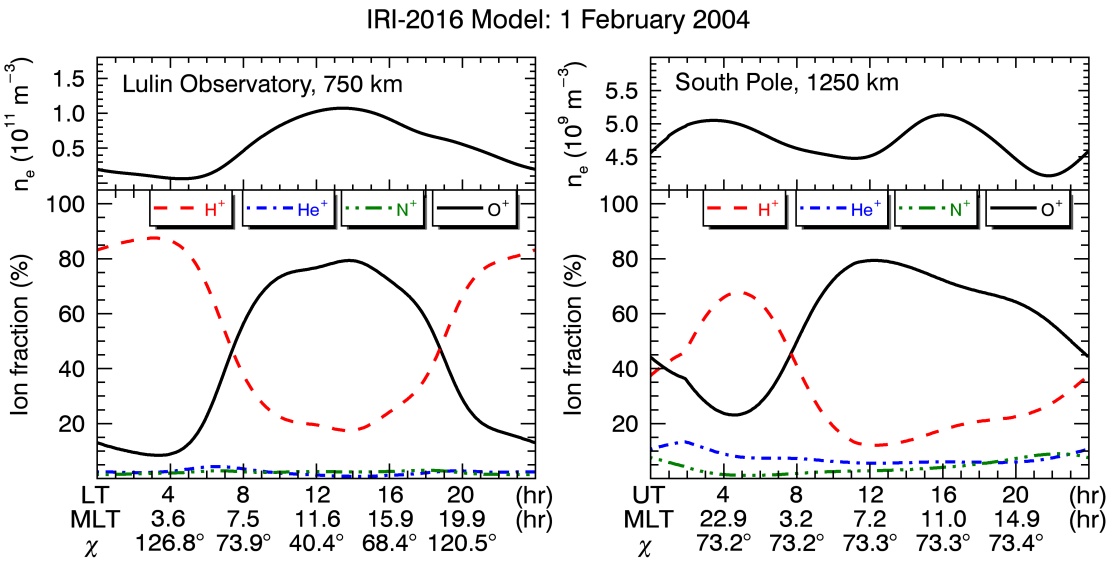

Figure 5-4: IRI-2016 model output for Lulin Observatory at 750 km as a function of LT (left) and South Pole Station at 1250 km as a function of UT (right). Top plots show electron density for both locations; bottom plots show fractional ion concentration of the four dominant ion species at the chosen altitudes.

5.4.2 Ionospheric Composition

The International Reference Ionosphere is a global, empirical model of the ionosphere, most recently updated in 2016 [Bilitza et al., 2017], that provides profiles of multiple ionospheric parameters up to altitudes of 2000 km. Plasma density and ion composition are determined using IRI-2016 for 1 February 2004 above both Lulin Observatory and the South Pole. A time series of ionospheric parameters at 750 km and 1250 km, respectively, are shown in Figure 5-4. Model output at 750 km above Lulin Observatory serves as a comparison to the calculations in Wang et al. [2011], but the date is chosen for a time when observations at Lulin Observatory and the South Pole overlap. IRI-2016 values were obtained through the NASA/GSFC Virtual Ionosphere, Thermosphere, Mesosphere Observatory (VITMO).

The plasma density, n_e, above Lulin Observatory (Figure 5-4, top left) reaches a minimum just before Local Time (LT) = 6, prior to exposure to the photoionizing effects of solar EUV radiation. Once χ passes 90°, the ion composition (Figure 5-4, bottom left) tran-

sitions from a H^+-dominated plasma to O^+-dominated. Plasma density reaches its peak just after LT = 12, when the solar zenith angle reaches its minimum, which corresponds to the decrease in occurrence rate from $t' = 12$ to $t' = 14$ shown in Figure 5-3. As χ increases again, photoionization decreases and chemical recombination begins to erode the plasma density. Slower timescales for recombination force the transition back to a H^+-dominated plasma to occur after $\chi > 90°$, or after sunset.

Comparison of Figures 5-3 and 5-4 shows that the occurrence rates of ELF whistlers at Lulin Observatory do not peak along with solar intensity ($\chi \to 0$) or plasma density (n_e). Rather, the highest occurrence rates coincide with the transition between dominant ion species in the topside ionosphere. The first transition begins after sunrise and continues after sunset, just like the ELF whistler occurrence distribution.

IRI-2016 output at 1250 km above the South Pole shows a transition in ion composition (Figure 5-4, bottom right) similar to low latitudes, but the change in plasma density (Figure 5-4, top right) is noticeably different. Solar zenith angle at the South Pole is nearly constant over the course of a 24 hour period, which means the change in photoionization due to solar EUV flux is minimal. The two peaks in plasma density at polar/cusp latitudes are due in part to solar wind controlled transport of plasma across the polar cap [Moen et al., 2008]. The peak in n_e closer to 2400 MLT may also be due in part to changes in neutral densities and neutral winds, similar to the Weddell Sea Anomaly [Richards et al., 2017]. Effects due to auroral processes are also a significant factor in high latitude plasma dynamics.

Ion composition above the South Pole, on the other hand, shows two transition times between H^+-dominated plamsa and O^+-dominated plasma, much like at low latitudes. The transitions between dominant ion species above the South Pole occur at $\sim$ 1900 MLT and $\sim$ 0300 MLT, which align with the peak times of ELF whistler occurrence [Kim et al., 2006].

Traditionally, empirical models like the IRI are most reliable at low- and mid-latitudes where there is sufficient data available to ingest. IRI-2016 tends to underestimate electron density in the polar cap, most notably at night-time and during solar maximum [Bjoland et al., 2016]. Older versions of IRI failed to capture the polar cap dynamics in plasma density [Moen et al., 2008], but IRI-2016 accounts for at least some effects of plasma transport in the polar cap and cusp regions if not the overall magnitude [Themens et al., 2014]. IRI is also more reliable closer to $h_m F_2$ which is well below the altitude used in Figure 5-4, but data has been added to improve accuracy at higher altitudes for plasma density [Reinisch et al., 2007], and ion composition [Bilitza and Reinisch, 2008].

5.4.3 Solar Flux Correlation

Previous studies attempted to connect the occurrence of ELF whistlers to geophysical indices like A_p or K_p. Heacock [1974] reported a weak correlation but no study since then has been able to confirm the correlation [Sentman and Ehring, 1994; Wang et al., 2005; Kim et al., 2006]. The present focus on a sufficiently sunlit atmosphere is further investigated by examining the correlation with the $F_{10.7}$ index, a measure of solar 10.7 cm radio emission that is widely used as an indicator of solar activity [Tapping, 2013].

The general level of solar activity in 2004 was moderate to low, as illustrated by a plot of the $F_{10.7}$ index in Figure 5-5 (left). The red line represents $F_{10.7A}$, the running 81-day average of the index. $F_{10.7}$ data were extracted from NASA/GSFC's OMNI data set through OMNIWeb. The minimum index value for 2004 was 80.9 solar flux units (sfu) and the maximum was 180.8 sfu, with a mean value of 106.5. The number of ELF whistlers were binned into daily totals for comparison to the daily index value, but no correlation was found between the solar activity level and the daily occurrence of ELF whistlers at either the South Pole or Taiwan.

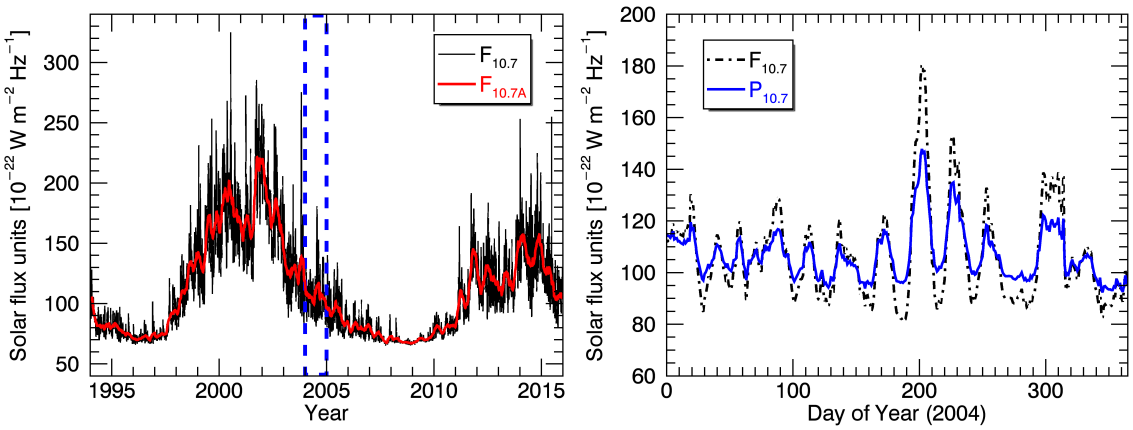

Figure 5-5: Left: $F_{10.7}$ index values for the year used in analysis of ELF data (highlighted by the blue dashed box) relative to the full solar cycle. The running 81 day average, $F_{10.7A}$, is shown in red. Right: $P_{10.7}$ calculated for 2004 (blue line) is plotted along with $F_{10.7}$ (black, dash-dot).

The $P_{10.7}$ proxy [Richards et al., 1994], defined as $P_{10.7} = (F_{10.7A} + F_{10.7})/2$, has been shown to be a better predictor of solar EUV output [Girazian and Withers, 2015] and a better linear indicator of ionospheric activity than the $F_{10.7}$ value alone [Liu et al., 2006]. $P_{10.7}$ was calculated for 2004 (Figure 5-5, right) but this index also failed to correlate strongly with ELF whistler activity. The overall trend throughout the year remains steady in both indices, even during the South Pole winter when the largest spikes in solar flux occur but zero ELF whistlers are detected at the South Pole.

The overall variability of solar flux is not large enough in 2004 to say with absolute certainty that no correlation exists. Day-to-day changes or short-term spikes in flux level have no strong correlation in 2004, but a comparison to years with much higher average flux levels (e.g. 2002 or 2014) might behave differently. Longer term studies of the data may reveal trends not seen in the 2004 data and may be worthy of future study.

5.5 Discussion

The effect of a sunlit ionosphere is a new physical characteristic that corresponds with the predominant occurrence times for ELF whistlers at multiple latitudes. Prior explanations have ranged from terrestrial sources [Liu et al., 2013] out to the magnetosphere, particularly those on the dayside such as ELF Hiss [Tsurutani et al., 2015] and Lion's Roar [Smith et al., 1969; Gurnett and Frank, 1972]. "Auroral roar" has been observed in the polar cap on the night side [Sato and Hayashi, 1985; Saito et al., 1987] and during polar winter [LaBelle and Weatherwax, 2002]. These signatures originate at ionospheric altitudes [Temerin and Lysak, 1984].

Sentman and Ehring [1994] suggested that a turbulent source causes Lion Roars in the dayside magnetosphere that enter the Earth-ionosphere cavity via the cusp. While it is possible for broadband, low frequency waves to duct into the ionosphere via the cusp [Lysak, 1999], Wang et al. [2005] dismissed the idea that a broadband, incoherent signal could become a narrow-band, coherent signal like an ELF whistler without a physical explanation for the mechanism. A lack of correlation between events recorded at different latitudes [Kim et al., 2006] also suggests that ELF whistlers are not likely reaching low latitudes by being ducted into the Earth-ionosphere cavity.

The detection of ELF whistlers at low latitudes during the South Pole winter blackout further contradicts the idea of magnetospheric waves being ducted, which should otherwise be observable at a wide range of latitudes. Ducting via the northern cusp does not explain the low latitude whistlers detected during the South Pole blackout. The times between the South Pole observation period and the equinoxes are still filled with low latitude observations, at a time when the North Pole is still in polar night. Ruling out the cusp-ducting mechanism decreases the likelihood of a magnetospheric source for ELF whistlers. The strong attenuation of signals in the lower ELF range (1-100 Hz) at local noon when plasma

density is at its highest further reduces the likelihood of magnetospheric waves being detected by a ground-based magnetometer. In the absence of a strong magnetospheric source candidate, the role of the local ionosphere must be considered.

The structure and composition of the ionosphere vary as a function of solar zenith angle, and this effect varies from low latitude [Thomson et al., 2014] to high latitude [Kitamura et al., 2011], particularly at low altitudes [Shimazaki, 1965]. Photoionization driven by solar EUV radiation is the primary driver for ionospheric formation. At auroral and polar latitudes, additional processes are important in addition to solar flux, including plasma transport, auroral precipitation, and polar outflow. Observations of ELF Whistlers at low latitudes, as illustrated by Figure 5-3, mirror the times of ionospheric compositional changes as illustrated in Figure 5-4. ELF Whistlers are not observed at low latitudes before sunrise but do persist well after sunset which follows the lag in ionospheric decay after the the loss of solar input.

Wang et al. [2011] determined that the Class III right-hand ion cyclotron mode is most likely responsible for ELF whistlers. Based on the Young et al. [1981] analysis of GEOS 1 and 2 observations, Rauch and Roux [1982] classified Class III ion cyclotron waves (ICWs) as a wave mode that propagates at non-zero angles to the magnetic field with frequencies from 0 up to a resonance determined by the propagation angle. In the limit of parallel propagation, the resonance frequency is the H^+ cyclotron frequency; in the limit of perpendicular propagation, the resonance frequency is the H^+-He^+ bi-ion hybrid frequency. Horne and Thorne [1990] expanded the multi-ion treatment to include O^+, and suggested strong damping of Class III waves due to second harmonic oxygen cyclotron absorption. Damping may explain the conspicuous lack of strong echoes in the detection of ELF whistlers, which are an otherwise commonly observed feature of VLF whistlers [Kennel, 1966].

Heacock [1974] suggested ELF whistlers may be hydromagnetic R-mode waves from

lightning strikes or chorus-like waves analogous to VLF phenomena. Sentman and Ehring [1994] ruled out both mechanisms by arguing that magnetospheric emissions should present distinct frequency characteristics between their observations in California and the Alaska observations [Heacock, 1974], whereas the spectra were nearly identical. Sentman and Ehring [1994] also ruled out the possibility that ELF whistlers are the low-frequency tail of lightning-strike VLF whistlers on the basis that many of their events grew out of noise well below the upper limit of their instrumental passband. ICWs that propagate in multi-species plasmas [Rauch and Roux, 1982] can be generated by instabilities associated with energetic protons on the dayside [Mauk and McPherron, 1980]. Energetic protons result in temperature anisotropies ($T_\perp > T_\parallel$) that may drive several wave-generating instabilities, such as the mirror and ion cyclotron anisotropy instabilities [Gary, 1992].

Despite the analogy to VLF whistlers, the instability responsible for exciting right-hand ICWs in the frequency range of ELF whistlers may well have a local origin. Various electrostatic ionospheric instabilities derive free energy from local sources [Kelley, 2009; Makarevich, 2016], including density gradients [Hoh, 1963; Simon, 1963; Maeda et al., 1963], drift velocities [Farley, 1963; Buneman, 1963], wind shears [Hysell et al., 2017], and photoelectrons [Oppenheim and Dimant, 2016]. Mode coupling between a locally excited electrostatic instability during periods of increasing or decreasing photoionization could drive ELF whistlers.

One plausible scenario for the generation of ELF whistlers would start with an analogy to Huba et al. [1978]. The drift cyclotron instability is produced by the coupling of a drift wave created by a small-scale density gradient and an ion cyclotron wave. An increase or decrease in photoionization as the solar angle changes throughout the day creates small gradients in electron density. Broadband ELF (BBELF) waves are often present in the upper ionosphere and have been shown to result from nonlinear emission processes from

intertial Alfvén waves [Seyler et al., 1998]. Coupling between a local cyclotron instability, such as the drift cyclotron instability, and free energy resulting from photoionization is a potential avenue for further exploration. The potential instability that results from such coupling may be responsible for the generation of ELF whistlers in the same manner as the mirror and ion cyclotron anisotropy instabilities [Gary, 1992].

The altitude at which the transition in ionospheric composition occurs should also be considered. This study demonstrates that ELF whistlers are not a globally transmitted phenomenon, but the distance from source to observer does not have to be along local zenith. Class III ICWs travel obliquely along the magnetic field, which implies that some spread in detectable range is likely. This adds to the suggestion by Kim et al. [2006] that a change in altitude may be responsible for the dispersive behavior of ELF whistlers.

The drastic swings in the dominant ion species shown in Figure 5-4 illustrate the variability in the composition as a result of EUV radiation [Anderson and Hawkins, 2016] and other plasma processes in the ionosphere [Moen et al., 2008]. The common times between the occurrence of ELF whistlers and the presence of solar radiation along with changes in ionospheric composition is worthy of further study.

5.6 Conclusions

The relationship between measurements of ELF whistlers and the solar zenith angle have been presented for two separate locations, the geographic South Pole (74.1° S MLAT) and Lulin Observatory, Taiwan (23.5° N, 16.6° N MLAT). Analysis of the data has led to the following conclusions:

1. Narrow-band ELF whistler waves only appear at the South Pole during polar summer, when $\chi < 80°$. Continued observations at low latitudes during the Antarctic winter contradict the notion of a magnetospheric source ducted into the Earth-ionosphere

cavity.

2. ELF whistlers are observed at Lulin Observatory only after the sun has risen above $\chi = 90°$, but are occasionally observed after the sun has set. Peak occurrence times align with the diurnal change in ionospheric composition.

3. Peak occurrence times near midnight MLT at the South Pole align with changes in ionospheric composition similar to the low latitude pattern.

4. ELF Whistlers are not correlated with the daily change in solar flux levels indicated by the $F_{10.7}$ index. The consistent flux levels during 2004 suggest that changing solar conditions alone likely do not explain the winter blackout.

The correlation (or lack thereof) with solar flux levels on a daily basis is not entirely conclusive. A longer study over the course of a solar cycle would be required to examine behavior under a variety of solar conditions. A statistical study of all ELF data acquired at the South Pole ($\sim$ 10+ years) compared to a full solar cycle would provide more definitive results, and such a study will be considered in the future.

The observation of ELF whistlers at polar latitudes when the sun is sufficiently high above the local horizon is a physical constraint that can be applied to any potential theory for the generation of ELF whistlers. The similar pattern observed at low latitudes gives some confidence in the observations at high latitudes, and leads to a second new physical characteristic of ELF whistlers. Changes in ionospheric composition mirror the peak occurrence times of ELF whistlers at both high and low latitudes, which provides a second constraint on their generation. Plasma instabilities generated by changing plasma composition, potentially as it relates to photoionization of the ionosphere, should be investigated as a possible source mechanism.

Acknowledgments: The authors thank the South Pole Station Cusp Lab technicians for keeping the ELF magnetometer system running for over a decade. We also thank Dr. Kaiti Wang of Taiwan for providing the list of ELF whistlers observed at Lulin Observatory. We acknowledge NASA/GSFC's Space Physics Data Facility's OMNIWeb service for providing F10.7 index values, and for access to IRI-2016. ELF data for this work is available at: http://mirl.sr.unh.edu/ELF/. Work was supported under NSF OPP Award #1247558.

Chapter 6

Neutral Upwelling in the Cusp

The following chapter is an analysis of observations from the RENU 2 sounding rocket mission. A paper based on analysis of ultraviolet emissions in the thermosphere will part of a special issue of Geophysical Research Letters*:*

> Fritz, B. A., M. R. Lessard, K. Dymond, K. Lynch, J. Hecht, J. Clemmons, T. Cook, S. Chakrabarti, and D. R. Kenward (2018), Remote detection of neutral upwelling in the cusp region from RENU 2 UV PMT and DMSP SSULI observations, *Geophys. Res. Lett.* (in prep.)

I analyzed the RENU 2 electron and UV PMT data, calculated excitation rate factors for both RENU 2 and DMSP measurements, analyzed the GRACE density measurement, prepared all text in this chapter, and formed the conclusions presented here. Co-author Ken Dymond performed the tomographic inversion of the SSULI data.

6.1 Introduction

The cusp region of the atmosphere exhibits complex behavior that has been a challenge for models to simulate. The cusp, illustrated in Figure 6-1, is a path for a wide variety of energy sources to directly enter the ionosphere and create a highly dynamic environment. Increased temperatures at high latitudes have been correlated with increased drag on satellites for

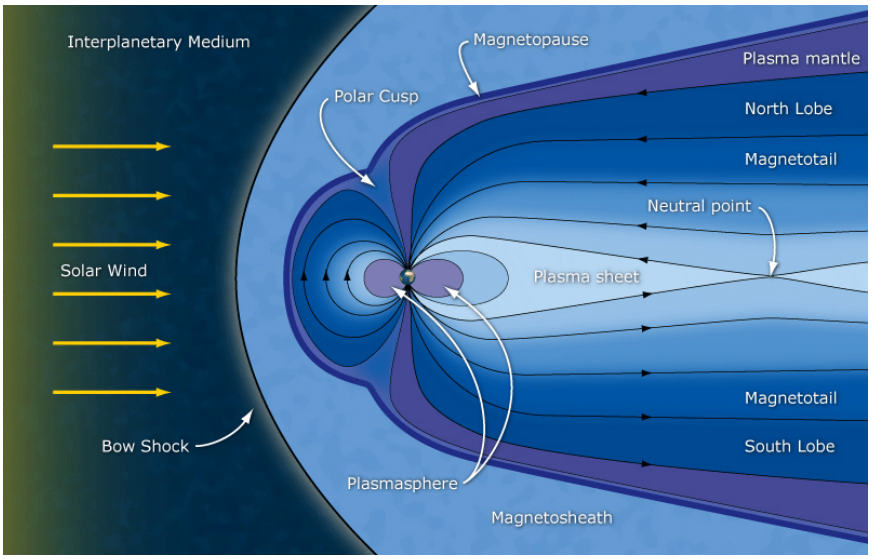

Figure 6-1: Diagram of the magnetosphere with the polar cusp region noted. Image taken from the NASA IBEX mission page (Credit ESA/C T. Russel; https://www.nasa.gov/mission_pages/ibex/news/spaceweather.html)

nearly as long as artificial satellites have been put in orbit [Jacchia and Slowey, 1964]. The small-scale physics that drive the temperature changes, however, have been difficult to fully understand and replicate.

Anomalous enhancements of neutral density in the cusp have been measured for decades. Examples include enhanced N_2 populations detected by OGO 6 during quiet [Taeusch and Hinton, 1975] and disturbed [Taeusch, 1977] conditions, and the Spades satellite [Moe et al., 1977]. High resolution measurements by the Challenging Minisatellite Payload (CHAMP) satellite accelerometer [Lühr et al., 2004] showed extreme density spikes in the cusp near 400 km altitude. Measurements by CHAMP and the Gravity Recovery and Climate Experiment (GRACE) have served as the basis for nearly two decades of focused research into the cusp anomaly.

Lühr et al. [2004] presented a single day example of the anomalous cusp behavior, suggesting that small-scale ($\sim$ 1-km) field-aligned currents (FACs) play an important role in heating the thermosphere in addition to the commonly accepted Joule heating mechanism.

Schlegel et al. [2005] followed with seven days of data across the entire polar cap, noting once again the density maxima located near the cusp, and for the first time compared CHAMP data to a model prediction of thermospheric density (Thermospheric General Circulation Model). Initial results showed that the model is unable to reproduce the structure seen in the high latitude thermosphere, noting that a much wider range of energetic inputs would be required to understand the observations.

6.1.1 Statistical properties of the cusp density anomaly

Several statistical studies have provided key insight into the general physical characteristics of cusp density enhancements. The first full year of global CHAMP density measurements (2002) showed that the cusp density anomaly grew with moderately geomagnetically disturbed conditions (high Kp) [Liu et al., 2005]. The first four years of data (2002-2005) [Rentz and Lühr, 2008] revealed an asymmetry in the northern hemisphere, as well as correlations with solar EUV flux, $P_{10.7}$, and the merging electric field, E_{merg}. The latter two results implied solar wind conditions had a direct effect on the presence of cusp anomalies. Rentz and Lühr [2008] determined minimum values of $P_{10.7} \sim 150$ and $E_{\text{merg}} \sim 1$ mV/m, and the effect of the two appeared to be additive, where the effect of E_{merg} was 50 times higher than $P_{10.7}$. Solar zenith angle and particle precipitation also played a minor role on seasonal variation of the density anomalies.

A more recent analysis of 2002-2005 CHAMP data related cusp density anomalies to electron temperature (T_e), smale-scale FACs, and vertical ion velocity [Kervalishvili and Lühr, 2013]. A superposed epoch analysis (SEA) showed peaks in all three variables co-located with the anomaly. Small-scale FACs were more prominent in the summer, while T_e & v_i were more prominent in the winter. The relative density enhancements, however, showed no seasonal variation. Kervalishvili and Lühr [2013] were unable to fully resolve the

discrepancy between the effect of enhanced Joule heating due to soft precipitation and the effect of direct heating by the precipitating electrons.

Examination of CHAMP data from 2002-2009 investigated the seasonal, solar cycle, and IMF B_y dependencies of the density anomaly, along with another SEA of neutral zonal wind velocity, large-scale FAC, small-scale FAC, and T_e [Kervalishvili and Lühr, 2014]. *Relative* density enhancements in the cusp did *not* depend on solar cycle phase, local season, or IMF B_y. IMF B_y was correlated with thermospheric zonal winds and large-scale FAC distributions, which calls into question the relationship of those quantities with the density anomaly. IMF B_z turning negative, on the other hand, correlated well with the density anomaly.

The most comprehensive study to date of the cusp density anomaly used approximately 20 years of data from both GRACE and CHAMP [Huang et al., 2017]. The peak in occurrence of localized density maxima had a FWHM of $\sim 10^\circ$ MLat, and appeared slightly poleward (typically $1-4^\circ$ MLat) of typical cusp latitudes, likely due to a sizeable number of events occurring poleward of 80° MLat. Under quiet geomagnetic conditions the poleward location of the density maxima was much more pronounced in frequency. Half of the density maxima coincided with FACs, which is indicative of localized heating. Huang et al. [2017] suggested that the remainder of density perturbations may be associated with atmospheric gravity waves.

6.1.2 Horizontal vs. vertical structure in the cusp

Single spacecraft in a circular orbit are inherently limited to in situ measurements of horizontal structure. Additional measurements of the cusp indicate that the density enhancements have vertical structure in addition to the localized horizontal anomaly. The Streak satellite at ~ 250 km [Clemmons et al., 2008] and the DE-2 satellite at ~ 360 km [Prölss, 2008]

both measured *depletions* in density, observations that were not made apparent by CHAMP or GRACE. Prölss [2008] found that the depletions coincided with a decrease in $[N_2]/[O]$, which was attributed to a loss of atomic oxygen caused by diverging wind flows.

Demars and Schunk [2007] reproduced density perturbations in the cusp with the Utah State University model [Ma and Schunk, 1995]. Increased frictional ion heating (i.e. Joule heating) by a factor of 110 produced a "neutral fountain" in the cusp, as shown in Figure 6-2. The altitude structure shown by Demars and Schunk [2007] provides at least a qualitative explanation for the discrepancy between CHAMP-measured density enhancements at 400 km and the Streak-measured depletions at 260 km. The "neutral fountain" would generate divergent winds around the cusp, and that idea is supported by two measurements.

1. A balloon-borne Fabry-Perot Interferometer (FPI) over Svalbard measured equatorward winds south of the cusp [Wu et al., 2012]
2. Re-analysis of CHAMP data from 2000 showed divergent wind patterns [Horvath and Lovell, 2017]

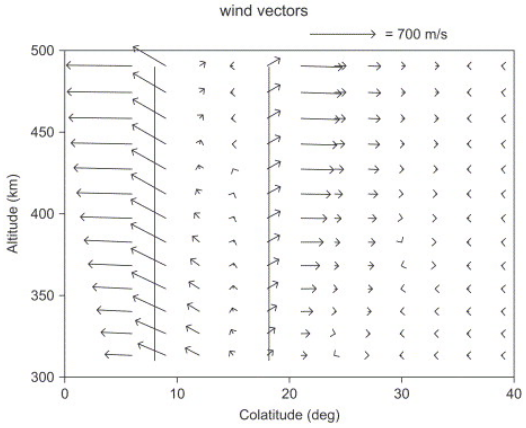

Figure 6-2: Neutral wind vectors as a function of altitude and geographic colatitude. The vertical lines superimposed delimit the region of enhanced ion-neutral frictional heating. (Figure from Demars and Schunk [2007])

Measurement of complicated structure in multiple dimensions requires a diversified, multi-scale approach. For example, Huang et al. [2016] studied thermospheric heating at high latitudes using measurements by CHAMP, GRACE, DMSP, and the Resolute Bay FPI (around 250 km nominal). Temperature and density enhancements were found at multiple altitudes during two

magnetic storms. The study showed that models underestimated the influence of Poynting flux and resulting thermospheric response in the polar region, just one of many examples where measurements inform and improve the current state of physical models. The **Utah State University model** [Ma and Schunk, 1995] shown in Figure 6-2 is one of many physical models that have attempted to simulate cusp density enhancements under a variety of driving conditions.

6.1.3 Simulations of the cusp anomaly

The National Center for Atmospheric Research (NCAR) **General Circulation Model (GCM)** is one of the most widely used models for thermosphere simulations. The Thermosphere GCM (TGCM) was used to perform one of the first three-dimensional, time-dependent simulations of density disturbances in the high-latitude thermosphere [Crowley et al., 1989]. The Thermosphere Ionosphere Mesosphere Electrodynamics GCM (TIME-GCM), with input from the Assimilative Mapping of Ionospheric Electrodynamics (AMIE) algorithm, reproduced cusp density enhancements during an interval of strongly positive (+20 nT) IMF B_y [Crowley et al., 2010] . Empirical specification of electrodynamic properties in the ionosphere (from AMIE) was critical for the TIME-GCM simulations to reproduce anomalous cusp behavior when IMF $B_z \approx 0$.

Prior to Kervalishvili and Lühr [2014], TIE-GCM simulations showed the amplitude of cusp density enhancements depend on B_z [Kwak et al., 2010]. Wilder et al. [2012] fed AMPERE data into the AMIE algorithm, which in turn drove TIME-GCM to show intense Joule heating in the dayside polar region during the recovery phase of two geomagnetic storms. This showed energy may be deposited in the cusp during $B_z \geq 0$ & $B_y > 0$ conditions, which counters the uncorrelated nature of B_y shown by statistical studies of CHAMP data [Kervalishvili and Lühr, 2014].

The NCAR GCM has also demonstrated the ability to simulate both vertical and horizontal structure in the thermosphere. TIE-GCM quantified the influence of Joule heating at different altitudes on the neutral temperature and density at 400 km, however the focus was not on the cusp [Huang et al., 2012]. TIME-GCM showed that disturbances in the cusp thermosphere due to localized Joule heating can propagate equatorward at speeds of about 700 m/s [Wilder et al., 2012], similar to the behavior observed by Wu et al. [2012] and Horvath and Lovell [2017].

The **Coupled Magnetosphere-Ionosphere-Thermosphere** (CMIT) model demonstrated the impact of soft electron precipitation on enhanced Joule heating processes at 250 km, which produced a cusp density enhancement [Zhang et al., 2012]. Two case studies using CMIT, one during a storm and one not during a storm, showed how the indirect pathway via increased F region Joule heating rate is a dominant process than direct heating during a storm [Zhang et al., 2015].

The **Global Ionosphere-Thermosphere Model** (GITM) showed that Poynting flux had a significant effect on cusp density enhancements [Deng et al., 2013]. Direct heating from soft precipitation had a fairly modest effect, but enhanced conductivity caused by ionization in the F region enhanced Joule heating, which produced a result closer to that of the Poynting flux, similar to Zhang et al. [2012]. GITM was able to replicate equatorward winds like those observed by Wu et al. [2012] only by increasing grid-size resolution from $5^\circ \times 5^\circ$ to $5^\circ \times 1^\circ$ resolution in longitude by latitude [Sheng et al., 2015], which underscored the importance of high-resolution modeling for small-scale physics.

The **Otto-Sadler** model [Otto et al., 2003] reinforced the importance of high-resolution simulations in the cusp [Sadler et al., 2012]. Soft precipitation was varied in an oscillating manner to simulate the effects of PMAFs passing overhead, and as a result generated the effects of neutral upwelling. The **Aerospace Dynamical Model** (ADM) showed that

direct particle heating due to precipitation can influence density structures, but models with resolution on the order of 2° are necessary [Brinkman et al., 2016].

The **Open Geospace General Circulation Model** (OpenGGCM) [Raeder et al., 1998] along with the **Coupled Thermosphere-Ionosphere Model** (CTIM) [Fuller-Rowell et al., 1996] modeled the response of the high-latitude thermosphere to a solar wind dynamic pressure enhancement [Shi et al., 2017]. CHAMP, GRACE and Defense Meteorological Satellite Program (DMSP) data were all used to characterize the event and then compare to the simulated thermospheric response to drivers. Enhancements in the thermosphere were attributed to the combined effect of enhanced dynamic pressure and B_y.

The Rocket Experiment for Neutral Upwelling (RENU) 2 was intended to examine an upwelling event in extreme detail to measure fine structure associated with the event. Several drivers were expected to play a role in generating thermospheric upwelling and used as launch criteria for the mission (see Table 6.1).

Observable	Measurement
IMF $B_z < 0$	ACE
Small-scale FACs	ASI / MSP
T_e enhancement	EISCAT
v_i enhancement	EISCAT

Table 6.1: RENU 2 Launch Criteria

6.2 RENU 2 Event Description

NASA sounding rocket mission 52.002 (RENU 2) launched at 0734 UTC on 13 December 2015 from the Andøya Space Center, Norway (67.3° N, 112.7° E geomagnetic). A remote science team, located at the Kjell Henriksen Observatory (74.9° N, 127.8° E geomagnetic) on the island of Svalbard, tracked the location of the cusp with the help of several global and local environmental monitors. Environmental parameters correlated with the cusp

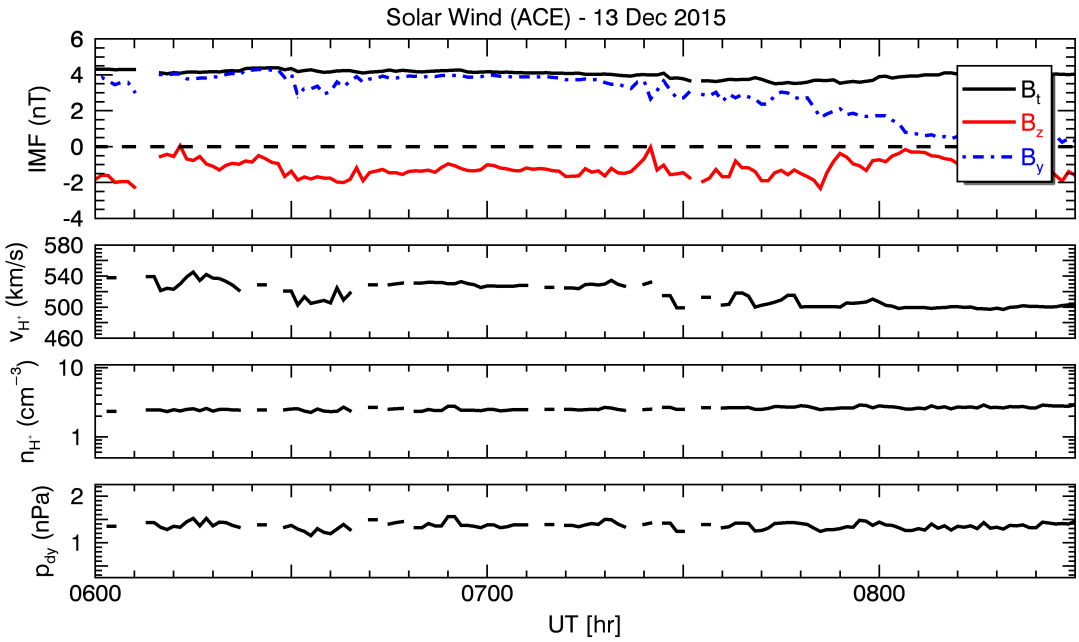

Figure 6-3: Solar wind values on 13 December 2015 time-shifted to the Earth bow shock – Panel 1: Total IMF (B_t), B_z, and B_y; Panel 2: Solar wind bulk velocity (v_p); Panel 3: Solar wind bulk density (n_p); Panel 4: Solar wind dynamic pressure (p_{dy}) (Data provided by NASA OMNI Service at GSFC/CDAWeb)

anomaly [Kervalishvili and Lühr, 2013, 2014] listed in Table 6.1 were used to judge the launch conditions.

The Advanced Composition Explorer (ACE) satellite monitors solar wind conditions at the L1 Lagrange point, $\sim$ 1.5 million km upwind from Earth. Figure 6-3 shows 1-minute averages of ACE measurements of the interplanetary magnetic field (IMF), solar wind bulk speed, proton density, and dynamic solar wind pressure on 13 December 2015. Data were retrieved from the OMNI database via the NASA GSFC/CDAWeb and are time-shifted to the nose of the Earth's bow shock. IMF B_z, shown in the top panel, turned southward at approximately 0615 UT and remained negative through launch at 0734 UT. The bottom three panels show steady levels of solar wind speed ($v_p \approx 520$ km/s), density ($n_p \approx 2$ cm^{-3}), and dynamic pressure ($p_{dy} = \rho_p v_p^2 \approx 1.4$ nPa).

Thermospheric enhancements in the cusp are correlated with $B_z \approx -1$ nT approximately

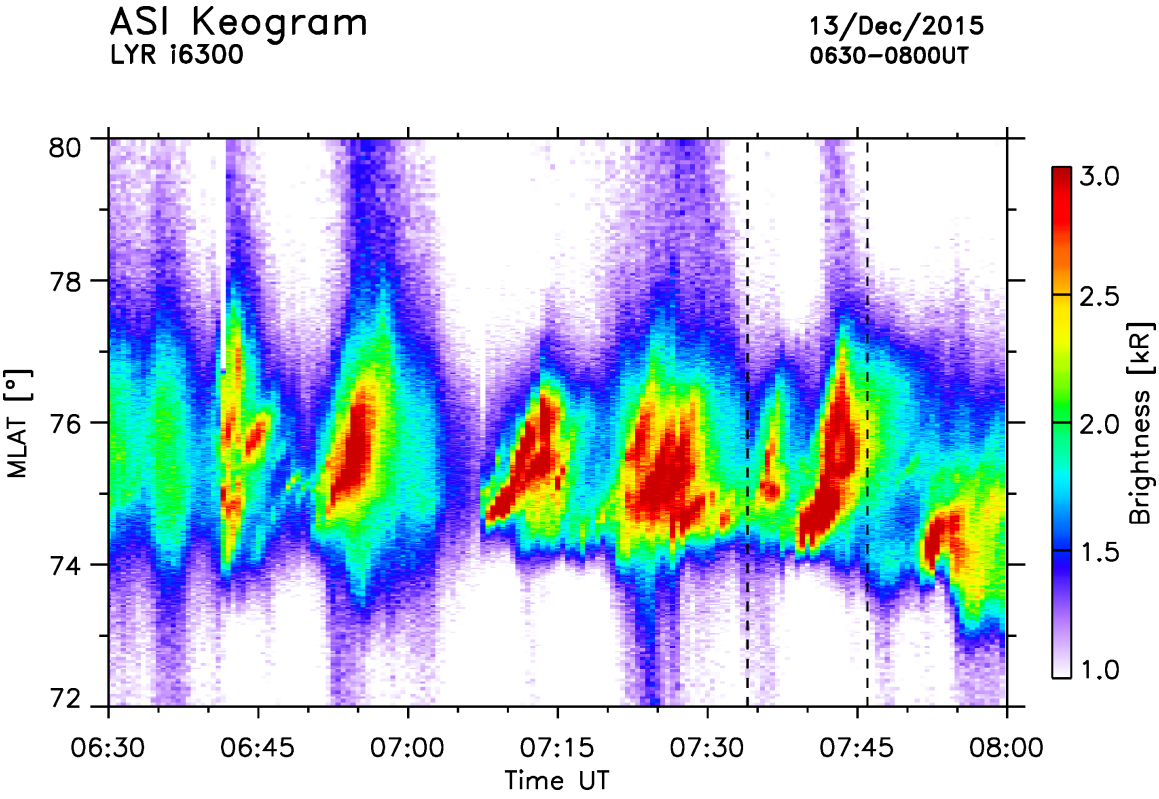

Figure 6-4: This keogram is contructed from UiO All-Sky Imager (ASI) data acquired during the RENU 2 sounding rocket mission at the Kjell Henriksen Observatory. This ASI is filtered to the O I 6300 Å emission line. Image pixels are mapped onto magnetic coordinates by projecting to 250 km. The vertical dashed lines indicate the launch and loss of signal times for the payload.

30 minutes prior to the enhancement, independent of season or solar cycle [Kervalishvili and Lühr, 2014]. Starting at 0630 UT, IMF $B_z < 0$ held for over an hour. IMF B_y does not correlate with the intensity of thermospheric density enhancements [Kervalishvili and Lühr, 2014] and was not included in the primary launch criteria, but was used to help track the cusp location relative to 1200 MLT [Moen et al., 1999]. Density and dynamic pressure remained fairly low and steady, which precluded any strong effects due to dynamic solar wind pressure.

Soon after IMF B_z turned southward, all-sky imagers (ASIs) from the University of Oslo (UiO), located at Kjell Henriksen Observatory (KHO), began to detect thin auroral forms stretching horizontally across the field of view. Figure 6-4 shows a keogram of 6300 Å

emissions extracted from ASI images between 0630 UT and 0800 UT. The keogram is constructed from a time series of intensity profiles by extracting the geomagnetic north-south column of image pixels. A thin layer of snow and ice covered the optical dome at KHO up until $\sim$ 0640 UT, which makes data prior to that time unreliable. Almost immediately upon clearing the ASI dome, aurora was observed overhead.

Pulsed magnetic reconnection at the magnetopause was initiated by $B_z < 0$, and the resulting soft electron precipitation generated the aurora in Figure 6-4. Thin auroral forms visible in the ASI slowly drifted poleward as the magnetic flux tubes began to convect over the polar cap. These poleward moving auroral forms (PMAFs) are represented in the keogram by the diagonal forms that move higher in MLAT over time. PMAFs are a common indicator of the cusp [Sandholt and Farrugia, 1999], and are also thought to be an indicator of the small-scale field aligned currents (FACs) that correlate with thermospheric neutral upwelling [Kervalishvili and Lühr, 2013].

In addition to ACE and the ground ASIs, the 42-meter EISCAT Svalbard incoherent scatter radar (ISR), located adjacent to KHO, monitored ionospheric conditions above Svalbard. Figure 6-5 shows 3 hours of EISCAT measurements along the local magnetic field line, beginning at 0600 UT. Altitude profiles of electron density (n_e), electron temperature (T_e), ion temperature (T_i), and ion drift velocity (v_i) are plotted as a function of time.

Plasma density, shown in the top panel, is low throughout the morning with only a few brief, minor enhancements, each accompanied by an increase in T_e. The most prominent enhancements were observed at 0650, 0710, 0725, and 0740, which correspond to the passage of PMAFs shown in Figure 6-4. Electron density reaches $\sim 10^{11}$ m^{-3} up to altitudes of $\sim$ 400 km, especially between 0715-0745 UT. Sufficient plasma density in the ionosphere provides confidence in all other measurements derived from the ISR signal up to $\sim$ 400 km during these intervals.

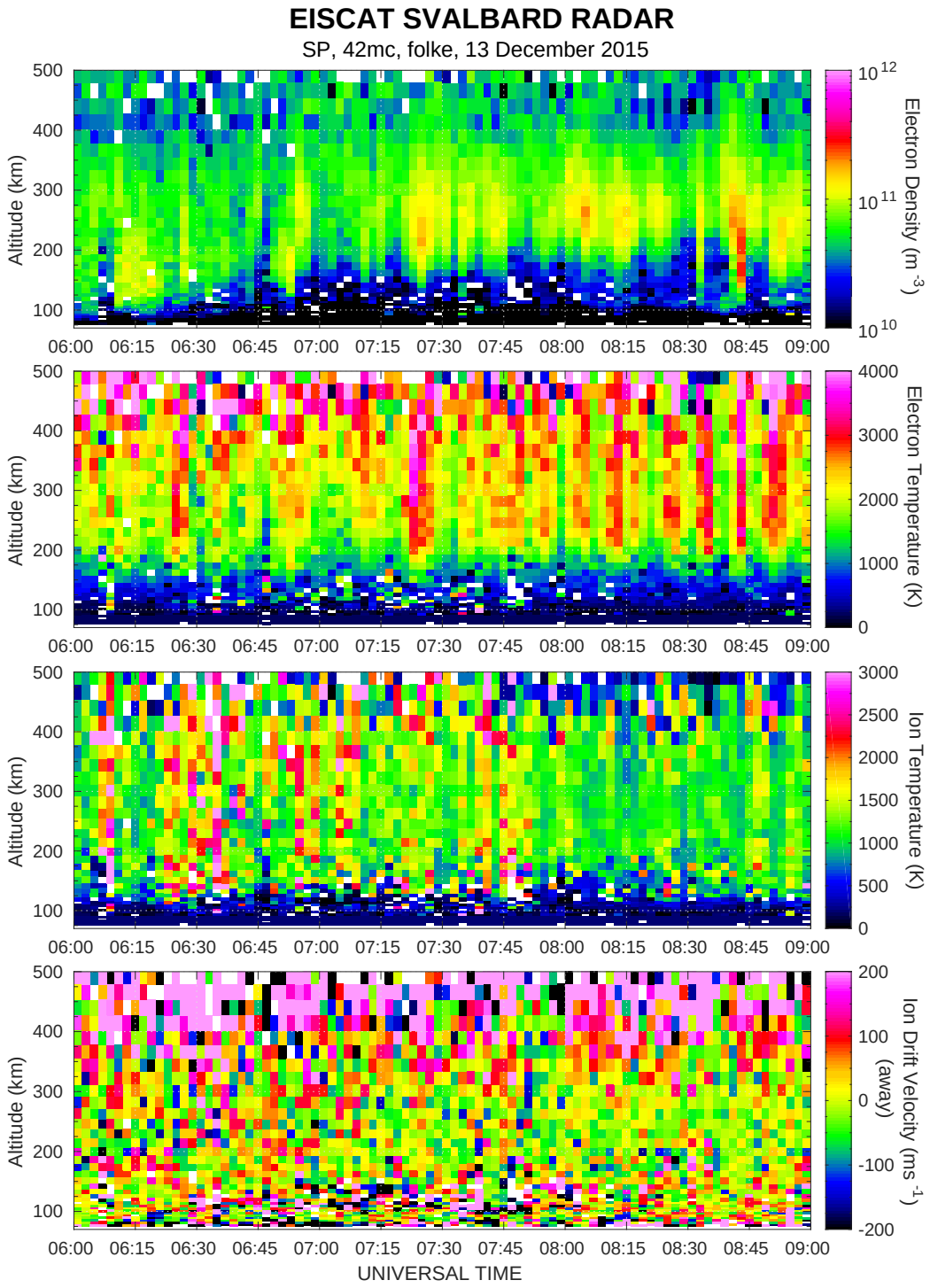

Figure 6-5: Ionospheric measurements on 13 December 2015 from the EISCAT Svalbard 42 m facility. Time-altitude profiles from top to bottom show electron density, electron temperature, ion temperature, and ion drift velocity.

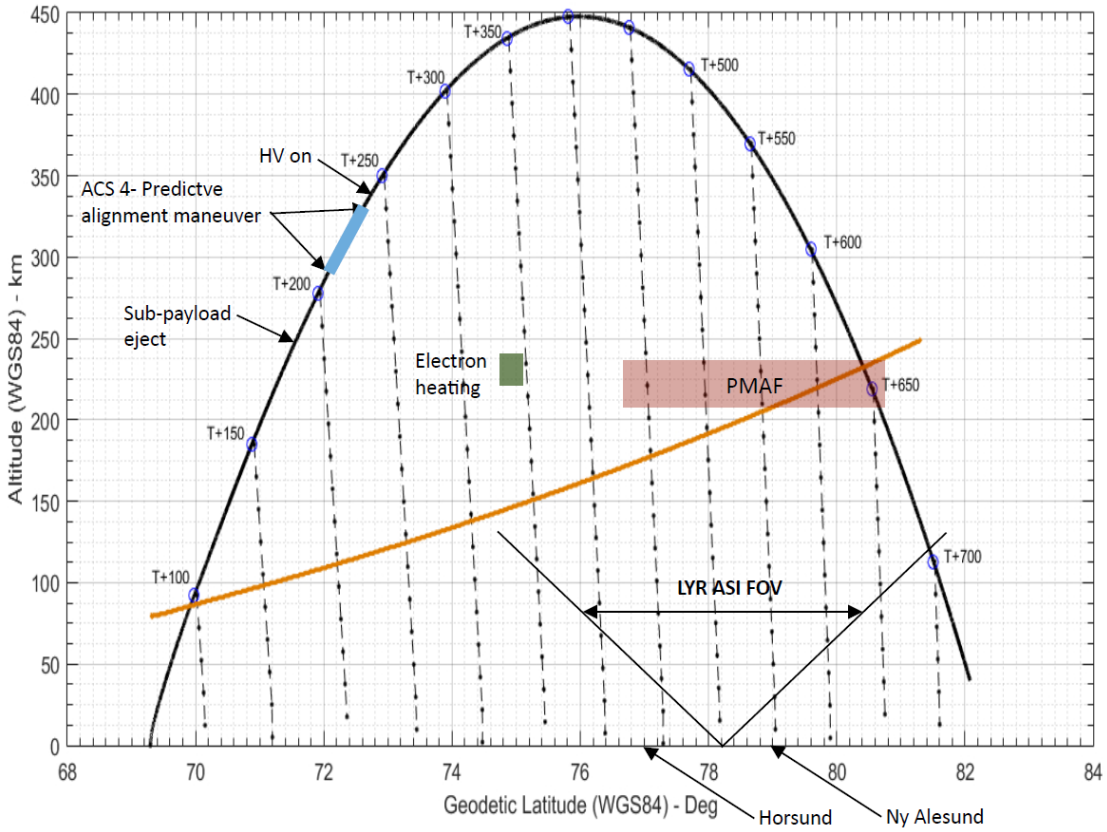

Figure 6-6: Trajectory of the RENU 2 sounding rocket payload, determined by the onboard GPS antenna is plotted as the thick black line. Dashed black lines represent the orientation of the local magnetic field. Time is marked for every 50 seconds after launch at 0734 UT, 13 December 2015.

Ion temperature is mostly unaffected between 0715 and 0745 UT. Brief enhancements in ion drift velocity ($\sim +100$ m/s) appear most notably at ~ 350 km near 0730 UT and 0745 UT. The data appear noisy and brief but long signal integration times increase confidence that the v_i signals are real. The ISR field of view is stationary along the local field line, so positive values (away) from the radar indicate upward, or roughly vertical, flows in the ionosphere. Enhanced upflow detected by EISCAT was the fourth and final launch criteria for RENU 2.

By 0700 UT, B_z had been negative for 30 minutes, which by itself suggested that a cusp density anomaly may be present. After the third PMAF passed through the ASI field of view and EISCAT detected the weak upflow at 0730 UT, the environmental conditions were

deemed sufficient and RENU 2 was launched at 0734 UT. The nominal rocket trajectory was designed to reach an apogee of 500 km prior to the cusp and descend through a density enhancement at 400 km. The payload target was the magnetic field line that coincided with the EISCAT and ASI FOV.

The actual trajectory of the RENU 2 payload is shown in Figure 6-6 as a function of altitude and latitude. The payload reached an apogee of $\sim$ 450 km and traveled over 12° in geographic latitude (1480 km on the ground). Once the payload reached its ballistic phase, the onboard attitude control system (ACS) used a predictive alignment maneuver to orient the payload to the field orientation over Svalbard ($\sim$T+500 sec). The predictive alignment minimized contamination of the particle detectors from the ACS cold gas thrusters. The orange line in Figure 6-6 represents the terminator of visible light from the sun.

Instrument	Institution	Measurement	Range
Ion Gauge (x6)	Aerospace	Neutral density	$\geq 10^{-10}$ Torr
EPLAS	UNH	Electron distribution	6eV - 15 keV
ERPA	UNH	Thermal T_e	0.06 - 3 eV
HEEPS-T	Dartmouth	3D thermal ions	0.1 - 22 eV
HEEPS-M	Dartmouth	3D superthermal ions	4 - 800 eV
BEEPS	Dartmouth	Ion mass spec. (H^+, O^+)	0.1 - 22 eV
Billingsley	Cornell	Tri-axis fluxgate mag	$\pm 60,000$ nT
COWBOY	Cornell	Electric field	0-20 kHz, 0-1,000 Hz
Visible PMTs	Aerospace	N_2II (3914 Å); OI (5577 Å, 6300Å)	30 cts/s/R
UV PMT	UNH	OI (1304 Å)	53 cts/s/R

Table 6.2: Instruments with successful measurements from the RENU 2 mission

6.3 RENU 2 Observations

The RENU 2 payload passed through the 4^{th} PMAF observed on the morning of 13 December 2015, bracketed by the dashed black lines in Figure 6-4. An anomaly in the third stage separation caused the payload to pass obliquely through the PMAF, a fortuitous event that provided the payload nearly 200 seconds in the region of precipitation. RENU 2 was a

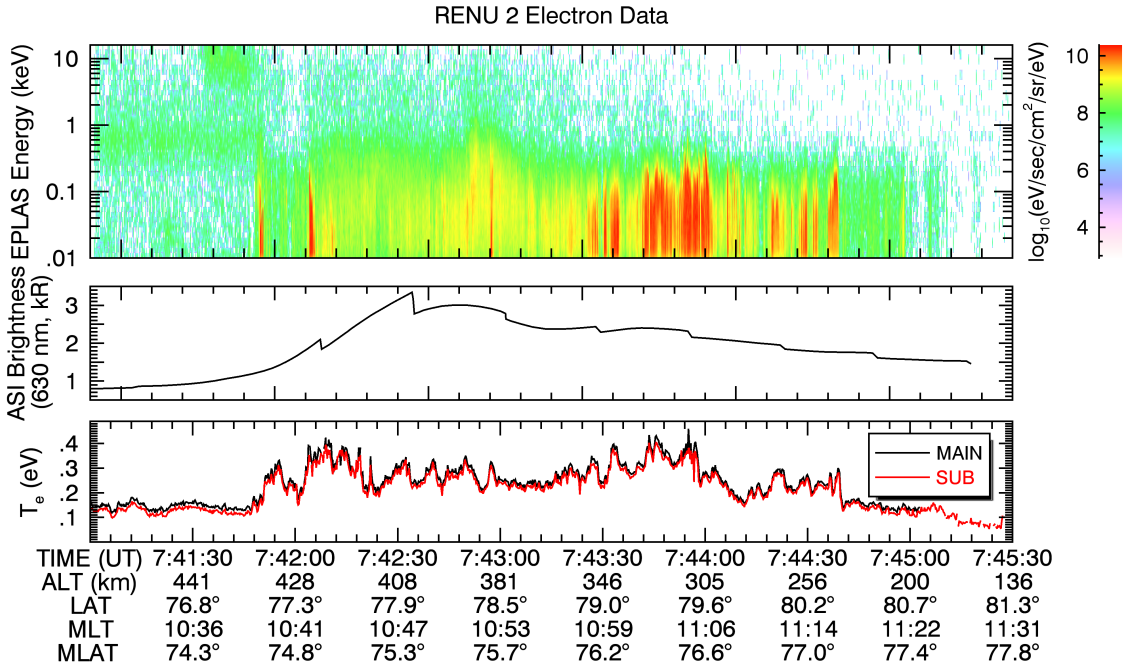

Figure 6-7: Top: Differential energy flux from the RENU 2 Electron PLASma (EPLAS) instrument. Middle: Brightness along payload footpoint extracted from UiO ASI (from Fig 6-4). Bottom: Electron temperature (T_e) from RENU 2 Electron Retarding Potential Analyzers (ERPAs), both main and sub payloads.

heavily instrumented payload that successfully measured a wide variety of environmental parameters. Instruments with successful measurements from RENU 2 are listed in Table 6.2, however only a few provide data for the current analysis.

The Electron PLASma (EPLAS) instrument and the Electron Retarding Potential Analyzer (ERPA) instrument both provided clear evidence that the payload passed directly through a PMAF. The EPLAS is a tophat electrostatic analyzer that sweeps $0.01 - 15$ keV with a full pitch-angle distribution every 42 ms. The differential energy flux spectrum is shown in the top panel of Figure 6-7 for the duration of time RENU 2 spent in the PMAF, summed across angular bins in the loss cone. Brightness measurements from the UiO ASI (Fig 6-4) along the payload footpoint is shown for a comparison to the electron measurements.

The EPLAS differential energy spectrum shows strong signatures of soft electron pre-

cipitation ($\leq$ 200 eV), an indicator of the cusp. All data shown were acquired with the payload on its downward, ballistic trajectory through the PMAF, shortly after the payload reached apogee ($\sim$ 450 km). Many short bursts of precipitation were detected throughout the region, including the region of strongest flux around 0744 UT. This structure helps to illustrate the spatial structure within PMAFs that is often not visible with lower resolution detectors or faster moving spacecraft. These structures are sometimes on the order of only a few km in spatial extent but are not bursty (temporally).

The ERPA is a traditional retarding potential analyzer that determines electron temperature near the payload [Frederick-Frost et al., 2007; Cohen et al., 2016]. The bottom plot in Figure 6-7 shows electron temperature (T_e) measured by ERPAs located on both the main payload and sub payload. The main and sub payloads slowly separated throughout the duration of the flight, ending $\approx$ 0.6 km in separation roughly along the same field line. The behavior in each instrument mirrors the other, which provided redundancy in the measurement but also shows the temperature within the thermosphere is roughly constant within a km along the same field line. The increase in local T_e aligns with the start of soft electron precipitation measured by the EPLAS, and the temperature remained elevated throughout the PMAF until the payload leaves the region of precipitation.

The brightness along the payload footpoint is an indicator of the electron precipitation as measured by a remote ground-based detector, which provides useful context for the payload measurement. This illustrates the difference between the immediate impact of the precipitation measured in situ and the effects as measured remotely.

Precipitating electrons measured by EPLAS generate auroral emissions when they collide with particles in the thermosphere, in this case primarily neutral atomic oxygen. Electron collisions excite oxygen atoms to higher energy states at a rate that is proportional to some rate factor. The excitation rate factor, or g-factor (g) may be calculated for any given

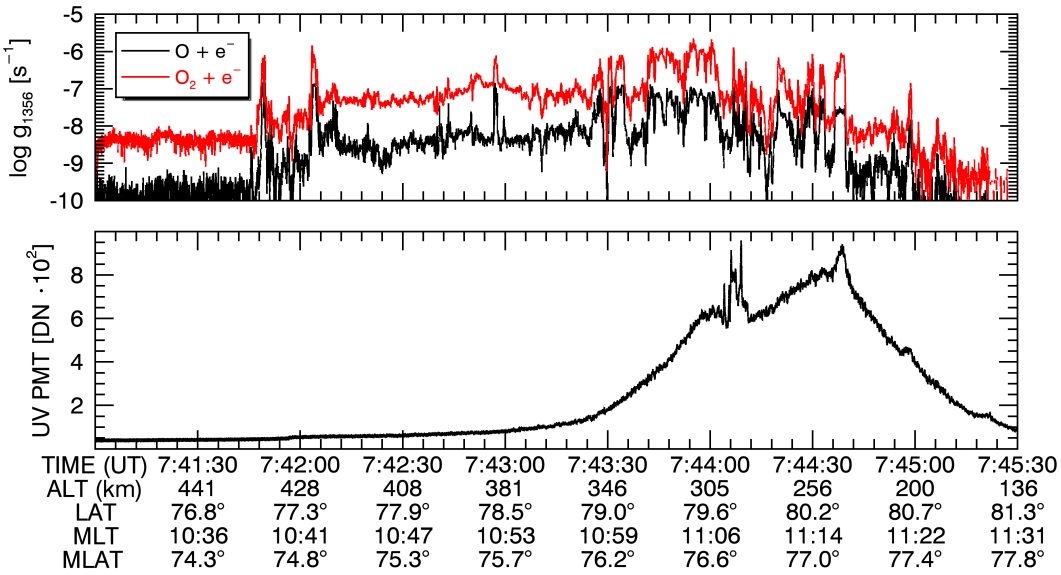

Figure 6-8: Top: Excitation rate factor (g_{1356}) calculated for both mechanisms of interest: $O, O_2 + e^- \rightarrow O^*$; Bottom: UV PMT measurement during the RENU 2 mission

reaction with the proper input. The reactions of interest ($O, O_2 + e^- \rightarrow O^*$) vary as function of altitude (z) and latitude (θ) due to the variability in the density of reactants.

$$g_i(z,\theta) = \int_0^\infty \sigma_i(E)\ \phi(E,z,\theta) dE \tag{6.1}$$

The rate factor calculation, g_i, for the i^{th} species depends on the cross-section, $\sigma_i(E)$, for the associated reaction [Meier, 1991; Kanik et al., 2003]. The g factor has been calculated for the O I UV emission, $O^* \rightarrow O + h\nu$ (1356 Å) based on both reactions. EPLAS provided the necessary electron flux distributions, $\phi(E,z,\theta)$, and the results are shown in the top panel of Figure 6-8. The rate factor for dissociative excitation ($O_2 + e^- \rightarrow O^*$) is generally much higher, as much as two orders of magnitude higher than simple collisional excitation ($O + e^- \rightarrow O^*$).

A strong enhancement in the UV PMT signal began at $\sim$ 0743 UT and lasted nearly until loss of signal (LOS) after 0745 UT. The instrument was located on the fore deck of

the payload looking up along the local magnetic field line. In an evenly excited, relaxed atmosphere, an increase in PMT signal would be expected as the payload dropped to lower altitudes where the density, and therefore number of emitters, rapidly increased. The sharp drop in signal at the end is unexpected, however. The altitude is not low enough that atmospheric absorption should outweigh the total emission. The drop in signal instead likely due to a drop in the number of emitters, which would be an indicator of the payload passing out from underneath an enhancement at higher altitudes.

The RENU 2 UV PMT (see Section 3.2 for instrument details) measured both O I 1304 Å and O I 1356 Å, shown in the bottom panel of Figure 6-8. O I 1304 Å is the lowest-energy, optically-allowed transition of oxygen: $O^*\ (^3S^0) \rightarrow O\ (^3P_2) + h\nu\ (1304\ Å)$. Optically allowed transitions are extremely optically thick, which typically precludes determination of any structure within a diffuse source. O I 1304 Å is most likely responsible for the broad, smooth trend in the PMT signal, which spans from 76° to 78° magnetic latitude (MLat), and peaks around 77° MLat.

The emission doublet at 1356 Å is very close in energy to O I 1304 Å, but is a spin-forbidden transition: $O^*\ (^5S^0) \rightarrow O\ (^3P_2) + h\nu\ (1356\ Å)$. O I 1356 Å is much more optically thin compared to O I 1304 Å, due to its spin-forbidden nature. The peaked structure at various points in the signal are likely due to O I 1356 Å. The potential to carry information about neutral density structure is the reason for calculating rate constants for the O I 1356 Å.

UV PMT remote measurements of neutral density supplement the six ion gauge instruments on the RENU 2 main payload that measured the neutral density in situ. Ion gauges were located on both the fore and aft decks, and the remaining four were oriented perpendicular to each other and the spin axis. At the time of this publication, ion gauge results from the RENU 2 are being prepared for publication [Clemmons et al., 2018].

6.4 Supporting spacecraft observations

The trajectory of the RENU 2 payload provided a unique measurement during a cusp transit. Comprehensive characterization of neutral upwelling during the event, however, has been enhanced through multi-point measurements from a variety of perspectives. Several polar-orbiting spacecraft passed near the cusp within 45 minutes of the RENU 2 flight and measured various ionospheric and thermospheric quantities. Figure 6-9 shows the orbital tracks for three spacecraft included in the current analysis, including GRACE and two DMSP spacecraft. The trajectory for RENU 2 is mapped for context.

The island of Svalbard, located near 78° N, 15° E geographic on the map, was positioned under the cusp throughout the duration of the following observations. GRACE (green line) traveled from top to bottom in the plot and intersected the eventual RENU 2 trajectory east of Svalbard around 0705 UT, nearly 40 minutes prior to the RENU 2 apogee. DMSP F19 (blue line) traversed the cusp region at approximately 0722 UT and DMSP F16 (red line) passed closest to Svalbard at approximately 0746 UT. Finally, the RENU 2 trajectory (black line), reached agpogee at ∼ 0741 UT with loss of signal occurring at approximately 0746 UT.

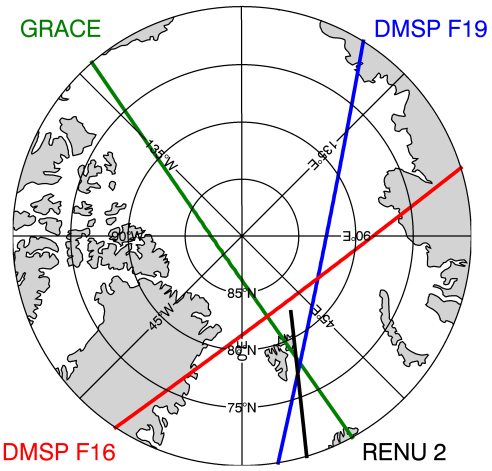

Figure 6-9: Polar geographic map of ground tracks for several spacecraft on 13 December 2015: GRACE (green), DMSP F16 (red), DMSP F19 (blue), and RENU 2 (black)

GRACE neutral density measurements provide context for the RENU 2 neutral density

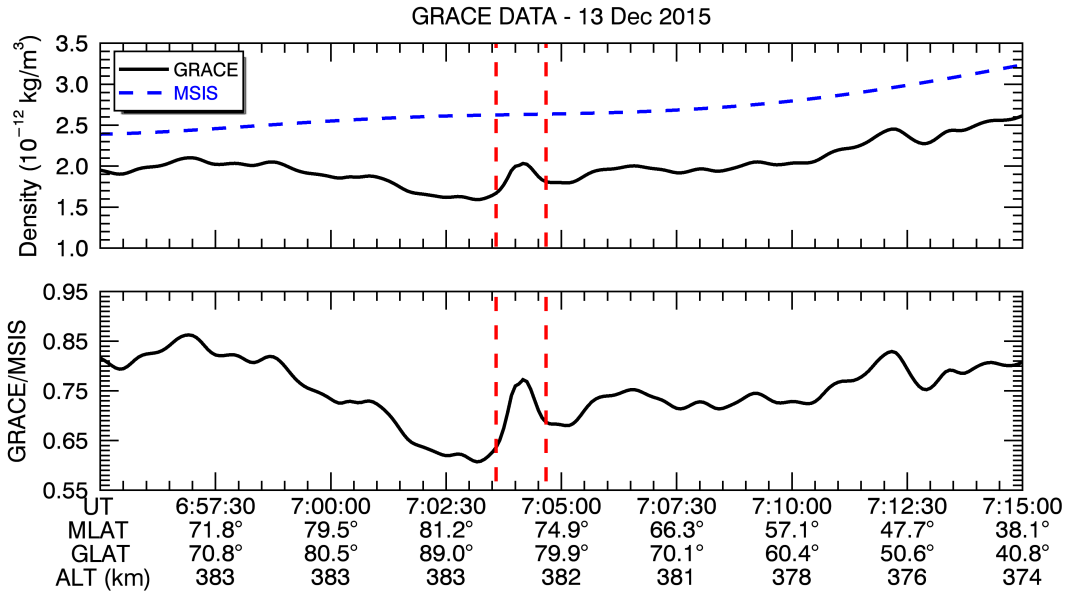

Figure 6-10: Top panel shows the GRACE neutral density measurement (black) and the NRLMSISE-00 model density at the GRACE altitude (blue dash). Bottom panel shows a ratio of the GRACE density measurement to the MSIS prediction. Red dashed lines in both panels indicate 79° and 76° magnetic latitude to highlight the bounds of the relative density enhancement.

measurement. The DMSP observations are the main focus, however, as UV instruments onboard provided key context for the RENU 2 UV PMT.

6.4.1 GRACE Accelerometer

GRACE neutral density measurements are shown in Figure 6-10 as the spacecraft passed over the polar cap and then equatorward through the cusp. The top panel shows a plot of both the GRACE density measurement (solid black) and the predicted MSIS density (dashed blue) at the spacecraft altitude. Dashed red lines mark both 79° and 76° MLat. The bottom panel shows the ratio of the GRACE measurement to the MSIS prediction.

The red dashed lines bracket a small density enhancement that peaks at $\sim 77°$ MLat. When GRACE reached 74.9° MLat, its geographic footpoint was ~ 300 km ENE of KHO at closest approach. The threshold used by Huang et al. [2017] for a relative mass density enhancement was $\rho_{rel} > 1.2$, with an average of $\rho_{rel} \approx 1.33$. The bump in Figure 6-10 is

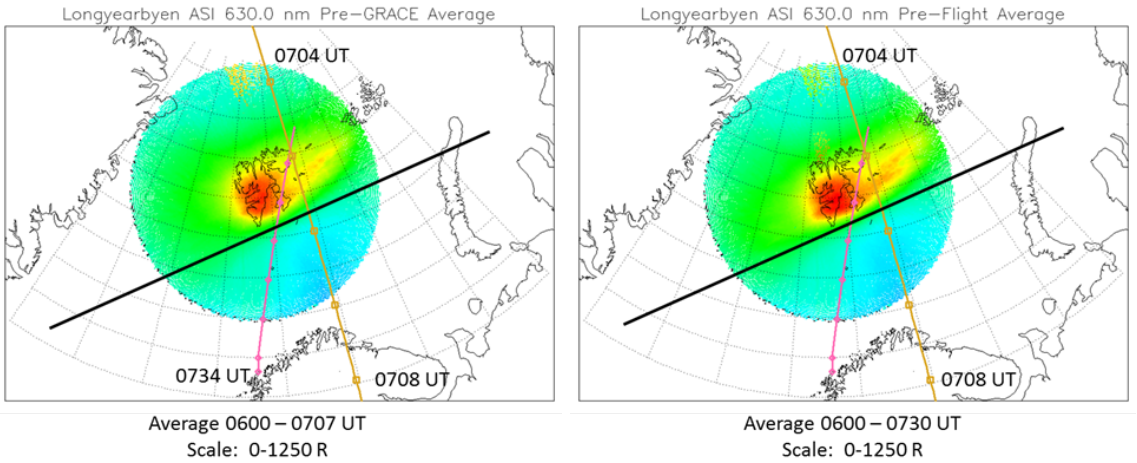

Figure 6-11: Averages of 6300 Å emissions acquired by the UiO ASI with trajectories plotted for GRACE (orange) and RENU 2 (pink); solid black line indicates approximate orientation of PMAF structure. Left: 67 minute average of emission prior to GRACE transit. Right: 90 minute average of emissions prior to RENU 2 launch. (Plot courtesy of J. Clemmons)

only $\rho_{rel} \approx 1.15$, slightly below the threshold for statistical studies. The location at the poleward edge of typical cusp latitudes, however, agrees with the distribution determined by Huang et al. [2017].

The UiO ASI provides evidence that GRACE may have only grazed the edge of the cusp, which would explain the sub-threshold ρ_{rel} measurement. Figure 6-11 is an average of ASI data over time, plotted over a map of Svalbard for reference. Much like PMAFs in Figure 6-4 were used as an indicator of the cusp during the launch call, the average auroral emission is used as a proxy for energy input into the cusp. The left plot is the 67 minute average of images prior to the GRACE transit, and the right plot is an average of the 90 minutes prior to RENU 2. The GRACE trajectory (yellow) and RENU 2 trajectory (pink) are plotted in both panels.

In neither plot does the GRACE trajectory intersect the region of high auroral emission intensity centered over Svalbard. The spacecraft passed through a region of lower relative emission intensity, which indicates a lesser, but non-zero, amount of cusp precipitation. GRACE may have grazed a flank of the cusp anomaly, but ρ_{rel} would not have surpassed

the Huang et al. [2017] threshold and would have been excluded from that database of events. Figure 6-11 shows that GRACE does not always transit the cusp directly, which must be taken into account when considering results from statistical studies.

RENU 2 passed through part of the region of highest auroral intensity, which indicates the rocket payload observed the cusp anomaly more directly. The UV PMT measurement in Figure 6-8 corroborates the notion that GRACE measured the flank of a cusp enhancement. The rise in PMT signal corresponds directly with the equatorward edge of the "bump" in the GRACE density measurement. The peak in the UV PMT measurement aligns with the peak in the GRACE density perturbation at 77° MLat. The trajectories of GRACE and RENU 2 are separated by nearly 40 minutes, but the integrated heating due to additional PMAF precipitation likely increases the upwelling effects.

An additional consideration for the GRACE measurement is as a baseline density measurement near the beginning of the event. Thermosphere simulations often rely on either MSIS values as an initial condition for the model, as a baseline for comparison, or both. Variability at high latitudes can reduce confidence in the use of empirical models, but in this case study an in situ measurement can be used to scale the model baseline.

6.4.2 DMSP SSUSI

DMSP spacecraft have carried the Special Sensor Ultraviolet Spectrographic Imager (SSUSI) [Paxton et al., 1993] since the launch of DMSP F16. The instrument consists of a scanning imaging spectrograph and a nadir-looking photometer system (not covered here). A scanning mirror rotates the spectrograph FOV from horizon to horizon across the satellite track below the spacecraft, which orbits at $\sim$ 830 km altitude. The spectrograph uses 160 spectral bins to image the $1150 - 1800$ Å spectral range with ~ 4 Å resolution. Five wavelength "colors" are recorded by SSUSI for transmission to the ground, and the species responsible

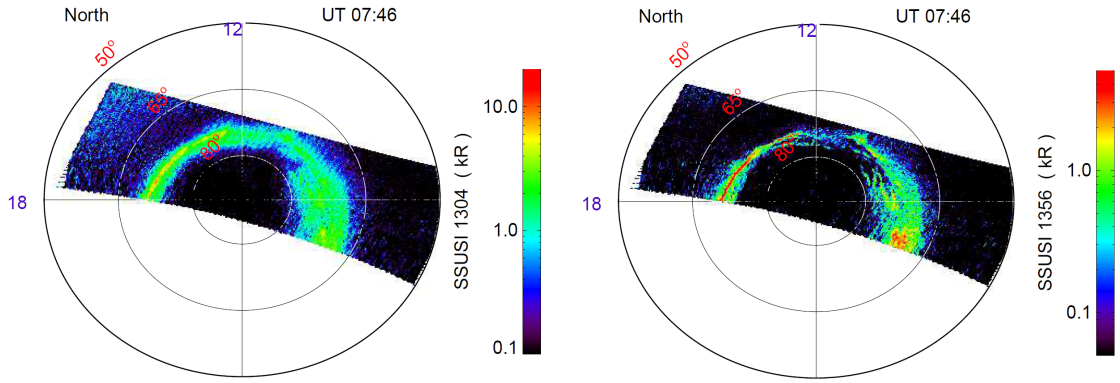

Figure 6-12: Polar maps of emission intensity for OI 1304 Å (left) and OI 1356 Å (right) acquired by the Special Sensor Ultraviolet Spectrographic Imager (SSUSI) on 13 December 2015

for each are listed in Table 6.3.

DMSP F16 passed by the cusp at $\sim$ 0746 UT, one minute after RENU 2 exited the PMAF. Figure 6-12 shows two polar plots with calibrated spectral emission intensities acquired by SSUSI. The left panel shows a map of OI 1304 Å and the right panel shows the same for OI 1356 Å, both with 1200 MLT at the top. The spacecraft moves left to right in the plots, and the cusp is located on the dawn side of 1200 MLT (top right), equatorward of 80°.

The OI 1304 Å plot on the left of Figure 6-12 reveals very little structure within the auroral band, a direct result of the optical thickness. The smeared out map supports the idea that 1304 Å emission comprises the broad, smooth part of the UV PMT measurement.

Wavelength (Å)	Source		Instrument
834	O^+		SSULI
911	O		SSULI
1085	N_2		SSULI
1216	H α	SSUSI	
1304	O	SSUSI	SSULI
1356	O	SSUSI	SSULI
1400-1500	N_2 LBH	SSUSI	
1641	O		SSULI
1650-1800	N_2 LBH	SSUSI	

Table 6.3: UV wavelengths observed by DMSP spectrographic instruments.

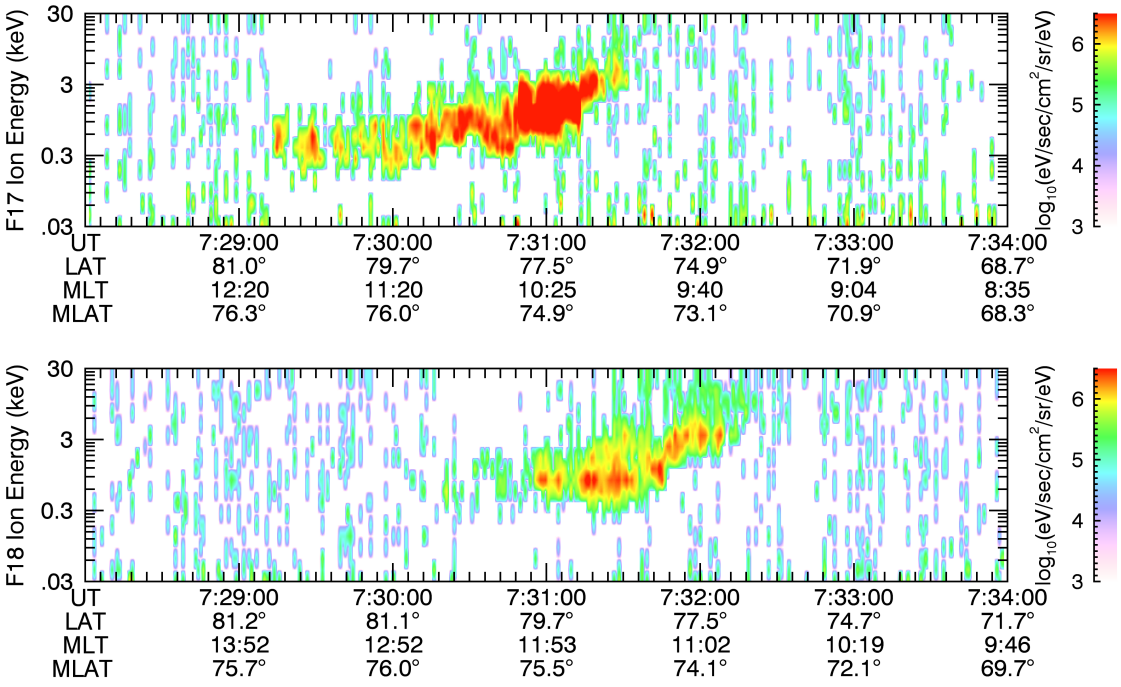

Figure 6-13: Differential ion energy flux spectrum from the DMSP SSJ5 instrument on the F17 (Top Panel) and F18 (Bottom Panel) spacecraft. Plots span from 0728 UT to 0734 UT on 13 December 2015. Both F17 and F18 spacecraft pass through the cusp between 0732 and 0734 ($\sim$ 10 min. before RENU 2)

The color scale for the OI 1304 Å emission plot reaches 10 kR, primarily due to a very bright feature in the post-noon sector. Pre-noon emissions are on the order of a few kR.

The OI 1356 Å plot shows significantly more structure than OI 1304 Å, primarily because it is the optically thin, spin-forbidden transition. Thin arcs are clearly visible in the dawn sector, which are possible indicators of PMAFs. Photon fluxes from above reach 1-2 kR in intensity, close to the same order as the 1304 Å flux. The structure seen in the SSUSI plot of OI 1356 Å likely contributes the structured peaks in the UV PMT signal.

6.4.3 DMSP SSJ5

The Special Sensor J5 (SSJ5) auroral charged particle detector is a triquadrispheric electrostatic analyzer that measures both positively and negatively charged particles in the energy range of 30 eV to 30 keV across 19 logarithmically spaced channels [Redmon et al., 2017].

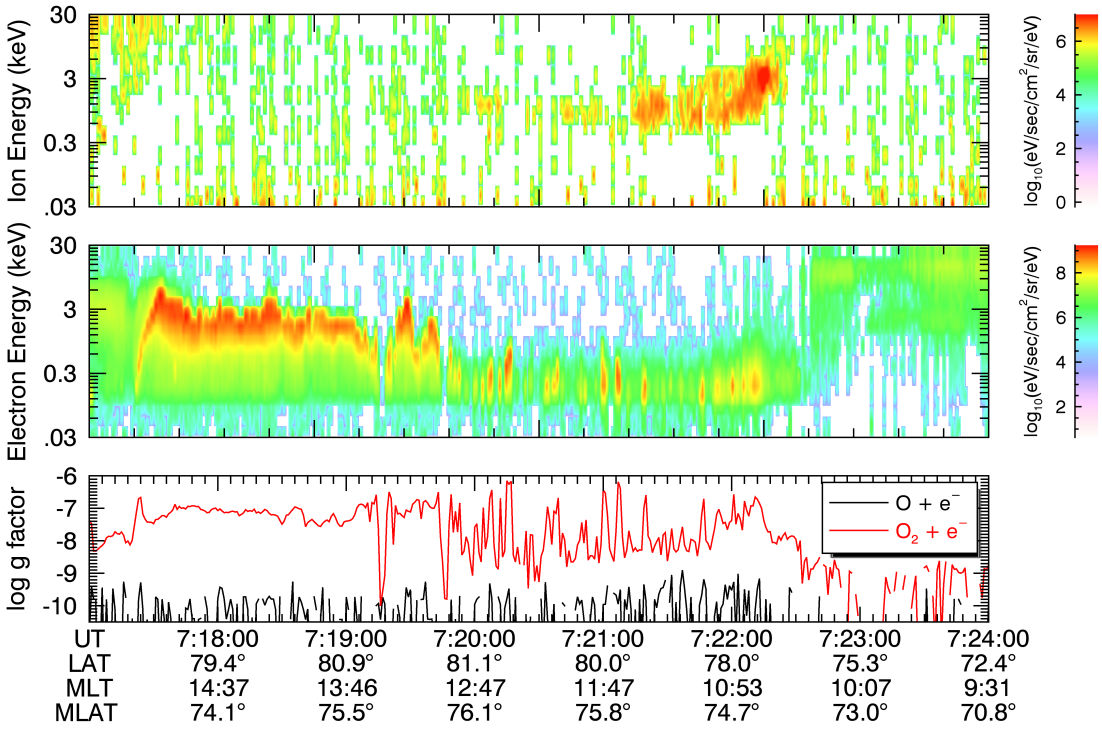

Figure 6-14: Differential ion (Top Panel) and electron (Middle Panel) energy flux spectra from the DMSP F19 SSJ5 instrument from 0717 UT to 0724 UT on 13 December 2015 ($\sim$ 20 min. before RENU 2); Bottom Panel: Excitation rate factor (g_O) calculated for the O + e^- $\rightarrow$ O* mechanism based on the electron energy flux

The instrument FOV is 4° $\times$ 90° and is oriented to cover 90° from the RAM direction to zenith. Telemetry constraints require that counts are summed across all six look directions within the FOV once per second.

Differential ion flux measured by the SSJ5 instrument on DMSP F17 and F18 is shown in Figure 6-13. The stepped ion signature apparent in both data sets is a classic signature of the cusp [Farrugia et al., 1998]. The discrete energy cutoffs in differential energy flux result from discrete plasma injections near the subsolar magnetopause, likely due to reconnection on the dayside.

Both plots in Figure 6-13 are plotted on the same time scale and color scale to allow for a direct comparison. The F17 SSJ5 instrument measured much higher flux levels than F18 during its cusp transit, which is most likely a spatial difference, not temporal, due

to the close proximity in time. The F17 spacecraft passed directly over Svalbard, which places it directly in the heart of the cusp energy flux as illustrated by the average of ASI data in Figure 6-11. The F18 spacecraft passed slightly east of Svalbard, almost directly in line with the RENU 2 trajectory, which provides additional confidence that the RENU 2 payload passed through the cusp.

SSJ5 ion and electron measurements from the DMSP F19 spacecraft are both shown in Figure 6-14. The SSJ5 electron measurement is analogous to the RENU 2 EPLAS electron flux shown in Figure 6-7, though this measurement was made $\sim$ 20 minutes *prior* to the RENU 2 cusp transit.

The F19 transit of the cusp occurred between two PMAFs shown in Figure 6-4, at approximately 0721 UT. The differential ion energy flux shown in Figure 6-13 demonstrates the stepped ion signature as a useful proxy for a cusp transit. The top panel in Figure 6-14 shows the same stepped ion signature to illustrate when the spacecraft transited the cusp. The differential electron energy flux distribution between 0720 UT and 0722 UT is significantly lower than that measured by EPLAS on RENU 2, particularly at low energy levels. The low level of soft precipitation agrees with the lack of PMAF activity at the time of transit.

The g-factors, shown in the bottom panel of Figure 6-14, were calculated using the differential energy flux in the top panel. The excitation rate due to the $O + e^- \rightarrow O^*$ mechanism is two orders of magnitude less than the rate factor determined from the RENU 2 measurements. This is due to a significant lack of flux at energies below 100 eV, where the energization cross section, σ_O, peaks. The excitation rate due to the $O_2 + e^- \rightarrow O^*$ mechanism is also much lower then the level detected by RENU 2, but shows slightly more consistency than the atomic oxygen factor.

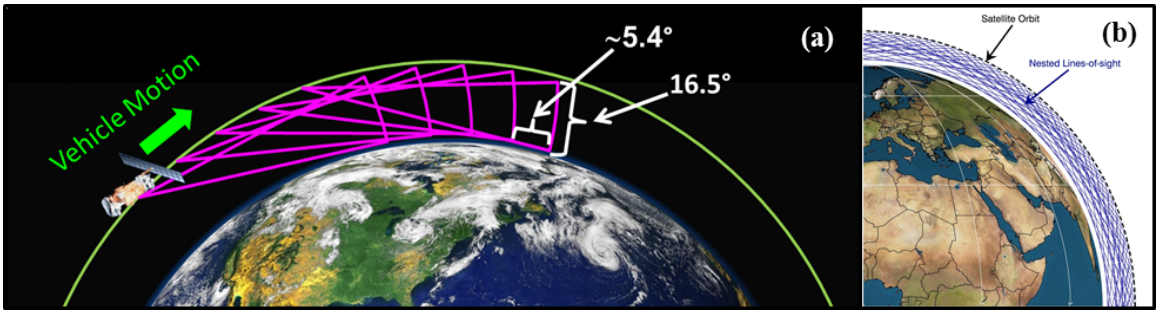

Figure 6-15: Panel (a): cartoon of the SSULI observing geometry ahead of the spacecraft along the orbit plane; Panel (b): illustration of nested lines-of-sight in the region beneath the DMSP orbit (Figure provided by K. Dymond, NRL)

6.4.4 DMSP SSULI

DMSP F19 passed through the cusp at $\sim$ 0721 UT, 13 minutes prior to the RENU 2 launch, and 20 minutes prior to apogee. F19 carried the Special Sensor Ultraviolet Limb Imager (SSULI), a UV spectrograph for imaging the Earth's limb ahead of the spacecraft along the orbit plane [McCoy et al., 1994; Dymond et al., 2017b]. A rotating mirror scans the limb from 100 km to $\sim$ 740 km tangent height with 10-15 km spatial resolution. A full vertical scan is acquired every 92 seconds at 5.4° phase spacing along the orbit plane. Figure 6-15 illustrates the geometry of the instrument field of view and the scan geometry.

SSULI observes the 800-1700 Å spectral range once per second at 16 Å resolution. A selection of emission lines detected by the instrument is listed in Table 6.3. Emission rates of the 1356 Å spectral line were acquired from the DMSP F19 spacecraft. Tomographic reconstruction of observations throughout the oversampled region will be discussed in the Section 6.5.

6.5 Analysis

The RENU 2 and supporting measurements provided a comprehensive picture of the cusp. The DMSP UV instruments provided such a complementary set of observations that they

merited further analysis on their own. Optical measurements of a diffuse source like the ionosphere are an integrated, line of sight intensity of a volume of emitters, each of which has its own volumetric emission rate (VER), ε.

$$4\pi I = 10^{-6} \int_0^\infty \varepsilon(z,\theta)\, ds(z,\theta) \tag{6.2}$$

Intensity, I, is integrated over the entire line of sight, the constant, 10^{-6}, converts the brightness to Rayleighs (R) and the 4π factor accounts for the steradians over which a set volume emits photons. The set of SSULI intensity measurements were used to solve for $\varepsilon(z,\theta)$ as a function of the altitude (z) and orbital phase (θ). The analysis began with 1356 Å observations by DMSP UV instruments.

The Volume Emission Rate Tomography (VERT) technique [Dymond et al., 2017a] was used to discretize the set of SSULI intensity measurements per Equation 6.2 to solve for $\varepsilon_{1356}(z,\theta)$. The tomographic technique is based on Image Space Reconstruction Algorithms (ISRAs), which require no prior information that may introduce biases into the solution. Solutions are driven optimally by data with additional weight given to measurements with a higher signal-to-noise ratio. Details of the inversion process are covered in Appendix A.

The VERT technique produces a two dimensional map of $\varepsilon_{1356}(z,\theta)$ in the altitude/orbit phase plane as shown in Figure 6-16. DMSP F19 emerged over the polar cap as it increased in orbit phase (left to right in the plot) moving equatorward as it passed through the cusp region. Vertical white lines in the figure represent the geodetic latitude of the DMSP F19 footprint. The solid yellow arc represents the trajectory of the RENU 2 payload as a function of latitude and altitude, with flight time marked by yellow circles along the trajectory every 50 seconds relative to launch at 0734 UT. The RENU 2 payload trajectory moved from right to left in Figure 6-16, opposite the direction of DMSP.

Between 60° and 75° orbit phase a feature in the volume emission rate is visible at

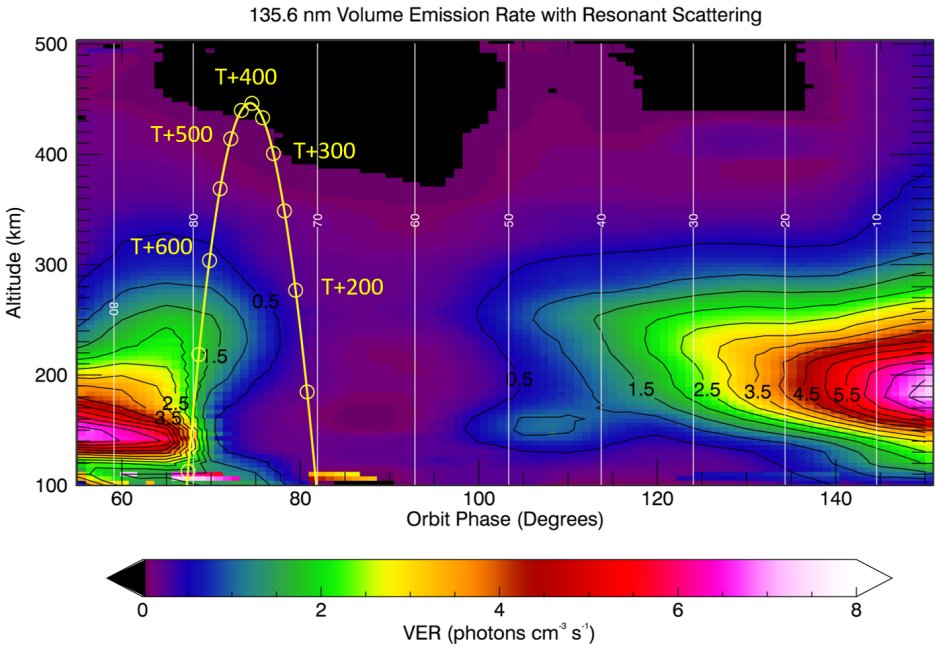

Figure 6-16: VERT reconstruction of the volumetric emission rate (VER) using DMSP SSULI data prior to correction for radiation transport effects. Vertical white lines indicate geographic latitude. RENU 2 trajectory is shown by the yellow arc with times along the trajectory marked in seconds after launch at 0734 UT.

$\sim$ 250 km altitude. This is likely due to soft electron precipitation in the cusp, a quantifiable effect with SSJ5 electron measurements. The map of ε_{1356} was produced from data acquired $\sim$ 20 minutes prior to RENU 2, but a comparison between the two is illustrative regardless. The RENU 2 UV PMT measured no signal until just after 0743 UT (T+540 sec). According to Figure 6-16, the payload passed through very little emission structure until T+550, which shows agreement between the UV PMT and the SSULI emission map.

The PMT signal began to rise as the payload dropped through the region of enhanced emission, which agrees in principle with the trajectory overlaid on the SSULI plot. The rise in signal indicates a rise in activity at altitudes above $\sim$ 250 km. Typically the bulk of energy is deposited at 250 km, so an enhancement in the signal above that altitude implies the presence of an unexpected additional population.

The PMT signal peaks near 7:44:30 UT (T+630), when the payload was at $\sim$ 250 km altitude, which supports the notion of the bulk of soft precipitation depositing its energy there. The PMT signal drops as the payload descends to lower altitudes, however, which is where the comparison breaks down. There is no measurement of the high emission rates at $\sim$ 150 km in what would appear to be the polar cap if considering only latitude. The PMT signal drops down to zero before the payload reaches altitudes where the emission lines are lost to absorption. Instead the RENU 2 payload is believed to have moved poleward out from underneath the region of enhanced emission.

Inspection of the SSUSI images in Figure 6-12, suggests that the bright emissions at 150 km may be the dawn sector of the auroral oval. The energetic electron flux measured by SSJ5 (Figure 6-14) supports this assumption. Figure 6-9 shows the trajectories of DMSP F19 and RENU 2 do not exactly align. The intersection between the two occurs closer to 75° Latitude and the orbits are not aligned in longitude. The RENU 2 trajectory is directed poleward relative to the F19 trajectory, away from the low altitude emission, which is why the low altitude emission does not appear in the PMT signal.

The goal of the tomographic reconstruction is to infer two-dimensional structure in thermospheric density. In order to do so, the VER calculation must account for several factors that complicate the inversion. The first correction is to account for radiation transport and transfer effects due to resonant scattering and pure absorption in the thermosphere. Photons created in the thermosphere undergo multiple resonant scattering, which affects both the distribution of photon flux and the observation of that flux. The optical depth for scattering (τ) and absorption (t) are calculated based on the density of species between the source and observer, n_s, and the scattering cross section for the mechanism, σ.

$$\tau(z) = \sigma^s \int_z^\infty n_{\mathrm{O}}(z')dz' \qquad \text{and} \qquad t(z) = \sigma^a \int_z^\infty n_{\mathrm{O}_2}(z')dz'$$

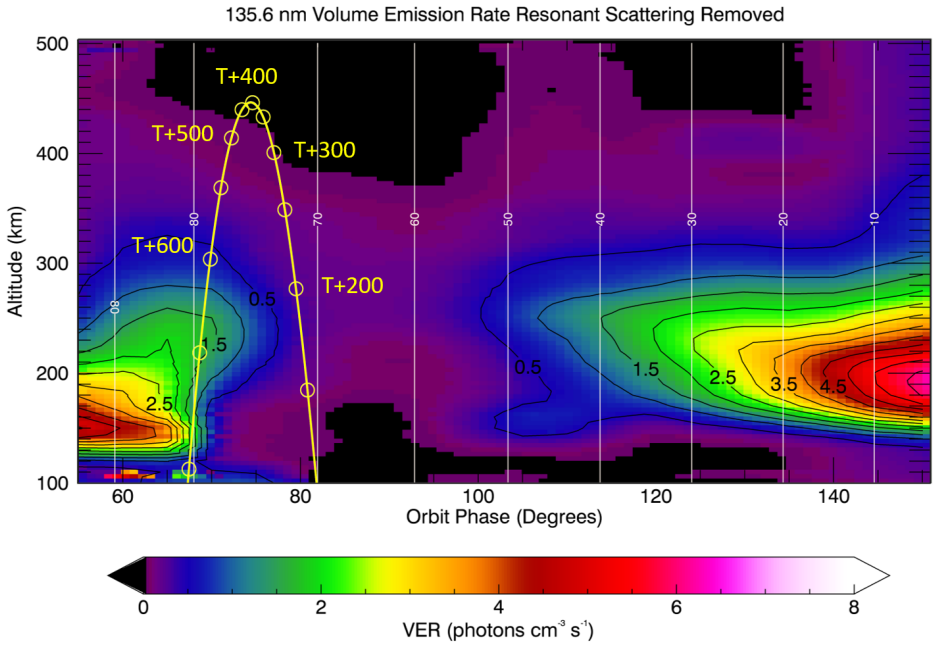

Figure 6-17: VERT reconstruction of the volumetric emission rate (VER) using DMSP SSULI data with radiation transport effects removed. Vertical white lines indicate geographic latitude. RENU 2 trajectory is shown by the yellow arc with times along the trajectory marked in seconds after launch at 0734 UT.

The OI 1356 Å spectral line is technically a doublet, with wavelengths at 1356 Å and 1358 Å, and both lines are resonantly scattered by atomic oxygen and absorbed by molecular oxygen. Line-center scattering cross-sections are $\sigma^s_{1356} = 2.499 \times 10^{-18}$ cm^2 and $\sigma^s_{1358} = 1.242 \times 10^{-18}$ cm^2 [Meier, 1991]. The absorption cross-sections are $\sigma^a_{1356} = 7.20 \times 10^{-18}$ cm^2 and $\sigma^a_{1358} = 7.15 \times 10^{-18}$ cm^2 [Wang et al., 1987]. All other factors being equal, the optical depth for the 1356 Å emission is approximately twice the optical depth at 1358 Å, whereas the absorption rates are roughly the same. The scattering optical depth of 1356 Å photons integrated from infinity to the altitude where the n_O peaks (∼105 km) approaches ∼1.

The effects of scattering have been calculated and subtracted from the initial VER map, and the results are shown in Figure 6-17. The layout is the same as the previous figure, with the RENU 2 trajectory plotted as a function of latitude and altitude and times marked

by yellow circles as seconds after launch.

Rates for VER are slightly reduced across the reconstruction with the scattering effects removed, but the overall structure is very similar. With scattering effects removed, the map is less of a direct comparison to the RENU 2 measurement because scattering effects have not been removed from the PMT signal.

A multitude of mechanisms will produce excited oxygen atoms in the ^{5}S state, and in the thermosphere those mechanisms vary depending on the altitude (z) and latitude (θ). The ideal volume emission rate, $\varepsilon_{1356}(z,\theta)$, would account for all possible excitation mechanisms responsible for creating 1356 Å photons.

$$\varepsilon_{1356}(z,\theta) = g_O(z,\theta)\, n_O(z,\theta) + g_{O_2}(z,\theta)\, n_{O_2}(z,\theta) + \alpha\, n_e(z,\theta)\, n_{O^+}(z,\theta) + ... \tag{6.3}$$

Individual terms in the total ε_{1356} are the product of the number density of potential source emitters (e.g. n_O) and an associated excitation reaction rate (e.g. g_O). The dominant photoproduction mechanisms for the SSULI observations are assumed to be collisional excitation of atomic oxygen and dissociative excitation of O_2, both as a result of soft electron precipitation.

$$\varepsilon_{1356}(z,\theta) = g_O(z,\theta)\, n_O(z,\theta) + g_{O_2}(z,\theta)\, n_{O_2}(z,\theta) \tag{6.4}$$

Notably, initial calculations do not include photoelectron impact or resonant excitation due to solar illumination, which are typically the dominant driver on the dayside. The cusp is a dayside feature, and according to Figure 6-6 the RENU 2 payload was sunlit during its trajectory. However, the terminator is at least 100 km higher for UV light than it is for visible light due to atmospheric absorption in layers below the thermosphere. This assumption is justified in part by the dropout in VER in Figure 6-17 between the cusp

latitudes and mid latitudes that are sunlit.

Future iterations of the tomographic reconstruction will use the g factor calculated from DMSP F19 electron flux (Equation 6.1, Figure 6-14) to simulate the emission due to cusp precipitation in a modeled background thermosphere from the NRLMSISE-00 empirical model. The background thermosphere can be scaled appropriately using the measurement by GRACE to account for global variation in overall density. The simulated emission map will then be compared to the SSULI inversion to look for significant differences that may be due to a mass enhancement.

The density map produced by the SSULI inversion will only be high enough resolution to resolve the broad trend in the PMT data, likely due to O I 1304 Å. The smaller scale features in the data are too fine in spatial context to be resolved by the SSULI measurements.

6.6 Conclusions

An comprehensive set of observations by the RENU 2 sounding rocket mission, along with supporting ground-based and space-based observations, have provided an uprecedented view of neutral upwelling in the cusp. Multiple environmental monitors indicated that a cusp anomaly, or thermospheric neutral upwelling event, was present for as long as 30 minutes and the RENU 2 measurements agreed with that prediction. Tomographic imaging with DMSP SSULI data provide a critical perspective on structure in the cusp. There are several key takeaways from the analysis in the present study.

1. GRACE did not observe a large cusp anomaly prior to RENU 2, although supporting observations suggest that the near-threshold value is indicative of a grazing coincidence. This highlights the transient nature of the cusp and is a point to keep in mind when considering statistical studies of the cusp anomaly from orbital spacecraft.

2. The RENU 2 UV PMT observed a strong enhancement in the cusp colocated with the small density bump measured by GRACE. A sharp dropout in signal prior to reaching significant optical depths suggests the payload passed horizontally out from under an emission structure in the cusp.

3. Tomographic reconstruction of SSULI measurements reveal two-dimensional structure of UV emission in the cusp during a suspected density enhancement. The map of volumetric emission rate provides critical context for understanding the structure of the RENU 2 UV PMT. Inversion of the SSULI emission rate into a thermospheric density will provide the first two-dimensional observation of neutral structure in the cusp as a function of altitude.

The RENU 2 payload provided a comprehensive data set for examining the potential drivers of neutral upwelling. Magnetic fields, electric fields, electron flux, ion flux, and neutral particle measurements that all vary both in latitude and altitude during the cusp transitl provide a thorough look at conditions that can serve as the benchmark for thermospheric models to simulate.

Acknowledgements: The authors would like to acknowledge D.J. McComas (SWRI) and the ACE SWEPAM team for density/velocity data, N. Ness (Bartol Research Institute) and the ACE MAG team for IMF data (Data provided by NASA OMNI Service at GSFC/CDAWeb). ASI data was graciously provided by Jøran Moen and Lasse Clausen at the University of Oslo. EISCAT is an international association supported by research organisations in China (CRIRP), Finland (SA), Japan (NIPR and STEL), Norway (NFR), Sweden (VR), and the United Kingdom (NERC), and the RENU 2 team is grateful to the EISCAT staff for excellent support during the RENU 2 rocket campaign. Eric Sutton (AFRL/RV) provided GRACE data. The DMSP SSJ5 particle detectors were designed by Dave Hardy of AFRL, and data obtained from JHU/APL. Dr. Larry Paxton (JHU/APL) provided SSUSI data and assistance in interpreting it. Finally, many thanks to Dr. Ken Dymond (NRL) for providing the SSULI data and tomographic reconstruction.

Chapter 7

Conclusions

Fine-scale structure plays an important role in the ionosphere and can be used to learn new information about a whole host of ionospheric processes. Fine scale features are sometimes indicators of larger geophysical phenomena, or sometimes as an indicator that an otherwise unobserved event has taken place. This dissertation has presented three separate studies that have addressed challenges in either observing or interpreting fine-scale structure in the ionosphere.

Chapter 4 showed how fine-scale black aurora may be an indicator of how pulsating aurora interacts with the ionosphere. Morphological behavior of black aurora as it relates to pulsating aurora was investigated by examining a collection of ground-based observations from January 2007 in support of the ROPA rocket campaign. The primary observations of black aurora recorded during the substorm recovery phase were between separate patches of pulsating aurora as well as pulsating aurora separated from diffuse aurora. The black aurora formed an apparent firm boundary between the auroral forms in a new behavior that is in contrast with previously reported observations. Also presented for the first time were black curls in conjunction with pulsating aurora. Curl structures that indicate shear plasma flows in the ionosphere may be used as a proxy for converging/diverging electric fields in and above the ionosphere. This new subset of black auroral behavior provided visual evidence of black aurora as an ionospheric feedback mechanism as related to pulsating aurora.

Chapter 5 showed how an unexplained, fine-scale spectral feature in the Extremely Low Frequency (ELF) range depends on a large-scale driver like solar illumination. Narrow bandwidth, whistler-like spectral features in the extremely-low frequency (ELF) range were recorded at South Pole Station over the duration of 2004. A full year of observation showed a distinct lack of activity over the Antarctic winter season. Calculation of solar zenith angle at the time of detection illustrated a connection between the occurrence of ELF whistlers and a sunlit ionosphere. ELF whistlers detected at low latitude followed a similar general trend between ELF whistler occurrence rate and changing solar zenith angle, but with an additional persistence of detections after local sunset. Temporal profiles from the International Reference Ionosphere 2016 show that the peaks in ELF whistler occurrence aligned with times of changing ionospheric composition. Correlation with solar activity per the $F_{10.7}$ index showed no connection to daily variations in activity, and the consistency of solar flux levels throughout 2004 appeared insufficient to explain the absence of events during the winter blackout.

The ELF observations placed new physical constraints on the conditions necessary for detecting ELF whistlers, and suggest the potential for localized generating mechanisms due to plasma instabilities in the ionosphere. The cause of the whistlers is still unknown but placing further constraints on their behavior relative to other physical phenomena will help to determine a root cause. Sources of free energy in the ionosphere that are well known consequences of common occurrences like solar photoionization may be responsible for instabilities that lead to the whistlers.

Chapter 6 showed the value of multi-scale observations in attempting to understand fine-scale structure in the ionosphere and thermosphere. The variable nature of the cusp and its dependence on external factors, like the IMF orientation, makes characterization a challenging task. The input of energy to the cusp varies on relatively short time scales and

is fine-scale in spatial extent, often much smaller than can be captured by any reasonable global simulation. The in situ GRACE neutral density measurement showed that a relative density "bump," one that would not otherwise satisfy the criteria for a large-scale statistical survey, may have only been the result of a transient cusp location.

Two dimensional structure in the thermosphere that had been hinted at by separate spacecraft observations was observed for the first time from multiple perspectives during the same event. The RENU 2 UV PMT measurement, which carries information about both latitudine and altitude structure provides further evidence that fine-scale structure plays an important role in understanding the physics of the cusp anomaly. Emission structure provided by the DMSP SSULI and SSUSI measurements provided critical context for interpreting the RENU 2 UV PMT measurements. Isolated interpretation of the UV PMT data included too many variables to make any substantive claims on its own merits. SSUSI measurements provided some context for overall structure. The tomographic reconstruction of DMSP SSULI measurements provided the first two-dimensional perspective of emission structure in the cusp as a function of latitude and altitude. This study highlights not only a new technique for examining structure at high latitudes, it also illuminates the vertical variation in cusp density that had been inferred from separate spacecraft measurements.

Ionospheric physics is inherently a multi-scale discipline, as changes occur on yearly, daily, or hourly timescales, depending on the mechanism involved. Fine-scale features may be used as an indicator of ionospheric processes that are difficult to measure in situ, as with the black aurora example. Fine-scale structure may also be an indicator of physical processes within large scale behavior that had been previously overlooked, as with the ELF whistlers and the suggested connection with instabilities in the ionosphere. Finally, multi-scale observations have been shown to be crucial for understanding fine-scale structure that is the result of multiple larger processes combined in not yet understood ways.

Appendices

Appendix A

Tomographic inversion

Tomographic inversion of SSULI observations was performed in the method described in detail by Dymond et al. [2017a]. The desired result is a two-dimensional reconstruction of volume emission rate, ε based on an overlapping set of line-of-sight intensity measurements.

$$4\pi I = 10^{-6} \int_0^\infty \varepsilon(z,\theta)\, ds(z,\theta) \tag{A.1}$$

The set of overlapping, line-of-sight SSULI intensity measurements can be tomographically inverted to provide a 2-D picture of the volume emission rate structure. Each spectrum is de-convolved using a variant of the Richardson-Lucy algorithm [Dymond et al., 2017a]. In order to solve the matrix of equations for the tomographic reconstruction, the integral equation for the 1356 Å brightness is discretized into voxels over which ε is assumed constant.

$$4\pi I = 10^{-6} \sum_i \varepsilon(z,\theta)\Delta s_i(z,\theta)$$

The path length through the i^{th} voxel is the differential path length along the line of sight, Δs_i. Photons are redistributed horizontally and vertically after initial creation by multiple resonant scattering with oxygen atoms and absorption by molecular oxygen. Photons at 1356 Å are created by the spontaneous emission of a spin-forbidden transition, where excited oxygen atoms in the ^{5}S orbital excited state decay to the ^{3}P ground state. This spectral line is technically a doublet, with wavelengths at 1356 Å and 1358 Å, but for simplicity of notation the doublet will typically be referred to as only 1356 Å.

$$\mathrm{O}^*\ (^5\mathrm{S}) \rightarrow \mathrm{O}\ (^3\mathrm{P}) + h\nu\ (1356\ \text{Å})$$

The plane-parallel approximation assumes the horizontal density gradients are much lower than the vertical density gradients, so most of the redistribution is vertical. The optical depth for scattering (τ) and absorption (t) are calculated based on the density of species between the source and observer, n_s, and the scattering cross section for the mechanism, σ.

$$\tau(z) = \sigma^s \int_z^\infty n_{\mathrm{O}}(z')dz' \qquad \text{and} \qquad t(z) = \sigma^a \int_z^\infty n_{\mathrm{O_2}}(z')dz'$$

Line-center scattering cross-sections are $\sigma^s_{1356} = 2.499 \times 10^{-18}$ cm^2 and $\sigma^s_{1358} = 1.242 \times 10^{-18}$ cm^2 [Meier, 1991]. The absorption cross-sections are $\sigma^a_{1356} = 7.20 \times 10^{-18}$ cm^2 and $\sigma^a_{1358} = 7.15 \times 10^{-18}$ cm^2 [Wang et al., 1987]. All other factors being equal, the optical

depth for O I 1356 Å is approximately twice the optical depth as O I 1358 Å, whereas the absorption rates are roughly the same. Photons are absorbed by molecular oxygen in the Schumann-Runge continuum [Meier, 1991].

The scattering optical depth of 1356 Å photons integrated from infinity to the altitude where the n_O peaks (∼105 km) approaches ∼1. This permits the use of the computationally fast Complete Frequency Redistribution Approximation [Meier, 1991; Dymond et al., 1997]. Radiation transport is first added to Equation A.1.

$$I_{1356} = 10^{-6} \sum \int_0^\infty T\left(|\tau(s) - \tau(0)|, |t(s) - t(0)|\right) \varepsilon\left(z(s), \theta(s)\right) ds \tag{A.2}$$

The summation is carried out over both lines in the doublet because the SSULI spectrograph cannot resolve them individually. The intensity is represented in Rayleighs (R), and the 10^{-6} factor converts from photon flux to R. Equation A.2 is an example of a Fredholm integral equation of the first kind. $T(|\tau(s) - \tau(0)|, |t(s) - t(0)|)$ is the Holstein transmission function, or T-function [Holstein, 1947].

$$T(\tau, t) = \frac{1}{\sqrt{\pi}} \int_{-\infty}^{\infty} e^{-x^2} \exp -\tau e^{-x^2} + t dx$$

Integration is carried out over all photon frequencies, x which are represented in "Doppler units," $x = (\nu - \nu_0)/\sigma_D\sqrt{2}$. A Doppler-broadened line profile is centered at frequency, ν_0, with line center optical depth, τ_0. σ_D is characteristic of the Doppler profile. $\sigma_D = (\nu_0/c)(kT/m)^{-1/2}$. Densities of O, N_2, and O_2 needed for the transport calculations are generated using NRLMSIS-00 [Picone et al., 2002] over the latitude/altitude grid.

The volume emission rate is assumed to vary bi-cubically and use bi-cubic splines to discretize the integrals, which results in a smoother solution for the volume emission rate field and improves the reconstruction accuracy. The Volume Emission Rate Tomography (VERT) technique [Dymond et al., 2017a] is used to solve Equation A.2 to produce a 2D distribution of photon emission in a latitude/altitude plane that crosses the orbital plane at the equator.

$$I_{1356} = 10^{-6} \sum W_i \, G_i \, \varepsilon(z_i, \phi_i) \, T(|\tau(s_i) - \tau(0)|, |t(s_i) - t(0)|) \Delta s_i \tag{A.3}$$

The total path length, s_i is measured from the observer to the i^{th} point in the line-of-sight. G_i is the quadrature weight and W_i is the bi-cubic spline weighting. Equation A.3 is solved by the Least-Squares Positive Definite (LSPD) algorithm, a fast non-negative iteration based on Gaussian statistics, necessary due to photon shot or Poisson noise in SSULI measurements. The VERT approach uses a physicality constraint applied between iterations to smooth or regularize the solution to the isotropic diffusion equation between steps [Dymond et al., 2017a]. The approach was validated using SSULI measurements at 911 Å and ALTAIR electron densities [Dymond et al., 2017b].

Inversion of the intensity measurements produces a grid of ε with radiation transport included. The effects of radiation transport are then modeled for removal from the ε grid using the integral version of the photon transport equation.

$$\varepsilon(z) = \varepsilon_0(z) + n_O(z) \, \sigma \int_{z_{min}}^{z_{max}} \varepsilon(z') H\left(|\tau(z) - \tau(z')|, |t(z) - t(z')|\right) dz' \tag{A.4}$$

The initial volume emission rate (VER), ε_0 is modified by the photon transport integral,

once again assuming the complete frequency redistribution approximation method holds. The integral is typically bounded between $z_{min} = 90$ km and $z_{max} = 1000$ km in altitude. The Holstein function (H) represents the probability that a photon originating at altitude z' reaches altitude z, integrated over the entire plane perpendicular to z.

$$H(\tau, t) = \frac{1}{2\sqrt{\pi}} \int e^{-2x^2} E_1(\tau \epsilon^{-x^2} + t) dx$$

The function, E_1, is an exponential integral function of the first kind. Equation A.4 is a Fredholm integral equation of the first kind. The equation is typically solved by discretization in z and then assuming that the volume emission rate is approximately constant over the z layers and evaluation of the integrals of the Holstein function over the layers. This procedure results in a system of equations that is solved by matrix inversion, producing a new grid of initial VER, ε_0. The emission rate is a function of oxygen density in the thermosphere, which varies in altitude, z, and latitude, θ.

$$\varepsilon_{1356}(z, \theta) = g_O(z, \theta)\, n_O(z, \theta) + g_{O_2}(z, \theta)\, n_{O_2}(z, \theta) \tag{A.5}$$

The excitation coefficient, $g_O(z, \theta)$, also known as the g-factor is associated with a specific excitation mechanism and is determined according to which mechanism is responsible for the excitation. For electron collisions with the particles, it depends on the excitation cross-section, σ, and the electron flux, ϕ.

$$g_O(z, \theta) = \int_0^\infty \sigma_O(E)\ \phi(E, z, \theta) dE \tag{A.6}$$

Equation A.5 is solved using a Newton-Raphson iteration [Press et al., 1992] to determine the oxygen densities that are given by the ε_0 grid, which can then be compared to the NRLMSISE-00 model output. The radiation transport process starts with O and O_2 densities, which requires iteration of this process until convergence using the newly inferred O and O_2 densities to model the radiation transport effects and g-factors.

Bibliography

S.I. Akasofu. *Polar and Magnetospheric Substorms*. Astrophysics and Space Science Library. Springer Netherlands, 1968. ISBN 9789401034616. doi: 10.1007/978-94-010-3461-6.

Phillip C. Anderson and Jessica M. Hawkins. Topside ionospheric response to solar euv variability. *Journal of Geophysical Research: Space Physics*, 121 (2):1518–1529, 2016. ISSN 2169-9402. doi: 10.1002/2015JA021202. URL http://dx.doi.org/10.1002/2015JA021202. 2015JA021202.

Edward V Appleton and MAF Barnett. On some direct evidence for downward atmospheric reflection of electric rays. *Proc. R. Soc. Lond. A*, 109(752):621–641, 1925.

J. Archer, H. Dahlgren, N. Ivchenko, B. S. Lanchester, and G. T. Marklund. Dynamics and characteristics of black aurora as observed by high-resolution ground-based imagers and radar. *International Journal of Remote Sensing*, 32(11):2973–2985, 2011. doi: 10.1080/01431161.2010.541517. URL http://dx.doi.org/10.1080/01431161.2010.541517.

G. Atkinson. Auroral arcs: Result of the interaction of a dynamic magnetosphere with the ionosphere. *Journal of Geophysical Research*, 75(25):4746–4755, 1970. ISSN 2156-2202. doi: 10.1029/JA075i025p04746. URL http://dx.doi.org/10.1029/JA075i025p04746.

W. Baumjohann and R.A. Treumann. *Basic Space Plasma Physics*. Imperial College Press, 2012. ISBN 9781848168947. URL http://books.google.com/books?id=zl4iLwEACAAJ.

Z. Bay. Electron-Multiplier as an Electron-Counting Device. *Nature*, 141:284, Feb 1938. doi: 10.1038/141284a0. URL https://www.nature.com/articles/1411011a0.

D. Bilitza and B.W. Reinisch. International reference ionosphere 2007: Improvements and new parameters. *Advances in Space Research*, 42(4):599 – 609, 2008. ISSN 0273-1177. doi: 10.1016/j.asr.2007.07.048. URL https://doi.org/10.1016/j.asr.2007.07.048.

D. Bilitza, D. Altadill, V. Truhlik, V. Shubin, I. Galkin, B. Reinisch, and X. Huang. International reference ionosphere 2016: From ionospheric climate to real-time weather predictions. *Space Weather*, 15(2):418–429, 2017. ISSN 1542-7390. doi: 10.1002/2016SW001593. URL http://dx.doi.org/10.1002/2016SW001593. 2016SW001593.

L. M. Bjoland, V. Belyey, U. P. Løvhaug, and C. La Hoz. An evaluation of international reference ionosphere electron density in the polar cap and cusp using eiscat svalbard radar measurements. *Annales Geophysicae*, 34(9):751–758, 2016. doi: 10.5194/angeo-34-751-2016. URL https://www.ann-geophys.net/34/751/2016/.

E. M. Blixt, M. J. Kosch, and J. Semeter. Relative drift between black aurora and the ionospheric plasma. *Annales Geophysicae*, 23(5):1611–1621, July 2005. URL https://hal.archives-ouvertes.fr/hal-00317814.

HG Booker and HW Wells. Scattering of radio waves by the f-region of the ionosphere. *Journal of Geophysical Research*, 43(3):249–256, 1938.

J. Bortnik, U. S. Inan, and T. F. Bell. L dependence of energetic electron precipitation driven by magnetospherically reflecting whistler waves. *Journal of Geophysical Research: Space Physics*, 107(A8):SMP 1–1–SMP 1–13, 2002. doi: 10.1029/2001JA000303. URL https://doi.org/10.1029/2001JA000303.

Robert P. Breault. Problems and techniques in stray radiation suppression, 1977. URL http://dx.doi.org/10.1117/12.964591.

A. Brekke, J. R. Doupnik, and P. M. Banks. Incoherent scatter measurements of e region conductivities and currents in the auroral zone. *Journal of Geophysical Research*, 79(25):3773–3790, 1974. doi: 10.1029/JA079i025p03773. URL https://doi.org/10.1029/JA079i025p03773.

Douglas G. Brinkman, Richard L. Walterscheid, James H. Clemmons, and James. H. Hecht. High-resolution modeling of the cusp density anomaly: Response to particle and joule heating under typical conditions. *Journal of Geophysical Research: Space Physics*, 121(3):2645–2661, 2016. ISSN 2169-9402. doi: 10.1002/2015JA021658. URL http://dx.doi.org/10.1002/2015JA021658. 2015JA021658.

N. B. Brown, T. N. Davis, T. J. Hallinan, and H. C. Stenbaek-Nielsen. altitude of pulsating aurora determined by a new instrumental technique. *Geophysical Research Letters*, 3(7):403–404, 1976. ISSN 1944-8007. doi: 10.1029/GL003i007p00403. URL http://dx.doi.org/10.1029/GL003i007p00403.

E. J. Bucsela. *Two Daytime Observations of Atomic Nitrogen Emissions in the Thermosphere.* PhD thesis, THE UNIVERSITY OF MICHIGAN., 1994.

O. Buneman. Excitation of field aligned sound waves by electron streams. *Phys. Rev. Lett.*, 10:285–287, Apr 1963. doi: 10.1103/PhysRevLett.10.285. URL https://link.aps.org/doi/10.1103/PhysRevLett.10.285.

S Chapman. The absorption and dissociative or ionizing effect of monochromatic radiation in an atmosphere on a rotating earth. *Proceedings of the Physical Society*, 43(1):26, 1931. doi: 10.1088/0959-5309/43/1/305. URL https://doi.org/10.1088/0959-5309/43/1/305.

C. C. Chaston and K. Seki. Smallscale auroral current sheet structuring. *Journal of Geophysical Research: Space Physics*, 115(A11), 2010. doi: 10.1029/2010JA015536. URL https://doi.org/10.1029/2010JA015536.

C. C. Chaston, J. W. Bonnell, C. W. Carlson, J. P. McFadden, R. E. Ergun, and R. J. Strangeway. Properties of small-scale alfvn waves and accelerated electrons from fast. *Journal of Geophysical Research: Space Physics*, 108(A4):n/a–n/a, 2003. ISSN 2156-2202. doi: 10.1029/2002JA009420. URL http://dx.doi.org/10.1029/2002JA009420. 8003.

J. H. Clemmons, J. H. Hecht, D. R. Salem, and D. J. Strickland. Thermospheric density in the earth's magnetic cusp as observed by the streak mission. *Geophysical Research Letters*, 35(24), 2008. ISSN 1944-8007. doi: 10.1029/2008GL035972. URL http://dx.doi.org/10.1029/2008GL035972. L24103.

E.W. Cliver. The 1859 space weather event: Then and now. *Advances in Space Research*, 38(2):119 – 129, 2006. ISSN 0273-1177. doi: 10.1016/j.asr.2005.07.077. URL

https://doi.org/10.1016/j.asr.2005.07.077. The Great Historical Geomagnetic Storm of 1859: A Modern Look.

I. J. Cohen, M. R. Lessard, S. R. Kaeppler, S. R. Bounds, C. A. Kletzing, A. V. Streltsov, J. W. LaBelle, M. P. Dombrowski, S. L. Jones, R. F. Pfaff, D. E. Rowland, B. J. Anderson, H. Korth, and J. W. Gjerloev. Auroral current and electrodynamics structure (aces) observations of ionospheric feedback in the alfvén resonator and model responses. *Journal of Geophysical Research: Space Physics*, 118(6):3288–3296, 2013. ISSN 2169-9402. doi: 10.1002/jgra.50348. URL http://dx.doi.org/10.1002/jgra.50348.

I. J. Cohen, M. R. Lessard, R. H. Varney, K. Oksavik, M. Zettergren, and K. A. Lynch. Ion upflow dependence on ionospheric density and solar photoionization. *Journal of Geophysical Research: Space Physics*, 120(11):10039–10052, 2015. ISSN 2169-9402. doi: 10.1002/2015JA021523. URL http://dx.doi.org/10.1002/2015JA021523. 2015JA021523.

I. J. Cohen, M. Widholm, M. R. Lessard, P. Riley, J. Heavisides, J. I. Moen, L. B. N. Clausen, and T. A. Bekkeng. Rocket-borne measurements of electron temperature and density with the electron retarding potential analyzer instrument. *Journal of Geophysical Research: Space Physics*, 121(7):6774–6782, 2016. ISSN 2169-9402. doi: 10.1002/2016JA022562. URL http://dx.doi.org/10.1002/2016JA022562. 2016JA022562.

G. Crowley, B. A. Emery, R. G. Roble, H. C. Carlson, and D. J. Knipp. "thermospheric dynamics during september 1819, 1984: 1. model simulations"". *Journal of Geophysical Research: Space Physics*, 94(A12):16925–16944, 1989. ISSN 2156-2202. doi: 10.1029/JA094iA12p16925. URL http://dx.doi.org/10.1029/JA094iA12p16925.

G. Crowley, D. J. Knipp, K. A. Drake, J. Lei, E. Sutton, and H. Lhr. Thermospheric density enhancements in the dayside cusp region during strong by conditions. *Geophysical Research Letters*, 37(7), 2010. ISSN 1944-8007. doi: 10.1029/2009GL042143. URL http://dx.doi.org/10.1029/2009GL042143. L07110.

T. N. Davis. Observed microstructure of auroral forms. *Journal of Geomagnetism and Geoelectricity*, 30:371–380, 1978.

H.G. Demars and R.W. Schunk. Thermospheric response to ion heating in the dayside cusp. *Journal of Atmospheric and Solar-Terrestrial Physics*, 69(6): 649 – 660, 2007. ISSN 1364-6826. doi: 10.1016/j.jastp.2006.11.002. URL http://www.sciencedirect.com/science/article/pii/S1364682606003154.

Yue Deng, Timothy J. Fuller-Rowell, Aaron J. Ridley, Delores Knipp, and Ramon E. Lopez. Theoretical study: Influence of different energy sources on the cusp neutral density enhancement. *Journal of Geophysical Research: Space Physics*, 118(5):2340–2349, 2013. ISSN 2169-9402. doi: 10.1002/jgra.50197. URL http://dx.doi.org/10.1002/jgra.50197.

K. F. Dymond, S. E. Thonnard, R. P. McCoy, and R. J. Thomas. An optical remote sensing technique for determining nighttime f region electron density. *Radio Science*, 32(5):1985–1996, 1997. ISSN 1944-799X. doi: 10.1029/97RS01887. URL http://dx.doi.org/10.1029/97RS01887.

K. F. Dymond, S. A. Budzien, and M. A. Hei. Ionospheric-thermospheric uv tomography: 1. image space reconstruction algorithms. *Radio Science*, 52(3):338–356, 2017a. ISSN 1944-799X. doi: 10.1002/2015RS005869. URL http://dx.doi.org/10.1002/2015RS005869. 2015RS005869.

K. F. Dymond, A. C. Nicholas, S. A. Budzien, A. W. Stephan, C. Coker, M. A. Hei, and K. M. Groves. Ionospheric-thermospheric uv tomography: 2. comparison with incoherent scatter radar measurements. *Radio Science*, 52(3):357–366, 2017b. ISSN 1944-799X. doi: 10.1002/2015RS005873. URL http://dx.doi.org/10.1002/2015RS005873. 2015RS005873.

Y. Ebihara, T. Sakanoi, K. Asamura, M. Hirahara, and M. F. Thomsen. Reimei observation of highly structured auroras caused by nonaccelerated electrons. *Journal of Geophysical Research: Space Physics*, 115(A8), 2010. ISSN 2156-2202. doi: 10.1029/2009JA015009. URL http://dx.doi.org/10.1029/2009JA015009. A08320.

Armin T. Ellis, Marc R. Lessard, Paul Bartel, Mike Disbrow, and Paul Riley. Despun rocket borne imager: Design aspects of a space based optical imaging instrument for auroral studies. *Review of Scientific Instruments*, 77(4):045112, 2006. doi: 10.1063/1.2195102. URL https://doi.org/10.1063/1.2195102.

David S. Evans. The observations of a near monoenergetic flux of auroral electrons. *Journal of Geophysical Research*, 73(7):2315–2323, 1968. ISSN 2156-2202. doi: 10.1029/JA073i007p02315. URL http://dx.doi.org/10.1029/JA073i007p02315.

D. T. Farley. A plasma instability resulting in field-aligned irregularities in the ionosphere. *Journal of Geophysical Research*, 68(22):6083–6097, 1963. ISSN 2156-2202. doi: 10.1029/JZ068i022p06083. URL http://dx.doi.org/10.1029/JZ068i022p06083.

Charles J. Farrugia, Per Even Sandholt, William F. Denig, and Roy B. Torbert. Observation of a correspondence between poleward moving auroral forms and stepped cusp ion precipitation. *Journal of Geophysical Research: Space Physics*, 103(A5):9309–9315, 1998. doi: 10.1029/97JA02882. URL https://doi.org/10.1029/97JA02882.

Gerard J. Fasel. Dayside poleward moving auroral forms: A statistical study. *Journal of Geophysical Research: Space Physics*, 100(A7):11891–11905, 1995. doi: 10.1029/95JA00854. URL https://doi.org/10.1029/95JA00854.

L. A. Frank and K. L. Ackerson. Observations of charged particle precipitation into the auroral zone. *Journal of Geophysical Research*, 76(16):3612–3643, 1971. ISSN 2156-2202. doi: 10.1029/JA076i016p03612. URL http://dx.doi.org/10.1029/JA076i016p03612.

K. M. Frederick-Frost, K. A. Lynch, P. M. Kintner, E. Klatt, D. Lorentzen, J. Moen, Y. Ogawa, and M. Widholm. Sersio: Svalbard eiscat rocket study of ion outflows. *Journal of Geophysical Research: Space Physics*, 112(A8), 2007. ISSN 2156-2202. doi: 10.1029/2006JA011942. URL http://dx.doi.org/10.1029/2006JA011942. A08307.

Bruce A. Fritz, Marc L. Lessard, Matthew J. Blandin, and Philip A. Fernandes. Structure of black aurora associated with pulsating aurora. *Journal of Geophysical Research: Space Physics*, 120(11):10096–10106, 2015. ISSN 2169-9402. doi: 10.1002/2015JA021397. URL http://dx.doi.org/10.1002/2015JA021397. 2015JA021397.

R. Fujii, T. Oguti, and T. Yamamoto. Relationships between pulsating auroras and field-aligned electric currents. *National Institute Polar Research Memoirs*, 36:95, July 1985.

TJ Fuller-Rowell, D Rees, S Quegan, RJ Moffett, MV Codrescu, and GH Millward. A coupled thermosphere-ionosphere model (ctim). *STEP Report*, 239, 1996.

S. Peter Gary. The mirror and ion cyclotron anisotropy instabilities. *Journal of Geophysical Research: Space Physics*, 97(A6):8519–8529, 1992. ISSN 2156-2202. doi: 10.1029/92JA00299. URL http://dx.doi.org/10.1029/92JA00299.

Z. Girazian and P. Withers. An empirical model of the extreme ultraviolet solar spectrum as a function of f10.7. *Journal of Geophysical Research: Space Physics*, 120(8):6779–6794, 2015. ISSN 2169-9402. doi: 10.1002/2015JA021436. URL http://dx.doi.org/10.1002/2015JA021436.

S. E. Golian, E. H. Krause, and G. J. Perlow. Cosmic radiation above 40 miles. *Phys. Rev.*, 70:223–224, Aug 1946. doi: 10.1103/PhysRev.70.223. URL https://link.aps.org/doi/10.1103/PhysRev.70.223.

James L. Green and Scott Boardsen. Duration and extent of the great auroral storm of 1859. *Advances in Space Research*, 38(2):130 – 135, 2006. ISSN 0273-1177. doi: 10.1016/j.asr.2005.08.054. URL https://doi.org/10.1016/j.asr.2005.08.054. The Great Historical Geomagnetic Storm of 1859: A Modern Look.

James L. Green, Scott Boardsen, Sten Odenwald, John Humble, and Katherine A. Pazamickas. Eyewitness reports of the great auroral storm of 1859. *Advances in Space Research*, 38(2):145 – 154, 2006. ISSN 0273-1177. doi: 10.1016/j.asr.2005.12.021. URL https://doi.org/10.1016/j.asr.2005.12.021. The Great Historical Geomagnetic Storm of 1859: A Modern Look.

Mike Gruntman. Energetic neutral atom imaging of space plasmas. 68:3617–3656, 10 1997.

D. A. Gurnett and A. Bhattacharjee. *Introduction to Plasma Physics*. Cambridge University Press, 2005. ISBN 9780511809125. URL http://dx.doi.org/10.1017/CBO9780511809125. Cambridge Books Online.

D. A. Gurnett and L. A. Frank. Elf noise bands associated with auroral electron precipitation. *Journal of Geophysical Research*, 77(19):3411–3417, 1972. ISSN 2156-2202. doi: 10.1029/JA077i019p03411. URL http://dx.doi.org/10.1029/JA077i019p03411.

B. Gustavsson, M. J. Kosch, A. Senior, A. J. Kavanagh, B. U. E. Brndstrm, and E. M. Blixt. Combined eiscat radar and optical multispectral and tomographic observations of black aurora. *Journal of Geophysical Research: Space Physics*, 113(A6), 2008. ISSN 2156-2202. doi: 10.1029/2007JA012999. URL http://dx.doi.org/10.1029/2007JA012999. A06308.

Thomas J. Hallinan and T.Neil Davis. Small-scale auroral arc distortions. *Planetary and Space Science*, 18(12):1735 – 1744, 1970. ISSN 0032-0633. doi: 10.1016/0032-0633(70)90007-3. URL http://www.sciencedirect.com/science/article/pii/0032063370900073.

D. A. Hardy, M. S. Gussenhoven, and E. Holeman. A statistical model of auroral electron precipitation. *Journal of Geophysical Research: Space Physics*, 90(A5):4229–4248, 1985. doi: 10.1029/JA090iA05p04229. URL https://doi.org/10.1029/JA090iA05p04229.

R. R. Heacock. Whistler-like pulsation events in the frequency range 20 to 200 hz. *Geophysical Research Letters*, 1(2):77–79, 1974. ISSN 1944-8007. doi: 10.1029/GL001i002p00077. URL http://dx.doi.org/10.1029/GL001i002p00077.

R. P. Heinisch and C. L. Jolliffe. Light baffle attenuation measurements in the visible. *Appl. Opt.*, 10(9):2016–2020, Sep 1971. doi: 10.1364/AO.10.002016. URL http://ao.osa.org/abstract.cfm?URI=ao-10-9-2016.

F. C. Hoh. Instability of penningtype discharges. *The Physics of Fluids*, 6(8):1184–1191, 1963. doi: 10.1063/1.1706878. URL http://aip.scitation.org/doi/abs/10.1063/1.1706878.

T. Holstein. Imprisonment of resonance radiation in gases. *Phys. Rev.*, 72:1212–1233, Dec 1947. doi: 10.1103/PhysRev.72.1212. URL https://doi.org/10.1103/PhysRev.72.1212.

R. B. Horne and R. M. Thorne. Ion cyclotron absorption at the second harmonic of the oxygen gyrofrequency. *Geophysical Research Letters*, 17(12): 2225–2228, 1990. ISSN 1944-8007. doi: 10.1029/GL017i012p02225. URL http://dx.doi.org/10.1029/GL017i012p02225.

Ildiko Horvath and Brian C. Lovell. Investigating the polar ionosphere during the development of neutral density enhancements on 2425 september 2000. *Journal of Geophysical Research: Space Physics*, 122(4):4600–4616, 2017. ISSN 2169-9402. doi: 10.1002/2016JA023799. URL http://dx.doi.org/10.1002/2016JA023799. 2016JA023799.

K. Hosokawa, A. Kadokura, N. Sato, S. E. Milan, M. Lester, G. Bjornsson, and Th. Saemundsson. Electric field modulation behind pulsating aurora. *Journal of Geophysical Research: Space Physics*, 113(A11), 2008. ISSN 2156-2202. doi: 10.1029/2008JA013601. URL http://dx.doi.org/10.1029/2008JA013601. A11322.

K. Hosokawa, Y. Ogawa, A. Kadokura, H. Miyaoka, and N. Sato. Modulation of ionospheric conductance and electric field associated with pulsating aurora. *Journal of Geophysical Research: Space Physics*, 115(A3), 2010. ISSN 2156-2202. doi: 10.1029/2009JA014683. URL http://dx.doi.org/10.1029/2009JA014683. A03201.

C. Y. Huang, Y. Huang, Y.-J. Su, T. Huang, and E. K. Sutton. High-latitude neutral mass density maxima. *Journal of Geophysical Research: Space Physics*, 122 (10):10,694–10,711, 2017. ISSN 2169-9402. doi: 10.1002/2017JA024334. URL http://dx.doi.org/10.1002/2017JA024334. 2017JA024334.

Yanshi Huang, Arthur D. Richmond, Yue Deng, and Ray Roble. Height distribution of joule heating and its influence on the thermosphere. *Journal of Geophysical Research: Space Physics*, 117(A8), 2012. ISSN 2156-2202. doi: 10.1029/2012JA017885. URL http://dx.doi.org/10.1029/2012JA017885. A08334.

Yanshi Huang, Qian Wu, Cheryl Y. Huang, and Yi-Jiun Su. Thermosphere variation at different altitudes over the northern polar cap during magnetic storms. *Journal of Atmospheric and Solar-Terrestrial Physics*, 146:140 – 148, 2016. ISSN 1364-6826. doi: 10.1016/j.jastp.2016.06.003. URL http://www.sciencedirect.com/science/article/pii/S1364682616301444.

J. D. Huba, P. K. Chaturvedi, S. L. Ossakow, and D. M. Towle. High frequency drift waves with wavelengths below the ion gyroradius in equatorial spread f. *Geophysical Research Letters*, 5(8):695–698, 1978. ISSN 1944-8007. doi: 10.1029/GL005i008p00695. URL http://dx.doi.org/10.1029/GL005i008p00695.

Robert E Huffman. *Atmospheric ultraviolet remote sensing*, volume 52. Academic Press, 1992.

D.M. Hunten, F.E. Roach, and J.W. Chamberlain. A photometric unit for the airglow and aurora. *Journal of Atmospheric and Terrestrial Physics*, 8(6):345 – 346, 1956. ISSN 0021-9169. doi: 10.1016/0021-9169(56)90111-8. URL http://www.sciencedirect.com/science/article/pii/0021916956901118.

D. L. Hysell, D. C. Fritts, B. Laughman, and J. L. Chau. Gravity wave-induced ionospheric irregularities in the postsunset equatorial valley region. *Journal of Geophysical Research: Space Physics*, 122(11):11,579–11,590, 2017. ISSN 2169-9402. doi: 10.1002/2017JA024514. URL http://dx.doi.org/10.1002/2017JA024514. 2017JA024514.

Luigi G. Jacchia and Jack Slowey. Atmospheric heating in the auroral zones: A preliminary analysis of the atmospheric drag of the injun 3 satellite. *Journal of Geophysical Research*, 69(5):905–910, 1964. ISSN 2156-2202. doi: 10.1029/JZ069i005p00905. URL http://dx.doi.org/10.1029/JZ069i005p00905.

A. N. Jaynes, M. R. Lessard, J. V. Rodriguez, E. Donovan, T. M. Loto'aniu, and K. Rychert. Pulsating auroral electron flux modulations in the equatorial magnetosphere. *Journal of Geophysical Research: Space Physics*, 118(8):4884–4894, 2013. ISSN 2169-9402. doi: 10.1002/jgra.50434. URL http://dx.doi.org/10.1002/jgra.50434.

A. D. Johnstone. Pulsating aurora. *Nature*, 274:119–126, July 1978. doi: 10.1038/274119a0.

S. L. Jones, M. R. Lessard, K. Rychert, E. Spanswick, and E. Donovan. Large-scale aspects and temporal evolution of pulsating aurora. *Journal of Geophysical Research: Space Physics*, 116(A3), 2011. ISSN 2156-2202. doi: 10.1029/2010JA015840. URL http://dx.doi.org/10.1029/2010JA015840. A03214.

S. L. Jones, M. R. Lessard, K. Rychert, E. Spanswick, E. Donovan, and A. N. Jaynes. Persistent, widespread pulsating aurora: A case study. *Journal of Geophysical Research: Space Physics*, 118(6):2998–3006, 2013. ISSN 2169-9402. doi: 10.1002/jgra.50301. URL http://dx.doi.org/10.1002/jgra.50301.

S.L. Jones, M.R. Lessard, P.W. Riley, and A.T. Ellis. Development of the de-spun rocket borne imager 2 in support of rocket observations of pulsating aurora. *IRF Sci. Rep.*, 292: 67 – 71, 2008. ISSN 0284-1703.

S.L. Jones, M.R. Lessard, P.A. Fernandes, D. Lummerzheim, J.L. Semeter, C.J. Heinselman, K.A. Lynch, R.G. Michell, P.M. Kintner, H.C. Stenbaek-Nielsen, and K. Asamura. {PFISR} and {ROPA} observations of pulsating aurora. *Journal of Atmospheric and Solar-Terrestrial Physics*, 71(6-7): 708 – 716, 2009. ISSN 1364-6826. doi: 10.1016/j.jastp.2008.10.004. URL http://www.sciencedirect.com/science/article/pii/S1364682608002769. Advances in high latitude upper atmospheric science with the Poker Flat Incoherent Scatter Radar (PFISR).

I. Kanik, C. Noren, O. P. Makarov, P. Vattipalle, J. M. Ajello, and D. E. Shemansky. Electron impact dissociative excitation of o2: 2. absolute emission cross sections of the oi(130.4 nm) and oi(135.6 nm) lines. *Journal of Geophysical Research: Planets*, 108(E11), 2003. ISSN 2156-2202. doi: 10.1029/2000JE001423. URL http://dx.doi.org/10.1029/2000JE001423. 5126.

S. Kasahara, Y. Miyoshi, S. Yokota, T. Mitani, Y. Kasahara, S. Matsuda, A. Kumamoto, A. Matsuoka, Y. Kazama, H. U. Frey, V. Angelopoulos, S. Kurita, K. Keika, K. Seki, and I. Shinohara. Pulsating aurora from electron scattering by chorus waves. *Nature*, 554:337–340, February 2018. doi: 10.1038/nature25505. URL https://doi.org/10.1038/nature25505.

Michael C. Kelley. *The Earth's Ionosphere: plasma physics and electrodynamics*. Academic Press, 2009.

C. Kennel. Lowfrequency whistler mode. *The Physics of Fluids*, 9(11):2190–2202, 1966. doi: 10.1063/1.1761588. URL http://aip.scitation.org/doi/abs/10.1063/1.1761588.

G. N. Kervalishvili and H. Lühr. The relationship of thermospheric density anomaly with electron temperature, small-scale fac, and ion up-flow in the cusp region, as observed by champ and dmsp satellites. *Annales Geophysicae*, 31(3):541–554, 2013. doi: 10.5194/angeo-31-541-2013. URL https://www.ann-geophys.net/31/541/2013/.

G. N. Kervalishvili and H. Lühr. Climatology of zonal wind and large-scale fac with respect to the density anomaly in the cusp region: seasonal, solar cycle, and imf b_y dependence. *Annales Geophysicae*, 32(3):249–261, 2014. doi: 10.5194/angeo-32-249-2014. URL https://www.ann-geophys.net/32/249/2014/.

George V. Khazanov, David G. Sibeck, and Eftyhia Zesta. Major pathways to electron distribution function formation in regions of diffuse aurora. *Journal of Geophysical Research: Space Physics*, 122(4):4251–4265, 2017. ISSN 2169-9402. doi: 10.1002/2017JA023956. URL http://dx.doi.org/10.1002/2017JA023956. 2017JA023956.

Hyomin Kim. Study of extremely low frequency waves observed at south pole station. Master's thesis, Dartmouth College, Hanover, NH, 2004.

Hyomin Kim, Marc R. Lessard, James LaBelle, and Jay R. Johnson. Narrow-band extremely low frequency (elf) wave phenomena observed at south pole station. *Geophysical Research Letters*, 33(6), 2006. ISSN 1944-8007. doi: 10.1029/2005GL023638. URL http://dx.doi.org/10.1029/2005GL023638. L06109.

J. Kimball and T. J. Hallinan. Observations of black auroral patches and of their relationship to other types of aurora. *Journal of Geophysical Research: Space Physics*, 103(A7):14671–14682, 1998a. ISSN 2156-2202. doi: 10.1029/98JA00188. URL http://dx.doi.org/10.1029/98JA00188.

J. Kimball and T. J. Hallinan. A morphological study of black vortex streets. *Journal of Geophysical Research: Space Physics*, 103(A7):14683–14695, 1998b. ISSN 2156-2202. doi: 10.1029/98JA00187. URL http://dx.doi.org/10.1029/98JA00187.

Paul M. Kintner, John Bonnell, Roger Arnoldy, Kristina Lynch, Craig Pollock, and Tom Moore. Scifer-transverse ion acceleration and plasma waves. *Geophysical Research Letters*, 23(14):1873–1876, 1996. ISSN 1944-8007. doi: 10.1029/96GL01863. URL http://dx.doi.org/10.1029/96GL01863.

N. Kitamura, Y. Ogawa, Y. Nishimura, N. Terada, T. Ono, A. Shinbori, A. Kumamoto, V. Truhlik, and J. Smilauer. Solar zenith angle dependence of plasma density and temperature in the polar cap ionosphere and low-altitude magnetosphere during geomagnetically quiet periods at solar maximum. *Journal of Geophysical Research: Space Physics*, 116(A8), 2011. ISSN 2156-2202. doi: 10.1029/2011JA016631. URL http://dx.doi.org/10.1029/2011JA016631. A08227.

C. A. Kletzing, J. D. Scudder, E. E. Dors, and C. Curto. Auroral source region: Plasma properties of the highlatitude plasma sheet. *Journal of Geophysical Research: Space Physics*, 108(A10), 2003. doi: 10.1029/2002JA009678. URL https://doi.org/10.1029/2002JA009678.

Y.-S Kwak, A Richmond, Yue Deng, B.-H Ahn, and Kyungsuk Cho. Sources of the high-latitude thermospheric neutral mass density variations. 27:329–335, 12 2010.

J. LaBelle and A. T. Weatherwax. Statistical study of auroral roar emissions observed at south pole station. *Journal of Geophysical Research: Space Physics*, 107 (A7):SIA 17–1–SIA 17–7, 2002. ISSN 2156-2202. doi: 10.1029/2001JA000319. URL http://dx.doi.org/10.1029/2001JA000319.

Y. S. Lee, Y. H. Kim, Y. Yi, and J. Kim. A Baffle Design for an Airglow Photometer onboard the Korea Sounding Rocket-III. *Journal of Korean Astronomical Society*, 33: 165–172, December 2000.

C. Leinert and D. Klüppelberg. Stray light suppression in optical space experiments. *Appl. Opt.*, 13(3):556–564, Mar 1974. doi: 10.1364/AO.13.000556. URL http://ao.osa.org/abstract.cfm?URI=ao-13-3-556.

M. R. Lessard. *A Review of Pulsating Aurora*, pages 55–68. American Geophysical Union, 2013. ISBN 9781118670286. doi: 10.1029/2011GM001187. URL http://dx.doi.org/10.1029/2011GM001187.

H. Liu, H. Lühr, V. Henize, and W. Khler. Global distribution of the thermospheric total mass density derived from champ. *Journal of Geophysical Research: Space Physics*, 110(A4), 2005. ISSN 2156-2202. doi: 10.1029/2004JA010741. URL http://dx.doi.org/10.1029/2004JA010741. A04301.

J. Y. Liu, K. Wang, C. H. Chen, W. H. Yang, Y. H. Yen, Y. I. Chen, K. Hatorri, H. T. Su, R. R. Hsu, and C. H. Chang. A statistical study on elf-whistlers/emissions and m $\geq$ 5.0 earthquakes in taiwan. *Journal of Geophysical Research: Space Physics*, 118(6):3760–3768, 2013. ISSN 2169-9402. doi: 10.1002/jgra.50356. URL http://dx.doi.org/10.1002/jgra.50356.

Libo Liu, Weixing Wan, Baiqi Ning, O. M. Pirog, and V. I. Kurkin. Solar activity variations of the ionospheric peak electron density. *Journal of Geophysical Research: Space Physics*, 111(A8), 2006. ISSN 2156-2202. doi: 10.1029/2006JA011598. URL http://dx.doi.org/10.1029/2006JA011598. A08304.

H. Lühr, M. Rother, W. Köhler, P. Ritter, and L. Grunwaldt. Thermospheric upwelling in the cusp region: Evidence from champ observations. *Geophysical Research Letters*, 31(6), 2004. ISSN 1944-8007. doi: 10.1029/2003GL019314. URL http://dx.doi.org/10.1029/2003GL019314. L06805.

Robert L. Lysak. Propagation of alfvén waves through the ionosphere: Dependence on ionospheric parameters. *Journal of Geophysical Research: Space Physics*, 104 (A5):10017–10030, 1999. ISSN 2156-2202. doi: 10.1029/1999JA900024. URL http://dx.doi.org/10.1029/1999JA900024.

Ti-Ze Ma and R. W. Schunk. Effect of polar cap patches on the polar thermosphere. *Journal of Geophysical Research: Space Physics*, 100(A10):19701–19713, 1995. ISSN 2156-2202. doi: 10.1029/95JA01122. URL http://dx.doi.org/10.1029/95JA01122.

Elizabeth A. MacDonald, Eric Donovan, Yukitoshi Nishimura, Nathan A. Case, D. Megan Gillies, Bea Gallardo-Lacourt, William E. Archer, Emma L. Spanswick, Notanee Bourassa, Martin Connors, Matthew Heavner, Brian Jackel, Burcu Kosar, David J. Knudsen, Chris Ratzlaff, and Ian Schofield. New science in plain sight: Citizen scientists lead to the discovery of optical structure in the upper atmosphere. *Science Advances*, 4(3), 2018. doi: 10.1126/sciadv.aaq0030. URL http://dx.doi.org/10.1126/sciadv.aaq0030.

K. Maeda, T. Tsuda, and H. Maeda. Theoretical interpretation of the equatorial sporadic e layers. *Phys. Rev. Lett.*, 11:406–407, Nov 1963. doi: 10.1103/PhysRevLett.11.406. URL https://link.aps.org/doi/10.1103/PhysRevLett.11.406.

Roman A. Makarevich. Toward an integrated view of ionospheric plasma instabilities: Altitudinal transitions and strong gradient case. *Journal of Geophysical Research: Space Physics*, 121(4):3634–3647, 2016. ISSN 2169-9402. doi: 10.1002/2016JA022515. URL http://dx.doi.org/10.1002/2016JA022515. 2016JA022515.

Guglielmo Marconi. Wireless telegraphic communication. *Resonance*, 7(1):95–101, 2002.

G. Marette and J.-C. Gérard. Rocket-borne baffled photometer: design and calibration. *Appl. Opt.*, 15(2):437–439, Feb 1976. doi: 10.1364/AO.15.000437. URL http://ao.osa.org/abstract.cfm?URI=ao-15-2-437.

Göran T Marklund, N Ivchenko, Tomas Karlsson, A Fazakerley, M Dunlop, P-A Lindqvist, S Buchert, C Owen, M Taylor, A Vaivalds, et al. Temporal evolution of the electric field accelerating electrons away from the auroral ionosphere. *Nature*, 414(6865):724, 2001.

Gran Marklund, Lars Blomberg, Carl-Gunne Flthammar, and Per-Arne Lindqvist. On intense diverging electric fields associated with black aurora. *Geophysical Research Letters*, 21(17):1859–1862, 1994. ISSN 1944-8007. doi: 10.1029/94GL00194. URL http://dx.doi.org/10.1029/94GL00194.

Gran Marklund, Tomas Karlsson, and James Clemmons. On low-altitude particle acceleration and intense electric fields and their relationship to black aurora. *Journal of Geophysical Research: Space Physics*, 102(A8):17509–17522, 1997. ISSN 2156-2202. doi: 10.1029/97JA00334. URL http://dx.doi.org/10.1029/97JA00334.

B. H. Mauk and R. L. McPherron. An experimental test of the electromagnetic ion cyclotron instability within the earth's magnetosphere. *The Physics of Fluids*, 23(10):2111–2127, 1980. doi: 10.1063/1.862873. URL http://aip.scitation.org/doi/abs/10.1063/1.862873.

R. P. McCoy, K. F. Dymond, G. G. Fritz, S. E. Thonnard, R. R. Meier, and P. A. Regeon. Special sensor ultraviolet limb imager: an ionospheric and neutral density profiler for the defense meteorological satellite program satellites. *Optical Engineering*, 33:33 – 33 – 7, 1994. doi: 10.1117/12.155904. URL http://dx.doi.org/10.1117/12.155904.

Carl E. McIlwain. Direct measurement of particles producing visible auroras. *Journal of Geophysical Research*, 65(9):2727–2747, 1960. doi: 10.1029/JZ065i009p02727. URL https://doi.org/10.1029/JZ065i009p02727.

R. R. Meier. Ultraviolet spectroscopy and remote sensing of the upper atmosphere. *Space Science Reviews*, 58(1):1–185, 1991. ISSN 1572-9672. doi: 10.1007/BF01206000. URL http://dx.doi.org/10.1007/BF01206000.

Kenneth Moe, Mildred M. Moe, Virginia L. Carter, and Michael B. Ruggera. The correlation of thermospheric densities with charged particle precipitation through the magnetospheric cleft. *Journal of Geophysical Research*, 82(22):3304–3306, 1977. ISSN 2156-2202. doi: 10.1029/JA082i022p03304. URL http://dx.doi.org/10.1029/JA082i022p03304.

J. Moen, H. C. Carlson, and P. E. Sandholt. Continuous observation of cusp auroral dynamics in response to an imf by polarity change. *Geophysical Research Letters*, 26(9):1243–1246, 1999. ISSN 1944-8007. doi: 10.1029/1999GL900224. URL http://dx.doi.org/10.1029/1999GL900224.

J. Moen, X. C. Qiu, H. C. Carlson, R. Fujii, and I. W. McCrea. On the diurnal variability in f2-region plasma density above the eiscat svalbard radar. *Annales Geophysicae*, 26(8):2427–2433, 2008. doi: 10.5194/angeo-26-2427-2008. URL https://www.ann-geophys.net/26/2427/2008/.

T.E. Moore, M.-C. Fok, and K. Garcia-Sage. The ionospheric outflow feedback loop. *Journal of Atmospheric and Solar-Terrestrial Physics*, 115-116(Supplement C):59 – 66, 2014. ISSN 1364-6826. doi: 10.1016/j.jastp.2014.02.002. URL https://doi.org/10.1016/j.jastp.2014.02.002. Sun-Earth System Exploration: Moderate and Extreme Disturbances.

P. T. Newell, T. Sotirelis, and S. Wing. Diffuse, monoenergetic, and broadband aurora: The global precipitation budget. *Journal of Geophysical Research: Space*

Physics, 114(A9), 2009. ISSN 2156-2202. doi: 10.1029/2009JA014326. URL http://dx.doi.org/10.1029/2009JA014326. A09207.

Y. Nishimura, J. Bortnik, W. Li, R. M. Thorne, L. R. Lyons, V. Angelopoulos, S. B. Mende, J. W. Bonnell, O. Le Contel, C. Cully, R. Ergun, and U. Auster. Identifying the driver of pulsating aurora. *Science*, 330:81, October 2010. doi: 10.1126/science.1193186.

Takanori Nishiyama, Takeshi Sakanoi, Yoshizumi Miyoshi, Ryuho Kataoka, Donald Hampton, Yuto Katoh, Kazushi Asamura, and Shoichi Okano. Fine scale structures of pulsating auroras in the early recovery phase of substorm using ground-based emccd camera. *Journal of Geophysical Research: Space Physics*, 117(A10), 2012. ISSN 2156-2202. doi: 10.1029/2012JA017921. URL http://dx.doi.org/10.1029/2012JA017921. A10229.

Y. Obuchi, T. Sakanoi, K. Asamura, A. Yamazaki, Y. Kasaba, M. Hirahara, Y. Ebihara, and S. Okano. Fine-scale dynamics of black auroras obtained from simultaneous imaging and particle observations with the reimei satellite. *Journal of Geophysical Research: Space Physics*, 116(A1), 2011. ISSN 2156-2202. doi: 10.1029/2010JA016321. URL http://dx.doi.org/10.1029/2010JA016321. A00K07.

Meers M. Oppenheim and Yakov S. Dimant. Photoelectron-induced waves: A likely source of 150 km radar echoes and enhanced electron modes. *Geophysical Research Letters*, 43(8):3637–3644, 2016. ISSN 1944-8007. doi: 10.1002/2016GL068179. URL http://dx.doi.org/10.1002/2016GL068179. 2016GL068179.

A. Otto, D. Lummerzheim, H. Zhu, Ø. LieSvendsen, M. H. Rees, and B. S. Lanchester. Excitation of tall auroral rays by ohmic heating in fieldaligned current filaments at f region heights. *Journal of Geophysical Research: Space Physics*, 108(A4), 2003. doi: 10.1029/2002JA009423. URL https://doi.org/10.1029/2002JA009423.

F. Paresce, S. Kumar, and C. S. Bowyer. Continuous discharge line source for the extreme ultraviolet. *Appl. Opt.*, 10(8):1904–1908, Aug 1971. doi: 10.1364/AO.10.001904. URL http://ao.osa.org/abstract.cfm?URI=ao-10-8-1904.

G.K. Parks. *Physics of Space Plasmas: An Introduction*. Westview Press, 2004. ISBN 9780813341293.

N. R. Parsons and I. L. Thomas. Spatially forbidden regions in the aurora. *Canadian Journal of Physics*, 51(12):1377–1378, 1973. doi: 10.1139/p73-182. URL http://dx.doi.org/10.1139/p73-182.

L. J. Paxton, C-I. Meng, G. H. Fountain, B. S. Ogorzalek, E. H. Darlington, S. A. Gary, J. O. Goldsten, D. Y. Kusnierkiewicz, S. D. Lee, L. A. Linstrom, J. J. Maynard, K. Peacock, D. F. Persons, B. E. Smith, D. J. Strickland, and R. E. Daniell. Ssusi - horizon-to-horizon and limb-viewing spectrographic imager for remote sensing of environmental parameters, 1993. URL http://dx.doi.org/10.1117/12.140846.

L. M. Peticolas, T. J. Hallinan, H. C. Stenbaek-Nielsen, J. W. Bonnell, and C. W. Carlson. A study of black aurora from aircraft-based optical observations and plasma measurements on fast. *Journal of Geophysical Research: Space Physics*, 107(A8): SMP 30–1–SMP 30–11, 2002. ISSN 2156-2202. doi: 10.1029/2001JA900157. URL http://dx.doi.org/10.1029/2001JA900157.

J. M. Picone, A. E. Hedin, D. P. Drob, and A. C. Aikin. Nrlmsise-00 empirical model of the atmosphere: Statistical comparisons and scientific issues. *Journal of Geophysical Research: Space Physics*, 107(A12):SIA 15–1–SIA 15–16, 2002. ISSN 2156-2202. doi: 10.1029/2002JA009430. URL http://dx.doi.org/10.1029/2002JA009430. 1468.

William H Press, Saul A Teukolsky, William T Vetterling, and Brian P Flannery. Numerical recipes: The art of scientific computing. *The art of scientific computing*, 1992.

Gerd W. Prölss. Perturbations of the upper atmosphere in the cleft region. *Journal of Atmospheric and Solar-Terrestrial Physics*, 70(18):2374 – 2380, 2008. ISSN 1364-6826. doi: 10.1016/j.jastp.2008.06.017. URL http://www.sciencedirect.com/science/article/pii/S136468260800196X. Transport processes in the coupled solar wind-geospace system seen from a high-latitude vantage point.

J. Raeder, J. Berchem, and M. AshourAbdalla. The geospace environment modeling grand challenge: Results from a global geospace circulation model. *Journal of Geophysical Research: Space Physics*, 103(A7):14787–14797, 1998. doi: 10.1029/98JA00014. URL https://doi.org/10.1029/98JA00014.

J. L. Rauch and A. Roux. Ray tracing of ulf waves in a multicomponent magnetospheric plasma: Consequences for the generation mechanism of ion cyclotron waves. *Journal of Geophysical Research: Space Physics*, 87(A10):8191–8198, 1982. ISSN 2156-2202. doi: 10.1029/JA087iA10p08191. URL http://dx.doi.org/10.1029/JA087iA10p08191.

Robert J. Redmon, William F. Denig, Liam M. Kilcommons, and Delores J. Knipp. New dmsp database of precipitating auroral electrons and ions. *Journal of Geophysical Research: Space Physics*, 122(8):9056–9067, 2017. ISSN 2169-9402. doi: 10.1002/2016JA023339. URL http://dx.doi.org/10.1002/2016JA023339. 2016JA023339.

M.H. Rees, A.I. Stewart, and J.C.G. Walker. Secondary electrons in aurora. *Planetary and Space Science*, 17(12):1997 – 2008, 1969. ISSN 0032-0633. doi: 10.1016/0032-0633(69)90137-8. URL https://doi.org/10.1016/0032-0633(69)90137-8.

B.W. Reinisch, P. Nsumei, X. Huang, and D.K. Bilitza. Modeling the f2 topside and plasmasphere for iri using image/rpi and isis data. *Advances in Space Research*, 39(5):731 – 738, 2007. ISSN 0273-1177. doi: 10.1016/j.asr.2006.05.032. URL http://www.sciencedirect.com/science/article/pii/S0273117706006028.

S. Rentz and H. Lühr. Climatology of the cusp-related thermospheric mass density anomaly, as derived from champ observations. *Annales Geophysicae*, 26(9):2807–2823, 2008. doi: 10.5194/angeo-26-2807-2008. URL https://www.ann-geophys.net/26/2807/2008/.

P. G. Richards, J. A. Fennelly, and D. G. Torr. Euvac: A solar euv flux model for aeronomic calculations. *Journal of Geophysical Research: Space Physics*, 99(A5):8981–8992, 1994. ISSN 2156-2202. doi: 10.1029/94JA00518. URL http://dx.doi.org/10.1029/94JA00518.

P. G. Richards, R. R. Meier, Shih-Ping Chen, D. P. Drob, and P. Dandenault. Investigation of the causes of the longitudinal variation of the electron density

in the weddell sea anomaly. *Journal of Geophysical Research: Space Physics*, 122(6):6562–6583, 2017. ISSN 2169-9402. doi: 10.1002/2016JA023565. URL http://dx.doi.org/10.1002/2016JA023565. 2016JA023565.

D. E. Robbins, A. J. Hundhausen, and S. J. Bame. Helium in the solar wind. *Journal of Geophysical Research*, 75(7):1178–1187, 1970. doi: 10.1029/JA075i007p01178. URL https://doi.org/10.1029/JA075i007p01178.

O Royrvik. Pulsating aurora: Local and global morphology[ph. d. thesis]. 1976.

O. Royrvik and T. N. Davis. Pulsating aurora: Local and global morphology. *Journal of Geophysical Research*, 82(29):4720–4740, 1977. ISSN 2156-2202. doi: 10.1029/JA082i029p04720. URL http://dx.doi.org/10.1029/JA082i029p04720.

F. Brent Sadler, Marc Lessard, Eric Lund, Antonius Otto, and Hermann Lhr. Auroral precipitation/ion upwelling as a driver of neutral density enhancement in the cusp. *Journal of Atmospheric and Solar-Terrestrial Physics*, 87-88: 82 – 90, 2012. ISSN 1364-6826. doi: 10.1016/j.jastp.2012.03.003. URL http://www.sciencedirect.com/science/article/pii/S1364682612000879. Physical Process in the Cusp: Plasma Transport and Energization.

Hiroki Saito, Takeo Yoshino, and Natsuo Sato. Narrow-banded elf emissions over the southern polar region. *Planetary and Space Science*, 35(6):745 – 752, 1987. ISSN 0032-0633. doi: https://doi.org/10.1016/0032-0633(87)90034-1. URL http://www.sciencedirect.com/science/article/pii/0032063387900341.

K. Sakaguchi, K. Shiokawa, E. Donovan, A. Nakajima, Y. Hiraki, T. Trondsen, and F. Plaschke. Periodic black auroral patches at the dawnside dipolarization front during a substorm. *Journal of Geophysical Research: Space Physics*, 116(A5), 2011. ISSN 2156-2202. doi: 10.1029/2010JA015957. URL http://dx.doi.org/10.1029/2010JA015957. A00I18.

T. Sakanoi, Y. Obuchi, Y. Ebihara, Y. Miyoshi, K. Asamura, A. Yamazaki, Y. Kasaba, M. Hirahara, T. Nishiyama, and S. Okano. *Fine-Scale Characteristics of Black Aurora and its Generation Process*, pages 271–278. American Geophysical Union, 2013. ISBN 9781118670286. doi: 10.1029/2011GM001178. URL http://dx.doi.org/10.1029/2011GM001178.

M. Samara, R. G. Michell, and G. V. Khazanov. First optical observations of interhemispheric electron reflections within pulsating aurora. *Geophysical Research Letters*, 44(6):2618–2623, 2017. doi: 10.1002/2017GL072794. URL https://doi.org/10.1002/2017GL072794.

Per Even Sandholt and Charles J. Farrugia. On the dynamic cusp aurora and imf b y. *Journal of Geophysical Research: Space Physics*, 104(A6):12461–12472, 1999. doi: 10.1029/1999JA900126. URL https://doi.org/10.1029/1999JA900126.

Natsuo Sato and Kanji Hayashi. Band-limited elf emission burst (auroral roar). *Journal of Geophysical Research: Space Physics*, 90(A4):3531–3535, 1985. ISSN 2156-2202. doi: 10.1029/JA090iA04p03531. URL http://dx.doi.org/10.1029/JA090iA04p03531.

K. Schlegel, H. Lühr, J.-P. St.-Maurice, G. Crowley, and C. Hackert. Thermospheric density structures over the polar regions observed with champ. *Annales Geophysicae*, 23(5):1659–1672, 2005. doi: 10.5194/angeo-23-1659-2005. URL https://www.ann-geophys.net/23/1659/2005/.

H. Schoute-Vanneck, M. W. J. Scourfield, and E. Nielsen. Drifting black aurorae? *Journal of Geophysical Research: Space Physics*, 95(A1):241–246, 1990. ISSN 2156-2202. doi: 10.1029/JA095iA01p00241. URL http://dx.doi.org/10.1029/JA095iA01p00241.

M Bruce Schulman, Francis A Sharpton, Sunggi Chung, Chun C Lin, and LW Anderson. Emission from oxygen atoms produced by electron-impact dissociative excitation of oxygen molecules. *Physical review A*, 32(4):2100, 1985. doi: 10.1103/PhysRevA.32.2100. URL https://doi.org/10.1103/PhysRevA.32.2100.

Robert Schunk and Andrew Nagy. *Ionospheres: physics, plasma physics, and chemistry*. Cambridge university press, 2009.

J. C. Seddon, A. D. Pickar, and J. E. Jackson. Continuous electron density measurements up to 200 km. *Journal of Geophysical Research*, 59(4):513–524, 1954. doi: 10.1029/JZ059i004p00513. URL https://doi.org/10.1029/JZ059i004p00513.

D. D. Sentman and D. A. Ehring. Midlatitude detection of elf whistlers. *Journal of Geophysical Research: Space Physics*, 99(A2):2183–2190, 1994. ISSN 2156-2202. doi: 10.1029/93JA02103. URL http://dx.doi.org/10.1029/93JA02103.

CE Seyler, AE Clark, J Bonnell, and J-E Wahlund. Electrostatic broadband elf wave emission by alfvén wave breaking. *Journal of Geophysical Research: Space Physics*, 103 (A4):7027–7041, 1998.

Charles E. Seyler. A mathematical model of the structure and evolution of smallscale discrete auroral arcs. *Journal of Geophysical Research: Space Physics*, 95(A10):17199–17215, 1990. doi: 10.1029/JA095iA10p17199. URL https://doi.org/10.1029/JA095iA10p17199.

Cheng Sheng, Yue Deng, Qian Wu, Aaron Ridley, and Ingemar Hggstrm. Thermospheric winds around the cusp region. *Journal of Geophysical Research: Space Physics*, 120(2):1248–1255, 2015. ISSN 2169-9402. doi: 10.1002/2014JA020028. URL http://dx.doi.org/10.1002/2014JA020028. 2014JA020028.

Y. Shi, E. Zesta, H. K. Connor, Y.-J. Su, E. K. Sutton, C. Y. Huang, D. M. Ober, C. Christodoulou, S. Delay, and D. M. Oliveira. High-latitude thermosphere neutral density response to solar wind dynamic pressure enhancement. *Journal of Geophysical Research: Space Physics*, 122(11):11,559–11,578, 2017. ISSN 2169-9402. doi: 10.1002/2017JA023889. URL http://dx.doi.org/10.1002/2017JA023889. 2017JA023889.

T. Shimazaki. Dependence of the Critical Frequency of the Ionospheric E-layer on Solar Zenith Angle and the Annual Variation in E-layer Ionization. *Nature*, 205:889–891, February 1965. doi: 10.1038/205889b0.

K. Shiokawa, A. Nakajima, A. Ieda, K. Sakaguchi, R. Nomura, T. Aslaksen, M. Greffen, and E. Donovan. Rayleigh-taylor type instability in auroral patches. *Journal of Geophysical*

Research: Space Physics, 115(A2), 2010. ISSN 2156-2202. doi: 10.1029/2009JA014273. URL http://dx.doi.org/10.1029/2009JA014273. A02211.

S.M. Silverman. Low latitude auroras prior to 1200 c.e. and ezekiels vision. *Advances in Space Research*, 38(2):200 – 208, 2006. ISSN 0273-1177. doi: 10.1016/j.asr.2005.03.158. URL https://doi.org/10.1016/j.asr.2005.03.158. The Great Historical Geomagnetic Storm of 1859: A Modern Look.

Albert Simon. Instability of a partially ionized plasma in crossed electric and magnetic fields. *The Physics of Fluids*, 6(3):382–388, 1963. doi: 10.1063/1.1706743. URL http://aip.scitation.org/doi/abs/10.1063/1.1706743.

A. K. Singh, K. K. Singh, S. B. Singh, A. K. Singh, and Lalmani. Multiflash whistlers in elf-band observed at low latitude. *Annales Geophysicae*, 29(1):91–96, 2011. doi: 10.5194/angeo-29-91-2011. URL http://dx.doi.org/10.5194/angeo-29-91-2011.

Edward J. Smith, Robert E. Holzer, and Christopher T. Russell. Magnetic emissions in the magnetosheath at frequencies near 100 hz. *Journal of Geophysical Research*, 74(11):3027–3036, 1969. ISSN 2156-2202. doi: 10.1029/JA074i011p03027. URL http://dx.doi.org/10.1029/JA074i011p03027.

H. C. Stenbaek-Nielsen. Pulsating aurora: The importance of the ionosphere. *Geophysical Research Letters*, 7(5):353–356, 1980. ISSN 1944-8007. doi: 10.1029/GL007i005p00353. URL http://dx.doi.org/10.1029/GL007i005p00353.

Thomas Howard Stix. The theory of plasma waves. *The Theory of Plasma Waves, New York: McGraw-Hill, 1962*, 1962.

R. J. Strangeway, R. E. Ergun, Y.-J. Su, C. W. Carlson, and R. C. Elphic. Factors controlling ionospheric outflows as observed at intermediate altitudes. *Journal of Geophysical Research: Space Physics*, 110(A3), 2005. ISSN 2156-2202. doi: 10.1029/2004JA010829. URL http://dx.doi.org/10.1029/2004JA010829. A03221.

A. V. Streltsov and W. Lotko. Multiscale electrodynamics of the ionosphere-magnetosphere system. *Journal of Geophysical Research: Space Physics*, 109(A9), 2004. ISSN 2156-2202. doi: 10.1029/2004JA010457. URL http://dx.doi.org/10.1029/2004JA010457. A09214.

A. V. Streltsov and G. T. Marklund. Divergent electric fields in downward current channels. *Journal of Geophysical Research: Space Physics*, 111(A7), 2006. ISSN 2156-2202. doi: 10.1029/2005JA011196. URL http://dx.doi.org/10.1029/2005JA011196. A07204.

D. R. Taeusch. Structure of electrodynamic and particle heating in the disturbed polar thermosphere. *Journal of Geophysical Research*, 82(4):455–460, 1977. ISSN 2156-2202. doi: 10.1029/JA082i004p00455. URL http://dx.doi.org/10.1029/JA082i004p00455.

D. R. Taeusch and B. B. Hinton. Structure of electrodynamic and particle heating in the undisturbed polar thermosphere. *Journal of Geophysical Research*, 80 (31):4346–4350, 1975. ISSN 2156-2202. doi: 10.1029/JA080i031p04346. URL http://dx.doi.org/10.1029/JA080i031p04346.

K. F. Tapping. The 10.7 cm solar radio flux (f10.7). *Space Weather*, 11(7):394–406, 2013. ISSN 1542-7390. doi: 10.1002/swe.20064. URL http://dx.doi.org/10.1002/swe.20064.

M. Temerin and R. L. Lysak. Electromagnetic ion cyclotron mode (elf) waves generated by auroral electron precipitation. *Journal of Geophysical Research: Space Physics*, 89(A5):2849–2859, 1984. ISSN 2156-2202. doi: 10.1029/JA089iA05p02849. URL http://dx.doi.org/10.1029/JA089iA05p02849.

David R. Themens, P. Thayyil Jayachandran, Michael J. Nicolls, and John W. MacDougall. A top to bottom evaluation of iri 2007 within the polar cap. *Journal of Geophysical Research: Space Physics*, 119(8):6689–6703, 2014. ISSN 2169-9402. doi: 10.1002/2014JA020052. URL http://dx.doi.org/10.1002/2014JA020052. 2014JA020052.

Neil R. Thomson, Mark A. Clilverd, and Craig J. Rodger. Low-latitude ionospheric d region dependence on solar zenith angle. *Journal of Geophysical Research: Space Physics*, 119(8):6865–6875, 2014. ISSN 2169-9402. doi: 10.1002/2014JA020299. URL http://dx.doi.org/10.1002/2014JA020299. 2014JA020299.

R. M. Thorne, B. Ni, X. Tao, R. B. Horne, and N. P. Meredith. Scattering by chorus waves as the dominant cause of diffuse auroral precipitation. *Nature*, 467:943–946, October 2010. doi: 10.1038/nature09467.

T. S. Trondsen and L. L. Cogger. High-resolution television observations of black aurora. *Journal of Geophysical Research: Space Physics*, 102(A1):363–378, 1997. ISSN 2156-2202. doi: 10.1029/96JA03106. URL http://dx.doi.org/10.1029/96JA03106.

Bruce T. Tsurutani, Barbara J. Falkowski, Jolene S. Pickett, Ondrej Santolik, and Gurbax S. Lakhina. Plasmaspheric hiss properties: Observations from polar. *Journal of Geophysical Research: Space Physics*, 120(1):414–431, 2015. ISSN 2169-9402. doi: 10.1002/2014JA020518. URL http://dx.doi.org/10.1002/2014JA020518. 2014JA020518.

J. A. Van Allen, G. H. Ludwig, E. C. Ray, and C. E. McIlwain. Observation of high intensity radiation by satellites 1958 alpha and gamma. *Journal of Jet Propulsion*, 28(9):588–592, 1958.

J. E. Wahlund, H. J. Opgenoorth, I. Häggström, K. J. Winser, and G. O. L. Jones. Eiscat observations of topside ionospheric ion outflows during auroral activity: Revisited. *Journal of Geophysical Research: Space Physics*, 97(A3):3019–3037, 1992. doi: 10.1029/91JA02438. URL https://doi.org/10.1029/91JA02438.

J. Wang, D.G. McCoy, A.J. Blake, and L. Torop. Effects of the close approach of potential curves in photoabsorption by diatomic moleculesii. temperature dependence of the o2 cross section in the region 130160 nm. *Journal of Quantitative Spectroscopy and Radiative Transfer*, 38(1):19 – 27, 1987. ISSN 0022-4073. doi: 10.1016/0022-4073(87)90106-3. URL https://doi.org/10.1016/0022-4073(87)90106-3.

Kaiti Wang, Yun-Ching Wang, Han-Tzong Su, Rue-Ron Hsu, and Tzu-Yuan Lin. Wave mode of the low-latitudinal elf-whistlers. *Journal of Geophysical Research: Space*

Physics, 116(A9), 2011. ISSN 2156-2202. doi: 10.1029/2011JA016832. URL http://dx.doi.org/10.1029/2011JA016832. A09323.

Yun-Ching Wang, Kaiti Wang, Han-Tzong Su, and Rue-Ron Hsu. Low-latitude elf-whistlers observed in taiwan. *Geophysical Research Letters*, 32(8), 2005. ISSN 1944-8007. doi: 10.1029/2005GL022412. URL http://dx.doi.org/10.1029/2005GL022412. L08102.

F. D. Wilder, G. Crowley, B. J. Anderson, and A. D. Richmond. Intense dayside joule heating during the 5 april 2010 geomagnetic storm recovery phase observed by amie and ampere. *Journal of Geophysical Research: Space Physics*, 117(A5), 2012. ISSN 2156-2202. doi: 10.1029/2011JA017262. URL http://dx.doi.org/10.1029/2011JA017262. A05207.

H.W. Wu, A Emadi, G Graaf, Johan Leijtens, and R.F. Wolffenbuttel. Design and fabrication of an albedo insensitive analog sun sensor. 25:527–530, 12 2011.

Qian Wu, W. Wang, R. G. Roble, Ingemar Hggstrm, and Anja Strmme. First daytime thermospheric wind observation from a balloon-borne fabry-perot interferometer over kiruna (68n). *Geophysical Research Letters*, 39(14), 2012. ISSN 1944-8007. doi: 10.1029/2012GL052533. URL http://dx.doi.org/10.1029/2012GL052533. L14104.

D. T. Young, S. Perraut, A. Roux, C. de Villedary, R. Gendrin, A. Korth, G. Kremser, and D. Jones. Wave-particle interactions near he+ observed on geos 1 and 2 1. propagation of ion cyclotron waves in he+-rich plasma. *Journal of Geophysical Research: Space Physics*, 86(A8):6755–6772, 1981. ISSN 2156-2202. doi: 10.1029/JA086iA08p06755. URL http://dx.doi.org/10.1029/JA086iA08p06755.

B. Zhang, W. Lotko, O. Brambles, M. Wiltberger, W. Wang, P. Schmitt, and J. Lyon. Enhancement of thermospheric mass density by soft electron precipitation. *Geophysical Research Letters*, 39(20), 2012. ISSN 1944-8007. doi: 10.1029/2012GL053519. URL http://dx.doi.org/10.1029/2012GL053519. L20102.

B. Zhang, R. H. Varney, W. Lotko, O. J. Brambles, W. Wang, J. Lei, M. Wiltberger, and J. G. Lyon. Pathways of f region thermospheric mass density enhancement via soft electron precipitation. *Journal of Geophysical Research: Space Physics*, 120(7):5824–5831, 2015. ISSN 2169-9402. doi: 10.1002/2015JA020999. URL http://dx.doi.org/10.1002/2015JA020999. 2015JA020999.